Measurement of the Neutrino Charged Current Coherent Pion Production Cross Section on Carbon and Oxygen with the T2K Near Detector

A thesis submitted in partial fulfilment of
the requirements for the award of
the degree of

Doctor of Philosophy

by

Paul Martins

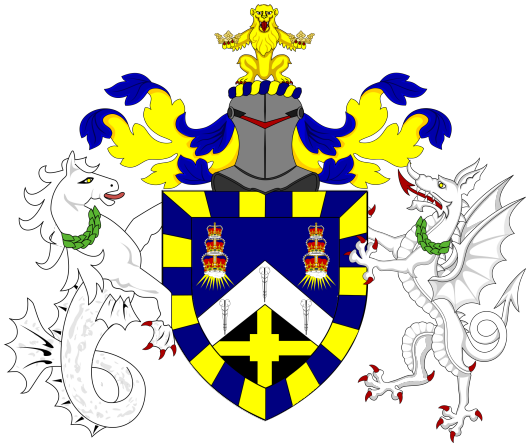

Queen Mary University of London,
School of Physics and Astronomy,
Particle Physics Research Centre,
United Kingdom

Submitted: July 4th, 2017

Assessment committee:

Dr. Marcella Bona

School of Physics and Astronomy, Queen Mary University of London, United Kingdom

Internal examiner

Dr. Jaroslaw Nowak

Physics Department, Lancaster University, United Kingdom

External examiner

Declaration

I, Paul Martins, confirm that the research included within this thesis is my own work or that where it has been carried out in collaboration with, or supported by others, that this is duly acknowledged below and my contribution indicated. Previously published material is also acknowledged below.

I attest that I have exercised reasonable care to ensure that the work is original, and does not to the best of my knowledge break any UK law, infringe any third party copyright or other Intellectual Property Right, or contain any confidential material.

I accept that the College has the right to use plagiarism detection software to check the electronic version of the thesis.

I confirm that this thesis has not been previously submitted for the award of a degree by this or any other university.

Signature:

Date:

Measurement of the Neutrino Charged Current Coherent Pion Production Cross Section on Carbon and Oxygen with the T2K Near Detector

Abstract

The goal of this thesis is to measure the coherent π^+ production cross section on carbon and oxygen nuclei, induced by muon neutrinos from the T2K beamline. This is performed using the tracker system of the off-axis near detector which consists of three argon gas Time Projection Chambers between which two Fine-Grained Detectors (FGD) are located. While the first FGD is made of plastic scintillator, the second one has alternate layers of scintillator and water which allows a measurement on oxygen target. The measurement on carbon target is reported as a function of the muon and pion momentum and angle, the sum of the pion and muon energies and the coplanarity angle between the muon and the pion. The statistics for the oxygen measurement remains too low and therefore an upper limit is set on both the differential cross sections and total flux-integrated cross section. The phase space considered is $0.2 < p_{\mu^-} < 5\,\mathrm{GeV/c}$, $\cos\theta_{\mu^-} > 0.7$, $0.15 < p_{\pi^+} < 1.5\,\mathrm{GeV/c}$, $\cos\theta_{\pi^+} > 0.45$, $0.5 < E_{\pi^+} + E_{\mu^-} < 6.5\,\mathrm{GeV}$, $\theta_{\pi^+\mu^-} > 90°$.

The values found for the flux-integrated cross section in the reduced phase-space are:

$$< \sigma_C >= 3.23 \pm 0.67(\mathrm{stat.}) \pm 0.82(\mathrm{syst.}) \times 10^{-40}\mathrm{cm}^2 \text{ per carbon nucleus}$$

$$\sigma_O \leq 9.57 \times 10^{-40}\mathrm{cm}^2 \text{ per oxygen nucleus, with } 95\,\% \text{ probability}$$

It was found that the 95 % upper limit on oxygen is always smaller than the Rein-Sehgal predictions, making this model unreliable for low neutrino energies. On the other hand, the limit remains compatible with the Berger-Sehgal model in every differential variables. The data for carbon target agree, within the systematic errors, with the Berger-Sehgal model except for pion momentum below 0.35 GeV/c and coplanarity angle below 155 degrees. In the latter cases an excess is observed in the data.

Acknowledgments

These four years were a real life experience on both professional and personal sides. Looking back to where I started, I would say that going from a master student, where you learn relatively old physics, to an active PhD student entering the territory of cutting-edge academic research first appears exciting. Little did I know about the joy of software debugging and other new physics related problems. Thankfully, I had the opportunity to meet a considerable number of inspiring people who made this transition feel smooth and easy. I will try my best to name everyone and I apologise in advance for the possible omissions.

Among them are many friends or T2K collaborators, or even both such as Leïla, Pierre, Laura and Simon. I really enjoyed the informal discussions about our respective analyses and will not forget the time we spent in Japan together. To them I should add all of the Queen Mary PhDs who contributed to the friendly atmosphere in the office, with a special mention to Sophie, Linda, Pierre and Nick who were always keen to answer my many questions about neutrinos and statistics, regardless of the time of the day.

My cross section analysis has allowed me to work within different subgroups in T2K. I owe a very important debt to Ryan who first introduced me to the world of neutrino interactions and events generators. His presence at Queen Mary was truly appreciated, not only for his technical help in getting NEUT running but also for the quality of his cultural references. I also thank Roberto who taught me everything I needed to know about the ECal Data Quality. Enrico and Anselmo made enormous contributions to the development of the various analysis softwares and to them I would like to show my greatest appreciation. I enjoyed working with you as much as I enjoyed our time in the karaoke booth in Tokai. Most of the detector systematics were calculated by the NuMu and NuE groups which deserve to be acknowledge. Many thanks to all their members for their incredible work and valuable feedback. Kendall, Callum and Andrea gave me warm encouragements and constructive comments for the cross section calculation and to them I want to say thank you very much. I would also like to express my gratitude to Jeanne and Teppei for their insightful comments, suggestions and availability within the department.

I would particularly like to thank my supervisor Prof. Francesca Di Lodovico without whom I wouldn't have been able to carry out this analysis. She trusted me at the start of my PhD and allowed me to work on some interesting phenomenology topics during my first year. As I joined T2K, she progressively let me more independence which allowed me to gain confidence and add my own contribution to T2K. Nevertheless, she always kept an eye on the progress of my thesis, making sure I didn't get lost.

I am also indebt to Dr. Marcella Bona and Dr Jaroslaw Nowak who kindly accepted to be my examiners.

The award of best flatmate goes undeniably to Dan, who became more than just a roommate. He truly contributed to sweep the thesis-related issues away from home while improving my knowledge about Switzerland politics. I couldn't thank him enough for all the fun I had living in London, for the endless discussions late at night, for the football skills and coding tips he taught me and for introducing me to Axel. To both of you guys, your generosity, understanding and mindset had a real positive influence on my personality.

Because I know they would never forgive me for not being represented, but especially because only them can tolerate my idiosyncrasies each time we get together, I address a big thanks to Mathieu, Loïc, Quentin and Mathilde. Meetings with you are always synonym of great fun and unexpected events, for the better or worse.

There are friends that I didn't see as often as I wished but they were always present whenever I needed them, which just illustrates how great and trustworthy they are. Starting by you Lucas, thank you for the couple of months we spend in London, for the long debates about existential problems of modern society and for your incomparable sarcasm. I would also like to thank the former members of Haddock's Eyes: Guillaume, Yann and Martin with whom I shared a passion for music and malt beverages. Of course this adventure would have been dull without our early hours fans: Anaïs, Yohann, Romain, Benoit, Clement and Charles. My thoughts also go to the NPAC 2012/2013 class, one of the craziest condensate of particle physicists and astrophysicists I ever met.

I would also like to thank Eunice for the patience and the composure she showed in the last steps of the analysis and the writing-up stage. Despite being busy, stressed and grumpy,

she still shared love and support during what was probably the most challenging moments of the PhD.

Last but not least, I am deeply grateful to my parents for their outstanding and constant support. They brought me the best possible education and environment that lead me to pursue a PhD in ideal conditions. Together with my sister Louise and my close relatives, they helped me keeping a cool head in many stressful and desperate situations.

Paul Martins

London, UK, July 2017

Preamble

The work described in the third part of this thesis would not have been possible without the help of many T2K collaborators. Therefore some pieces of the analysis don't entirely reflect my personal work. For examination purposes, it is important to clarify, in each analysis chapter, which parts are original contributions and which are not.

- Chapter 7

  This entire chapter reflects my own work. However it is worth mentioning that I worked in collaboration with Jakub Zmuda, who was in charge of implementing the same model in the NuWro generator, and Ryan Terri, who helped me getting started with NEUT.

- Chapter 8

  I implemented the selection cuts specific to the CC Coherent interaction. I also investigated the phase space and choose the differential variables. The ν_μ and ν_e groups developed the pre-selection cuts, up to the single pion cut.

- Chapter 9

  I spend some time investigating the background scale factors issues encountered in the case of low statistic samples. I was also in charge of the cross section extraction and developed the code to extract the limit.

- Chapter 10

  I implemented the vertex activity systematic error, from the control samples selection to the error propagation within the software. I also tuned the propagation of theoretical errors such that it matches the needs of the analysis. Please note that all the other detector systematic, statistical and flux errors were studied by other members of the collaboration.

- Chapter 11

  This chapter presents the final measurements of the analysis and reflect my own work.

Contents

List of Figures

List of Tables

Part I

Neutrino Physics

The elusive particle

With more than forty experiments currently running or planned in the near future and thousands of researchers, neutrino physics is without any doubt a very active field in the high energy physics community. Since the discovery of neutrino oscillations about two decades ago [1, 2], neutrino physicists managed to measure the oscillation parameters with a relatively good accuracy. However the elusive particles are yet to be completely understood: the mass hierarchy, the absolute mass scale, the octant degeneracy and the charge-parity violation in the leptonic sector of the Standard Model are the main known unknowns. They are the reasons driving neutrino experimentalists to enter into a precision era with new experiments under design studies such as Hyper-Kamiokande [3] and Deep Underground Neutrino Experiment (DUNE) [4]. Meanwhile, neutrino theorists are trying to develop mixing models and interactions models that are compatible with the latest experimental measurements.

The purpose of this first part is to introduce the building blocks of neutrino physics necessary to understand the analysis. The first chapter explains the specific place held by neutrinos within the framework of the Standard Model. Chapter 2 details the physics of neutrino oscillations, one of the most important characteristic of neutrinos for which the discovery was recently awarded a Nobel Prize. Last but not least, Chapter 3 summarises the different interactions in which a neutrino is involved with special emphasis on the coherent pion production models.

1

Neutrinos in the Standard Model

The Standard Model (SM) of particle physics is the reference theory to describe the interactions and the kinematics of subatomic particles. It uses a quantum field theory along with gauge principles to encompass the electromagnetic, the weak and the strong nuclear forces into a single framework. Developed in the second half of the XXth century, its predictions have now been successfully tested at an impressive level of accuracy thanks to the establishment of colliders such as the Tevatron in the USA and the large electron-positron collider (LEP) in Switzerland. However, the SM remains an effective theory as it completely passes over the gravitational interaction. Another weakness of the model concerns the prediction of massless neutrinos and one needs to go beyond that framework to understand how they acquire mass.

This chapter introduces the fundamental notions of the SM related to neutrino physics. It starts with a historical recap, from the very first thoughts of the existence of the neutrino to the much more complete theory of Glashow-Weinberg-Salam. A more detailed picture of the weak interaction is then presented. Finally, the most widespread mechanism in charge of explaining the neutrino masses known as the seesaw mechanism is briefly discussed.

1.1 Historical Introduction

The story of the particle physics starts at the beginning of the XXth century. In 1911, Rutherford with his gold foil experiment showed that the atoms were composed of a positively charged core. Therefore the nucleus was thought to be a bound state of A

protons and $A - Z$ electrons, both regarded as elementary particles. This is why the β-decay was initially described as a two-body process:

$$(\text{A, A-Z}) \rightarrow (\text{A, A-Z-1}) + e^- \tag{1.1}$$

This was confirmed in 1911-1912 by the first measurement of the energy spectrum of the β-electron by O. Van Bayer, O. Hahn and L. Meitner who observed a discrete spectrum. Three years later, James Chadwick performed a similar experiment with a mixture of ^{214}Pb and ^{214}Bi and he found a continuous spectrum, which is incompatible with a two-body decay. Several interpretations of this result followed in the next ten years such as energy loss of the electron caused by secondary effects (Meitner) or photon emitted by the nucleus via internal conversion providing energy to orbital electrons (Ellis). The debate was closed in 1927 with the Ellis and Wooster experiment who performed a calorimetric measurement with ^{210}Bi. The released heat they observed was compatible with a continuous β-spectrum [5]. The puzzle was only partly solved as the theoretical motivations in favour of a continuous spectrum were still lacking, which led Niels Bohr to question the energy conservation law for β-decay [6].

In December 1930, in an open letter addressed to nuclear physicists gathered in Tubingen, Wolfgang Pauli first proposed the idea of a neutral, light and weakly interacting fermion that would escape the nucleus along with the β-electron [7]. That letter is now regarded as the birth of the neutrino, even if Pauli initially named it neutron. Two years later, J.Chadwick discovered the existence of a penetrating radiation emitted from beryllium when bombarded by α particles. He concluded that these forms of radiation came from particles of mass close to the proton mass and charge 0 and therefore he named them neutrons, as we know them today [8, 9]. In order to avoid confusion between Chadwick's neutron and Pauli's hypothetical particle, the latter was renamed by Fermi "neutrino"[i] for the 1933 Solvay Congress. The following year, Fermi built the first theory of the weak interaction where he described the β-decay as a nuclear transition: a neutron transforms into a proton and an electron along with an antineutrino are created and emitted during this process [10, 11], similarly to a photon emission process [ii], as illustrated in Figure 1.1.

[i] meaning "little neutral" in Italian

[ii] It is amusing to see that Fermi's theory of weak interaction, despite being correct, was very controversial: the latter references were rejected by Nature publication board because it was "too remote from reality"

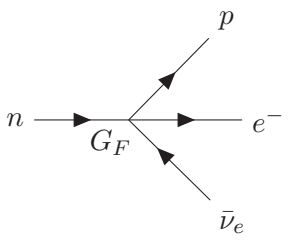

Figure 1.1: Feynman diagram of a β-decay according to Fermi's theory of weak interaction

Influenced by Dirac's quantum electrodynamics (QED) theory, Fermi later wrote the amplitude $\mathcal{A}_\beta$ of such a process as a coupling between two vector currents J_μ^{np} and $J_{e\bar{\nu}_e}^{\mu}$. The Fermi coupling constant G_F characterises the strength of the interaction:

$$\mathcal{A}_\beta = G_F \; J_\mu^{np} J_{e\bar{\nu}_e}^{\mu} = G_F(\bar{\psi}_p \gamma_\mu \psi_n)(\bar{\psi}_e \gamma^\mu \psi_{\bar{\nu}_e}) \tag{1.2}$$

where ψ are the fermion fields describing the particles and γ_i are the gamma (or Dirac) matrices.

In 1937, just one year after receiving the Nobel Prize for his observation of the first positron in cosmic rays, which validated Dirac's theoretical prediction of anti-matter particles [13], Carl Anderson and his student Seth Neddermeyer detected the first muon [14] and therefore confirmed the existence of a second family of particles. 1956 was a milestone year in neutrino physics: the first observation of a neutrino-type particle occurred near the Savannah river reactor, USA [15]. Reines and Cowan used a cadmium-enriched water target surrounded by liquid scintillator to tag the positron and neutron from an inverse beta decay signal:

$$\bar{\nu}_e + p \rightarrow e^+ + n \tag{1.3}$$

Later this year, the Wu experiment demonstrated that parity was not conserved by the weak interaction [16]. By looking at the angular distribution of the electrons emitted during the β-decay of a polarised ^{60}Co sample, Wu *et al.* concluded that the electrons favoured

and people like Sir A.S. Eddington didn't believe in the existence of the neutrino [12]

a specific direction: the one of the nuclear spin. That was a clear evidence of parity violation as one would have expected a more isotropic distribution if parity was conserved. Driven by this discovery, Golhaber *et al.* designed an experiment to determine the neutrino helicity [17] and their results were compatible with the "left-handed" hypothesis. These two astonishing experimental results matched the predictions of the neutrino two-components spinor theory by Lee and Yang, for which they received the Nobel Prize in 1957 [18, 19]. Inspired by this work, Feynman and Gell-Mann revised Fermi's interaction theory [20] in light of the work of Sudarshan and Marshak on the so called "vector minus axial" theory [21]. They introduced the coupling between vector terms γ_μ (Fermi transitions) and axial terms $\gamma_\mu\gamma^5$ (Gamow-Teller transitions) where $\gamma^5 = i\gamma^0\gamma^1\gamma^2\gamma^3$, ensuring that only left-handed neutrinos and right-handed antineutrinos interact. Hence the new amplitude is written:

$$\mathcal{A}_\beta = \left(\bar{\psi}_p\gamma_\mu(g_V - g_A\gamma^5)\psi_n\right)\left(\bar{\psi}_e\gamma^\mu(1-\gamma^5)\psi_{\bar{\nu}_e}\right) \tag{1.4}$$

The two constants g_V and g_A account for the hadronic process and can be derived from experimental measurements: $g_V = 1$, $g_A = 1.27$. In 1962, Lederman, Schwarz and Steinberger demonstrated the existence of another kind of neutrino, the muon neutrino ν_μ. This discovery was awarded the 1988 Nobel Prize [22]. These muon neutrinos were produced in the decay of charged pions, themselves produced using the first neutrino beam. Probing higher and higher energy processes led to unveil discrepancies between V-A theory predictions and experimental data. Indeed, in the simple example of the electron-neutrino elastic scattering, the cross section is proportional to the centre of mass energy s and therefore diverges as $s \to \infty$. In analogy with electrodynamics, Glashow was the first to propose a solution to that problem by suggesting that the weak interaction could be mediated by bosons [23]. Salam and Weinberg later developed this idea and unified the electromagnetic and the weak forces into the electroweak force [24, 25], a gauge theory based on $SU(2) \times U(1)$ symmetry which is spontaneously broken into $U(1)$ by the Higgs mechanism [26, 27]. In this theory, three massive bosons, W^+, W^- and Z^0 mediate the weak interaction. While the first two are responsible of charged current interactions, the Z^0 intervenes in neutral current ones. The observation of neutral current in 1973 [28] and the further direct detection of the $W^\pm$, Z^0 and Higgs bosons confirmed the robustness of

the GSW theory [29, 30, 31, 32].

Finally, the τ lepton was discovered in 1975 at Fermilab [33] and Perl and Reines shared the Nobel Prize in 1995 for discovering this third family of particles. Nevertheless, it took 25 years before the ν_τ was first observed by the DONUT experiment [34] at Fermilab.

1.2 The Weak Interaction

Among the three interactions encompassed in the theory of the Standard Model (SM), the weak interaction is certainly the most relevant to discuss when it comes to neutrinos. Indeed, unlike quarks and charged leptons, neutrinos are the only elementary particles of matter to interact via the weak force only, as shown in Table 1.1. Therefore, a brief overview of the electroweak part of the SM and its spontaneous symmetry breaking is necessary to understand the basic features of neutrino physics. This topic is however described in great details in Chapter 20 of [35].

Table 1.1: Properties of the Standard Model elementary particles of matter (fermions). The masses are extracted from [36]. The interactions are represented by their initials: strong (S), weak (W) or electromagnetic (EM). One can easily build a similar table for anti-particles by simply reversing the sign of the electric charge.

	Generation	Flavour	Mass	EM Charge	Interaction
Quarks	1^{st}	u	$2.3^{+0.7}_{-0.5}\,\mathrm{MeV/c^2}$	2/3	S, W, EM
		d	$4.8^{+0.5}_{-0.3}\,\mathrm{MeV/c^2}$	-1/3	S, W, EM
	2^{nd}	c	$1.275 \pm 0.025\,\mathrm{GeV/c^2}$	2/3	S, W, EM
		s	$95 \pm 5\,\mathrm{MeV/c^2}$	-1/3	S, W, EM
	3^{rd}	t	$173.21 \pm 1.22\,\mathrm{MeV/c^2}$	2/3	S, W, EM
		b	$4.18 \pm 0.03\,\mathrm{GeV/c^2}$	-1/3	S, W, EM
Leptons	1^{st}	e	$510.99\,\mathrm{keV/c^2}$	-1	W, EM
		ν_e	$< 2\,\mathrm{keV/c^2}$	0	W
	2^{nd}	μ	$105.66\,\mathrm{MeV/c^2}$	-1	W, EM
		ν_μ	$< 190\,\mathrm{keV/c^2}$	0	W
	3^{rd}	τ	$1.776\,\mathrm{GeV/c^2}$	-1	W, E
		ν_τ	$< 18.2\,\mathrm{MeV/c^2}$	0	W

Note that in Table 1.1, the charge corresponds to the electric charge, in unit of e. The strong charges, namely the colours of the quarks, are not detailed but each quark can be

in a red, blue or green state.

1.2.1 Electroweak Lagrangian

This section briefly describes the lepton and gauge bosons interaction terms of the electroweak lagrangian. The mass terms resulting of the interaction with the Higgs field are detailed soon after.

The electroweak sector of the SM is described by the $SU(2)_L^g \times U(1)_Y^{g'}$ gauge group where L and Y denote the left-handed chirality and the hypercharge, respectively. g and g' denote their coupling constants. Given the order of the groups, we assign three gauge bosons to $SU(2)$ that we denote W_a^μ with $a = 1$, 2 or 3 and one gauge boson B^μ for $U(1)$. In order to ensure the local gauge invariance of the lagrangian, the covariance derivative is written as:

$$D^\mu = \partial^\mu - ig \sum_{a=1}^{3} W_a^\mu T_a - ig' B^\mu Y \tag{1.5}$$

where T_a, the isospin vector) and Y (the hypercharge) are the generators of the $SU(2)$ and $U(1)$ groups respectively. They are related by the Gell-Mann Nishijima relation which unifies weak and electromagnetic interaction:

$$Q = T_3 + Y \tag{1.6}$$

with Q the electric charge operator and T_3 the third component of the isospin. Five fermion fields can be distinguished in the Standard Model, where the left-handed components of the lepton and quark sectors are grouped into weak isospin doublets. Note that in this two-dimensional representation, the $SU(2)$ generators are related to the Pauli matrices by just a factor two: $T_a = \sigma_a/2$. Table 1.2 gives the eigenvalues of Q, T_3 and Y operators when acting on the fermion fields ψ enumerated below, where $\ell = \{e, \mu, \tau\}$, $q_u = \{u, c, t\}$ and $q_d = \{d, s, b\}$.

$$L_{\ell L} = \begin{pmatrix} \nu_{\ell L} \\ \\ \ell_L \end{pmatrix}, Q_L = \begin{pmatrix} q_{uL} \\ \\ q_{dL} \end{pmatrix}, \ell_R, q_{uR}, q_{dR}$$

Table 1.2: Eigenvalues of the Q, T_3 and Y operators acting on each of the fermion field, gauge boson (here the photon field is represented as A) and Higgs fields h

	$L_{\ell L}$	Q_L	ℓ_R	q_{uR}	q_{dR}	$W^\pm$	Z^0	A	h
Q	(0, -1)	(⅔, -⅓)	-1	⅔	-⅓	$\pm$ 1	0	0	0
T_3	(½, -½)	(½, -½)	0	0	0	$\pm$ 1	0	0	$-\frac{1}{2}$
Y	-½	⅙	-1	⅔	-⅓	0	0	0	½

Similarly to T_3, the two operators T_1 and T_2 only act on the left-handed fields, therefore $T_1\psi_R = T_2\psi_R = 0$. Moreover, deriving the coupling between the $W_{1,2}$ and the fermion doublets reveals the charged current terms $\bar{\nu}_{\ell R}(W_1^\mu - iW_2^\mu)\ell_L$ and $\bar{\ell}_R(W_1^\mu + iW_2^\mu)\nu_{\ell L}$ in the anti-diagonal of D^μ. It is therefore useful to define the $W_\pm^\mu$ operators which create W^+ and W^- particles respectively.

$$W_+^\mu = \frac{W_1^\mu - iW_2^\mu}{\sqrt{2}}\ , \quad W_-^\mu = \frac{W_1^\mu + iW_2^\mu}{\sqrt{2}} \tag{1.7}$$

The same method can be applied to the diagonal terms which represent the neutral current. However we observe in the term $\bar{\nu}_{\ell R}(gW_3^\mu/2 - g'B^\mu/2)\nu_{\ell L}$ that both W_3 and B bosons couple to the neutrino field, which is problematic as one of these two bosons needs to mediate the electromagnetic force. By rotating the $(W_3^\mu,\ B^\mu)$ basis by an angle θ_w called the weak mixing angle (or Weinberg angle), we define two new operators A^μ and Z^μ that must be responsible of the photon and Z^0 creation, respectively.

$$\begin{aligned} A^\mu &= \sin\theta_w W_3^\mu + \cos\theta_w B^\mu \\ Z^\mu &= \cos\theta_w W_3^\mu - \sin\theta_w B^\mu \end{aligned} \tag{1.8}$$

If we replace W_3^μ and B^μ by A^μ and Z^μ, the coupling to the neutrino and charged lepton fields becomes

$$\begin{aligned} &\bar{\nu}_{\ell R}\left[\frac{g}{2}(\sin\theta_w A^\mu + \cos\theta_w Z^\mu) - \frac{g'}{2}(\cos\theta_w A^\mu - \sin\theta_w Z^\mu)\right]\nu_{\ell L} \\ &\bar{\ell}_R\left[-\frac{g}{2}(\sin\theta_w A^\mu + \cos\theta_w Z^\mu) - \frac{g'}{2}(\cos\theta_w A^\mu - \sin\theta_w Z^\mu)\right]\ell_L \end{aligned} \tag{1.9}$$

The requirement that the neutrino can only interact with Z^μ and that the eigenvalue of A^μ acting on the electron field should be the elementary charge e allows to find the relationship

between g, g', θ_w and e given below:

$$g = \frac{e}{\sin\theta_w} \ , \quad g' = \frac{e}{\cos\theta_w} \tag{1.10}$$

We have now all the ingredients to derive the minimal, local gauge invariant, lagrangian describing the interactions between fermions and gauge bosons. Few reorganisation steps in the covariant derivative are required to go from the set of operators (W_1^μ, W_2^μ, W_3^μ, B^μ) to the new introduced ones (W_+^μ, W_-^μ, Z^μ, A^μ). The new covariant derivative is:

$$D^\mu = \partial^\mu - i\frac{g}{\sqrt{2}}\left(W_+^\mu T_+ + W_-^\mu T_-\right) - i\frac{g}{\cos\theta_w}Z^\mu\left(T^3 - \sin^2\theta_w Q\right) - ieA^\mu Q \tag{1.11}$$

where we introduce $T_\pm = (\sigma_1 \pm i\sigma_2)/2$. The fermion lagrangian now reads:

$$\begin{aligned}
\mathcal{L}_{\text{fermion}} &= i\bar{\psi}\gamma_\mu D^\mu\psi \\
\mathcal{L}_{\text{fermion}} &= i\bar{\psi}\gamma_\mu\partial^\mu\psi \\
&\quad + \frac{g}{\sqrt{2}}\bar{\psi}\gamma_\mu(W_+^\mu T_+ + W_-^\mu T_-)\psi \\
&\quad + \frac{g}{\cos\theta_w}\bar{\psi}\gamma_\mu Z^\mu(T_3 - \sin^2\theta_w Q)\psi + e\bar{\psi}\gamma_\mu A^\mu\psi
\end{aligned} \tag{1.12}$$

where the first, second and third lines represent the fermion kinetic term, the charged-current and neutral current interactions, respectively.

In order to describe the gauge boson self interaction, two new tensors $W_a^{\mu\nu}$ and $B^{\mu\nu}$ are defined.

$$\begin{aligned}
W_a^{\mu\nu} &= \partial^\mu W_a^\nu - \partial^\nu W_a^\mu + g\varepsilon^{abc}W^{\mu,b}W^{\nu,c} \\
B^{\mu\nu} &= \partial^\mu B^\nu - \partial^\nu B^\mu
\end{aligned} \tag{1.13}$$

The extra term in $W^{\mu\nu}$ is due to the non-abelian character of $SU(2)$, allowing the self-interaction of weak gauge bosons, and ε_{abc} is the three dimensions Levi-Civita symbol. The lagrangian term is written:

$$\mathcal{L}_{\text{boson}} = -\frac{1}{4}W_a^{\mu\nu}W_{a,\mu\nu} - \frac{1}{4}B^{\mu\nu}B_{\mu\nu} \tag{1.14}$$

This includes cubic and quartic self-interactions between gauge bosons. One can again

perform the same substitution than in the fermion lagrangian to extract the $W^{\pm}, Z$ and A self couplings in terms of g and θ_w. The result of this tedious derivation is given in Appendix A.

1.2.2 Spontaneous Symmetry Breaking

In order to include the lepton and gauge boson mass terms, an additional complex scalar field ϕ is introduced to break spontaneously the $SU(2) \times U(1)$ symmetry. ϕ is chosen as $SU(2)$ doublet with a charged component ϕ^+ and a neutral component ϕ^0

$$\phi = \frac{1}{\sqrt{2}} \begin{pmatrix} \phi^+ \\ \\ \phi^0 \end{pmatrix} \tag{1.15}$$

The introduction of this new field adds an extra term $\mathcal{L}_H$ to the lagrangian which is written as the usual kinetic term minus a quartic potential $V(\phi) = \lambda(\phi^*\phi - v^2/2)^2$, with v its vacuum expectation value. The shape of V is given in Figure 1.2 for $\lambda = 1$ and $v = 4$.

$$\mathcal{L}_H = |D^\mu \phi|^2 - \lambda(\phi^*\phi - v^2/2)^2 \tag{1.16}$$

Apart from the trivial case where $v = 0$, V reaches its minimum for $|\phi|^2 = \frac{v^2}{2} \neq 0$. Hence ϕ acquires a non trivial vacuum expectation value (VEV) $\langle\phi\rangle$ which breaks the $SU(2)_L \times U(1)_Y$ symmetry into $U(1)_{EM}$ and is expressed as:

$$\langle\phi\rangle = \frac{1}{\sqrt{2}} \begin{pmatrix} 0 \\ \\ v \end{pmatrix} \tag{1.17}$$

To derive the physical properties of the gauge bosons, it is convenient to write the fluctuations of ϕ around the VEV by introducing the real scalar fields ξ_a and h:

$$\phi = \frac{1}{\sqrt{2}} exp\left(\frac{i}{v} T_a \xi_a\right) \begin{pmatrix} 0 \\ \\ v + h \end{pmatrix} \tag{1.18}$$

It is clear that the ξ_a can be rotated away by a $SU(2)_L$ gauge transformation. Doing so,

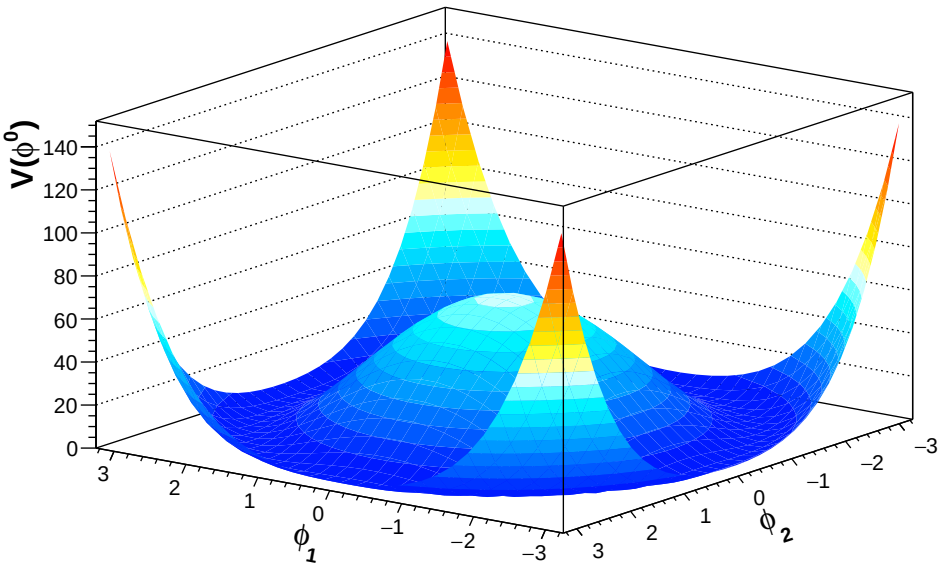

Figure 1.2: Shape of the Higgs potential $V(\phi^0)$ taken for $\lambda = 1$ and $v = 4$. The x and y axis represent ϕ_1 and ϕ_2, the real and imaginary parts of ϕ^0 respectively.

we define the unitary gauge. The field h corresponds to the physical Higgs boson. In the unitary gauge, the Higgs field ϕ simply reads:

$$\phi = \frac{1}{\sqrt{2}} \begin{pmatrix} 0 \\ v + h \end{pmatrix} \tag{1.19}$$

Deriving equation (1.16) with the expression (1.19) for ϕ gives the Higgs kinetic term, mass term and self-coupling terms. The gauge boson mass terms and their couplings to the Higgs field also appear explicitly as shown below:

$$\begin{aligned} \mathcal{L}_H = & \frac{1}{2}(\partial_\mu h)^2 - \frac{1}{2}\left[\sqrt{2\lambda}v\right]^2 h^2 - \lambda v h^3 - \frac{\lambda}{4}h^4 \\ & + \frac{1}{2}\left[\frac{gv}{2}\right]^2 (W_{+\mu}W_+^\mu + W_{-\mu}W_-^\mu) + \frac{1}{2}\left[\frac{gv}{2\cos\theta_w}\right]^2 Z_\mu Z^\mu \\ & + \frac{g^2 v}{4}(W_{+\mu}W_+^\mu + W_{-\mu}W_-^\mu)h + \frac{g^2}{8}(W_{+\mu}W_+^\mu + W_{-\mu}W_-^\mu)h^2 \\ & + \frac{g^2 v}{4\cos^2\theta_w} Z_\mu Z^\mu h + \frac{g^2}{8\cos^2\theta_w} Z_\mu Z^\mu h^2 \end{aligned} \tag{1.20}$$

The first line of equation (1.20) represents the Higgs boson kinetic term, its mass term where $m_h = \sqrt{2\lambda v^2}$ and the cubic and quartic self-interaction respectively. The mass terms of the gauge bosons appear in the square brackets of second row with $m_W = \frac{gv}{2}$ and $m_Z = \frac{gv}{2\cos\theta_w}$. Note that there is no mass term for A_μ as the photon must be massless Finally the third and fourth rows contain the couplings of the gauge bosons with 1 or 2 Higgs bosons, respectively.

1.2.3 Yukawa Coupling

The last piece necessary to complete the elecro-weak lagrangian concerns the charged leptons mass terms. The introduction of the Higgs field in the previous section requires to consider an extra term $\mathcal{L}_Y$ which couples the contraction of left-handed fermions and Higgs field ϕ with the right-handed fermions. The construction of such a gauge invariant lagrangian leads to write:

$$\mathcal{L}_Y = -\sum_{\alpha,\beta=e,\mu,\tau} Y_{\alpha\beta}(\bar{L}_{\alpha L}\phi)\ell_{\beta R} - \sum_{(\alpha,\beta)\in 1,2,3} Y_{\alpha\beta}(\bar{Q}_{\alpha L}\phi)q_{d\beta R} + \text{h.c.} \tag{1.21}$$

where α, β represent the family of the leptons and quarks. Note that the right-handed up-type quark does not appear in equation (1.21). Indeed, in order to preserve the gauge invariance, the up-type quark field needs to couple to a Higgs doublet $\tilde{\phi}$ of hypercharge $Y = -1$. It is possible to obtain such a field from the known ϕ with the transformation $\tilde{\phi} = iT_2\phi$. If the Higgs field is taken at its VEV, it gives::

$$\tilde{\phi} = iT_2\phi = \frac{1}{\sqrt{2}}\begin{pmatrix} v+h \\ \\ 0 \end{pmatrix} \tag{1.22}$$

The lagrangian term for up-type quark is therefore :

$$\mathcal{L}_Y = -\sum_{\alpha,\beta=1,2,3} Y_{\alpha\beta}(\bar{Q}_{\alpha L}.\tilde{\phi})q_{u\beta R} + \text{h.c.} \tag{1.23}$$

Each matrix $Y_{\alpha\beta}$ is diagonalised using the singular value decomposition method: $Y = UMV^*$ where M is the diagonal mass matrix and U and V are unitary matrices that change the left-handed and right-handed fields respectively from interaction states to mass

states: $\ell_L \to U_\ell \ell_L$, $\nu_{\ell L} \to U_\ell \nu_{\ell L}$, $\ell_R \to V_\ell \ell_R$, $q_{uL} \to U_{uL} q_{uL}$, $q_{dL} \to U_{dL} q_{dL}$, $q_{uR} \to V_u q_{uR}$, $q_{dR} \to V_d q_{dR}$. In this new basis, the equations (1.21) and (1.23) are evaluated for ϕ fluctuating around its VEV.

$$\begin{aligned}\mathcal{L}_Y = & -\sum_{\alpha=e,\mu,\tau}\left(\left[\frac{vM^{\ell}_{\alpha\alpha}}{\sqrt{2}}\right]\overline{\ell}_{\alpha L}.\ell_{\alpha R} + \frac{M_{\alpha\alpha}}{\sqrt{2}}\overline{\ell}_{\alpha L}.\ell_{\alpha R}.h\right) \\ & -\sum_{\alpha=1,2,3}\left(\left[\frac{vM^{u}_{\alpha\alpha}}{\sqrt{2}}\right]\overline{q_u}_{\alpha L}.q_{u\alpha R} + \frac{M_{\alpha\alpha}}{\sqrt{2}}\overline{q_u}_{\alpha L}.q_{u\alpha R}.h\right) \\ & -\sum_{\alpha=1,2,3}\left(\left[\frac{vM^{d}_{\alpha\alpha}}{\sqrt{2}}\right]\overline{q_d}_{\alpha L}.q_{d\alpha R} + \frac{M_{\alpha\alpha}}{\sqrt{2}}\overline{q_d}_{\alpha L}.q_{d\alpha R}.h\right) + \text{h.c.}\end{aligned} \tag{1.24}$$

The first line of (1.24) corresponds to the mass terms of charged leptons where for example $m_e = \dfrac{vM^{\ell}_{ee}}{\sqrt{2}}$, followed by their interaction term with the Higgs boson. The second and third lines are similar for the up-type quark and down-type quark, respectively. Notice that the coupling to the Higgs is proportional to $\dfrac{M^{\ell}_{\alpha\alpha}}{\sqrt{2}} = \dfrac{g m_\ell}{2m_W}$, which means that the heavier is the fermion, the more important is the Higgs coupling. Moreover, none of the terms in equation (1.24) involves the neutrinos which are therefore massless in the Standard Model.

To summarise, the neutrinos are the only particles that interact only via the weak force. The theoretical framework of such an interaction was established by Glashow, Weinberg and Salam [24, 25] around 1965 and provides an explanation for the masses of bosons and fermions through the Higgs mechanism. It is described by the lagrangian $\mathcal{L}_{GWS} = \mathcal{L}_{\text{fermion}} + \mathcal{L}_{\text{boson}} + \mathcal{L}_H + \mathcal{L}_Y$. However, we know from neutrino oscillations, discussed in Chapter 2, that neutrino must acquire somehow a mass. Hence, one needs to go beyond the Standard Model and the GWS theory to describe neutrino masses.

1.3 Neutrino Mass

There are two approaches that one could take regarding the addition of a neutrino mass terms in the SM. They both rely on the nature of the neutrinos: whether they are Dirac particles like the other fermions, or Majorana particles.

The first and most straightforward way is to add a Dirac right-handed neutrino field $\nu_{\ell R}$, even if such a particle has not been observed yet. Indeed, it is a singlet under $SU(2)_L$ and has no charge (nor hypercharge) which means it does not couple to any of the gauge bosons and is therefore called "sterile". Introducing this field leads to a so called Dirac mass term $m_{\nu_\alpha}\overline{\nu_\alpha}_L.\nu_{\alpha R}$, where $m_{\nu_\alpha} = \frac{vM^\nu_{\alpha\alpha}}{\sqrt{2}}$ (similarly to the one found in Section 1.2.3). $M^\nu_{\alpha\beta}$ is the diagonal neutrino mass matrix.

$$\mathcal{L}_{Dirac} = -\sum_{\alpha=1,2,3}\left(\left[\frac{vM^\nu_{\alpha\alpha}}{\sqrt{2}}\right]\overline{\nu}_{\alpha L}.\nu_{\alpha R} + \frac{M^\nu_{\alpha\alpha}}{\sqrt{2}}\overline{\nu}_{\alpha L}.\nu_{\alpha R}.h\right) + \text{h.c.} \tag{1.25}$$

In order for $M^\nu_{\alpha\beta}$ to be diagonal, the change of basis $\nu_R \to V_\nu \nu_R$ is performed, like in the quark and charged lepton sectors. The second term in the right-hand side of equation (1.25) shows the neutrino coupling to the Higgs boson. From Table 1.1, one notices that the absolute values of the neutrino masses have not yet been measured and only upper limits have been set. These limits are far below the other fermion masses, and this phenomenon remains unexplained by this mechanism.

The second approach is based on the assumption that neutrino are Majorana particles. Ettore Majorana was the first to suggest that a fermion carrying no electric charge could be its own anti-particle [37], writing the Majorana condition:

$$\nu^C_L = \mathcal{C}\overline{\nu_L}^T \tag{1.26}$$

where ν^C_L denotes the charge conjugate partner of ν_L, T is the transpose operator and $\mathcal{C}$ s the charge conjugation matrix. In that scenario, the charge parity operator $\mathcal{C}$ applied to the left-handed neutrino field ν_L [iii] gives a right-handed neutrino field. Under the assumption that neutrinos satisfy equation (1.26) one can write a Majorana mass term:

$$\mathcal{L}_{Majorana} = -\frac{1}{2}m\overline{\nu^C_L}\nu_L + \text{h.c.} \tag{1.27}$$

Note the factor 1/2 is to avoid double counting since ν_L and ν^C_L are related by (1.26). The Majorana condition also shows that, unlike Dirac, Majorana mass term allows mixing between neutrinos and antineutrinos and therefore violates the conservation of lepton

[iii] In reality, it is applied to the adjoint of the left-handed neutrino field, which is then transposed

number. However this could not couple to any Higgs field since a term like $\overline{\nu_L^C}\nu_L$ have $T_3 = 1$ and $Y = -2$ which are different from the known Higgs boson h (that has $(T_3, Y) = (-1/2, 1)$). Introducing a right-handed "heavy" neutrino field N_R with $T_3 = 0$ and $Y = 0$ and considering $N_R^C = N_L$ would fix this issue. A mass matrix M^ν containing Dirac-like m_D and Majorana-like m_L and m_R mass matrices can be built:

$$\mathcal{L}_{\nu \text{ mass}} = -\frac{1}{2}\left(\overline{\nu_L^C}\ \overline{N_L^C}\right) \underbrace{\begin{pmatrix} m_L & m_D^T \\ m_D & m_R \end{pmatrix}}_{M^\nu} \begin{pmatrix} \nu_L \\ N_L \end{pmatrix} \tag{1.28}$$

where we set $m_L = \mathbb{0}$ to allow Higgs coupling. In the approximation where $\|m_R\| \gg \|m_D\|$ and $\|m_D\|$ of the order of other SM fermions, M^ν can be diagonalised by block[iv]. This gives rise to mass eigenstate mixing ν_L and N_L and two sets of mass eigenvalues: small masses for left-handed neutrino mass eigenstates and heavy masses for the right-handed neutrinos.

$$W^T M^\nu W \simeq \begin{pmatrix} M_{\text{light}} & 0 \\ 0 & M_{\text{heavy}} \end{pmatrix} \tag{1.29}$$

where we have

$$\begin{aligned} m_\nu &\simeq \|M_{\text{light}}\| = \|m_D\|^2 . \|m_R\|^{-1} \\ m_N &\simeq \|M_{\text{heavy}}\| = \|m_R\| + \|m_D\|^2 . \|m_R\|^{-1} \end{aligned} \tag{1.30}$$

Despite requiring the neutrino to be Majorana and adding an extra heavy right-handed neutrino field to the SM that is yet to be observed, this mechanism, named seesaw mechanism, is one of the best candidate to explain the smallness of the neutrino masses.

The fact that neutrinos are Majorana has not been proved yet but is currently investigated by several experiment such as SNO+ [38], MAJORANA [39], GERDA [40], EXO-200 [41] and Cuore [42]. Most of these experiments rely on the observation of a neutrino-less double beta decay as a clear signature of Majorana neutrinos [43].

[iv] Up to corrections of the order $\|m_R\|^{-1} . \|m_D\|$

2

Neutrino Oscillations

The Standard Model predicts that neutrinos must be massless particles, as discussed in Section 1.2.3. However, the discovery of neutrino oscillations in the second half of the XX$^{\text{th}}$ century was a definitive evidence that this theory must be overhauled. Indeed, neutrino oscillations occur as different massive neutrino states interfere coherently, leading to the detection of a neutrino flavour different from the flavour in which it was produced. This chapter first deals with the discovery of this phenomenon before going through its theoretical description. Finally, the experimental evidences are reviewed.

2.1 The Solar Neutrino Problem

The American chemist William Harkins first proposed the idea that stars could gain their energy through nuclear fusion, in particular in the fusion of 4 hydrogen nuclei [44]. This was the premises of the stellar nucleosynthesis. The mechanisms known today as the proton-proton chain reaction as well as the CNO cycle came 23 years later in 1939 when Hans Bethe published his works about the energy production mechanisms in stars [45]. Both mechanisms produce neutrinos and because of their small cross sections, they escape the Sun's core to give the solar neutrino energy spectrum represented in Figure 2.1.

John Bahcall is the first to give an estimate of the number of solar neutrinos, mainly from ^{7}Be and ^{8}B, that can be detected at the Earth surface [47]. His calculation uses the reaction

$$\nu_e + {}^{37}\text{Cl} \rightarrow {}^{37}\text{Ar} + e^- \tag{2.1}$$

In 1968, the Homestake experiment led by Ray Davis announces the first detection of solar neutrinos [48]. By counting the number of argon nuclei in a tank filled with C_2Cl_4, they always observe about only a third of what was predicted by Bahcall, even after 25 years of

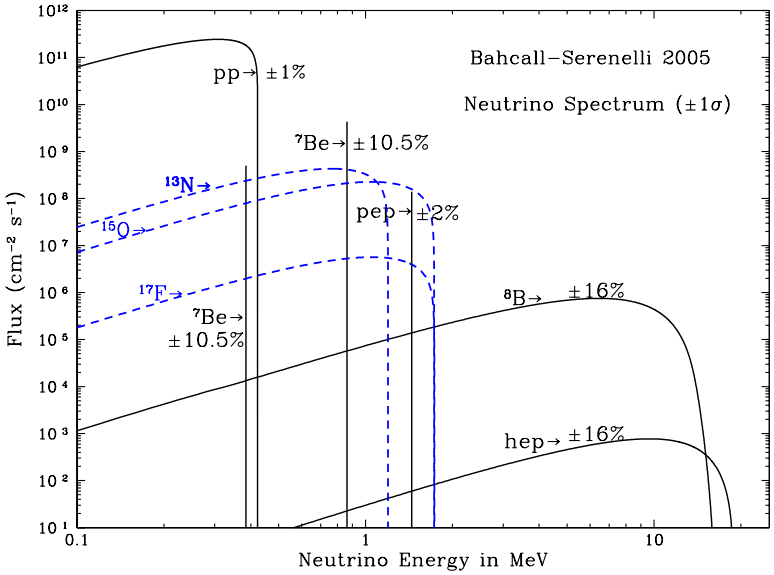

Figure 2.1: Solar neutrino energy spectrum. The black curves represent the neutrinos that originate from the pp chain while the blue dashed curves are for the neutrinos emitted during the beta decays in the CNO cycle [46]. The percentages show the fractional 1σ uncertainties.

data taking. In order to check this result, other radiochemical experiments such as SAGE [49] and GALLEX [50] were designed in the late '80s. These used ^{71}Ga instead of ^{37}Cl in order to have a lower energy threshold, and therefore be more sensitive to solar neutrinos from pp fusion. Around that time, the KamiokaNDE experiment [51] also looked at solar neutrinos via elastic scattering on electrons

$$\nu_e + e^- \rightarrow \nu_e + e^- \tag{2.2}$$

As we see in the three leftmost rates comparisons in Figure 2.2, all of these experiments observed less neutrinos than what was predicted by Bahcall. This puzzle, known as the solar neutrino problem, was a big concern: it was important to understand which one between the Sun model or the experiments was wrong.

The answer is that both were right, but the neutrino propagation from the Sun to the Earth did not occur as expected. The idea of neutrino oscillation first came from Pontecorvo in 1960 [53]. Using the analogy with kaon oscillations, he proposed a theory in which neutrinos can oscillate into antineutrinos. Soon after, Maki, Nakagawa and Sakata developed a

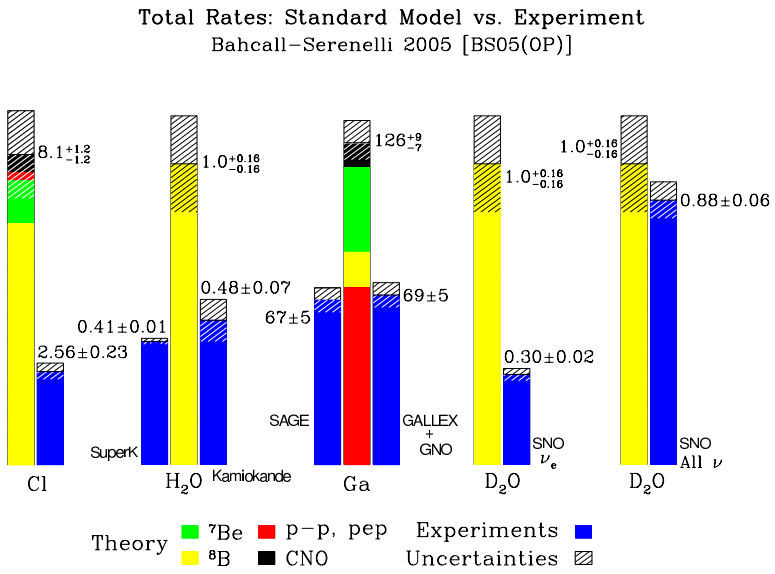

Figure 2.2: Total neutrino detection rates expected from the Solar Standard Model vs experimental results (blue). The rates are calculated by dividing the predicted (for the model) or observed (for the experiment) flux by the total flux [52].

theory of two flavours neutrino mixing where an electron neutrino turns into a muon neutrino, under the hypothesis that the two neutrinos are massive and their mass difference is very small [54]. This mechanism later generalised to the three flavours would explain the neutrino deficit because all the experiments were sensitive to the electron neutrino, they were not able to see the fraction of electron neutrinos that oscillate into muon and tau neutrino. This was confirmed when the formalism of neutrino oscillations in matter was derived (see Section 2.2.2).

2.2 The Oscillation Framework

We discussed in Section 1.3 that the neutrino mass terms arise from the seesaw mechanism, where the mass matrix M^ν contains Dirac and Majorana masses. M^ν is diagonalisable by block and this is done thanks to the matrix W in equation (1.29), for which the expression

as a function of m_D and m_R can be derived:

$$W = \begin{pmatrix} W_\nu & (m_R^{-1} m_D)^\dagger W_N \\ -(m_R^{-1} m_D) W_\nu & W_N \end{pmatrix} \tag{2.3}$$

W_ν and W_N represent here the mixing matrices of left-handed and right-handed neutrinos, respectively. In the limit where $\left\| m_R^{-1} m_D \right\| \ll 1$, the anti-diagonal terms in W becomes negligible and therefore, light and heavy neutrinos do not mix together. Using the convention that charged lepton mass eigenstates correspond to the flavour states, the charged current fermion lagrangian reads:

$$\mathcal{L}^{\text{CC}}_{\text{fermion}} = \frac{g}{\sqrt{2}} \overline{\nu}_L W_\nu^\dagger \gamma_\mu (W_+^\mu T_+ + W_-^\mu T_-) U_\ell \ell_L \tag{2.4}$$

where the matrix U_ℓ was defined in Section 1.2.3. The neutrino flavour states associated to the lepton flavour states are therefore defined as

$$\begin{pmatrix} \nu_e \\ \nu_\mu \\ \nu_\tau \end{pmatrix} = U_{PMNS} \begin{pmatrix} \nu_1 \\ \nu_2 \\ \nu_3 \end{pmatrix} \tag{2.5}$$

where $U_{PMNS} = U_\ell^\dagger W_\nu$ is the three-flavour neutrino mixing matrix named after Pontecorvo, Maki, Nakagawa and Sakata. U_{PMNS} is a unitary matrix that and therefore can be parametrised with 3 angles and 3 phases.

$$U_{PMNS} = \begin{pmatrix} 1 & 0 & 0 \\ 0 & c_{23} & s_{23} \\ 0 & -s_{23} & c_{23} \end{pmatrix} \begin{pmatrix} c_{13} & 0 & s_{13} e^{-i\delta} \\ 0 & 1 & 0 \\ -s_{13} e^{i\delta} & 0 & c_{13} \end{pmatrix} \begin{pmatrix} c_{12} & s_{12} & 0 \\ -s_{12} & c_{12} & 0 \\ 0 & 0 & 1 \end{pmatrix} \begin{pmatrix} e^{i\varphi_1} & 0 & 0 \\ 0 & e^{i\varphi_2} & 0 \\ 0 & 0 & 1 \end{pmatrix} \tag{2.6}$$

where $c_{ij} = \cos\theta_{ij}$ and $s_{ij} = \sin\theta_{ij}$ are the cosines and sines of the 3 mixing angles. In the case where the neutrinos are Dirac particles, two of the three phases can be absorbed by rephasing two Dirac charged-lepton fields. This process does not affect the respective kinetic and (Dirac) mass Lagrangians given in equations (1.12) and (1.24). Therefore only

one Dirac phase δ remains in the PMNS matrix. This phase is also called the charge-parity (CP) phase. On the other hand, if neutrinos are Majorana particles, the phases cannot be eliminated by a rephasing of the fields because the Majorana mass term given in equation (1.27) is not invariant under such transformation. This is why we need the two phases φ_1 and φ_2 in equation (2.6), also called the the Majorana phases.

2.2.1 Vacuum Oscillations

The neutrino oscillations in vacuum is based on two hypothesis. The first one assumes that all neutrinos are ultra-relativistic particles which appear to be true for any neutrino with an energy larger than 1 keV. The second axiom is that neutrino mass and flavour states have the same momentum, but different masses, and therefore different energies $E_i^2 = p^2 + m_i^2$. Assuming that a neutrino is produced in the flavour ν_α ($\alpha = e, \mu, \tau$), we can write its decomposition in the mass eigenstates basis ν_i ($i = 1, 2, 3$) thanks to a unitary transformation T.

$$|\nu_\alpha\rangle = \sum_i T_{\alpha i} |\nu_i\rangle \tag{2.7}$$

The propagation in time is then obtained via Schrödinger's equation, where we denote $\mathcal{H}_0$ as the vacuum hamiltonian

$$i\frac{d}{dt}|\nu_\alpha(t)\rangle = \mathcal{H}_0 |\nu_\alpha(t)\rangle = \sum_i T_{\alpha i}(t)\mathcal{H}_0 |\nu_i\rangle \tag{2.8}$$

Solving (2.8) considering that the mass eigenstates are similar to the hamiltonian eigenstates, i.e. $\mathcal{H}_0 |\nu_i\rangle = E_i |\nu_i\rangle$, gives the following expression for $T_{\alpha i}(t)$

$$T_{\alpha i}(t) = U_{\alpha i}^* e^{-iE_i t} \tag{2.9}$$

where $U_{\alpha i}$ denotes the matrix element of U_{PMNS}. Under the ultra-relativistic assumption, we can write the equality $t = L$ in the natural units system. The probability $P_{\alpha\to\beta}$ to detect a neutrino ν_β at a distance L from the source of ν_α now reads

$$\begin{aligned} P_{\alpha\to\beta} &= |\langle\nu_\beta(L)|\nu_\alpha(L)\rangle|^2 \\ &= \left|\sum_{ij} U_{\alpha i}^* U_{\beta j} e^{-i(E_i - E_j)L}\right|^2 \end{aligned} \tag{2.10}$$

On top of that, a first order development of E_i gives

$$E_i = p + \frac{m_i^2}{2p} = E + \frac{m_i^2}{2E} \tag{2.11}$$

where we use the hypothesis on the masses and we consider the momentum p to be similar to the mean energy $E = \langle E_i \rangle$. We can now write $E_i - E_j = \dfrac{\Delta m_{ij}^2}{2E}$ with $\Delta m_{ij}^2 = m_i^2 - m_j^2$, the difference of the squared masses. Few rearrangements steps using the unitarity property of U_{PMNS} leads to the general 3 flavours neutrino oscillation probability

$$\begin{aligned} P_{\alpha\to\beta} = \delta_{\alpha\beta} &- 4\sum_{i>j} \mathcal{R}\Big(U_{\alpha j}U_{\alpha i}^* U_{\beta i} U_{\beta j}^*\Big)\sin^2\left(\frac{\Delta m_{ij}^2}{4E}L\right) \\ &+ 2\sum_{i>j} \mathcal{I}\Big(U_{\alpha j}U_{\alpha i}^* U_{\beta i} U_{\beta j}^*\Big)\sin\left(\frac{\Delta m_{ij}^2}{2E}L\right) \end{aligned} \tag{2.12}$$

where $\mathcal{R}$ and $\mathcal{I}$ are the real and imaginary part respectively. Few points in equation (2.12) are worth discussing:

- The last matrix in (2.6) contains only Majorana phases which all vanishes in the product $U_{\alpha j}U_{\alpha i}^* U_{\beta i} U_{\beta j}^*$. Neutrino oscillations are not therefore sensitive to Majorana phases.

- Neutrino oscillations only depend on the difference of the masses square Δm_{ij}^2 through the argument of the sinus and, as a matter of fact, oscillations are not sensitive to the value of the neutrino absolute masses. However, under the condition that U_{PMNS} is complex and that the imaginary part $\mathcal{I}\Big(U_{\alpha j}U_{\alpha i}^* U_{\beta i} U_{\beta j}^*\Big)$ does not vanish, the mass hierarchy can be measured. This is not the only condition under which the mass hierarchy can be measured. As we will see later, oscillations in matter are sensitive to the sign of Δm_{ij}^2, even if U_{PMNS} is real.

- The equivalent formula for anti-neutrinos is obtained by replacing U_{PMNS} with its complex conjugate U_{PMNS}^*. The difference between neutrino and anti-neutrino mixing is

$$P_{\alpha\to\beta} - P_{\bar{\alpha}\to\bar{\beta}} = 4\sum_{i>j} \mathcal{I}\Big(U_{\alpha j}U_{\alpha i}^* U_{\beta i} U_{\beta j}^*\Big)\sin\left(\frac{\Delta m_{ij}^2}{2E}L\right) \tag{2.13}$$

  If the Dirac phase δ is different from 0 or π, U_{PMNS} is complex. In the case where

its imaginary part does not vanish, then neutrino oscillations are a CP violation phenomenon.

- The only physical quantities which appear in $P_{\alpha\to\beta}$ and that can be tuned by experimentalists are the propagation length L and the neutrino mean energy E. In a simplified case where only 2 neutrino flavours exist, it is easy to draw $P_{\alpha\to\beta}$ as a function of the ratio L/E

$$P_{\alpha\to\beta} = \sin^2(2\theta_{12})\,\sin^2\left(1.27\Delta m^2_{12}\frac{L}{E}\right) \tag{2.14}$$

where the units are $[\Delta m^2_{12}] = \text{eV}^2$, $[L] = \text{km}$ and $[E] = \text{GeV}$. This function is represented in Figure 2.3 where we take $\sin^2 2\theta_{12} = 0.861$.

The value of $\sin^2(2\theta_{12})$ gives the amplitude of the oscillations while L/E is related to the period. Because the quantity $E/\Delta m^2_{12}$ has the dimension of a length, we often define the oscillation length L_{osc} as

$$L_{osc} = \frac{\pi E}{1.27\Delta m^2_{12}} \tag{2.15}$$

We can distinguish 3 regions of L/L_{osc}.

  - When $\dfrac{L}{L_{osc}} \ll 1$ the energy is too high or the propagation length is too short to observe any oscillation.

  - On the other hand, when $\dfrac{L}{L_{osc}} \simeq 1$, the neutrinos have time to oscillate once or twice. This is the region covered by oscillation experiments which choose their baseline L and their neutrino energy E to observe the first oscillation.

  - Finally when $\dfrac{L}{L_{osc}} \gg 1$, neutrinos have oscillated many times and the experiments only measure an averaged transition probability.

2.2.2 Matter Effects

In the vacuum, the hamiltonian $\mathcal{H}_0$ is the diagonal matrix composed of the energies of the mass eigenstates: $\left(\mathcal{H}_0\right)_{ij} = E_i\delta_{ij}$. Transposing $\mathcal{H}_0$ in the flavour basis gives

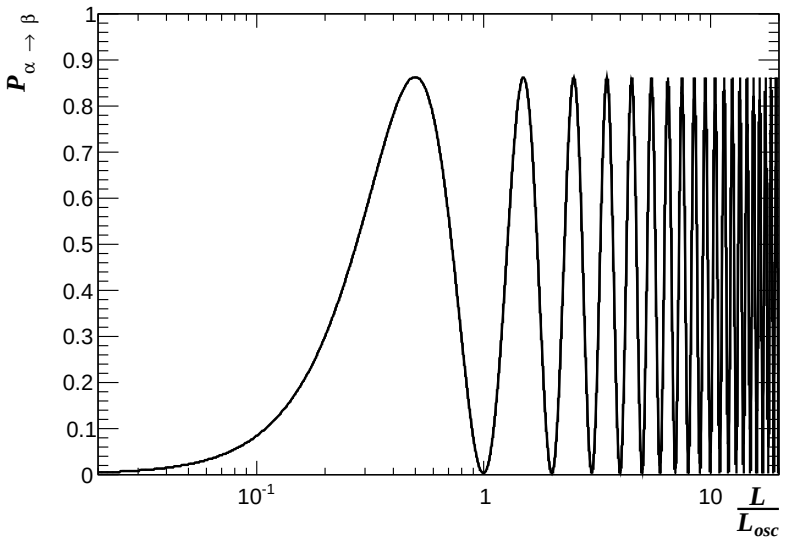

Figure 2.3: Neutrino oscillation probability $P_{\alpha\to\beta}$ as a function of $1.27\Delta m^2_{12}L/E$ in the case of 2 flavours oscillation as defined in equation (2.14).

$(\mathcal{H}_0)_{\alpha\beta} = \sum_{ij} U_{\alpha i}E_i\delta_{ij}U^*_{\beta j}$. When we want to include matter effects, we consider an extra potential $\mathcal{V}$ such that $\mathcal{H}_m = \mathcal{H}_0 + \mathcal{V}$. This new potential takes different forms depending on the neutrino flavour and the matter density. If the medium is rich in nucleons with a nucleon density of $n_n(x)$ then $(\mathcal{V})_{\alpha\beta} = -\frac{G_F}{\sqrt{2}}n_n(x)\delta_{\alpha\beta}$. The potential is therefore identical for all neutrino flavours and can be factorised in $\mathcal{H}_0$.

If however the medium is rich in electrons such as in the Sun's core, ν_e would interact with them via charged and neutral currents while ν_μ and ν_τ would only interact via neutral current. Once again the neutral current part can be absorbed in a redefinition of $\mathcal{H}_0$ and we are left with $(\mathcal{V})_{\alpha\beta} = \pm\sqrt{2}G_F n_e(x)\delta_{e\alpha}\delta_{e\beta}$ where the $+$ is in the case of neutrinos and $-$ for anti-neutrinos. This term was first introduced by Wolfenstein in 1978 [55]. He noticed that replacing $\mathcal{H}_0$ by $\mathcal{H}_m$ modifies equation (2.8) hence the oscillation probability in (2.12). In the case of two flavours oscillations, the new probability reads

$$P_{\alpha\to\beta} = \sin^2(2\theta_m)\,\sin^2\left(1.27\Delta m^2_m\frac{L}{E}\right) \tag{2.16}$$

where we have defined the new oscillation parameters as

$$\begin{aligned} \Delta m^2_m &= \sqrt{\left(\Delta m^2_{12}\cos 2\theta_{12} \mp 2\sqrt{2}EG_F n_e\right)^2 + \left(\Delta m^2_{12}\sin 2\theta_{12}\right)^2} \\ \sin 2\theta_m &= \frac{\Delta m^2_{12}}{\Delta m^2_m}\sin 2\theta_{12} \end{aligned} \tag{2.17}$$

Where the - is for the neutrino and the + is for the antineutrino case. Therefore matter effects modify the oscillation probabilities differently for neutrino and anti-neutrinos. It is possible to have $P_{\alpha\to\beta} \neq P_{\bar{\alpha}\to\bar{\beta}}$ without necessarily having CP violation. We also dropped the spatial dependance of the electron density $n_e(x) \to n_e$ as we assumed a constant density. Finally, as Smirnov and Mikheev noticed in 1987 [56], the equations (2.17) show a resonance behaviour when

$$n_e = n_{res} = \pm\frac{\Delta m^2_{12}\cos 2\theta_{12}}{2\sqrt{2}EG_F} \tag{2.18}$$

where again the + corresponds to the neutrino and the − to the anti-neutrino case. This resonance, called MSW effect, only occurs if $\Delta m^2_{12} > 0$[i], thus matter effects enable the determination of the neutrino mass hierarchy through neutrino oscillation. In the case where $n_e \ll n_{res}$ we find back the results obtained for vacuum oscillations. On the other hand, $n_e \gg n_{res}$ leads to a suppression of the oscillations. At resonance $n_e = n_{res}$, we have $\sin^2 2\theta_m = 1$ independently of $\sin 2\theta_{12}$ and oscillations are amplified.

A proper treatment of oscillations in matter would require to solve Schrödinger's equation with a variable density $n_e(x)$. This cannot be done analytically unless the variation of the density is small compared to the oscillation length and that neutrinos traverse a region where $n_e(x) = n_{res}$. In this case, called adiabatic regime, it is possible to consider layers of constant density and then to integrate over the number of layers [57]. This calculation was performed for solar neutrinos where the electron density inside the Sun is almost an exponential decrease. Two cases, corresponding to two different values of mixing angle θ_{12}, were considered: the large mixing angle (LMA) and small mixing angle (SMA).

2.3 Oscillation Evidences

The first hint that neutrinos do oscillate came in 1998 with the Super-Kamiokande (SK)

[i] Assuming that $-45° < \theta_{12} < 45°$

experiment. The large water Cherenkov detected neutrinos from cosmic ray interactions in the atmosphere. The data show a clear preference for simulations including $\nu_\mu \to \nu_\tau$ oscillations rather than no oscillations as shown in Figure 2.4. SK also managed to confirm the L/E dependence [1].

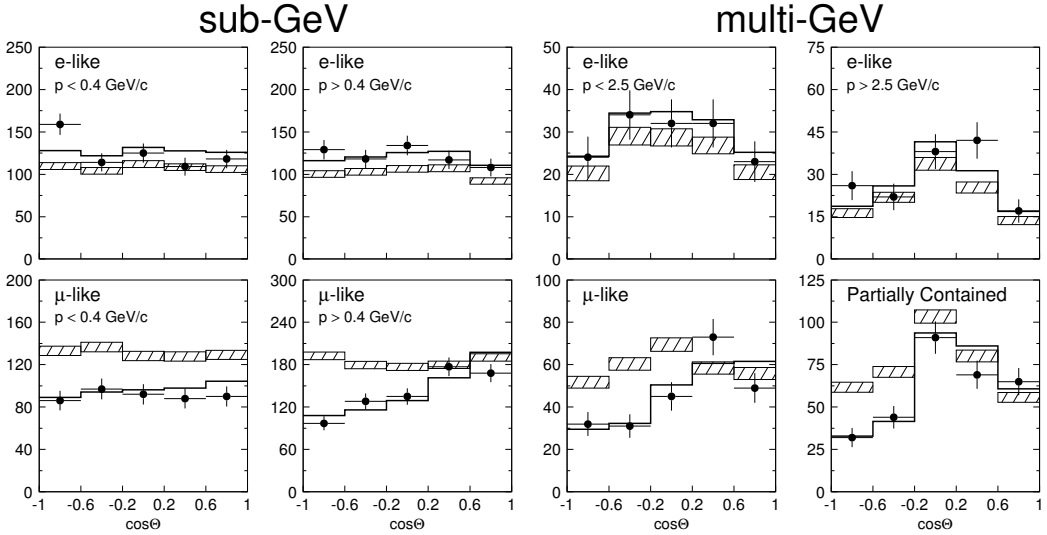

Figure 2.4: Zenith angle distribution of μ-like and e-like events for sub-GeV and multi-GeV data sets, where sub-GeV data are shown for both $p < 0.4\,\mathrm{GeV/c}$ and $p > 0.4\,\mathrm{GeV/c}$. Multi-GeV e-like data are shown for $p < 2.5\,\mathrm{GeV/c}$ and $p > 2.5\,\mathrm{GeV/c}$ and μ-like data for fully contained (FC) and partially contained (PC) events. The hatched regions show Monte Carlo predictions for no oscillations including whereas the solid line show the best fit expectation for $\nu_\mu \to \nu_\tau$ oscillations (with overall normalisation fitted as a free parameter) [1].

In order to verify that the solar neutrino puzzle was indeed due to oscillations, the Sudbury Neutrino Observatory (SNO) experiment was set up. This heavy water Cherenkov detector was designed to detect the ^{8}B electron neutrinos from charged current scattering off deuterium along with all three neutrino flavours through the neutral current channel. It also detected electron neutrinos with elastic scattering. As illustrated by the two rightmost comparisons of Figure 2.2, the SNO results confirmed the existence of oscillations [58].

The coloured bands in Figure 2.5 give the combined flux of $\nu_\mu + \nu_\tau$ versus the flux of ν_e as observed by SNO for each detection channels and by SK. The standard solar model (SSM) predictions are also shown in the dashed black lines. The non-zero values for the combined $\nu_\mu + \nu_\tau$ flux is a clear evidence of solar neutrino oscillations. The same year, the Kamioka Liquid scintillator Anti-Neutrino Detector (KamLAND) experiment validates the large

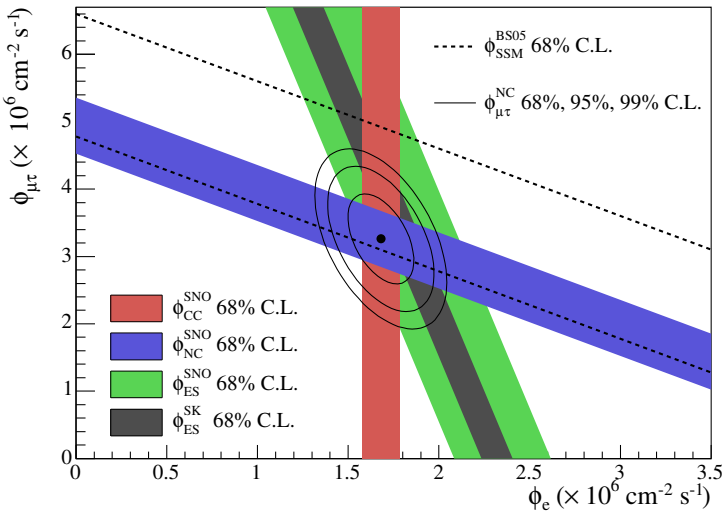

Figure 2.5: Flux of combined $\nu_\mu + \nu_\tau$ neutrinos versus flux of ν_e neutrino observed by SNO for the charged-current (red) neutral current (blue) and elastic scattering (green) channels. SK elastic results are also shown in the grey. The dashed lines represent the ^{8}B standard solar model predictions. The ellipses show the 68%, 95% and 99% confidence levels of the combined measurements of ϕ_e vs $\phi_{\mu,\tau}$ [59].

mixing angle scenario [60].

Further experiments were designed to precisely measure the oscillation parameters θ_{12}, θ_{13}, θ_{23}, Δm^2_{12}, Δm^2_{32} and δ via their appearance channel: $P_{\alpha\to\beta}$, and disappearance channel: $1 - P_{\alpha\to\alpha}$. They are split into 3 categories according to which parameters they want to measure.

- Solar neutrino experiments are sensitive to θ_{12} and Δm^2_{12}
- Experiments detecting anti-neutrinos from the reactors are sensitive to θ_{13}
- Atmospheric and accelerators experiments can measure θ_{23} and Δm^2_{32}

The current values of the oscillation parameters along with their 3σ range uncertainties are given in Table 2.1, where we define $\Delta m^2 = m_3^2 - (m_2^2 + m_1^2)/2$ such that in the normal hierarchy $\Delta m^2 = \Delta m^2_{31} - \Delta m^2_{21}/2 > 0$ and in the case of inverted hierarchy $\Delta m^2 = \Delta m^2_{32} - \Delta m^2_{21}/2 < 0$. From this table we notice what are the next challenges for the upcoming neutrino oscillation experiments such as Hyper-Kamiokande [61] and DUNE [62]. The sign of Δm^2, and therefore the mass hierarchy, remains unknown. Moreover

Table 2.1: Current values of the neutrino oscillation parameters with their 3σ allowed ranges where we have $\Delta m^2 = m_3^2 - (m_2^2 + m_1^2)/2$. The values are given for the normal hierarchy, the values in brackets are in the inverted hierarchy case [36].

Parameter	Best fit	3σ range
$\sin^2\theta_{12}$	0.308	0.259 - 0.359
$\sin^2\theta_{23}$	0.437 (0.455)	0.374 - 0.628 (0.380 - 0.641)
$\sin^2\theta_{13}$	0.0234 (0.0240)	0.0176 - 0.0295 (0.0178 - 0.0298)
Δm^2_{12} $[10^{-5}\,\mathrm{eV}^2]$	7.54	6.99 - 8.18
$\lvert\Delta m^2\rvert$ $[10^{-3}\,\mathrm{eV}^2]$	2.43 (2.38)	2.23 - 2.61 (2.19 - 2.56)
δ/π	1.39 (1.31)	0.00 - 0.16 $\oplus$ 0.86 - 2.00 (0.00 - 0.02 $\oplus$ 0.70 - 2.00)

the octant of θ_{23} is yet to be measured even if the best fit has a preference for the first octant in case of normal hierarchy and second octant if $\Delta m^2 < 0$. Last but not least, the 3σ range of the Dirac phase δ remains very large for both normal and inverted hierarchies, and include $\pi/2$ and $3\pi/2$ respectively, which prevent us from knowing whether there is CP violation in the leptonic sector.

3

Neutrino Interactions

The physics of neutrino scattering changes depending on the neutrino energy as described in [63]. Coherent scattering off nucleus, electron neutrino capture and elastic scattering off lepton occur at any neutrino energy, but are dominant in the low energy spectrum. As the energy increases and becomes larger than 100 MeV, the neutrino starts probing inside the nucleus and interact with protons and neutrons. In this energy range, three reactions overlap: charged-current quasi-elastic (CCQE), baryonic resonance (RES) and deep inelastic scattering (DIS), as shown in Figure 3.1 for ν_μ (left) and $\overline{\nu}_\mu$ (right). There also exists other neutrino-nucleus scattering not represented in this figure such as coherent pion production, diffractive pion production and neutral current elastic (NCE) scattering off nucleon.

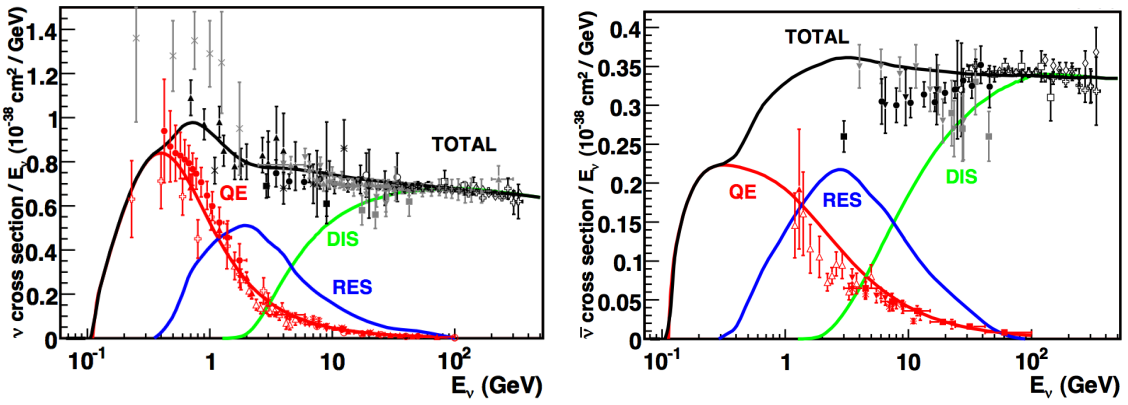

Figure 3.1: Muon neutrino (left) and anti-neutrino (right) cross section of charged-current scattering off nucleus as a function of neutrino energy where the three main contributions are represented: CCQE in red, baryon resonance in blue and DIS in green. [64]. Note the y axis is the cross section per neutrino energy.

Note that neutrinos are involved in other weak interaction processes. As we are only interested in reactions where the neutrino is the incoming particle, hadron decays are

not discussed here. This chapter first describes the three main neutrino-nucleon reaction. Section 3.2 highlights the different approaches to treat the coherent pion production channel. Finally an overview of different nuclear effects is given.

3.1 Neutrino-Nucleon Scattering

Accelerator neutrinos produced by wide band beam experiments cover an energy range from 0.5 GeV to 20 GeV, which corresponds to the range where CCQE, RES and DIS overlap. These channels all enter into the description of a generic charged-current neutrino-nucleon scattering of the type $\nu_\ell + \mathcal{N} \to \ell^- + \mathcal{X}$ illustrated by Figure 3.2. The corresponding amplitude is given in equation (3.1) where $\mathcal{N}$ and $\mathcal{X}$ are the hadronic initial and final states respectively.

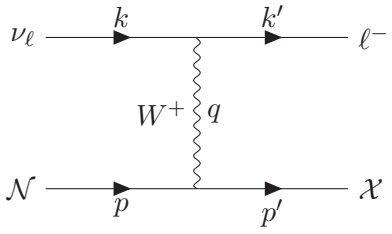

Figure 3.2: Feynman diagram of a generic charged-current neutrino-nucleon inelastic scattering where $\mathcal{N}$ and $\mathcal{X}$ are respectively the hadronic initial and final states. The leptons initial and final four momentum are represented by k and k' and the hadronic initial and final four momentum are represented by p and p' respectively. q is the four momentum transferred by the neutrino to the nucleon.

$$\mathcal{A} = \left(\frac{g}{2\sqrt{2}}\right)^2 \overline{U}_\ell(k')\gamma_\alpha(1-\gamma_5)U_\nu(k)\left[\frac{i}{q^2 - M_W^2}\Big(-g^{\alpha\beta} + \frac{q^\alpha q^\beta}{M_W^2}\Big)\right]\langle \mathcal{X}(p')|J_\beta|\mathcal{N}(p)\rangle \quad (3.1)$$

Four parts can be distinguished in this amplitude: a constant factor, the leptonic current, the propagator term and the hadronic current where J is an operator describing the interaction between nucleons. The expression of J is rather cumbersome as protons and neutrons are not elementary particles. In the hypothesis where the momentum transferred is small with respect to the W mass, $Q^2 = -q^2 \ll M_W^2$, the propagator term simplifies

according to (3.2).

$$\frac{i}{q^2 - M_W^2}\Big(- g^{\alpha\beta} + \frac{q^\alpha q^\beta}{M_W^2}\Big) \xrightarrow[Q^2 \ll M_W^2]{} \frac{ig^{\alpha\beta}}{M_W^2} \tag{3.2}$$

which further simplifies the amplitude:

$$\mathcal{A} = \frac{ig^2}{8M_W^2}\overline{U}_\ell(k')\gamma_\alpha(1-\gamma_5)U_\nu(k)\left\langle \mathcal{X}(p')\right|J_\alpha\left|\mathcal{N}(p)\right\rangle \tag{3.3}$$

Recalling that only the modulus square of the amplitude is important in the derivation of the cross section, we write

$$|\mathcal{A}|^2 = \frac{G_F^2}{2} L_{\alpha\beta}H^{\alpha\beta} \tag{3.4}$$

where the $L_{\alpha\beta}$ and $H^{\alpha\beta}$ are the leptonic and hadronic tensors. As leptons are elementary particles, it is possible to express $L_{\alpha\beta}$ as a function of the components of k and k'.

$$L_{\alpha\beta} = 8\left[k_\alpha k'_\beta + k'_\alpha k_\beta - g_{\alpha\beta}k.k' - i\varepsilon_{\alpha\mu\beta\nu}k^\mu k'^\nu\right] \tag{3.5}$$

However the expression of $H^{\alpha\beta}$ vary according to the final state $\mathcal{X}$ and the momentum transfer $Q^2 = -q^2$. Once the energy-momentum conservation principle has been taken into account and the summation over the spins of the incoming and outgoing particles has been done, the expression of the double differential cross section is given by (3.6) where $d\Omega = d\cos\theta_\ell\ d\phi$ with θ_ℓ the angle between the incoming neutrino and the outgoing lepton.

$$\frac{d^2\sigma}{d\Omega dE_\ell} = \frac{G_F^2}{4\pi^2}\frac{|\vec{k'}|}{|\vec{k}|}L_{\alpha\beta}H^{\alpha\beta}(Q^2) \tag{3.6}$$

It is more convenient to express this differential cross section in terms of Lorentz invariant variables: the momentum transfer Q^2 and the invariant mass W_{inv}^2 of the final state $\mathcal{X}$. They are defined in (3.7) and the new differential cross section is given in (3.8).

$$\begin{aligned} Q^2 &= -(k-k')^2 = 2E_\nu E_\ell - 2|\vec{k}||\vec{k'}|\cos\theta_\ell - M_\ell^2 \\ W_{inv}^2 &= p'^2 = M_\mathcal{N}^2 + 2M_\mathcal{N}(E_\nu - E_\ell) - Q^2 \end{aligned} \tag{3.7}$$

$$\frac{d^2\sigma}{dQ^2 dW_{inv}} = \frac{G_F^2 W}{4\pi M_{\mathcal{N}}} \frac{1}{E_\nu^2} L_{\alpha\beta} H^{\alpha\beta}(Q^2) \tag{3.8}$$

The expression (3.8) is valid for both neutrino and anti-neutrino as the only difference between both interactions lies in the expression of the hadronic tensor. In the neutral current case the expression is the same as we assumed $Q^2 \ll M_W^2 \sim M_Z^2$.

3.1.1 Elastic and Quasi-Elastic Scattering

In the lowest energy regime, a neutrino-nucleon interaction is elastic when the gauge boson exchanged is Z^0 or quasi-elastic if a charged lepton is produced and a $W^\pm$ is exchanged.

$$\begin{aligned}
&\text{NCE:} && \nu_\ell + n, p \to \nu_\ell + n, p \\
&\text{CCQE:} && \nu_\ell + n \to \ell^- + p \\
&\text{CCQE:} && \overline{\nu}_\ell + p \to \ell^+ + n
\end{aligned}$$

The hadronic current can be split into several parts according to the behaviour of each term under rotation (and boost) and parity transformation, which is related to their content in γ matrices.

$$J_\alpha^{CC}(Q^2) = \cos\theta_c \, \overline{U}_p(p') \Big(V(Q^2) - A(Q^2) + P(Q^2) \Big) U_n(p) \tag{3.9}$$

where V contains the terms with one γ_α and thus contributes to the vector current. Similarly A contains terms with $\gamma_\alpha\gamma_5$ and contributes to the axial (or pseudo-vector) current while P contains only one γ_5 and contributes to the pseudo-scalar current. Here θ_c represents the Cabibbo angle. It is shown in [63] that the P factor can be neglected as it is of the order of $(M_\ell/M_p)^2$ ($\sim 1\%$ of the total ν_μ CCQE cross section). The V, A and P terms also contain different form factors which describe the internal structure of the nucleons. The presence of the cosine of the Cabibbo angle is due to the charged current interaction, where a down-type quark becomes up-type. The hadronic tensor $H^{\alpha\beta}$ can be calculated from (3.9) and factorised with the leptonic tensor in (3.8). This was derived by Llewelly-Smith [65] where the vector form factors are assumed to be the same as in electron-nucleon scattering,

as a result of the conservation of the vector current (CVC) [66]. Thus only the axial form factor remains to be defined. The usual procedure is to take a dipole form parametrised by the value of the form factor at $Q^2 = 0$ and the a parameter which has the dimension of a mass, called the axial mass M_A (by analogy to the propagator term in equation (3.1)).

$$F_A(Q^2) = \frac{F_A(0)}{\left(1 + \frac{Q^2}{M_A^2}\right)^2} \tag{3.10}$$

The value of these parameters are $F_A(0) = g_A = 1.27$, which can be extracted from neutron β-decay experiment [67] and $M_A = \sim 1\,\mathrm{GeV/c^2}$ [68]. A more complete description of the form factors along with the integration of the cross section over Q^2 and W is given in [69].

This differential cross section was derived in the impulse approximation where only the target nucleon is considered and the surrounding nucleons are spectators. Therefore it is important to know the state of the target nucleon. There are two main approaches: the Relativistic Fermi Gas model (RFG) [70] and the spectral function model (SF) [71]. The RFG describes the nucleus as an interaction-free many-fermions system, meaning that all the possible states are occupied by the free protons and neutrons up to the so-called Fermi energy ε_F. By solving the relativistic Dirac equation, one can predict the excited nuclear levels and the nucleon binding energy. The advantage of this model is that Pauli blocking effects are treated correctly. However, the nucleus has a finite size and correlations between nucleons cannot always be neglected. Therefore the second approach is using spectral functions that characterise the probability of removing a nucleon from the nucleus as a function of its momentum.

3.1.2 Resonant Pion Production

As the neutrino energy increases, the available phase space expands and the interaction becomes inelastic. The pion production becomes possible given that $E_\nu > M_{\ell,\nu} + M_{\pi^{\pm,0}}$. The pion is produced as a result of the decay of the baryonic resonance N^* or Δ. We can see that unlike for CCQE, the target nucleon can either be a proton or neutron in all the

charged current channels. The Feynman diagram for this kind of interaction is given in Figure 3.3.

$$
\begin{aligned}
\text{NC resonant:}\quad & \nu_\ell + n \to \nu_\ell + \Delta^0 \\
& \qquad \hookrightarrow \pi^0 + n \text{ or } \pi^- + p \\
& \nu_\ell + p \to \nu_\ell + \Delta^+ \\
& \qquad \hookrightarrow \pi^+ + n \text{ or } \pi^0 + p \\
\text{CC resonant:}\quad & \nu_\ell + n \to \ell^- + \Delta^+ \\
& \qquad \hookrightarrow \pi^+ + n \text{ or } \pi^0 + p \\
& \nu_\ell + p \to \ell^- + \Delta^{++} \\
& \qquad \hookrightarrow \pi^+ + p \\
\text{CC resonant:}\quad & \overline{\nu}_\ell + p \to \ell^+ + \Delta^0 \\
& \qquad \hookrightarrow \pi^- + p \text{ or } \pi^0 + n \\
& \overline{\nu}_\ell + n \to \ell^+ + \Delta^- \\
& \qquad \hookrightarrow \pi^- + n
\end{aligned}
$$

Starting from an expression equivalent to the one given in (3.8), Rein and Sehgal built a model [72] where they consider the effect of 18 resonances below 2 GeV in the expression of the tensor $H^{\alpha\beta}$ along with their interference terms. They also assume the presence of a non-resonant background of isospin 1/2 is not interfering with the remaining amplitudes. This background is expressed as a nucleon-like excitation as it corresponds to a fraction of the $N(1440)$ excitation, known as the Roper resonance [73]

3.1.3 Deep Inelastic Scattering

In inelastic interactions with $E_\nu > M_\mathcal{N}$ and $Q^2 > 1\,\text{GeV}^2$, the neutrino starts to probe inside the nucleon and directly scatters off a quark. The neutrino most probably scatters off an up or down type quark which will recoil and trigger the hadronisation process, as illustrated in Figure 3.4. However, if the momentum transfer is large enough, the

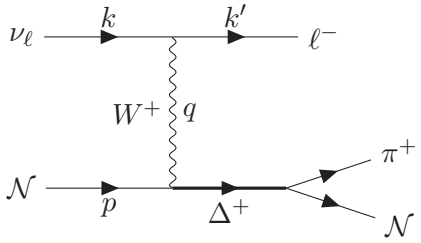

Figure 3.3: Feynman diagram of a charged-current neutrino-nucleon resonant scattering where the initial nucleon $\mathcal{N}$ undergoes a Δ resonance which then decays back to a nucleon and pion. The leptons initial and final four momentum are represented by k and k'.

neutrino can scatters off any of the sea quarks and anti-quarks. Like in electron-proton DIS interactions, it is convenient to define the Bjorken variables x and y to describe this phenomenon:

$$x_B = \frac{Q^2}{2p.q}, \quad \text{fraction of the nucleon momentum carried by the struck quark}$$
$$y_B = \frac{p.q}{p.k}, \quad \text{fractional energy loss of the incoming neutrino}$$

By definition, we have $0 < x_B, y_B \leq 1$. In addition, $x_B = 1$ implies that the reaction is elastic. The hadronic tensor $H^{\alpha\beta}$ is then expressed in terms of structure functions that depend on Q^2 and x_B. It is detailed in [69] that these functions can be easily related to the parton distribution functions in the hadron model introduced by Feynman [74].

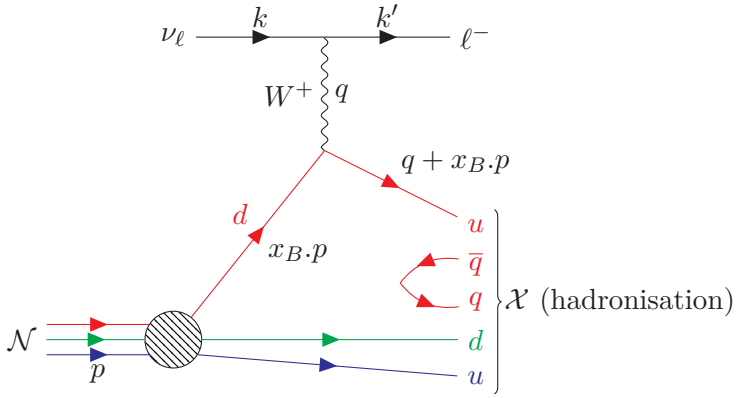

Figure 3.4: Feynman diagram of a charged current DIS interaction. The lepton initial and final four momentum are represented as k and k' respectively. The nucleon four momentum is p and the final state $\mathcal{X}$ is represented as the hadronisation process started.

3.2 Neutrino-Nucleus Scattering

When a neutrino scatters off a nucleus with A nucleons, one can assume that the phases of the amplitude of each nucleon are independent and that the real part of the amplitudes are identical:

$$\mathcal{A}_k = \rho . e^{i\phi_k}, \quad \forall k \in [\![1, A]\!] \tag{3.11}$$

Therefore, the total scattering amplitude on the nucleus is expressed as the sum of all the nucleon amplitudes:

$$\mathcal{A}_{\text{tot}} = \sum_{k=1}^{A} \mathcal{A}_k = \rho \sum_{k=1}^{A} e^{i\phi_k} \tag{3.12}$$

Taking the modulus square of equation (3.12) gives the factor which contributes to the cross section:

$$\sigma \propto |\mathcal{A}_{\text{tot}}|^2 = \rho^2 \left(A + 2 \sum_{k=1}^{A} \sum_{l=1}^{k} \cos(\phi_k - \phi_l) \right) \approx \rho^2 \times A \tag{3.13}$$

This approximate calculation gives a hint on the relation between the neutrino-nucleus and neutrino-nucleon cross sections: the neutrino-nucleus cross section grows linearly with A.

In the case where the amplitude phases of each nucleon interfere constructively, all the phases differences in (3.13) vanish. The neutrino interacts coherently with all the nucleons and the cross section becomes proportional to $A^2 \times |\mathcal{A}_k|^2$. Such interactions are characterised by a set of selection rules [75]:

- A small amount of energy t (defined in equation (3.14)) must be transferred to the nucleus so that all the nucleons react in phase and remain bound. Thus the nucleus recoils as a whole while staying in its ground state (no breakup, no excitation nor spin flip). In the case of coherent pion production, it is useful to define the energy transfer to the nucleus t as:

$$|t| = |(q - p_\pi)^2| = |(k - k' - p_\pi)^2| \tag{3.14}$$

- No quantum number such as charge, spin and isospin must be exchanged as it would be a sign of an interaction with a single nucleon.

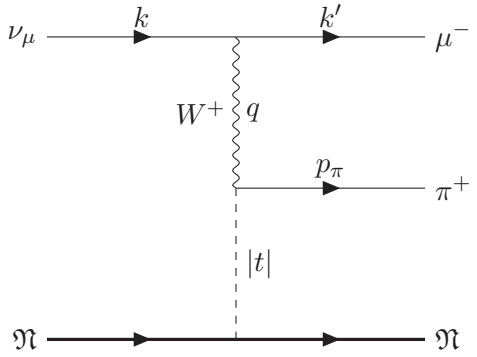

Figure 3.5: Feynman diagram of a charged current coherent pion production where $|t|$ represents the square of the four-momentum transferred to the nucleus $\mathfrak{N}$. The pion four-momentum is denoted as p_π and q is the four-momentum of the W^+ particle.

The Feynman diagram of such an interaction is given in Figure 3.5. We notice that, if the neutrino energy is large enough, this process produces a pion with four-momentum p_π. Such a coherent behaviour is also possible at the nucleon level and is named diffractive scattering, as described by Rein in [76]. There exists two categories of theoretical framework to describe this interaction. The first category encompasses models based on the partially conserved axial current (PCAC) and the second covers the microscopic models. The differences between the two PCAC models, namely Rein-Sehgal (RS) and Berger-Sehgal (BS) [77, 78, 79], are discussed below and a quick overview of the Alvarez-Ruso *et al.* microscopic model [80] is given afterwards.

3.2.1 Rein-Sehgal Model

The expression of the cross section given by the Rein and Sehgal model [77] starts again with equation (3.8) where the hadronic tensor is split into vector and axial part. Calling the conservation of the vector current and the partial conservation of the axial current for $Q^2 = 0$, Adler's theorem relates the coherent pion production differential cross section with the strong pion-nucleus cross section [81]:

$$\frac{d^2\sigma(\nu + \mathfrak{N} \to \ell^- + \mathfrak{N}')}{dQ^2 dW} = \frac{G_F^2 W}{2\pi^2 M_{\mathcal{N}}} \frac{E_\ell}{E_\nu(E_\nu - E_\ell)} f_\pi^2 \sigma(\mathfrak{N} + \pi \to \mathfrak{N}') \tag{3.15}$$

where $f_\pi = 0.93\, m_\pi$ is the pion decay constant factor. Assuming the incoming nucleus $\mathfrak{N}$ is at rest, one can redefine the DIS variables x_B and y_B as:

$$x_B = \frac{Q^2}{2M_{\mathcal{N}}(E_\nu - E_\ell)} \quad , \quad y_B = \frac{E_\nu - E_\ell}{E_\nu} \tag{3.16}$$

with $M_{\mathcal{N}}$ the mass of the nucleon.

Using (3.7) along with (3.16), it is easy to build the Jacobian to change the differential cross section expression. Taking the final state $\mathfrak{N}' = \mathfrak{N} + \pi$, one obtains the formula given in the original Rein-Sehgal paper [77].

$$\left(\frac{d\sigma}{dx_B\, dy_B\, d|t|}\right)_{Q^2=0} = \frac{G_F^2\, M_{\mathcal{N}}\, E_\nu}{\pi^2}\, \frac{1}{2}\, f_\pi^2\, (1 - y_B)\, \frac{d\sigma(\pi\mathfrak{N} \to \pi\mathfrak{N})}{d|t|}\Big|_{E_\nu y = E_\pi} \tag{3.17}$$

In order to extrapolate equation (3.17) to the non-forward direction, a dipole-like propagator term is multiplied to this formula, with an axial mass M_A of $1\,\mathrm{GeV/c^2}$. The pion-nucleus differential cross section $d\sigma(\pi\mathfrak{N} \to \pi\mathfrak{N})$ is then expressed as a function of the pion-nucleon elastic differential cross section $d\sigma(\pi\mathcal{N} \to \pi\mathcal{N})$ times a nuclear form factor $F_{\mathfrak{N}}(t)$. Additionally, a scaling with A^2 is added due to the coherent nature of the interaction.

$$\frac{d\sigma(\pi\mathfrak{N} \to \pi\mathfrak{N})}{d|t|} = A^2\, |F_{\mathfrak{N}}(t)|^2\, \frac{d\sigma(\pi\mathcal{N} \to \pi\mathcal{N})}{d|t|} \tag{3.18}$$

The nuclear form factor is written as the product of an exponential decreasing with $|t|$ and an attenuation factor F_{abs} that takes into account the pion absorption for which the complete expression is detailed in reference [77].

$$|F_{\mathfrak{N}}(t)|^2 = e^{-b|t|} F_{\mathrm{abs}}, \quad \text{with } b = \frac{R_0^2}{3} A^{2/3} \tag{3.19}$$

with R_0 the Bohr radius.

Finally, the pion-nucleon differential cross section is simplified thanks to the optical theorem

$$\frac{d\sigma(\pi\mathcal{N}\to\pi\mathcal{N})}{d|t|} = \frac{1}{16\pi}\left[\sigma_{\rm tot}^{\pi\mathcal{N}}\right]^2(1+r^2) \tag{3.20}$$

where we have $r = \mathbf{Re}[f_{\pi N}(0)]/\mathbf{Im}[f_{\pi N}(0)]$ the ratio between the real and imaginary part of the pion-nucleon forward scattering amplitude. Plugging everything into (3.17) gives the RS triple differential coherent cross section for neutral current:

$$\frac{\mathrm{d}\sigma^{\rm NC}}{\mathrm{d}x\,\mathrm{d}y\,\mathrm{d}|t|} = \frac{G_F^2\,M_{\mathcal{N}}\,E_\nu}{4\,\pi^2}\,f_{\pi^0}^2\,(1-y_B)\left(\frac{m_A^2}{m_A^2+Q^2}\right)^2 A^2\,F_{abs}\,e^{-b|t|}\,\frac{1}{16\pi}\left[\sigma_{tot}^{\pi^0 N}(Ey)\right]^2(1+r^2) \tag{3.21}$$

The relation between the charged current and neutral current cross sections is straightforward as only the pion decay constant factor must be changed: $f_{\pi^+}^2 = 2\,f_{\pi^0}^2$. It is shown in reference [78] that the effects of a non zero lepton mass on the CC coherent cross section are not negligible. A deficit of forward going muons for $Q^2 < 0.1\,\mathrm{GeV}^2$ was found and the authors decided to add a correction factor $\mathcal{C}$ to equation (3.21) that reduces the CC phase space according to equation (3.22).

$$\mathcal{C} = \left(1 - \frac{1}{2}\frac{Q^2_{\rm min}}{Q^2+m^2_{\pi^+}}\right)^2 + \frac{1}{4}y_B\frac{Q^2_{\rm min}(Q^2-Q^2_{\rm min})}{(Q^2+m_\pi^2)^2} \tag{3.22}$$

where $Q^2_{\rm min} = m^2_{\rm lep}y_B/(1-y_B)$. The RS differential coherent cross-section for charged current (CC) interaction is expressed as:

$$\frac{\mathrm{d}\sigma^{CC}}{\mathrm{d}x_B\,\mathrm{d}y_B\,\mathrm{d}|t|} = \frac{\mathrm{d}\sigma^{NC}}{\mathrm{d}x_B\,\mathrm{d}y_B\,\mathrm{d}|t|}\times 2\mathcal{C}\theta(Q^2-Q^2_{\rm min})\theta(y_B - y_{\rm B,\,min})\theta(y_{\rm B,\,max}-y_B) \tag{3.23}$$

where θ is the Heaviside step function, $y_{\rm B,\,min} = m_\pi/E$ and $y_{\rm B,\,max} = 1 - m_{\rm lep}/E$. These conditions define the integration borders for x_B and y_B. The integration over t is more tedious as the t expression depends not only on x_B and y_B but also on the pion angle with respect to the neutrino direction θ_π and the coplanarity angle with the outgoing lepton ϕ_L.

3.2.2 Berger-Sehgal Model

The Berger-Sehgal model described in [79] differs from the Rein-Sehgal model on two aspects. The first one is in the kinematic term. The use of PCAC leads to a factor $(1-y_B)$

in (3.17) which should be valid for $Q^2 = 0$ only. In the BS model, the complete term is derived, which gives:

$$1 - y_B + \frac{y_B^2}{4}\left(1 - \left|\frac{Q^2}{(E_\nu - E_\ell)^2} + 1\right|\right) \tag{3.24}$$

The second difference lies in the value of the pion-nucleus elastic differential cross section. Instead of trying to model nuclear processes (see (3.18), (3.19), (3.20)), the authors used the available data on pion-carbon scattering [82, 83] to describe more accurately the pion-nucleus cross section. This implies a big decrease of this elastic cross section in the resonance region as shown on the left plot in Figure 3.6. These two changes reduce the total cross section by a factor two with respect to the RS model, as seen on the right plot in Figure 3.6.

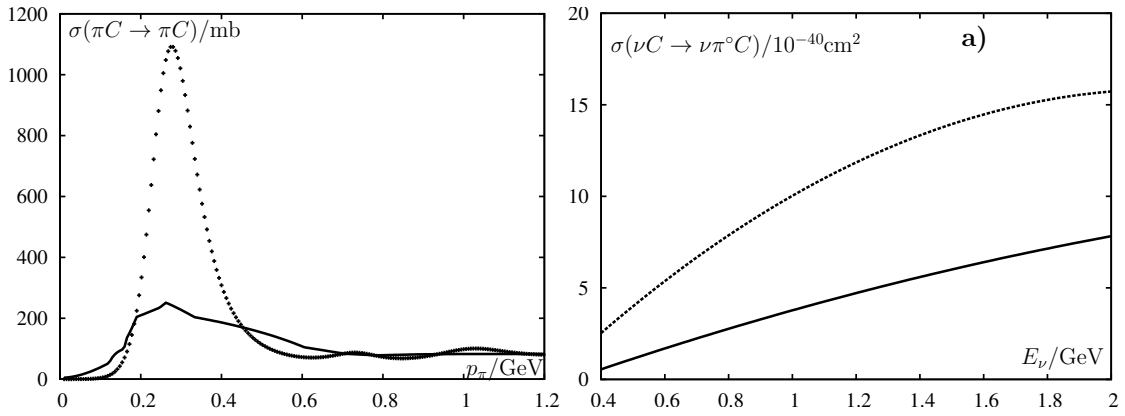

Figure 3.6: Pion-carbon elastic cross section as a function of pion momentum (left) and coherent π^0 production cross section as a function of neutrino energy for carbon target (right). The dotted line represents the RS model and the solid line the BS model for both plots (extracted from [79])

For charged current interactions, the lepton mass correction factor from equation (3.22) is still applied in the BS model.

3.2.3 Microscopic Approach

The microscopic models such as the one from Alvarez-Ruso *et al.* [80] take another approach to describe the coherent pion production. The scattering occurs at the nucleon level where the pion is produced through a Δ or N^* decay. The propagation of such excitation states is strongly modified by the nuclear medium. Constraints on the decay products are also considered: the wave function of the outgoing pion is distorted by the

nuclear potential and the nucleon must be in the same quantum state as initially. The differential cross section in lepton kinematics (E_ℓ, Ω_ℓ) and pion solid angle Ω_π is given as:

$$\frac{d\sigma}{dE_\ell d\Omega_\ell d\Omega_\pi} = \frac{1}{8(2\pi)^5} \frac{|\vec{k'}|.|\vec{p_\pi}|}{|\vec{k}|} |\mathcal{A}|^2 \tag{3.25}$$

where $\mathcal{A}$ is the coherent sum of the amplitudes of the diagrams contributing contributing to this process. At low neutrino energy, the diagram represented in Figure 3.3 is largely dominant.

3.3 Nuclear Effects

It was discussed in Section 3.1.1 the importance of the initial state of the nucleon. The leftmost sketch of Figure 3.7 illustrates a bare CCQE interaction in the impulse approximation. It is shown in [84] that the impulse approximation is only reliable for Q^2 larger than $300\,\mathrm{MeV}^2$. For smaller Q^2, one should start to consider the state of the initial nucleon using for example a relativistic Fermi gas model or a spectral function model, as shown in the second sketch. At these low values of Q^2, one should also consider the impact of the dense nuclear medium surrounding the initial nucleon which modifies the scattering process. Such nuclear effects take into account short and long-range correlations. Short-range correlations are characterised by n particles - n holes excitations (np-nh) where the gauge boson couples to correlated nucleons (2p-2h if the nucleons form a pair) as represented in the third sketch of Figure 3.7. Meson exchange current (MEC) is the dominant process in 2p-2h excitations and its contribution to the genuine CCQE cross section was proved essential to understand the measurements from various experiments [85].

Long-range correlations between nucleons affect the propagation of the gauge boson in the nucleus, before it interacts with a nucleon. The random phase approximation (RPA) describes these correlations in terms of collective effects and medium polarisation which result in a weak and Coulomb screenings [86]. Last but not least, the final state particles produced at the primary vertex scatter off other nucleons before leaving the nucleus. These final state interactions (FSI) are represented in the rightmost sketch of Figure 3.7.

To summarise, neutrino nucleus/nucleon interactions are hard to understand due to the

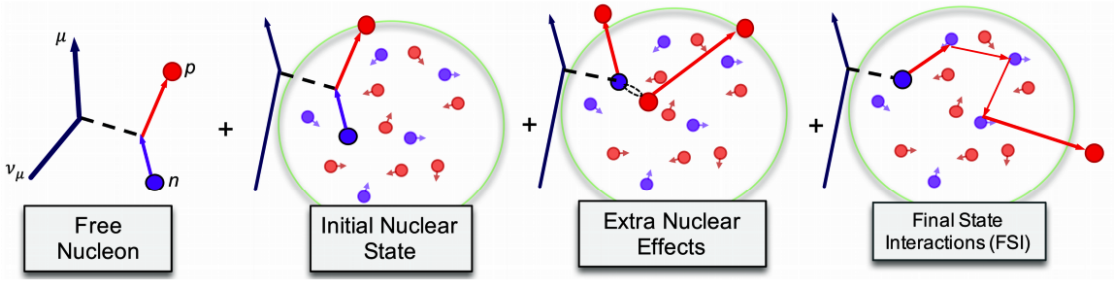

Figure 3.7: Illustration of the different steps to compute the neutrino-nucleon cross section in the case of a CCQE interaction.

interplay of different effects:

- Unlike electron scattering where the energy of the incoming lepton is well known, accelerator-based neutrino suffer from having a rather broad energy spectrum (from 0.5 to 20 GeV). The initial energy of the neutrino is therefore never accurately known. In addition, different interactions overlap in this energy range so one must rely on the final state observables to guess which interaction channel the neutrino underwent.

- Nuclear effects such as 2p-2h and RPA modify the genuine interactions rate and must be properly accounted for in the event generators.

- Final state interactions perturb the measurement of exclusive channels and are an important source of error in the cross section measurements. For example, a charged-current resonant event where the pion is absorbed by the nucleus looks like a CCQE event where the proton does not exit the nucleus. In both cases, only the outgoing lepton is observed.

- None of the previous point can be isolated. They must be all considered simultaneously, at least for low Q^2 events, as all these effects alter the kinematics of the detected particles. Thus it introduces a bias in the reconstructed neutrino energy, important for the determination of neutrino oscillation probability (2.12).

Part II

The T2K Experiment

An introduction to T2K

The Japanese neutrino adventure started with the establishment of the Kamioka Underground Observatory in 1983 when the 4.5 kt water Cherenkov detector KamiokaNDE was installed 1 km underground in the Mozumi mine. The main goal of this experiment was to search for proton decay [87]. No longer than two years later, a detector upgrade started to be considered in order to increase its sensitivity. Kamiokande-II was then able to observe neutrinos from the Sun [51], from cosmic rays interactions in the atmosphere [88] and from supernovae explosion, such as the one that occurred in the Large Magellanic Cloud in 1987 [89].

Backed by the successful achievements of this neutrino observatory and with the will of making progress in this exciting new field (higher statistics were needed to improve the significance level of the current measurements), the Super-Kamiokande (SK) detector was designed in the early 90's. The technology remained water Cherenkov, but the volume of the tank was increased to 50 kt. It started to collect data from April 1996 and is still running today. The main result of that experiment was the observation of atmospheric neutrino oscillations [1], which was awarded the Nobel Prize in 2015.

On the other coast of Japan, in Tsukuba, the National Laboratory for High Energy Physics (KEK) had been equipped with a proton synchrotron KEK-PS in 1998. In order to confirm the oscillation hypothesis claimed by SK in the atmospheric sector, this particle accelerator was used to produce a neutrino beam towards Super-Kamiokande, 250 km west of Tsukuba. The long baseline neutrino experiment K2K, standing for KEK to Kamioka, was born [90]. It ran for about 10 years and managed to show the evidence of ν_μ disappearance in a ν_μ neutrino beam as well as measuring a few neutrino-nucleus interaction parameters.

Around 2008, the Japan Proton Accelerator Research Complex (J-PARC) located in Tokai was established and its accelerator began operation at a higher power than that of KEK. The Tokai to Kamioka (T2K) experiment was therefore created and started taking data in January 2010.

In the following chapters, we describe the different apparatus required by T2K, starting from the neutrino beam, the near and the far detectors in Chapter 4. The software part of the experiment, which consists of the Monte Carlo simulation and analysis tools, is discussed in Chapter 5. Finally, Chapter 6 presents the ECal Data Quality checks that was my service task within the T2K collaboration.

4

T2K Hardware

T2K (Tokai-to-Kamioka) is a long-baseline neutrino experiment located in Japan. It is designed to measure the neutrino oscillation parameters such as the mixing angle θ_{13} via the appearance of ν_e in a ν_μ beam. It also assesses $\sin^2 2\theta_{23}$ and the mass difference Δm^2_{23} trough the ν_μ disappearance analysis. As it also runs in anti-neutrino mode since May 2014, T2K becomes sensitive to the CP violation phase δ_{CP} and puts constrain on this phase [91]. Other goals of the experiment include neutrino interaction cross-section measurements and exotic physics such as sterile neutrino and Lorentz violation searches.

In order to achieve these challenges, T2K uses a neutrino beam produced at the Japan Proton Accelerator Research Complex (J-PARC), in Tokai-Mura, on the East coast of Japan. This 2.5° off-axis beam narrows the energy spectrum and focuses the neutrino energy around 600 MeV. This allows to maximise the oscillation probability at the far detector Super-Kamiokande (SK), located 295 km westward in the Mozumi mine. The two near detectors 280 m downstream of the neutrino beamline target station are used to assess the beam properties on-axis and off-axis, which is an important step to understand signals and backgrounds observed at SK. On top of that, cross-sections on carbon and water are measured with these two near detectors to reduce the systematic error at the far detector. A schematic view of the journey of a T2K neutrino is represented in Figure 4.1. This chapter explains how the T2K neutrino beam is created in Section 4.1, while the near and far detectors are described in Section 4.2 and Section 4.3 respectively.

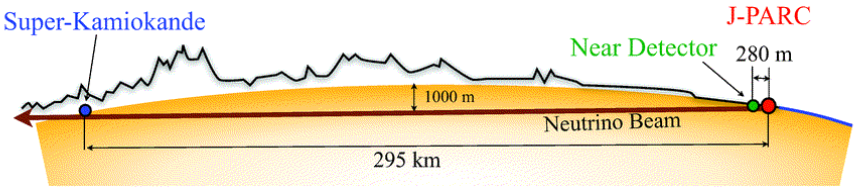

Figure 4.1: Schematic view of the T2K neutrino beamline, from J-PARC to Kamioka Observatory [92].

4.1 The Neutrino Beam

To generate the muon neutrino beam, T2K first requires the acceleration of protons up to 30 GeV towards a graphite target. The charged hadrons (mainly pions and kaons) resulting from these collisions are then focused by magnetic horns described in Section 4.1.2.2. The hadrons decay into muons and muon neutrinos. A beam dump is placed after the decay pipe to stop most of the particles apart from the neutrinos. In the case where energetic muons escape the beam dump, a muon monitor is located downstream of the dump to check the beam direction and stability. The T2K neutrino beam and the flux prediction are described in details in [92, 93].

4.1.1 The J-PARC Accelerator Complex

J-PARC is an accelerator facility located in the village of Tokai-Mura, Ibaraki prefecture. This accelerator provides a high-intensity proton beam that is used to study material and life sciences, nuclear and particle physics. It features three accelerators: a linear accelerator (LINAC), a rapid-cycling synchrotron (RCS) and the main ring synchrotron (MR).

A schematic view of the J-PARC complex is represented in Figure 4.2. The proton beam is produced as follows:

- The LINAC accelerates H^- anions from an ion source (Cesium) up to 180 MeV. It is designed to provide a stable and high beam intensity while minimising the beam

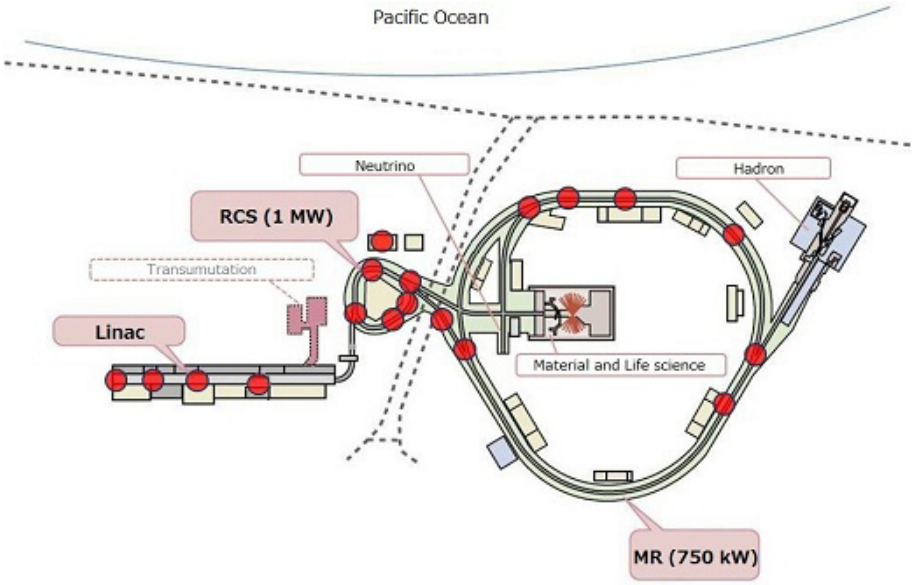

Figure 4.2: Schematic view of the J-PARC accelerators. The proton beam is extracted from the ion source and accelerated to 180 MeV in the LINAC. It is further accelerated to 3 GeV in the RCS and injected to the MR, which increases the proton kinetic energy up to 30 GeV. From `https://j-parc.jp/public/Acc/en/index.html`

losses, as explained in [94]. As they enter the RCS, the H^- pass through a thick carbon foil that strips two electrons from each H^-, converting them to protons.

- The purposes of the RCS can be split into three parts according to its three-sided symmetry: injection/collimation, acceleration and extraction. The H^+ ions from the LINAC are injected and accelerated to 3 GeV with a 25 Hz cycle rate. The RCR can hold two bunches in a cycle which are either injected to the MR for 5 % of the time, or extracted for the Material and Life Sciences facility the remaining time.

- The Main Ring total circumference is 1567 m. It can contain up to nine proton bunches, but only eight are used for the neutrino operation. These bunches are accelerated up to 30 GeV and they can be extracted at two locations. The slow extraction point provides the high energy protons to the hadron hall. The fast extraction point diverts the eight bunches into the neutrino beamline within a single turn, which consists in one beam spill. The spills are extracted by a set of five kicker magnets that turn on during the passing of the ninth empty bunch. The spill cycle and width are 0.5 Hz and 5 μs respectively, giving a maximum beam power of 750 kW.

It is very important to understand the bunch timing structure as it is used to reject background events from cosmic rays.

4.1.2 Neutrino Beamline

The neutrino beamline is composed of two sections. Once extracted from the MR, the beam spills enter the primary beamline which consists of the preparation section, the arc section and the final focusing section. This is where the proton bunches are bent toward Kamioka. The secondary beamline includes the target station, the decay volume and the beam dump. This is where the neutrino beam is produced, from the collision of protons with the target. The mesons produced are then focused and decay into neutrinos. A schematic view of the beamline is shown in Figure 4.3.

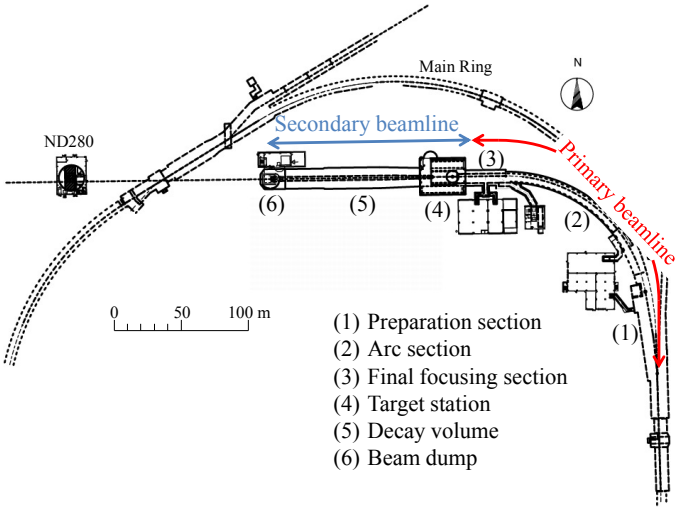

Figure 4.3: Schematic view of the T2K neutrino beamline. The beam spills are extracted and bent towards Kamioka in the primary beamline, while the neutrino beam is generated in the secondary beamline from the decay of the mesons resulting from the protons colliding with the target [92].

4.1.2.1 Primary Beamline

- The preparation section is 54 m long and contains 11 normal-conducting magnets (4 steering, 2 dipole and 5 quadrupole magnets) which focus and deflect the proton beam, ensuring that it is ready for acceptance into the Arc Section.

- The arc section is 147 m long and has a radius of curvature of 104 m, which bends the beam by 80.7° in order to be aligned in the Kamioka direction. The bending

and focusing of the beam is achieved by 14 doublets of Superconducting Combined Function Magnets (SCFMs). Each of them is cooled at 4.5 K with supercritical helium. They generate simultaneously a dipole field of 2.6 T and a quadrupole field of 19 $T.m^{-1}$ [95]. Three additional pairs of horizontal and vertical superconducting steering magnets correct the beam orbit.

- The final focusing section is 37 m long and constitutes 10 normal conducting magnets (4 steering, 2 dipole and 4 quadrupole) guiding and focusing the beam onto the target. It also bends the beam downward by 3.637° with respect to the horizontal to refine the alinement with Kamioka.

A stable and well-tuned beam operation is extremely important to minimise beam loss while producing a high intensity and consistent neutrino beam. Therefore, the primary beamline contains a large suite of 96 instruments to monitor the beam. The intensity is measured by 5 Current Transformers (CTs), the beam position by 21 Electrostatic Monitors (ESMs), the beam profile by 19 Segmented Secondary Emission Monitors (SSEMs) and the losses by 50 Beam Loss Monitors (BLMs). The location of these detectors along the primary beamline is shown in Figure 4.4.

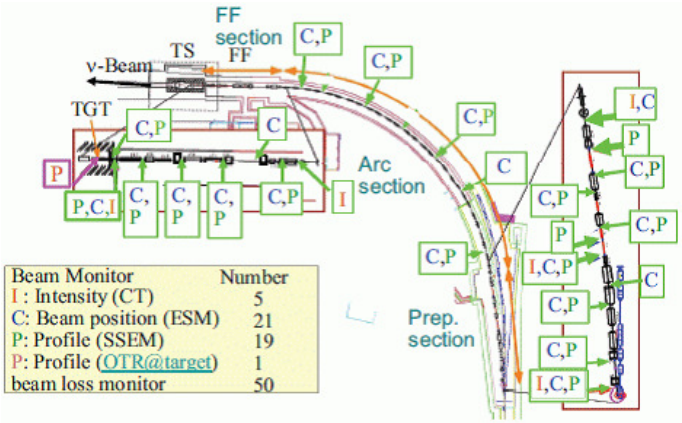

Figure 4.4: Schematic view of the primary beamline with the location of the beamline monitors [92].

4.1.2.2 Secondary Beamline

The entire secondary beamline consists of a total volume of ∼1500 m^3 filled with helium gas at 1 atm to reduce pion absorption and suppress tritium and NO_x production by the

beam. In order to separate the primary proton beamline vacuum from the helium vessel, the spills first pass through a beam window made of two 0.3 mm thick titanium-alloy skins.

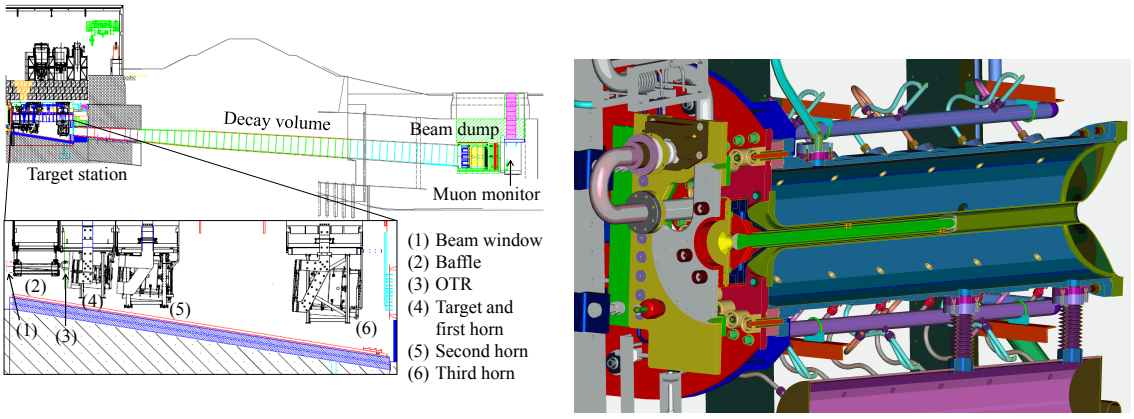

Figure 4.5: Left: Side view of the secondary beamline. Right: Cross section of the graphite target (green) surrounded by the first horn (blue) and the cooling system [92].

- The target station is 12 m underground and contains a baffle, an Optical Transition Radiation monitor (OTR), the target itself and three magnetic horns as detailed in Figure 4.5. Iron blocks are placed around the aluminium volume filled with helium to ensure a good shielding from radiation. The baffle is a 1.7 m long, 0.3 m wide and 0.4 m high graphite block with a 30 mm diameter beam hole. It acts like a collimator to protect the magnetic horns. The OTR monitor uses a thin titanium-alloy foil tilted by 45° with respect to the beam direction. This foil has a different dielectric constant than helium and therefore transition radiation light is emitted in a narrow cone, reflected at 90° to the beam, while it passes through the foil. This light is then transported out of the radiation shielding by parabolic mirrors and collected by a camera, imaging the beam profile. The beam position and direction are known with an error smaller than 1 mm and 0.5 mrad respectively [96].

  The T2K target core consists of two layers. The inner one is a graphite rod, 91.4 cm long (1.9 radiation length) with a diameter of 2.6 cm and a density of 1.8 g.m^{-1}. It is surrounded by a 2 mm thick graphite tube and sealed in a 0.3 mm titanium case. The two graphite cylinders and the case are cooled by helium gas flowing between each layer at 250 m s^{-1}, keeping the temperature at the centre around 700 °C. The choice

of a graphite target is motivated by its high melting point, good thermal resistance and low atomic number [97]. About 80 % of the protons interacts with the target, producing mostly pions and kaons.

These charged mesons are focused by a series of three magnetic horns in order to obtain a neutrino beam as narrow as possible. They consist of a pair of coaxial conductors made of an aluminium alloy, which encompass a closed volume. When a very intense current runs through the conductor, it generates a toroidal magnetic field within the horn volume:

$$B = \frac{\mu_0 I}{2\pi r} = 0.2 \frac{I\ (\text{kA})}{r\ (\text{mm})} \tag{4.1}$$

with μ_0 the magnetic permeability, I the current and r the distance to the beam axis. A sketch illustrating the principle of a magnetic horn is shown in Figure 4.6. While the first horn collects pions generated at the target sitting in its inner conductor, the second and third horns focus the charged mesons. By reversing the polarity of the magnetic field, positively or negatively charged mesons can be selected and focused, producing a neutrino or anti-neutrino beam respectively. The average current in the three horns is set to $+250 \pm 5$ kA for neutrino runs and -250 ± 5 kA for anti-neutrino runs, which provides a magnetic field of 1.7 T. Around the spectrum peak energy, an increase of the neutrino flux by a factor of $\sim$17 can be observed at the far detector with respect to no current.

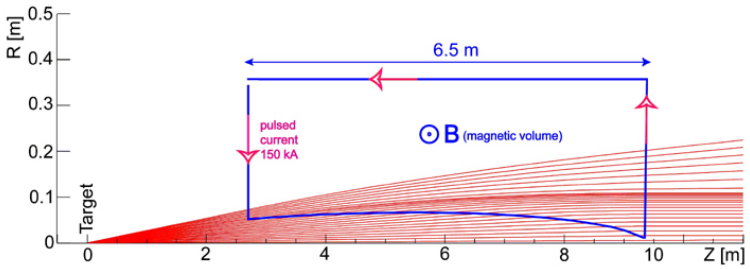

Figure 4.6: Principle of a magnetic horn. The charged mesons produced at the target station (red lines) are focused via the magnetic field produced by the high intensity current running in the conductor (blue lines) [98]. The Figure represents the spread of the beam (y axis) as a function of the distance to the target.

- The decay volume is a 96 m long tunnel filled with helium. This distance is long

enough to have as many muon neutrino as possible via the reactions:

$$\pi^+ \to \mu^+ + \nu_\mu \quad \textit{(dominant)}$$
$$K^+ \to \mu^+ + \nu_\mu$$
$$K^+ \to \pi^0 + \mu^+ + \nu_\mu$$

and it is short enough to avoid, as far as possible, the background contamination from:

$$K^+ \to \quad \pi^0 + e^+ + \nu_e$$
$$\mu^+ \to \quad e^+ + \nu_e + \bar{\nu}_\mu$$

The width of the tunnel is 1.4 m (3.0 m) and its height is 1.7 m (5.0 m) at its upstream (downstream) end which is big enough to contain the beam up to a spread angle of 3°. The walls are made of 16 mm thick steel surrounded by a 6 m thick reinforced concrete shielding. Forty plate coils are welded to the steel along the beam axis to cool the walls and the shielding below 100°C using water.

- The beam dump is located at the end of the decay volume, 109 m downstream from the target. It is contained in a helium vessel and consists of a 3.17 m long, 1.94 m wide and 4.69 m high block of graphite weighting 75 tons along with two iron plates downstream of the graphite core. Fifteen additional iron plates are located downstream of the vessel, which makes a total iron thickness of 2.40 m. This facility stops all the hadrons as well as any muons with an energy below ∼5 GeV. The remaining energetic muons enter the muon monitor (MUMON).

4.1.2.3 Muon Monitor and Emulsion Tracker

The muon monitor (MUMON) is designed to measure the neutrino beam direction to an accuracy of 0.25 mrad and monitor the stability of the beam intensity to a precision of 3 % [99]. This is achieved by measuring the position profile of the energetic muons that manage to pass the beam dump. Since these muons are produced from the same parent particles as the neutrinos, their properties can be studied to characterise the neutrino beam intensity and direction on a bunch-by-bunch basis. MUMON is composed of two types of detector: an upstream array of ionisation chambers at 117.5 m from the target

and a downstream array silicon photodiodes 1.2 m further. They both cover a $1.5 \times 1.5\,\mathrm{m}^2$ area and reconstruct the 2D muon profile from the distribution of the observed charge. The beam direction can then be recovered from the vector between the target and the measured muon profile centre.

The muon flux and momentum are evaluated by two types of nuclear emulsion detector located downstream the MUMON. The first one measures the muon flux with a systematic uncertainty of 2 % and the second one measures the muon momentum with a precision of 28 % at a muon energy of 2 GeV [100].

4.1.2.4 Off-axis Method

The angle between the beam focusing axis and the T2K far detector is 2.5°. This off-axis method is used to generate a narrow-band neutrino beam peaked at an energy of 0.6 GeV. Calling the momentum conservation in the two-body pion decay $\pi^+ \rightarrow \mu^+ + \nu_\mu$, one can derive the angular energy dependence of the neutrino beam. Assuming the neutrino to be massless, we find:

$$E_\nu = \frac{m_\pi^2 - m_\mu^2}{2(E_\pi - \mid \boldsymbol{p}_\pi \mid \cos\theta)} \tag{4.2}$$

where E_π, m_π and $\boldsymbol{p}_\pi$ are the energy, mass and 3-momentum of the pion respectively, E_ν is the neutrino energy, m_μ the muon mass and θ the angle between the neutrino and the pion directions. It shows that, as θ increases, the denominator in (4.2) increases too, therefore the neutrino energy decreases. This phenomenon is shown in Figure 4.7 where can see that the energy of the T2K neutrino off-axis beam is more focused around 600 MeV as the angle is getting closer to 2.5°. This precise angle has been chosen because, for an energy of 600 MeV, the muon-neutrino survival probability at 295 km reaches one of its minimum. This also allows to reduce the high energy neutrino tail that would contribute to background processes.

4.1.3 T2K Flux

The T2K neutrino flux is divided into 4 parts according to the different neutrino types.

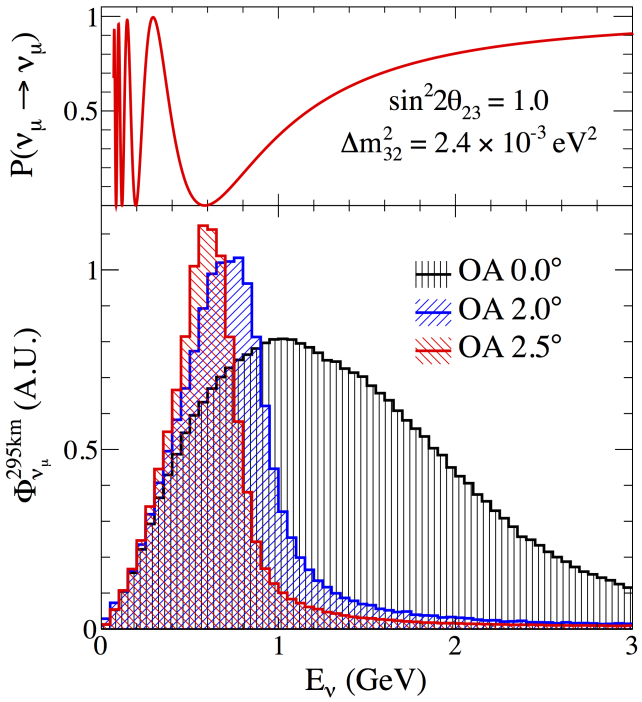

Figure 4.7: T2K neutrino flux spectrum for different off-axis angles and muon neutrino survival probability at 295 km as a function of neutrino energy [93].

The neutrino energy also gives us information about which is the most probable neutrino parent.

- ν_μ beam: this constitutes the main contribution of the total beam (in neutrino mode). These neutrinos comes from the two-body decay of π^+ up to ∼2 GeV. The higher energy ν_μ come mostly from the K^+ two-body decay and a small fraction is produced during in the three-body decay as detailed in 4.1.2.2. A very small amount of ν_μ come from neutral kaon decays.

- $\bar{\nu}_\mu$ beam: this mainly comes from the decays of π^- (up to 4 GeV) and K^- (for higher energies) that remain in the beam despite the action of the magnetic horns. Some of them are also produced via the μ^+ decay-in-flight. The contribution of the charged kaons three-body decay and of the neutral kaon decay is negligible.

- ν_e beam: most of the ν_e are produced by μ^+ decay (up to ∼2 GeV). The other source of ν_e is the three-body decay of charged and neutral kaons.

- $\bar{\nu}_e$ beam: the neutral kaon decays, followed by the three-body decay of charged kaons, are the two main production modes of these anti-neutrinos. For energies below 2 GeV, the μ^- decays are not negligible.

The fractional contribution to the flux predictions from different neutrino parents along with the fraction of each neutrino flavour in the total neutrino flux at the near detector are listed in Table 4.1.

Table 4.1: Fractional contributions (in %) to the neutrino flux predictions at ND280 from different neutrino parents and fractions (in %) of each neutrino flavour in the total neutrino flux [101].

		Neutrino parents				
	Total fractions	$\pi^{\pm}$	$K_2^{\pm}$	$K_3^{\pm}$	K_L^0	$\mu\pm$
ν_μ	92.4	95.5	4.2	0.2	0.1	<0.01
$\bar{\nu}_\mu$	6.39	85.8	4.0	0.2	1.2	8.8
ν_e	1.02	1.0	-	30.7	11.1	57.2
$\bar{\nu}_e$	0.15	0.4	-	13.6	76.7	9.2

The neutrino flux at the near and far detectors is obtained by a suite of data-driven Monte-Carlo (MC) simulation packages. The interaction of the protons within the graphite target is simulated by FLUKA [102] which passes the kinematic information of the emitted particles to the JNUBEAM simulation. JNUBEAM has been developed by the T2K collaborators to simulate the whole secondary beamline. It is based on GEANT 3 [103] for the particle transport and GEANT3/GCALOR [104] to simulate interactions outside the target. The total integrated neutrino flux at the near and far detectors $\tilde{\phi}(E)$ corresponds to the sum of the flux predictions for the i^{th} run $\phi_i(E)$ (calculated by the MC simulations), weighted by the number of protons on target (POT) accumulated in this run N_i^{POT}, as follows:

$$\tilde{\phi}(E) = \frac{1}{N_{\mathrm{tot}}^{\mathrm{POT}}} \sum_{i^{th}run} N_i^{\mathrm{POT}} \phi_i(E) \tag{4.3}$$

The number of accumulated POT along with the beam power is shown in Figure 4.8.

The primary interaction of the 30 GeV protons with the graphite target is a large source of error in the neutrino flux predictions. This is due to the complexity in modelling the proton-nuclear interactions which leads to large uncertainties in the hadron production. To address this problem, the NA61/SHINE experiment located at CERN recorded and

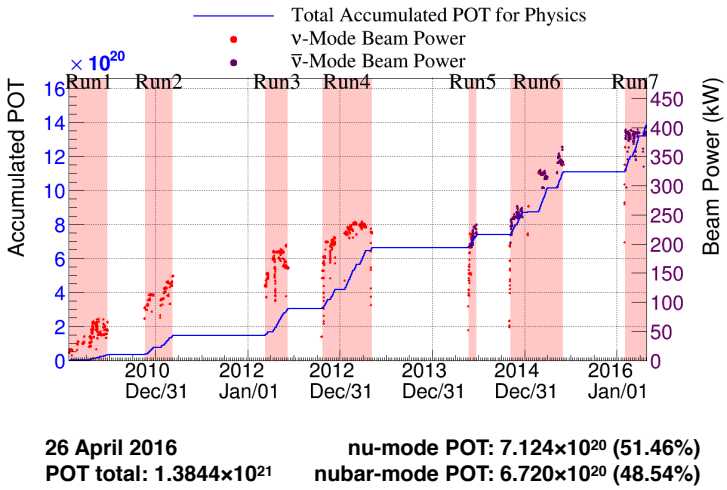

Figure 4.8: Number of accumulated POT and beam power for each run.

analysed data using a 30 GeV proton beam from the Super Proton Synchrotron (SPS) and a replica of the T2K target [105]. These hadron production data were used to reweight the FLUKA + JNUBEAM predictions and to constrain the flux for up to 90 % of the phase space in the region around the peak energy [106]. The final flux predictions at the near (far) detector for the first 4 neutrino runs are shown in the left (right) plot of Figure 4.9. They are normalised to 10^{21} POT, which is the expected POT per year with a beam power of 750 kW.

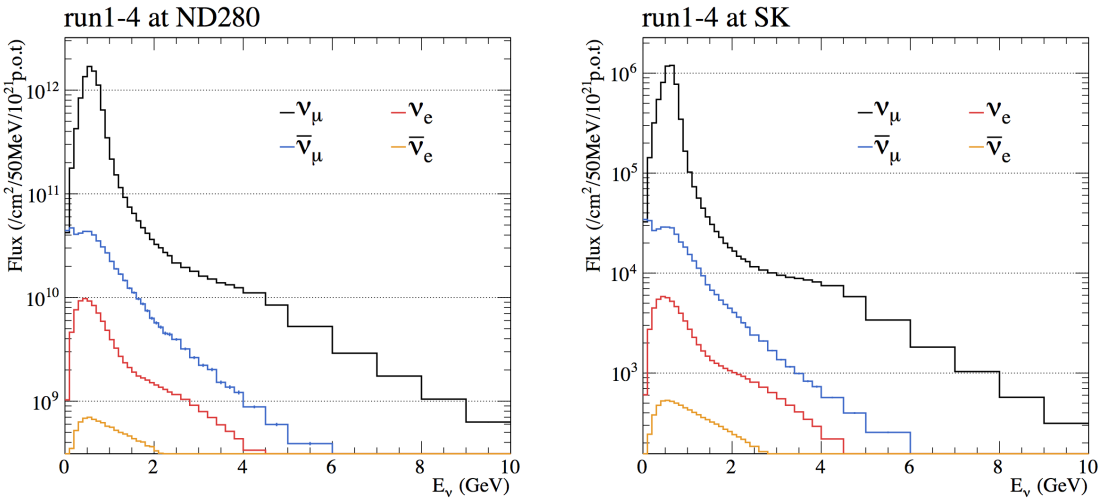

Figure 4.9: Flux predictions at the near (left) and far (right) detectors, normalized to 10^{21} POT

4.2 The Near Detectors

At 280 m from the target station, in a 37 m deep cylindrical pit with a 17.5 m diameter, sits the near detector complex which consists of two detectors. The 2.5° off-axis near detector (ND280) is a magnetised tracking detector capable of measuring the neutrino flux, energy spectrum, beam contamination along with a wide range of neutrino-nucleus cross-sections. The Interactive Neutrino GRID (INGRID) is an on-axis detector aiming at measuring the neutrino beam profile and its direction at 280 m. An overview of the detector arrangement in the pit is shown in Figure 4.10.

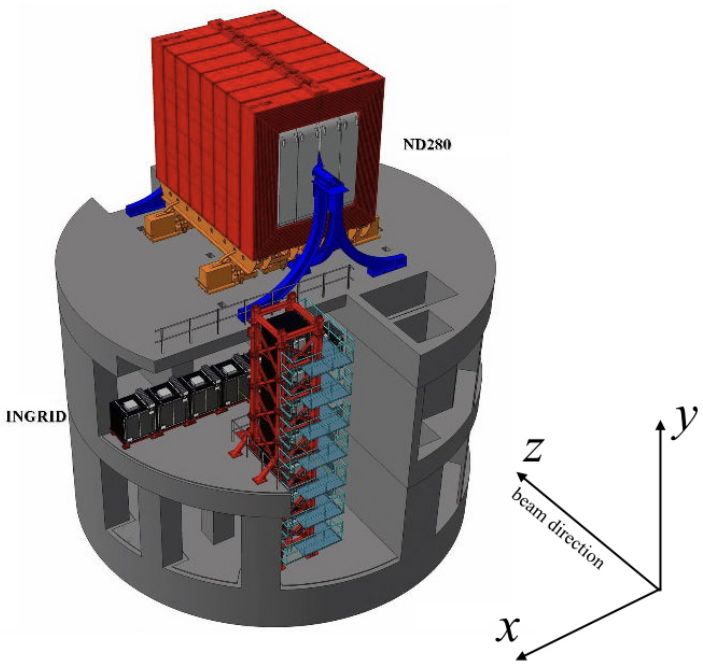

Figure 4.10: The near detector complex. ND280 is located on the upper floor of the pit. Note that the magnet is closed in the sketch. The horizontal INGRID modules are located on the level below while the vertical INGRID modules are stacked from the lower floor. (Figure extracted from `https://www2.warwick.ac.uk/fac/sci/physics/research/epp/exp/t2k/overview_scientific/`)

The sub-detectors make extensive use of various plastic scintillators. When struck by an incoming particle, these materials return the ionization energy as light which is extracted towards the readout system using wavelength shifting (WLS) fibres. The multi-pixel photon counters (MPPC) are the photosensors chosen for the near detectors as they can operate in a magnetic field and fit into a small space, unlike photo-multiplier tubes (PMT). They are

designed to match with the emission spectra of the WLS of 476 nm. Each MPPC consists of a 26 × 26 array of independent avalanche photodiodes making the total pixel number equal to 676, of which 9 are lost to fit an electrode on the diode. Each pixel is held at 0.8-1.5 V above their breakdown voltage, giving a gain of $\sim 1 \times 10^6$. When a photon from the WLS fibre strikes a pixel, a Geiger avalanche is created. The pixel then gives a binary response according to whether it has been struck or not, which is independent from the number of photo-electrons created. The total MPPC output is the sum of all the fired pixels within a given time period, which should be proportional to the number of photons observed. It can occur that individual pixels generate a signal when there is no incident photon. This "dark noise" is ignored during the track reconstruction. More details about those photosensors are available in [107].

4.2.1 INGRID

The INGRID detector is centred on the neutrino beam axis. It is composed of one high granularity module (called proton module) and 16 identical standard modules. While 14 of them form a cross (7 modules per axis) and are used to measure the beam profile and intensity, 2 modules are symmetrically off-axis from the main cross, on top of the second and sixth horizontal modules as illustrated in Figure 4.11. They check the beam's axial symmetry.

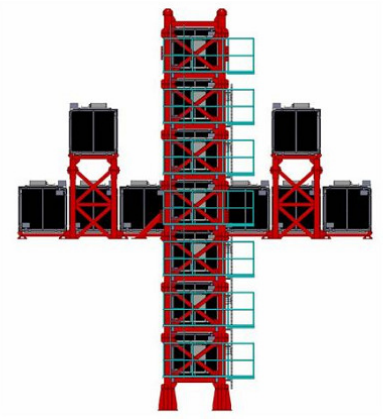

Figure 4.11: INGRID on-axis near detector [92].

The centre of the cross corresponds to the neutrino beam centre. Each of the 16 standard modules has a sandwich structure of 11 scintillator tracking planes separated by 9 iron

plates used as a target (there is no iron plate between the 10^{th} and 11^{th} scintillator planes due to weight restrictions) .The total iron mass is 7.1 tons per module so that, at the nominal beam intensity, there are enough neutrino interactions in each module to monitor the beam direction on a day-by-day basis. Four scintillator planes are located around the previous structure and, along with the most upstream and downstream planes, they are used to veto any interactions occurring outside the module, as shown in Figure 4.12. Each tracking plane consists of 2 layers of 24 scintillator bars glued together. The first (second) layer has its bars arranged horizontally (vertically), and the dimension of one bar is 1.0 cm $\times$ 5.0 cm $\times$ 120.3 cm. The veto planes are made of 22 scintillator bars aligned along the beam axis. A 3 mm diameter hole runs the length of each bar so that a wavelength shifting (WLS) fibre may be inserted to transport the light produced in the bar to the multi-pixel photon counter (MPPC) for electronic read-out. INGRID is able to measure the beam centre to a precision of 28 cm (i.e. the direction is known within less than 1 mrad) and the neutrino event rate is measured with 1.7 % uncertainty.

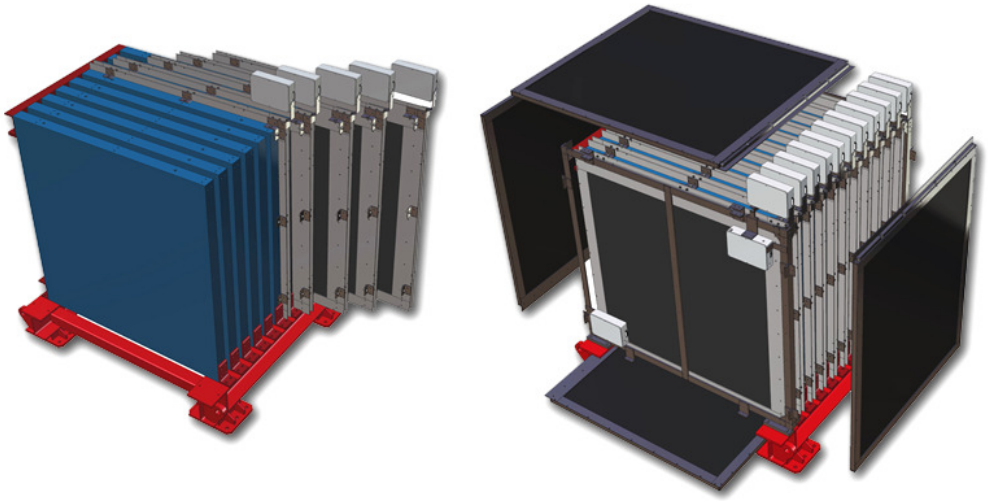

Figure 4.12: Left: an INGRID module with the tracking planes (black) and the iron plates (blue). The right image shows the module surrounded by the veto planes. [92].

The proton module is located between the two central standard modules on each axis of the cross and is composed of smaller scintillator bars. Its high granularity tracking capabilities allow it to measure both muons and protons from charged current interactions so that quasi-elastic channel can be identified and compared with the beamline MC and neutrino generators.

4.2.2 ND280

The off-axis near detector is a device composed of many sub-detectors, each having different purposes and using different detection techniques that are detailed below. However, one can start by summarising the global goals of ND280:

- To provide information to determine the ν_μ flux at Super-Kamiokande,
- To measure the ν_e content of the beam as a function of neutrino energy as it is an intrinsic background for the ν_e appearance search,
- To measure the ν_μ interactions that can be a source of background for the ν_e appearance such as the neutral current π^0 production,
- To measure inclusive and exclusive neutrino cross-sections.

To achieve these requirements, the ND280 detector must be able to reconstruct exclusive event types such as ν_μ and ν_e CCQE, CC inelastic and NC π^0 in addition to measuring inclusive event rates. All of these goals were considered in the design of the detector. It is housed in the refurbished magnetic coils and flux return yokes of the previous UA1 and NOMAD experiments [108, 109, 110] as shown in Figure 4.13. The external dimensions of the magnetic yokes are 7.6 m × 5.6 m × 6.1 m (length × width × height) for a total weight of 850 tons. Inside, the ND280 sub-detectors are arranged as follow:

- an upstream π^0 detector (P0D) followed by a tracker system made of three time-projection chambers (TPCs) with 2 fine-grained detectors (FGDs) in between each TPC. The P0D and the tracker are placed inside a big metallic frame called the "basket". The internal basket size is 6.5 m × 2.6 m × 2.5 m.
- an electromagnetic calorimeter (ECal) that surrounds the basket.

4.2.2.1 Magnet

The magnet provides a dipole magnetic field of 0.2 T to determine with high resolution the sign and the momenta of the charged particles in the tracker.

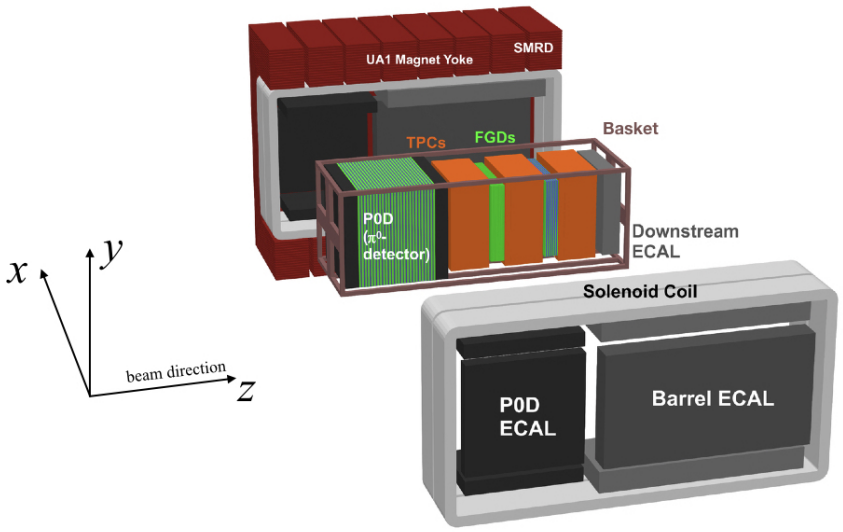

Figure 4.13: Exploded view of the off-axis near detector [92].

The horizontal field is produced by four water-cooled aluminium coils (2 per side) and a return flux yoke. The magnet yoke consists of two mirror-symmetric halves (or "clam"). Each half is segmented into eight C-shaped elements made of 16 low-carbon steel plates and they both stand on movable carriages.

4.2.2.2 Side Muon Range Detector (SMRD)

The SMRD measures the momentum of muons escaping at large angles with respect to the beam direction. It also triggers on cosmic ray muons entering the ND280 detector. These cosmic rays are often used in detector calibration and validation studies. Its last function is to act as a veto for particles entering the detector from the outside. These particles can be related to beam events where the neutrino interacts in the surrounding cavity walls or in the iron of the magnet.

The SMRD is made of 440 scintillator paddles inserted in the 1.7 cm air gaps between the 4.8 cm thick steel plates of the flux return yokes. Going from upstream to downstream, the first five elements of the yoke have their three most internal layers instrumented with the scintillator paddles. The remaining elements have their three most internal layers instrumented in their top and bottom portions only, whereas the side portions of the 6^{th} (7^{th} and 8^{th}) element(s) have their 4 (6) innermost layers instrumented, respectively.

This increase of the number of SMRD paddles towards the downstream area gives better reconstruction for the forward going tracks. Each paddle is 7 mm deep and 875 mm long. Their width varies from 167 to 175 mm, allowing the WLS to snake through as shown in Figure 4.14. More information about the SMRD can be found in [111]

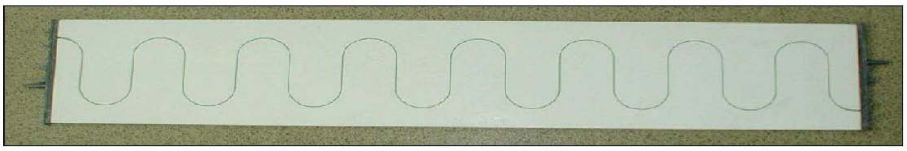

Figure 4.14: Picture of an SMRD paddle. We see the wavelength shifting fibre that snakes through the scintillator module[111].

The MPPCs are coupled to the WLS ends via a snap-on mechanism. A total of 4016 MPPCs are connected to a miniature printed circuit which couples the MPPC signals into mini-coaxial cables leading the signal to the Trip-T front-end board (TFBs).

4.2.2.3 π^0 Detector (P0D)

The π^0 detector was designed to measure the neutrino induced neutral current π^0 production (NCπ^0) on a water target in order to constrain the uncertainty in the ν_e appearance study at the far detector.

The P0D active region, measuring 2103 mm wide by 2239 mm high by 2400 mm deep, consists of 40 (x, y) planes of scintillator bars (134 vertical bars and 126 horizontal bars) interleaved with fillable water target bags and lead or brass sheets. The most upstream and downstream sections, namely the "upstream ECal" and "central ECal", use alternating scintillator planes and lead sheets. The central section is composed of the upstream and central water targets, which use alternating scintillator planes, water bags and brass sheets. The scintillator planes are made of triangular bars to increase the tracking precision, each one being 33 mm wide and 17 mm high as displayed in Figure 4.15. These bars have a hole for the WLS, which are optically read by MPPC at one end and mirrored at the other end. MPPCs are then read out with TFB electronics. The water bags can be filled or emptied, enabling a subtraction method to measure water target cross-sections. More details about the P0D are available in [112].

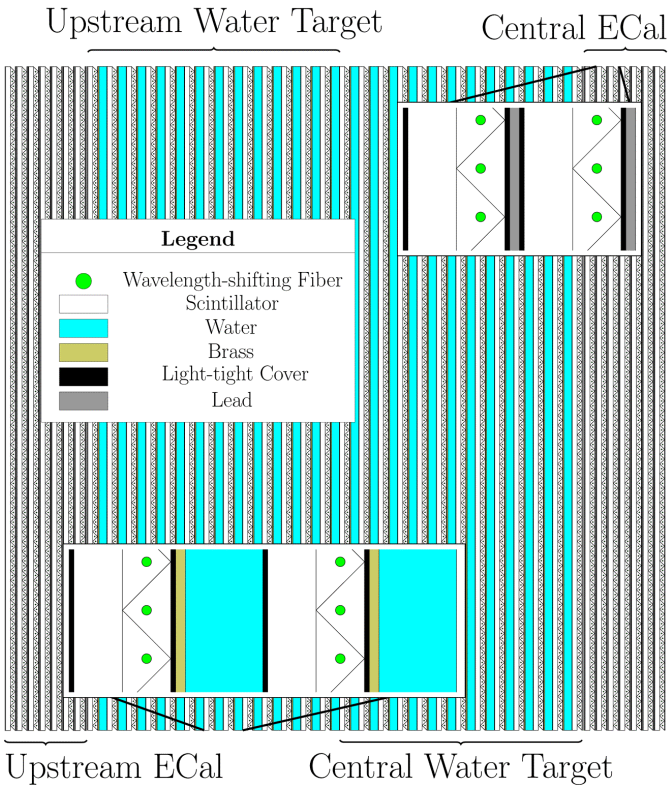

Figure 4.15: A schematic of the P0D detector where the scintillator bars, the water bags, the brass and lead sheets arrangement is detailed the insets. The beam arrives from the left hand side.[112].

4.2.2.4 Electromagnetic Calorimeter (ECal)

The Electronic calorimeter is vital to the reconstruction of neutral particles such as photons and to measure their energy and direction. It also helps in the identification of charged particles escaping the inner detectors.

The ECal surrounds the ND280 tracker on all the faces but the upstream one, located between the inner sub-detectors (namely the P0D) and the magnetic coils (Figure 4.13). 13 plastic scintillator modules are shared between the three ECal parts: the P0DECal and the barrel ECal (BrECal) gathered six modules each while the downstream ECal (DsECal) consists of a single module. The modules are consecutive layers of scintillator bars glued to a sheet of lead converter. Unlike the P0D, the ECal scintillator bars are rectangular with a 4.0 cm $\times$ 1.0 cm cross-section and an elliptical hole running along their full length in the middle is used to insert the WLS fibres. The 34 (31) consecutive layers

of the DsECal (BrECal) module(s) are separated by a 1.75 mm thick lead sheet. They also have their bar orientation alternating at 90° to allow three-dimensional reconstruction of electromagnetic clusters and charged particles tracks. The length of the bars varies from 1.52 m to 3.84 m according to their location (top, bottom, sides) and direction (x, y, z). DsECal bars and BrECal bars running in the z direction are read by MPPCs at both ends whereas BrECal bars running in x and y directions are read at one end. The six P0DECal modules have a slightly simpler structure. Each of them contains six scintillator layers interleaved with 4 mm thick lead sheets. Each bar is aligned in the z direction and is read by a single MPPC. The electronics, calibration and performances of the ECal are described in details in [113], but one can say that the ECal energy resolution varies from 10 % to 20 % depending on the momentum of the particles (the higher the momentum, the better is the energy resolution).

4.2.2.5 Fine Grained Detectors (FGDs)

The two FGDs located between the three time-projection chambers are used as targets for neutrino interactions. They are each 1.1 t and have external dimensions of 2300 mm wide by 2400 mm high by 365 mm deep. Both FGDs are composed of xy scintillator modules, where one xy module consists of 192 scintillator bars aligned in the x direction (horizontal) glued with another set of 192 bars aligned in the y direction (vertical). The bars are 1864.3 mm long with a square cross-section of 9.61 mm × 9.61 mm. The WLS fibre runs along a hole in their center and is read out at one end of the bar, whereas the other end is mirrored by vacuum deposition of aluminium. While the most upstream FGD, labelled as FGD1, is made of pure scintillator (15 xy modules), the downstream FGD (FGD2) is made of seven xy modules interleaved with six 25 mm thick water modules. The water containers are made of sealed panels of rigid corrugated-polycarbonate. Using a vacuum pump, the water is kept at below the atmospheric pressure so that, in case of a leak, water does not go inside the FGD.

The water bags in FGD2 are important as they allow cross-section measurements on the same target as the far detector. Such measurements are then used to constrain the predicted event rate at Super-Kamiokande, hence reducing the uncertainty on the estimation of the oscillation parameters. The analysis presented in part III uses a subtraction method

between interactions in FGD2 and FGD1 to extract a cross section on water. More detailed information about the FGDs can be found in [114].

4.2.2.6 Time Projection Chambers (TPCs)

The three TPCs are essential to the three-dimensional reconstruction of the charged particles. They also play a key role in the measurement of the charged particles momentum as they are operating in a magnetic field. Last but not least, they are used in the particle identification, which is based on the energy loss pattern recognition (dE/dx) and the momentum.

The outer volume of each TPC is 2302 mm wide by 2400 mm high by 974 mm deep. The inner volume contains around 3000 litres of an Argon-based drift gas Ar:CF_4:iC_4H_{10} in the proportion 95:3:2. This mixture was chosen for its low diffusion properties and 90 % of the exhaust gas is purified and recycled. The inner (outer) walls are made of copper (aluminium) respectively and an insulating CO_2 gas is contained in between the two volumes. One can split the inner volume into a left and a right part separated in the middle by the central cathode (in the zy plane). The voltage applied on the strip pattern machined into the copper walls of the inner volume and on the cathode is set to specific values so that a uniform electric field is generated and aligned with the magnetic field. When a charged particle crosses the drift volume, it ionises the gas and releases electrons which drift away from the central cathode to the read out planes, where they are multiplied by the micromega (MM) anode modules. Each MM module is 342 mm by 359 mm and is segmented into 1728 anode pads that are 7.0 mm wide by 9.8 mm high and are used to amplify the signal. There are 12 MM in each readout plane organised into two slightly offset vertical columns (Figure 4.16). These pads are used in the 3D track reconstruction. The x position is known from the arrival time of signal (hit time + ionisation drift velocity) while the y and z positions are determined by the pattern on the MM pad module. The spatial resolution, which depends of the drift length, is always below 1 mm and the relative momentum resolution is around $0.1\,p_T/GeV/c^2$. The resolution of the deposited energy is of the order of 8 % for minimum ionising particles, which allows muons to be distinguished from electrons. Reference [115] contains a full description of the construction, the performances and the calibration of the TPCs.

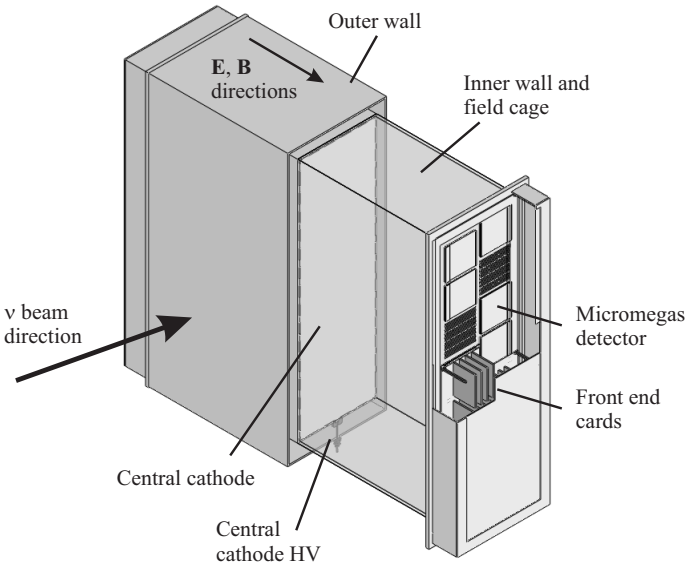

Figure 4.16: Simplified cut-away drawing showing the main aspects of the TPC design.[93].

4.3 The Far Detector: Super-Kamiokande

Super-Kamiokande (Super-K, SK) is used by the T2K experiment as a far detector located 295 km west of the beam source. It is the largest land-based water Cherenkov tank which lies at a depth of 1 km below the Ikeno mountain (2.7 km water equivalent) in the Mozumi zinc mine, Gifu prefecture. This underground location reduces the rate of cosmic ray interactions by around five orders of magnitude with respect to the surface of the Earth. The goal of Super-K is to measure the flavour composition of the T2K neutrino beam at a distance where the oscillation probability is maximised and therefore observe the conversion of ν_μ to either ν_e or ν_τ as a function of the reconstructed neutrino energy. This is done by counting the number of interactions induced by muon and electron neutrinos via the observation of the produced leptons of their respective flavour, the latter emitting Cherenkov light in the SK tank.

The Super-K detector consists of a cylindrical cavern filled with 50 kt of pure water surrounded by 13000 photo-multiplier tubes (PMTs) which collect the Cherenkov light from the neutrino interactions (Figure 4.17). It has been running since 1996 and has already produced some of the major results in flavour oscillations [1] and proton decay [116]. Because of its long-running operation, SK is a well understood detector: the energy

scale accuracy is known to the percent level and the calibrated data matches the Monte Carlo simulation samples to the percent level as well.

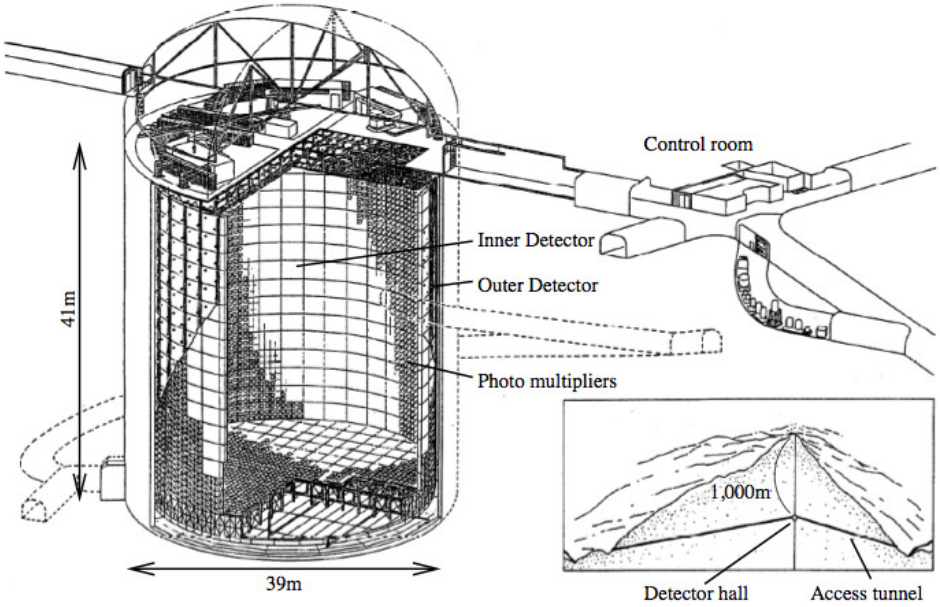

Figure 4.17: Diagram of the Super-Kamiokande detector and its position under Mt. Ikenoyama.[93].

As shown in Figure 4.17, the water tank can be separated into 2 sections:

- the inner detector (ID) is 33.8 m in diameter and 36.2 m high with 11129 inward-facing PMTs along its inner walls. These 50 cm diameter PMTs represent 40 % of surface coverage and have a photon detection efficiency of 20 %. A set of horizontal and vertical Helmholtz coils are used to reduce the Earth magnetic field below 50 mG so that the PMTs are not affected by it. The ID fiducial volume is defined such that any event vertex is reconstructed at least 2 m away from the internal walls.

- the outer detector (OD) is a 2 m thick cylindrical space surrounding the ID. Its inner walls contain 1885 outward facing 20 cm-PMTs that are used as an active veto against incoming particles (mostly cosmic ray muons). Despite the sparse 7 % coverage of the PMTs, this veto is almost 100 % effective in rejecting the external backgrounds. The walls separating the ID from the OD are made of stainless steel and covered by black plastic sheeting to prevent light reflection and transmission.

Super-K can operate on its own as a solar and atmospheric neutrino observatory but for the T2K experiment, the data acquisition system triggers in time with the beam spills produced at J-PARC. Each beam spill is given a GPS timestamp that is used to define a 1 ms window around the T2K beam arrival time. All the hit information recorded in that window is collected and written to disk.

4.3.1 Particle Identification with Cherenkov Light

The electrons and muons produced by the neutrino interactions in SK exceed the speed of light within the water and therefore, a cone of Cherenkov radiation is produced. This radiation is emitted as the superluminal particles polarise the water molecules, which then turn back rapidly to their ground state. The emitted light forms a coherent wave front at an angle of $\cos\theta = c/(n \cdot v)$, with $n = 1.33$ the refractive index of the water and v the speed of the particle in water. The minimum kinetic energy of a particle of mass m to radiate Cherenkov light, namely the Cherenkov threshold T_{Ch} can be calculated according to (4.4).

$$T_{Ch} = m\left(\sqrt{\frac{n^2}{n^2-1}} - 1\right) \tag{4.4}$$

It corresponds to 264 keV (55 MeV) for an electron (muon) in water. By looking at this emission of blue Cherenkov light, one can build a particle identification hypothesis in order to distinguish muons from electrons. Note that it is also possible to consider the case where the neutrino interaction produces extra particles like pions.

By having a much larger mass than the electron, the muon trajectory is not deviated as it passes through the detector. Therefore, the Cherenkov radiation ring detected by the PMTs has a sharp and well defined edge. On the other hand, the electron undergoes multiple scattering, inducing electromagnetic showers in the water medium. Therefore, instead of having a single Cherenkov ring as for the muon case, the electron produces multiple overlapping rings which give a fuzzy edge to the final Cherenkov ring. An example of muon (left) and electron (right) SK event displays are shown in Figure 4.18. The energy of the incoming neutrino can also be inferred from the total number of photoelectrons collected by the PMTs. For more details on SK, see [92].

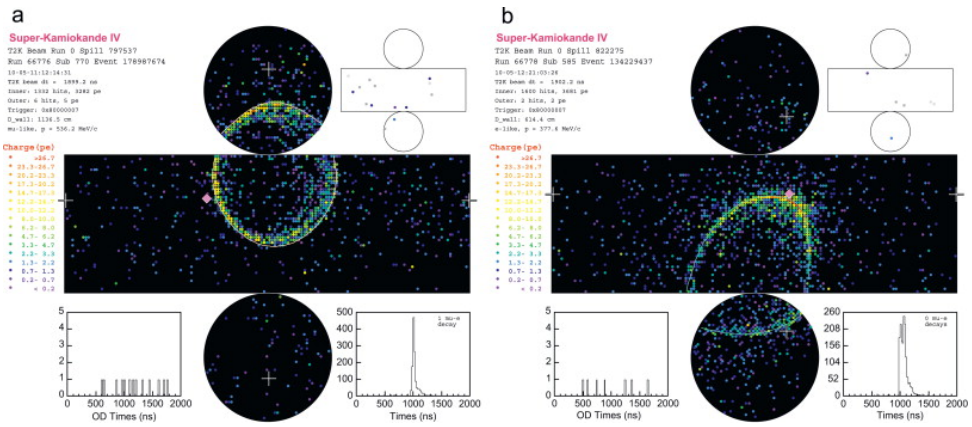

Figure 4.18: Example of SK event displays. The left picture, with the clear edges of the ring, shows a ν_μ-like interaction. The ring on the right picture is less sharp; it represents a ν_e-like interaction)

5

ND280 Software

The T2K experiment uses simulation and analysis softwares that are essential to perform an analysis. They are responsible of the Monte Carlo events simulation, electronic simulation, detector calibration and event reconstruction. This chapter focuses on the tools needed to perform an analysis with the ND280 detector, namely the NEUT [117] event generator and the ND280 offline software packages. They are written in Fortran and/or C++ and are built around ROOT [118] and GEANT4 [119] libraries. A schematic of the package structure of the ND280 Software Suite is shown in Figure 5.1.

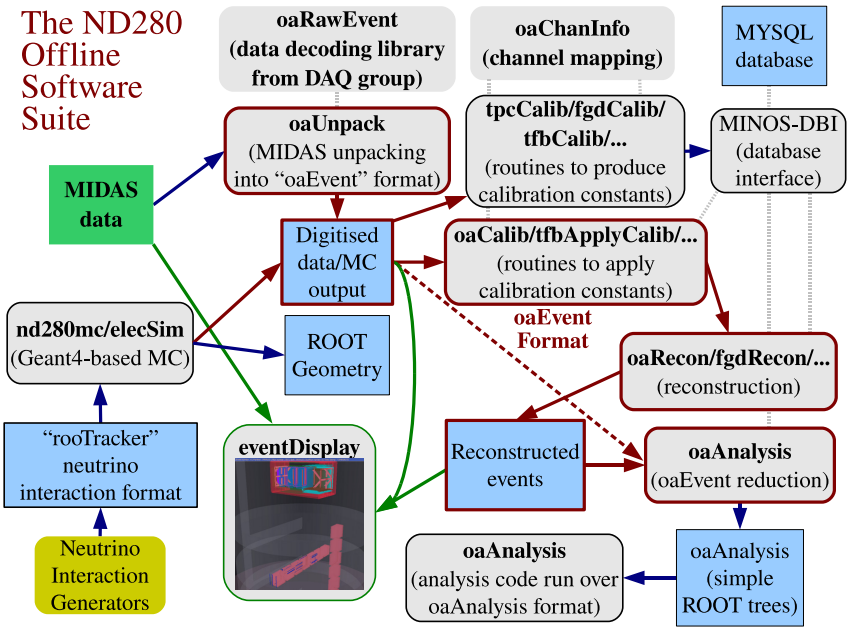

Figure 5.1: Schematic of the package structure of the ND280 Software Suite [92]. Only the most representative packages are included. The box "Neutrino Interaction Generator" corresponds to NEUT.

5.1 The NEUT Event Generator

NEUT [117] is an event generator that, together with the `nd280mc` package simulates the neutrino interactions within ND280. It uses the flux as an input to model the energy, direction, position and flavour of the incoming neutrino, as discussed in Section 4.1.3. The ND280 geometry is also given so that the cross sections can be computed for the target nucleus at a given vertex position. The kinematic variables and the trajectories of the final state particles with an energy above 25 MeV are then stored in and oaEvent format file. In the case where the neutrino interacts in the material surrounding ND280, a so-called "sand" production is processed, where the neutrino vertex is outside the ND280 magnet. The files are then processed through the `elecSim` package which simulates the electronic response of ND280 (detector noise, light attenuation in the scintillator, read out saturation, etc.). After this point, the MC simulation files are processed similarly to the real data files, through all the ND280 offline software (see Section 5.2).

Multiple theoretical models are implemented in NEUT. They describe specific neutrino-nucleus interaction channels, characterise the behaviour of nucleons within the target nucleus and predict how particles propagate in the nuclear medium. The models used in the official release of the Monte Carlo production for this analysis (NEUT v5.3.2) are described below.

5.1.1 Interaction Models

Charged Current Quasi-Elastic and Neutral Current Elastic

The default CCQE and NCE models correspond to the Llewellyn-Smith model [65] integrated with the Spectral Function (SF) model from Benhar and collaborators [120] for carbon, oxygen and iron targets. For other targets, the Llewellyn-Smith model is integrated with the relativistic Fermi gas (RFG) model by Smith and Moniz [121] which describes the nucleus as a many-body system where all the energy states are occupied by free nucleons up to the Fermi energy. The SF model has a more realistic description of the momentum and energy distributions of the initial nucleons compared to the RFG model as it is based on nuclear spectroscopy data, but these functions are not available for every nucleus. In

both cases, the impulse approximation is assumed, which means that the scattering process only involves one nucleon and the remaining nucleons are spectators.

Note that short-range correlations such as meson exchange current (MEC) are also considered following the Nieves *et. al.* description [122] but are treated as a separate channel in NEUT[i]. The long-range inter-nucleon correlations described by the random phase approximation (RPA) have been taken into account only when the RFG model is used as there is no RPA calculation available for the SF model. This RPA correction describes, for example, a screening effect when particles propagate in the nuclear medium.

To summarise, SF + MEC is used for C, O and Fe targets. RFG + MEC + RPA is used for other targets. It is possible to have RFG + MEC + RPA for every target using a reweighting routine.

Resonant Pion Production

The baryon resonance is modelled according to the Rein-Sehgal calculation [72] where the axial and vector form factors have been improved with the results from [123]. This model covers the 18 resonances in the invariant hadronic mass W region below 2 GeV. It also takes into account the interference terms, which are the only ones available for neutrino energies $E_\nu \lesssim 2\,\text{GeV}$. The $\Delta(1232)$ is the dominant resonance for T2K neutrino energy scale. It is assumed that 20 % of the Δ are absorbed before decaying leading to no pion production. This is based on the K2K measurement [124].

Coherent Pion Production

NEUT uses the Rein-Sehgal model [77] for charged and neutral current coherent pion production. The lepton mass correction from [78] is taken into account in the charged-current case. This effect is particularly important for low energy transfer Q^2 and low neutrino energy where it suppresses the coherent cross section of about 25 %, thus reducing the discrepancy with K2K [125] and SciBooNE [126] searches. Note that there is no model for diffractive pion production currently implemented in NEUT, which can directly affect the analysis presented in part III in light of the recent MINERνA excess [127].

[i] labelled "2p-2h" for 2 particles - 2 holes

Deep Inelastic Scattering

DIS interactions are simulated with the GRV98 parton distribution function [128]. In order to improve the agreement with the experiments at low Q^2, the corrections from Bodek and Yang [129] have been implemented. For $W < 2\,\text{GeV}$, only multiple pion production processes are considered so that there is no double counting with the resonant pion production. PYTHIA/JETSET [130] is used for hadronisation at energies above 2 GeV and internal NEUT method otherwise.

5.1.2 Final State Interaction

Once the neutrino-nucleon interaction is simulated, the final state hadrons (mostly protons and pions) may re-interact with other nucleons before leaving the nucleus. These final state interactions (FSI) are important to understand as they can change the charge, multiplicity and kinematics of the outgoing hadrons and, therefore, bias the reconstruction of the neutrino energy. The cascade model is used in NEUT where each particle is propagated step by step inside the nucleus. The step size is determined by the mean free path which depends on the momentum of the hadron and its position in the nucleus (or the nuclear density). For each step, the probability of interaction is calculated (elastic and inelastic scattering, absorption, charge exchange). If an interaction occurs, the resulting particles are stepped through the rest of the nucleus. This continues until all the particles are absorbed or escape the nucleus.

It is possible to tune this model using external data from pion scattering experiments on proton or Carbon.

In order to take into account Pauli exclusion principle, and therefore avoid having two nucleons in the same state, it is required that, for CCQE and resonance pion production cases, the outgoing nucleons have a momentum larger than the Fermi surface momentum p_F. For a carbon (oxygen) nucleus, $p_F = 217\,\text{MeV}$ ($p_F = 225\,\text{MeV}$).

5.2 ND280 Offline Software Packages

At this stage, the real data and the MC simulations are stored in the same file format

and must follow the processing chain that takes care of the detector calibration and event reconstruction.

5.2.1 Detector Calibration

The calibration is done using constants that are stored in a MySQL database. These calibration constants can vary for different experimental running periods. The oaCalib package contains all the routines necessary to calibrate the data.

The calibration of all scintillator-based detectors is very similar. It can be broken down into two categories: energy (or light yield) and timing calibration. The goal of the energy calibration is to make sure that the energy response is uniform across all the scintillator modules of a given detector and that the data/MC agreement is correct. It includes several corrections such as the electronic noise subtraction, the conversion from ADC count into a readout charge, bar-to-bar correction, etc. The timing calibration is important as the hit timing is used to determine the direction of tracks and showers, to reject noise and to find potential clusters. Hence it is crucial to correct for the electronic offset caused by different cable lengths and for electronic time-walk. Note that delays up to 10 ns can be observed between TPCs and ECals as there is no inter-detector calibration.

For the TPCs, a specific laser calibration system is placed on the central cathode. It produces a control pattern of electrons used to precisely determine the electron drift velocity and the inhomogeneity of the electric and magnetic fields. Finally, it can also measure the absolute gain of the readout system [115].

5.2.2 Tracker Reconstruction

The events reconstruction in ND280 is done in two stages. First the local reconstruction where specific routines reconstruct the tracks in each sub-detector by gathering hits from MPPCs or micromega pads. Then the global reconstruction takes care of matching objects previously found in each sub-detector so that reconstructed tracks can span multiple sub-detectors [131].

The tracker reconstruction starts by clustering hits that are close to each others (in both space and time) from the TPC micromegas pads. A likelihood fit is then performed to

these TPC segments to determine their start and end positions and direction along with their curvatures. A Kalman filter [132] is used to extrapolate these TPC tracks into the FGDs resulting in tracks which span the whole tracker. The momentum $|\mathbf{p}|$ (in GeV) of the track can be reconstructed according to

$$|\mathbf{p}| = 0.3 \cdot q \cdot B \cdot R \tag{5.1}$$

where q is the charge (in units of e), R is the curvature radius in m and B the magnetic field in T.

If there are isolated FGD hits that are not added to the TPC tracks by the filter, an independent FGD reconstruction routine is called. This FGD reconstruction starts to look for hits in the xz and yz scintillator planes independently. Hits in a given plane are then matched to give a 2-dimensional FGD track. By projecting the 2D track from the xz plane onto the 2D track from the yz plane, one can reconstruct a full 3D object.

A measurement of the energy loss per unit length dE/dx of each TPC track is used for particle identification (PID). For a given momentum, a PID hypothesis is built by calculating a "pull":

$$Pull_\alpha = \frac{\left(\frac{dE}{dx}\right)^{meas} - \left(\frac{dE}{dx}\right)^{exp}_{\alpha}}{\sigma_\alpha} \tag{5.2}$$

where $\left(\frac{dE}{dx}\right)^{meas}$ is the measured energy loss which is compared to $\left(\frac{dE}{dx}\right)^{exp}$, the expected energy loss value for a particle α with $\alpha = \mu, e, p, \pi, K$. Note that σ_α is the resolution of the deposited energy for the hypothesis α. The energy loss distributions for negatively (left) and positively (right) charged particles as a function of their momentum is shown in Figure 5.2.

5.2.3 Analysis Tools

In order to reduce the size of the reconstruction files, a final skimming process is done by the `oaAnalysis` package. The output is oaAnalysis files that are lighter and suitable for

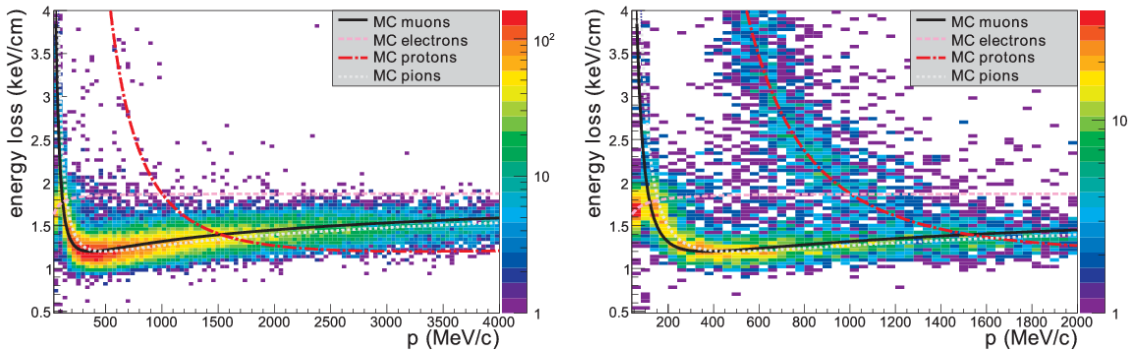

Figure 5.2: Distribution of the energy loss as a function of the momentum for negatively (left) and positively (right) charged particles produced in neutrino interactions, compared to the expected curves for muons, electrons, protons, and pions [115].

analysis. A general analysis framework called HighLAND[ii] has been developed to ensure consistency between analyses and speed up the analysis development. This framework contains C++-based classes and core packages that the user inherits from when doing the event selection and the detector systematic propagation (`psyche` package). It also provides tools to skim the oaAnalysis files to lighter NTuples containing only specific variables required by a user (`HighlandIO` package) and tools for quickly drawing distributions at any stages of the selection (`HighlandTools` package).

[ii] for High Level Analysis at the Near Detector

6

Data Quality

It is of paramount importance to make sure that the data collected is of good quality. For this purpose, the T2K data quality (DQ) group assesses the quality of data collected at the ND280 complex coming from both beam and cosmic triggers. This is done by checking the hardware status of each sub-detector along with the distribution of some low level variables on a weekly basis. A flag summarising the quality of data for each sub-detector is uploaded to the offline database. The global ND280 flag combines the flags for all the sub-detectors and is good only when all the sub-detectors have a good data quality flag. This flag will then be used in the selection to remove data acquired in bad conditions.

This chapter first briefly describes the data acquisition (DAQ) and triggering system of the ND280 detector in Section 6.1. The data quality assessment for the electromagnetic calorimeter is then presented in Section 6.2.

6.1 Data Acquisition System

The ND280 and INGRID DAQ are monitored using the MIDAS software framework. As described in Chapter 4, the ECal, P0D, SMRD and INGRID detectors are made of similar scintillator detectors. They also share the same electronic read out, based on Trip-T ASIC [133]. The bars are read out by one or two MPPCs and signals from up to 64 MPPCs are connected to custom-designed Trip-T front-end boards (TFBs). The back-end of the electronics system consists of readout merger modules (RMMs) that can control up to 48 TFBs: they distribute the clock and trigger signals coming from the slave clock modules (SCM) and read out the data from TFBs once the trigger is received. There is one SCM per sub-detector that allows to run this sub-detector separately from the rest of the ND280 for calibration and debugging.

The master clock module (MCM) receives signals from the accelerator that determine when the neutrino spill happens (beam trigger) and from a GPS-based clock. The MCM is also connected to two cosmic trigger modules that receive signals from TFBs or crate master boards (in the case of the FGD) and can therefore determine if there is a cosmic events. The first cosmic trigger is issued when there is no beam trigger and coincident hits are seen in both FGDs. The second cosmic trigger is issued when there are coincident hits in opposite sides of the detector (top and bottom, SMRD; P0D and DsECal,...) and no beam trigger. A schematic of the ND280 DAQ is given in Figure 6.1. and more information about the ND280 DAQ system (for TPC and FGD) can be found in [92].

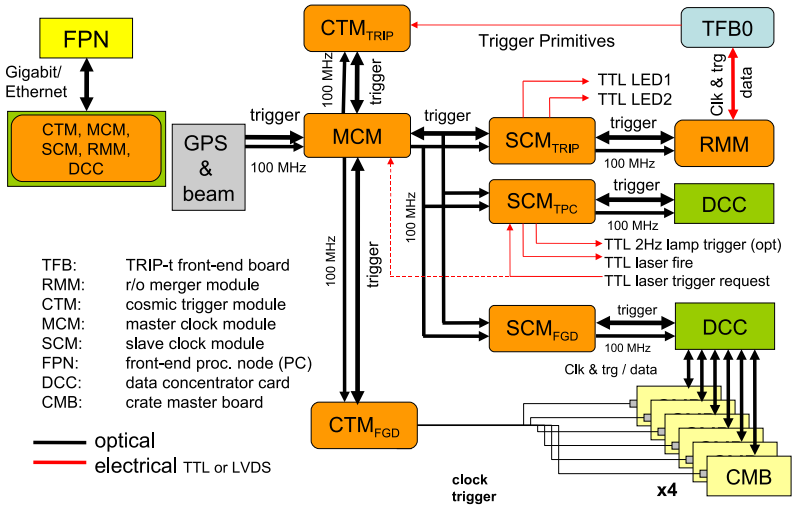

Figure 6.1: Schematic view of the general layout of the ND280 electronics [92].

6.2 ECal Data Quality

The weekly assessments of the data quality for the electromagnetic calorimeter can be split into two. First, the hardware status is checked via the global slow control (GSC) database. This includes the monitoring of the temperature, voltage and current sensor located around the ECal TFBs, or from flowmeters connected to the cooling loops. Second, the data is reconstructed and calibrated for assessing the quality of the reconstructed physical variables. This previous step is done by the `soffTasks` package that converts raw data files from the MIDAS file format to calibrated ROOT files. Another package, `oaDataQuality` provides all the scripts necessary to perform the checks and to interact with the off-line database when the flags need to be uploaded.

6.2.1 GSC Data

The GSC monitoring relies on visual inspection, however, it was automated from run 3 onward. Note that since the March 2011 great Tohoku earthquake, the TFB 13 and TFB 25 on RMM9 are completely silent.

Temperatures

Each ECal TFB has two temperature sensors located on the inner board and the exterior. For the run 5 of data taking, 19 out of 728 of these sensors were not working. This issue was due to an I2C bus failure on the TFB. An exhausted list of these TFB is available in the corresponding technical note [134]. Depending on the magnet status and weather conditions, the temperature reported by the sensors in the ECal can exhibit different behaviour. A diurnal variation may be observed when the outside temperature is low. With warmer conditions in the pit, the diurnal cycle may completely disappear and the TFB temperatures follow the general variations seen for the outside temperature.

Voltages

Voltage monitoring using GSC data is tricky. For some TFBs, voltage reading is widely oscillating. In some cases, according to our monitoring, individual TFBs should have been off; this is very likely due to problems with the on-board I2C bus, as already noticed for temperature monitoring. For each TFB, four voltages lines (2.2 V, 3.2 V, 3.8 V and 5.5 V) were monitored by reading out voltages and currents. Hence, the voltage drawn by the bias voltage supply (72 V) are monitored too.

Cooling Water Flow

The water flow in the 112 ECal cooling loops is 4 to 5 L min^{-1}, with small and very slow variations expected during the year.

6.2.2 Raw Data Analysis

Information on the quality of the data taken for the run 5 period can be extracted from the analysis of the data itself. From run 5 onward, it has been decided that the Tript-T

occupancy, the Hit-maps and the RMM offsets will no longer contribute to the weekly checks since they are time consuming and do not add much to the checks.

6.2.2.1 Gain and Pedestal Monitoring

A useful low-level check for data quality is to ensure that the electronic pedestals and MPPC gains (in ADC) are stable over time. Variations are normally due to temperature excursions, but may also indicate other problems such as voltage supply issues. Large variations in gain are highly undesirable as they affect the efficiency and resolution of the detector. The gain and pedestal for a channel can be calculated from a histogram of ADC counts observed from the channel in the absence of a light signal; i.e. showing only thermal noise. This spectrum is dominated by a large pedestal peak corresponding to no pixels having fired, and also contains a series of uniformly spaced higher peaks with rapidly decreasing amplitudes, corresponding to different numbers of fired pixels. The pedestal is given by the fitted position of the largest peak, and the gain from the spacing between the first and second peaks, as illustrated in Figure **??**.

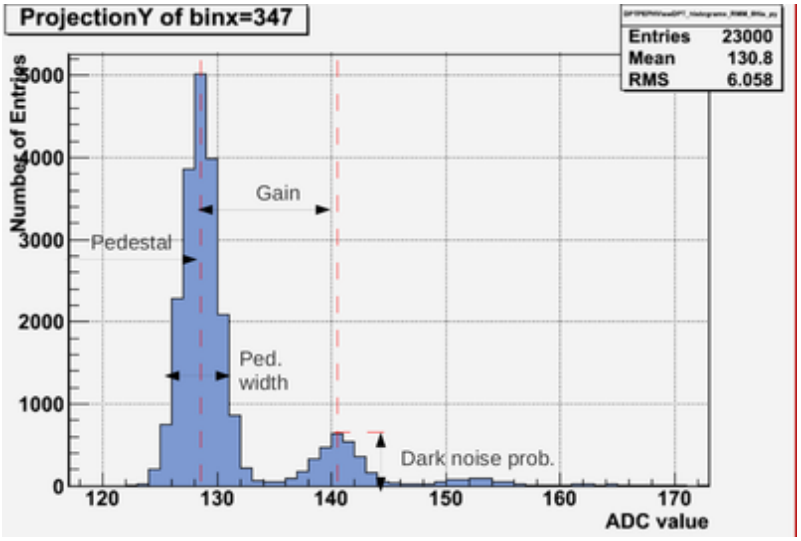

Figure 6.2: Histogram of the ADC values (number of pixel fired) for a given ECal channel.

The data processing task (DPT) of the ND280 DAQ generates these histograms for every 500 beam/pedestal events in the data stream (around once every 20 minutes). An automated job on the semi-offline machines processes the DPT histograms from the raw data files as they arrive. Since the time taken to process the histograms is significant, several

histograms are aggregated and pedestal and gain values for each channel are calculated with a granularity of 3 hours. The readout should resolve signals of a few photo-electrons and signals from a full range of MPPCs. Hence, each MPPC signal is divided into low and high gain channels. One can then fit the pedestal peaks for these high and low gain channels separately.

A reference gain and pedestal are chosen during the week and the variation from those references are plotted. Examples of gain and pedestal drifts are given in Figures 6.3 and 6.4.

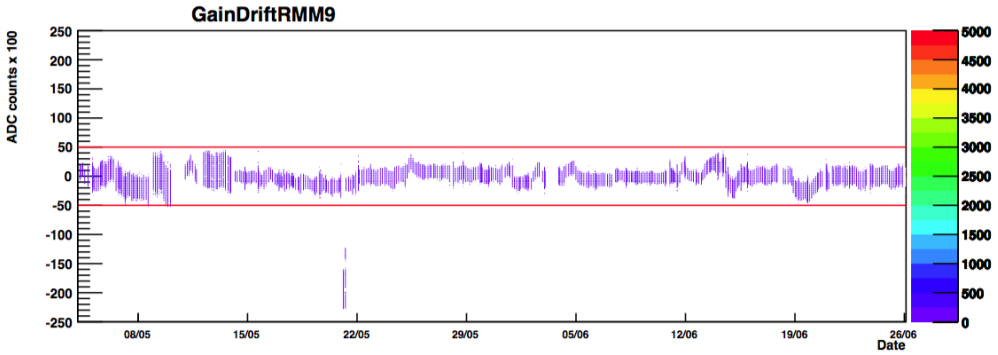

Figure 6.3: Gain variation versus time during run 5 for RMM9. The two red lines correspond to the ±0.5 ADC counts where the gain drift is allowed

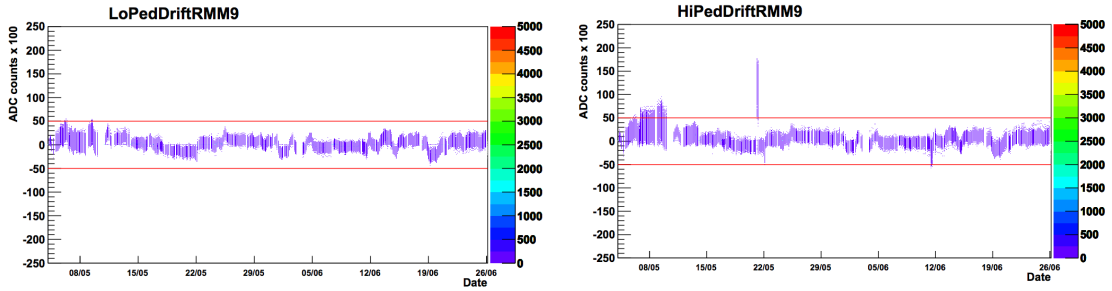

Figure 6.4: Low (left) and high (right) pedestal variation versus time during run 5 for RMM9. The two red lines correspond to the ±0.5 ADC counts where the gain drift is allowed.

The two strips that are outside the acceptable region in both the gain drift and the high pedestal drift are due to a bad set of high voltage trims and it has been quickly corrected.

6.2.2.2 Dead Channels

In order to find dead or bad channels, the DPT histograms are analysed. The gain for each

sub-run is then calculated using the histograms. Channels for which the photo-electron peak cannot be found by the fitting algorithm nor recovered in time, by scanning a different time window, are either non instrumented or dead. A list of dead channels at the end of run 5 can be found in [134]. A total of 56 channels were reported dead at the end of run 5. This brings the total number of dead channels to 184 (counting the channels from the two silent TFBs since the earthquake). Channels for which the photo-electron peak cannot be found by the fitting algorithm but can be recovered in time are bad channels.

6.2.2.3 Beam Timing

On beam triggers, we can calculate the hit time relative to beam trigger time. After taking into account all the offsets introduced by the readout electronics, it is possible to predict where the bunch structure should appear within the TFB readout cycles. Trigger offsets have been set in such a way that the first of the eight beam bunches is centred in the fifth (out of 23) readout cycle. Since run 2, checks were made to see the impact of beam time jitter in the data.

The beam group reported that there could be fluctuations of up to 100 ns in the beam timing. As a consequence, specific checks were made to be sure that beam-related hits peak more than 100 ns away from either end of the integration window, and is stable as a function of time. Indeed, time distributions for all modules and all bunches are more than 150 ns away from the beginning of the integration window, and the observed jitter is up to 40 ns.

Figure 6.5 shows the timing distribution for the RMM 9, for the entirety of run 5.

6.2.3 ECal Cluster Rate

In order to check the ECal neutrino event rate, hits are selected in beam spills, calibrated and clustered using standard clustering algorithms. The resulting rate is shown in bins of 24 hours in Figure 6.6.

For the main ring run 55, the ECal cluster rate is measured to be: **4.26** $\pm$ **0.036** Clusters/10^{14} POT. For the main ring run 56, the first one in reversed horn current, the ECal cluster rate has been measured as: **1.69** $\pm$ **0.007** Clusters/10^{14} POT. We notice

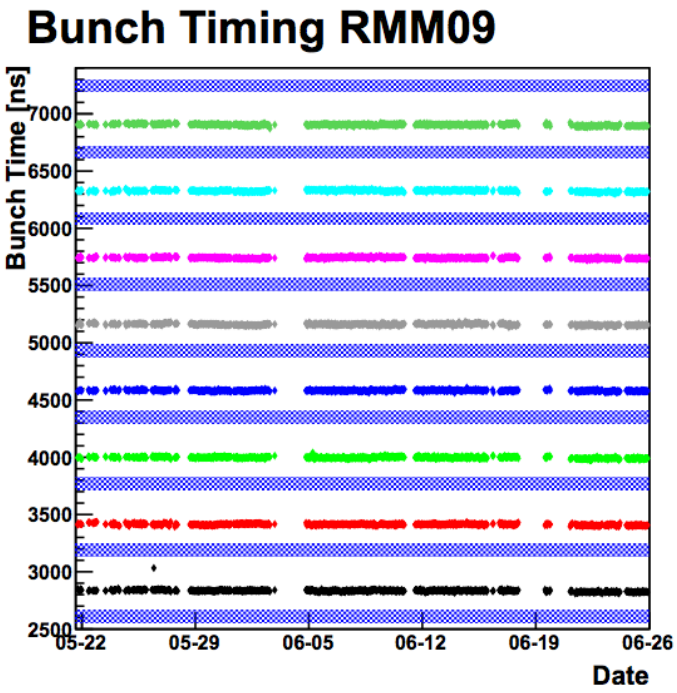

Figure 6.5: Hit time relative to beam trigger time for ECal hits in RMM9, for run 5.The dashed blue regions correspond to the 100 ns reset windows between 480 ns readout cycles.

a significant decrease of the ECal cluster rate for MR run 56 with respect to the MR run 55 due to the passage from ν to $\bar{\nu}$ mode. At the very end of MR run 56, the horn current was reversed again back to neutrino mode. That explains the increase of the cluster rate for the last two points in Figure 6.6.

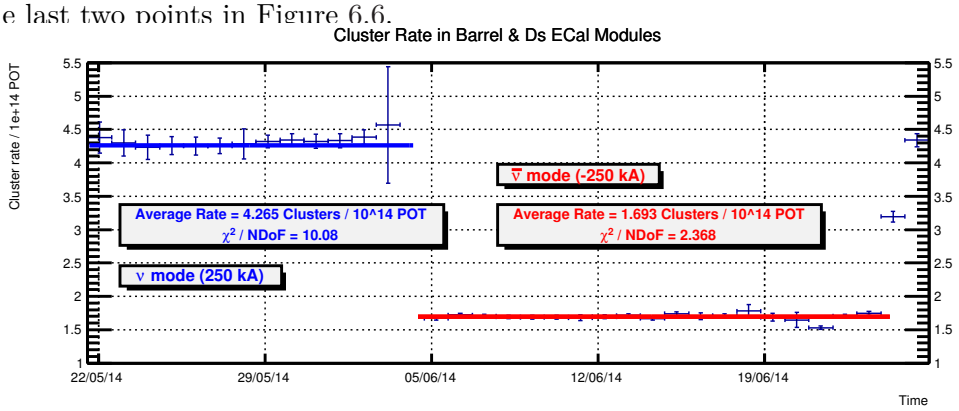

Figure 6.6: ECal cluster rate during MR runs 55 and 56. Note that the cluster rate is lower in the $\bar{\nu}$ mode.

6.2.4 Data Quality Flags

For ECAL, we use 12 bits to encode the status of each module in the Data Quality flag. The full ECAL status is good when the flag is set to 0; if it is greater than 0, the global flag is bad. A flag of -1 means that there is no data taking. The encoding of the status of single modules is done according to Table 6.1. For instance, if the RMM2 and RMM8 look bad, the flag will be $2^2 + 2^8 = 260$. When the ECal is out of the global DAQ, the flag is set to 4095. Once validated by the DQ group, the flags are uploaded to the database for cosmic and beam triggers.

Table 6.1: Encoding of the status of ECal modules in DQ flag.

bit number	decimal	binary value	ECal module
1	1	2^0	RMM0 - DsECal
2	2	2^1	RMM1 - DsECal
3	4	2^2	RMM2 - P0D South
4	8	2^3	RMM3 - Barrel Top South
5	16	2^4	RMM4 - Barrel Bottom South
6	32	2^5	RMM5 - Barrel Side South
7	64	2^6	RMM6 - Barrel Side South
8	128	2^7	RMM7 - P0D North
9	256	2^8	RMM8 - Barrel Side North
10	512	2^9	RMM9 - Barrel Side North
11	1024	2^{10}	RMM10 - Barrel Bottom North
12	2048	2^{11}	RMM11 - Barrel Top North

During the run 5 period the ECal has flagged bad few short periods: when the ECal was out of global for calibration or when there was an RMM skew.

Part III

Cross Section Analysis

Motivations

Being a long-baseline neutrino oscillation experiment, the main goal of T2K is to measure the oscillation parameters θ_{23}, θ_{13}, $|\Delta m^2_{32}|$ and δ_{CP}. The different oscillation analyses carefully account for various sources of systematic errors such as flux, detector and cross sections. The near detector data are used to constrain the expected un-oscillated spectra at the far detector. The dominant error prior to the near detector fit comes from the neutrino interaction cross sections, accounting for 4 - 5 % of the total 7 % uncertainty. Moreover, due to the lack of knowledge on the coherent pion production below 3 GeV and the strong disagreement with MINERvA data [135], the prior uncertainty on the normalisation rate of coherent events was set to 100 %. Hence the implementation of a better coherent model into the NEUT neutrino event generator, along with appropriate reweighting methods, is needed to decrease this prior. This work is described in Chapter 7 and as a result, the prior error on the coherent normalisation was set down to 30 %.

Coherent pion production is also an intriguing channel by itself as it was subject to a low energy puzzle. Indeed, this cross section has already been measured for neutrino energy larger than 2 GeV and target atomic number $A > 20$ [136, 137, 138, 139, 140, 141]. But the two searches by K2K [125] and SciBooNE [126] below 3 GeV were not sensitive enough to measure the cross section and therefore upper limits were set. Recently MINERvA [135] and T2K [142] provided the first coherent pion production data on carbon target below 2 GeV, which confirmed the presence of the low energy coherent channel. In order to have an extra measurement in this energy range and to facilitate the extrapolation of the cross section from carbon to oxygen nuclei in the near detector constraint on the far detector, Chapters 8, 9, 10 and 11 report the detailed cross section measurement of ν_μ-induced coherent pion production scattering off carbon and oxygen nuclei in the T2K near detector.

Please note that the present analysis is currently in the process of being approved by the T2K collaboration. Therefore the results shown are not yet official nor published and still constitute preliminary work.

7

Berger-Sehgal Model Implementation

In the recent results from MINERvA [135], the NEUT MC events generator [117] overestimates the charged-current coherent cross section and differential cross sections for both neutrino and anti-neutrino modes, as shown in Figure 7.1

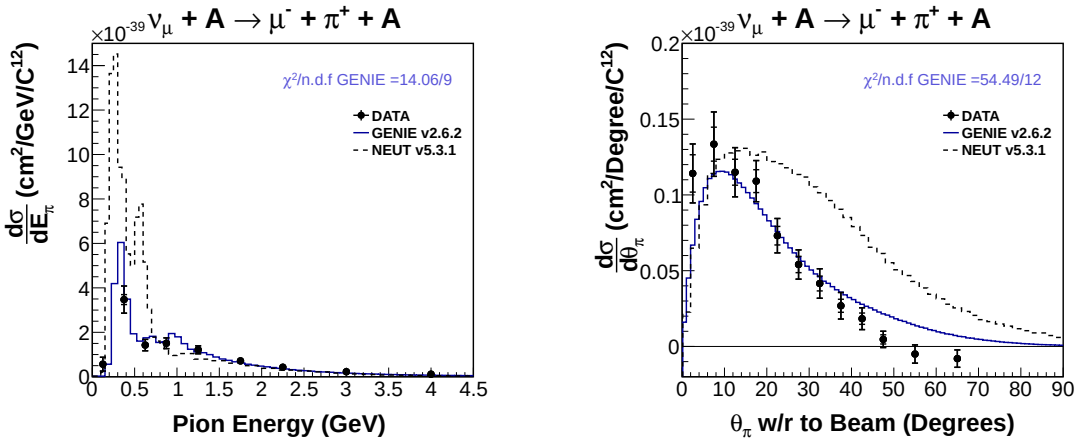

Figure 7.1: MINERvA $d\sigma/dE_\pi$ (left) and $d\sigma/d\theta_\pi$ (right) measurements for charged-current coherent pion production induced by a neutrino scattering off carbon compared against GENIE and NEUT prediction. Plots are extracted from [135].

Both NEUT and GENIE [143, 144] generators used the Rein and Sehgal (RS) coherent model [77], taking into account the lepton mass corrections, as it is shown in reference [78] that not neglecting the lepton mass predicts a decrease of the differential cross section at very low Q^2 in charged-current mode. Their disagreement is likely to come from different approaches in the model implementation. For example, GENIE uses a constant value of the forward scattering amplitude, defined in equation (3.20), $r = 0.3$ while in NEUT r is parametrised as a function of E_π. Other differences come from the phase space considered

while performing the integration over the energy transfer $|t|$ (defined by equation (3.14)) and which data set is used for the pion-nucleus cross sections.

In light of this poor agreement between NEUT, GENIE and the MINERvA data, the more recent Berger-Sehgal (BS) model [79] is added in NEUT.

The theoretical differences between both models have been summarised in Chapter 3. In Section 7.1 we discuss the details of the implementation. Results of the NEUT implementation along with a comparison with NuWro [145] and GENIE predictions are shown in Section 7.2. Section 7.3 deals with the reweighting methods allowing to switch from RS to BS model as well as varying the internal BS parameters.

7.1 Implementation Details

The BS model is added into NEUT following the same structure as the RS model as they are both based on the PCAC hypothesis. We recall here the expression of the differential cross section where $\nu = E_\nu - E_\ell$:

$$\frac{\mathrm{d}\sigma^{NC}}{\mathrm{d}x_B\,\mathrm{d}y_B\,\mathrm{d}|t|} = \frac{G^2\,M_{\mathcal{N}}\,E_\nu}{\pi^2}\,\frac{1}{2}\,f_{\pi^0}^2\,\left[1 - y_B + \frac{{y_B}^2}{4}\left(1 - \left|\frac{Q^2}{\nu^2} + 1\right|\right)\right]\,\left(\frac{M_A^2}{M_A^2 + Q^2}\right)^2\,\frac{\mathrm{d}\sigma_{el}}{\mathrm{d}|t|} \tag{7.1}$$

The relation (3.23) still holds in order to obtain the charged current differential cross section from the neutral current one. To stay consistent with the RS implementation in NEUT which uses the four variables $(x_B, y_B, z, \phi_{\pi\mu}$ and not $(x_B, y_B, |t|)$, we define $z = \cos(\theta_\pi)$ and $\phi_{\pi\mu} = \pi - \theta_{\pi\mu}$. They represent the cosine of the angle θ_π between the pion momentum and the neutrino beam direction and the angle $\phi_{\pi\mu}$ between the pion momentum and the scattering plane (the plane defined by the neutrino beam direction and the lepton momentum) as shown in Figure 7.2. The relation between t, z and $\phi_{\pi\mu}$ is given in [77]. This equation is recalled here where we simplify $M = M_{\mathcal{N}}$ and $E = E_\nu$:

$$\begin{aligned}|t| = 2E^2 y_B^2\Bigg(1 + \frac{Mx_B}{Ey_B} - \frac{m_\pi^2}{2E^2y_B^2} - \sqrt{(}1 - z^2)\sqrt{1 - \frac{m_\pi^2}{E^2y_B^2}}\times \\ \left[z\Big(1 + \frac{Mx_B}{E}\Big) - \sqrt{1 - z^2}\,\cos\phi_{\pi\mu}\sqrt{\frac{2Mx_B}{Ey_B}(1 - y_B) - \left(\frac{Mx_B}{E}\right)^2}\,\right]\Bigg)\end{aligned} \tag{7.2}$$

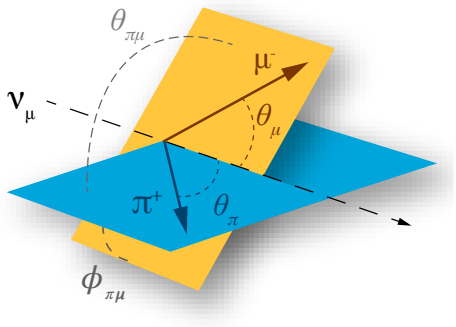

Figure 7.2: Sketch of a CC coherent pion production where the two pion angles θ_π and $\phi_{\pi\mu}$ are represented.

Replacing $|t|$ in (7.1) by its expression in equation (7.2) gives the differential cross section such as implemented in NEUT:

$$\frac{\mathrm{d}\sigma^{NC}}{\mathrm{d}x_B\,\mathrm{d}y_B\,\mathrm{d}z} = \int \frac{\mathrm{d}\phi_{\pi\mu}}{2\pi} \frac{\mathrm{d}\sigma^{NC}}{\mathrm{d}x_B\,\mathrm{d}y_B\,\mathrm{d}|t|} \times \frac{\mathrm{d}|t|}{\mathrm{d}z} \tag{7.3}$$

7.1.1 Pion-Nucleus Elastic Cross Section

One of the main improvements in the Berger-Sehgal model is the expression of the elastic pion-nucleus (carbon) differential cross section. It is based on the data recorded by various experiments instead of assuming nuclear response. Its expression reads

$$\frac{d\sigma_{el}}{dt} = A_1 e^{-b_1 t} \tag{7.4}$$

where the coefficients A_1 and b_1 are given for 11 values of pion kinetic energy T_π between 0.076 GeV and 0.870 GeV. A linear interpolation is then performed such that the elastic cross section can be computed for any pion kinetic energy. This explains the non-continuous shape of the leftmost plot in Figure 3.6.

The choice of the values for the parameters A_1 and b_1 outside of the range given in the paper was studied and the results are shown in Figure 7.3. For $T_\pi > 0.870$ GeV the last values of (A_1, b_1) can be kept as it did not affect much the shape of the elastic cross section. As $T_\pi \to \infty$, σ_{el} gently converges towards 0.123 mb. However for $T_\pi = 0$ GeV, A_1 is set to

$0\,\text{mb GeV}^{-2}$ and several values of b_1 have been tested (Figure 7.3).

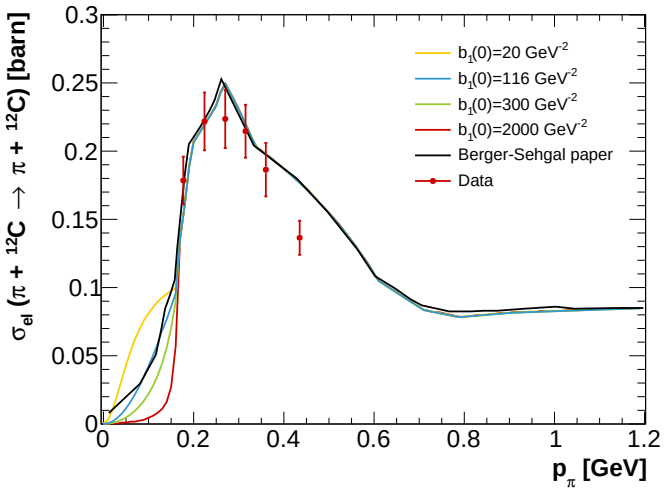

Figure 7.3: Pion-nucleus elastic cross section as a function of pion momentum, for several values of b_1 at $T_\pi = 0\,\text{GeV}$ (coloured lines) and as in the original Berger-Sehgal paper (black line). Data points are taken from reference [146].

The best option is to set $b_1 = 116\,\text{GeV}^{-2}$ as it is the value for which the interpolation is the closest to the one in the original paper. Unfortunately, there is no data available at pion momentum below $200\,\text{MeV/c}$ that would allow us to better constrain the elastic cross section in this range. We also note that this parametrisation for the elastic pion-carbon cross section agrees well with the data points from [146] except for $p_\pi > 400\,\text{MeV/c}$ where the results of the Berger and Sehgal interpolation overestimates the data.

As there was no uncertainty given for the parameters A_1 and b_1, two additional parameters f_{A_1} and f_{b_1} are added so that the effect of a slight variation of A_1 and b_1 on the cross section can be checked. The new parameters are defined as:

$$\frac{d\sigma_{el}}{dt} = A_1\ (1 + f_{A_1})\ e^{-b_1\ (1+f_{b_1})\ t} \tag{7.5}$$

Their default values is therefore 0. The effect on the shape of the differential cross section when varying f_{A_1} and f_{b_1} is presented in Figures 7.4 and 7.5 for all the kinematic variables in the case of a charged-current interaction with a neutrino energy fixed at 1 GeV. We

noticed that changing the value of A_1 by $\pm 20\%$ or $\pm 50\%$ has no effect on the shape of the differential distributions, which is expected as it can be seen as an overall normalisation factor[i]. On the other hand, varying f_{b_1} has a large effect on the shape of the $|t|$, Q^2 and angles distributions. No effect is observed on the muon and pion $d\sigma/dE_{\text{lep},\pi}$. These shape variations are expected since b_1 is involved in the exponential term in equation (7.5) and therefore plays a role in the energy dependance of the differential cross section.

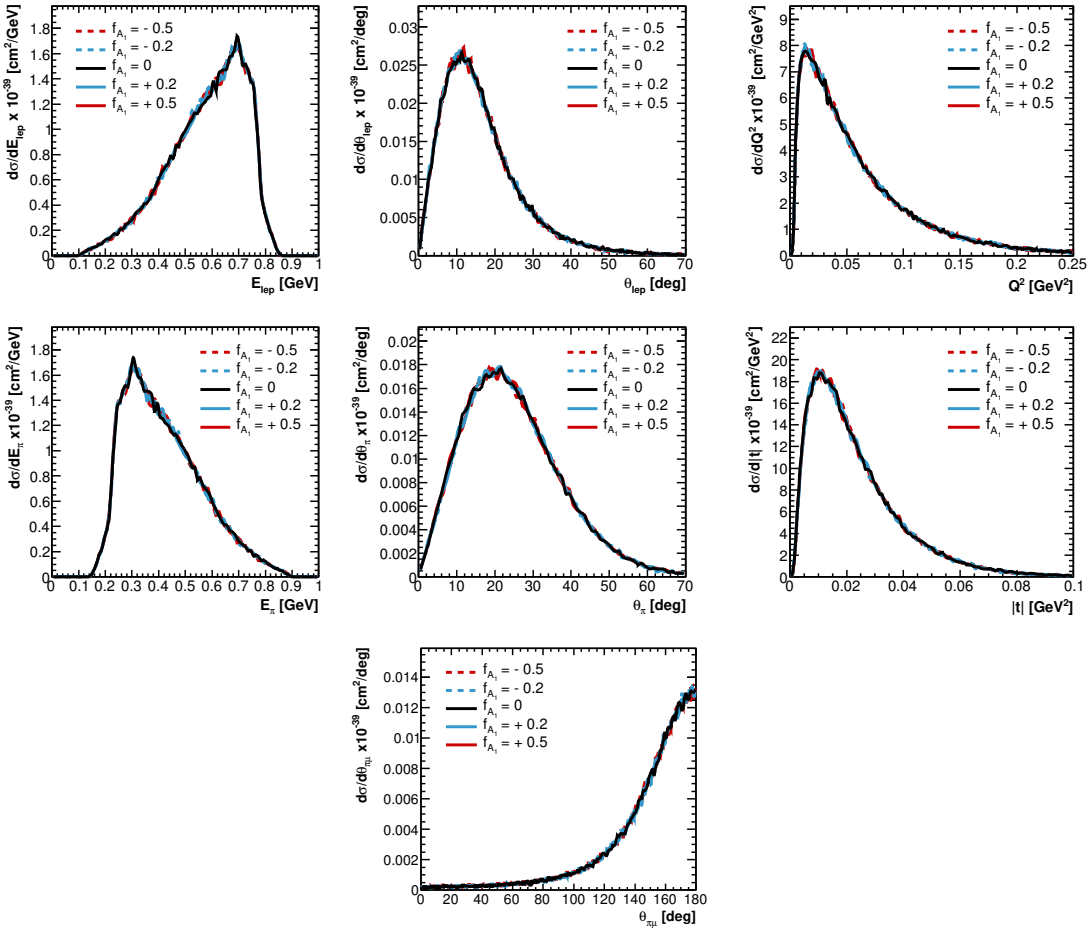

Figure 7.4: Shape comparison of differential cross section for different values of f_{A_1} as a function of kinematic variables for $E_\nu = 1\,\text{GeV}$. From top left to bottom right: muon energy, muon angle w.r.t. neutrino direction, Q^2, pion energy, pion angle w.r.t. neutrino direction and transferred energy t. Bottom plot is the muon-pion coplanarity angle. All the graphs are normalised using the nominal total cross section.

7.1.2 Scaling to Atomic Number A

The previous definition of the pion-nucleus elastic cross section reduces the use of the

[i]The plots are normalised with the nominal value of the cross section at 1 GeV

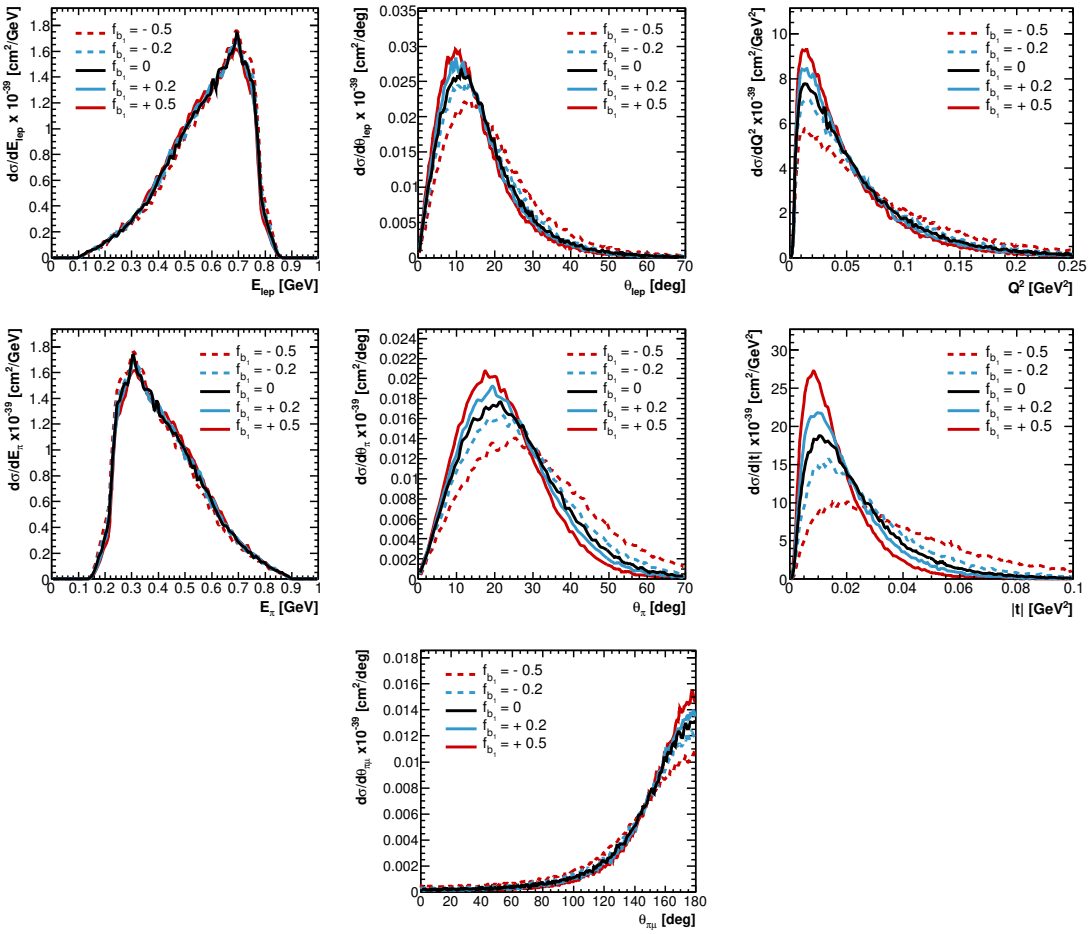

Figure 7.5: Shape comparison of differential cross section for different values of f_{b_1} as a function of kinematic variables for $E_\nu = 1\,\text{GeV}$. From top left to bottom right: muon energy, muon angle w.r.t. neutrino direction, Q^2, pion energy, pion angle w.r.t. neutrino direction and transferred energy t. Bottom plot is the muon-pion coplanarity angle. All the graphs are normalised using the nominal total cross section.

model to carbon target only. Therefore a scaling needs to be added to make it available for other targets. The first idea is to extract the A dependance $f(A, T_\pi, |t|)$ from the RS cross section in equation (3.21):

$$f(A, T_\pi, |t|) = \left(\frac{A}{12}\right)^2 exp\left(- \frac{9(A^{1/3} - 12^{1/3})}{16\pi R_0^2}\sigma_{inel.}(T_\pi) - \frac{r_0^2}{3}(A^{2/3} - 12^{2/3})|t|\right) \tag{7.6}$$

However, the σ_{inel} term in equation (7.6) as well as the $|t|$ dependence make this scaling incompatible for both NC and CC channels for neutrino energies below 500 MeV as seen on Figure 7.6, where the scaling introduce a divergence of the Argon/Carbon cross section ratio.

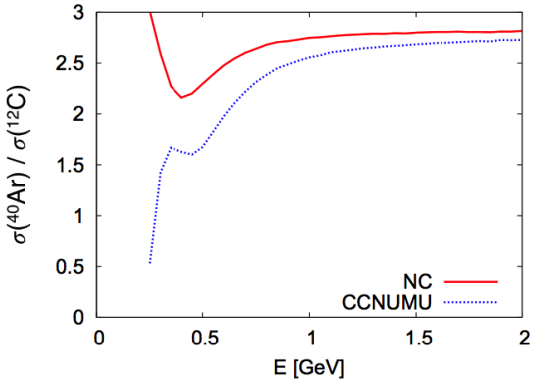

Figure 7.6: Ratio between the Argon and Carbon Berger-Sehgal coherent cross-section as a function of neutrino energy for neutral current (red) and charged current (dashed blue) tested with NuWro using the A-scaling described in eq. (7.6) (kindly provided by Jakub Zmuda).

The easiest approach is to scale the cross section using powers of A. Thus a linear scaling by $A/12$ is first tested in NEUT and the values of the cross sections obtained with this scaling are compared to other experimental results in Table 7.1 and Figure 7.7. We observe a reasonable agreement with the experimental data: the BS prediction often lies within the errors of most of the experimental data points. NEUT uses cross section lookup tables to access the total cross section and, for example, to normalise differential distributions. In order to avoid having one table for each target, a general scaling by $A/12$ is also applied in these tables. The behaviour of the cross section while varying the atomic number A is studied for different neutrino energies and the results are shown in Figure 7.8.

Another more sophisticated scaling was also studied and is documented in Appendix B. It was found that, despite agreeing with the data, its energy dependance make it incompatible for energies below 0.5 GeV and nucleus with $A > 50$.

Table 7.1: Total coherent cross sections measured by several experiments compared against Rein-Sehgal predictions (using the $A^{1/3}$ scaling rule) and the linear scaling for Berger-Sehgal predictions. The unit of the given cross sections is 10^{-40} cm^2.

Experiments	Channel	A	$< E_\nu >$ (GeV)	σ_{exp} (10^{-40} cm^2)	σ RS ($A^{1/3}$ rule)	σ BS (linear)
Aachen-Padova [136]	NC	27	2	29 ± 10	32.6	18.3
Gargamelle [137]	NC	30	2	31 ± 20	33.8	20.4
CHARM [138]	NC	20	30	96 ± 42	74.5	100.6
SKAT [139]	NC	30	7	79 ± 28	59.5	58.9
NOMAD [140]	NC	12.8	24.8	72.6 ± 10.6	61.9	57.9
ArgoNeuT [141]	ν_μ CC	40	9.6	260 ± 150	139.5	181.1
MINERvA [135]	ν_μ CC	12	4.11	34.9 ± 6.8	65.4	27.6
MINOS [147]	NC	48	4.9	77.6 ± 17	60.2	71.4

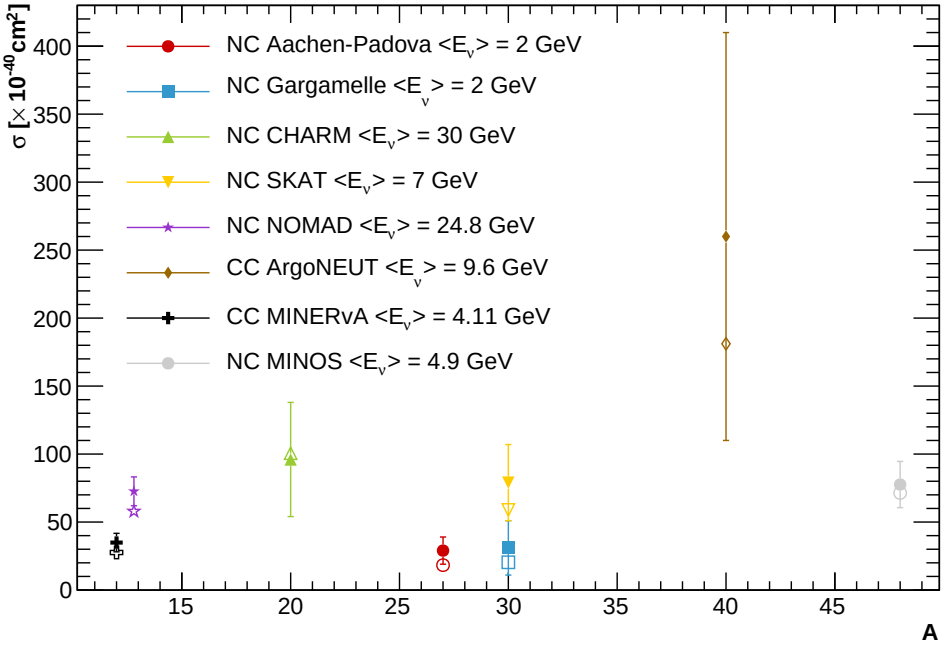

Figure 7.7: Comparison of NC and CC coherent cross section measurements from various experiments (plain markers) with the BS predictions using the linear A/12 scaling (empty marker) as a function of the target atomic number A. The experiments have different mean neutrino energies $< E_\nu >$ detailed in the legend.

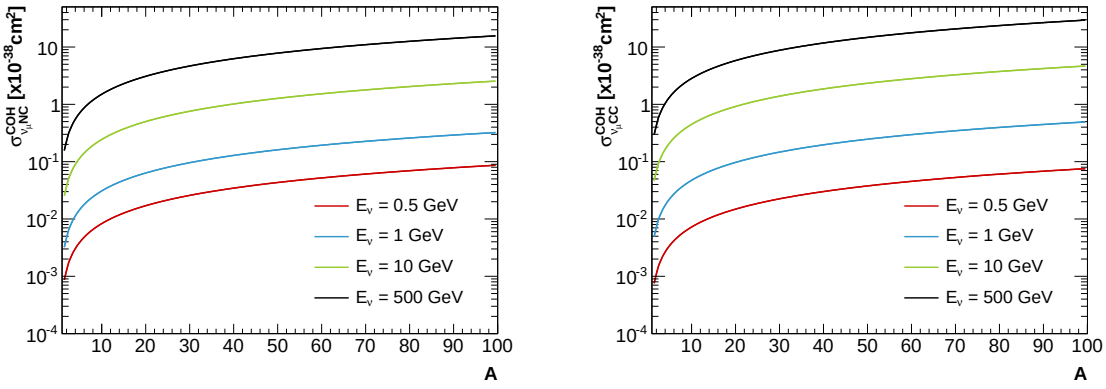

Figure 7.8: NC (left) and CC (right) cross sections as a function of the target atomic number A where a linear scaling is assumed.

7.2 NEUT Predictions

To ensure the model is implemented properly, a cross-check between NEUT, NuWro and GENIE generators is done for different variables and the phase space of the new NEUT model is given for different input energies.

7.2.1 NEUT, NuWro and GENIE Comparison

For a fixed neutrino energy of 1 GeV, we compare the muon and pion momentum and angles as well as the Q^2 distributions for both neutral current and charged current channels. The t distribution is also given along with the coplanarity angle $\theta_{\pi\mu}$ between the muon and pion tracks. While NuWro and NEUT contain only one version of the model, two different Berger-Sehgal models are available in the recent version of GENIE. One corresponds to the model "as in the paper" [79], where the target nucleus is considered as infinitely heavy, and therefore is not allowed to recoil[ii]. The second GENIE model is an improved Berger-Sehgal (BSFM) where the nucleus has a finite mass, thus it can potentially recoil. Their predictions are shown in Figure 7.9 and 7.10.

The agreement between NEUT, NuWro and GENIE shapes is rather good for both neutral and charged currents in the lepton kinematics, pion momentum and Q^2. We notice a small discrepancy in the normalisation where GENIE and NuWro agree well in neutral current for the above mentioned variables and NEUT predictions are slightly below in them. In the charged current, GENIE and NEUT show a good agreement while NuWro predicts a slightly more peaked lepton angle and Q^2.

Important differences are observed for the last three variable : θ_π, $|t|$ and $\theta_{\pi\mu}$ in both CC and NC channels. NEUT and NuWro shapes are similar but NuWro curves still lie above the NEUT ones. It is worth reminding that the implementations are different in both generators. For instance, instead of using the 4 variables $(x_B, y_B, z, \phi_{\pi\mu})$ in the cross section, such as it is done in NEUT, NuWro uses the 3 variables $(x_B, y_B, |t|)$ from equation (7.1).

[ii] This approach is also the one considered in NEUT and NuWro.

The original BS predictions from GENIE is less peaked than NEUT around 20° for θ_π, $0.01\,\mathrm{GeV}^2$ for $|t|$ and 180° for the coplanarity angle $\theta_{\pi\mu}$. In the charge-current channel, the original GENIE predictions differ from NEUT and NuWro in a similar way.

The last point to mention concerns the finite mass nucleus GENIE model. For the lepton kinematic variables as well as Q^2 and E_π it is close to all the other generators. However it changes drastically for the pion angle, $|t|$ and coplanarity. The fact that in this case the nucleus can get recoil energy (still without excitation) would potentially explain that the pion scattering angle is much larger while the energy transferred $|t|$ can reach values up to 10 times larger than before. However it is worth saying that the development version of GENIE was used for this plot and work might still be on progress.

7.2.2 Phase Space

The phase space of both RS and BS NEUT models is given in terms of x_B vs y_B, E_μ vs θ_μ and E_π vs θ_π in Figure 7.11 for neutral current and Figure 7.12 for charged current, calculated on a carbon nucleus for $E_\nu = 1\,\mathrm{GeV}$. Extra phase space maps calculated with the T2K (ND280) flux are given in Figure 7.13 and 7.14 for neutral and charged current. We can see in the (E_π, θ_π) map the effect of the difference between the pion-nucleus elastic cross section in both models as the double peak disappear in the Berger-Sehgal pion phase space.

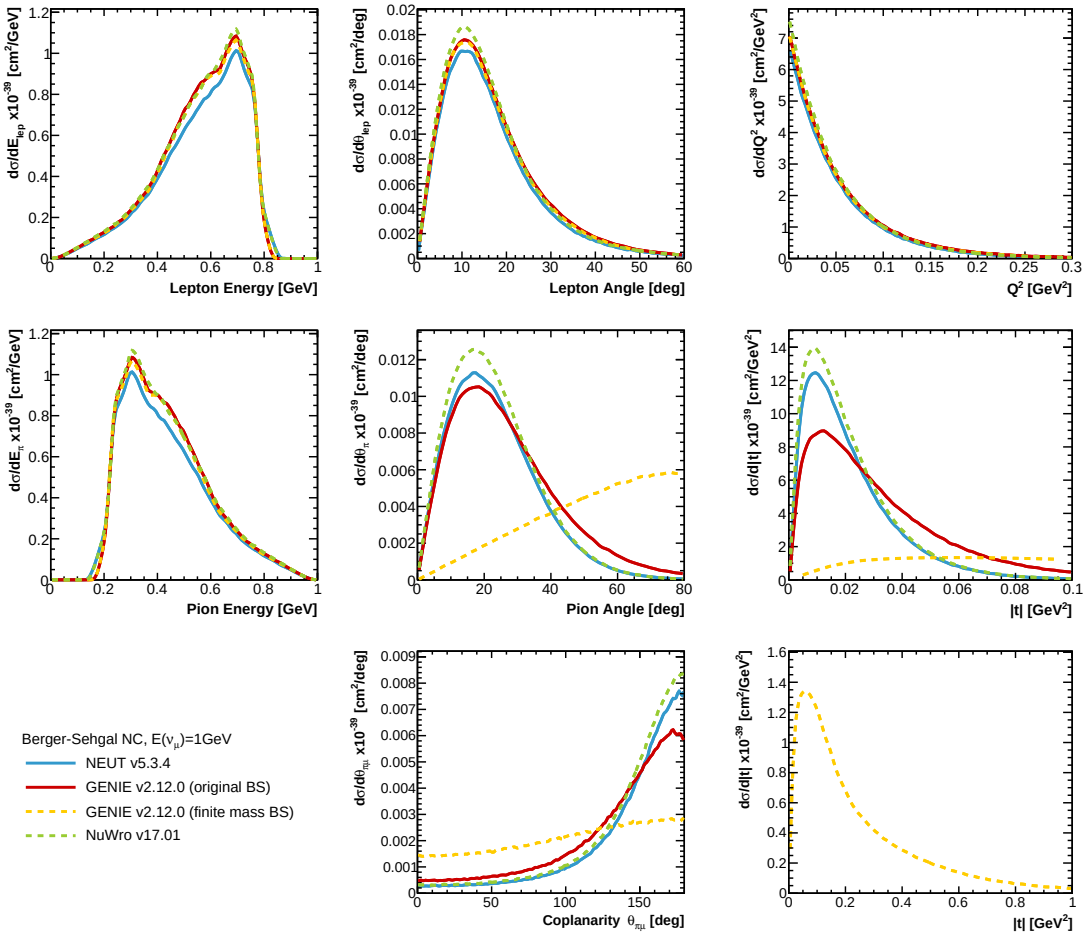

Figure 7.9: Comparison of lepton energy (top left), angle (top center), Q^2 (top right) and pion energy (middle left), angle (middle center), t (middle and bottom right) distributions for **neutral current** interaction with E_ν=1 GeV. The coplanarity angle between the muon and the pion $\theta_{\pi\mu}$ is also given. The results are given for different implementations of the Berger-Sehgal model: NEUT (plain blue), NuWro (dashed green), GENIE (plain red), and GENIE where the nucleus has a finite mass (dashed yellow).

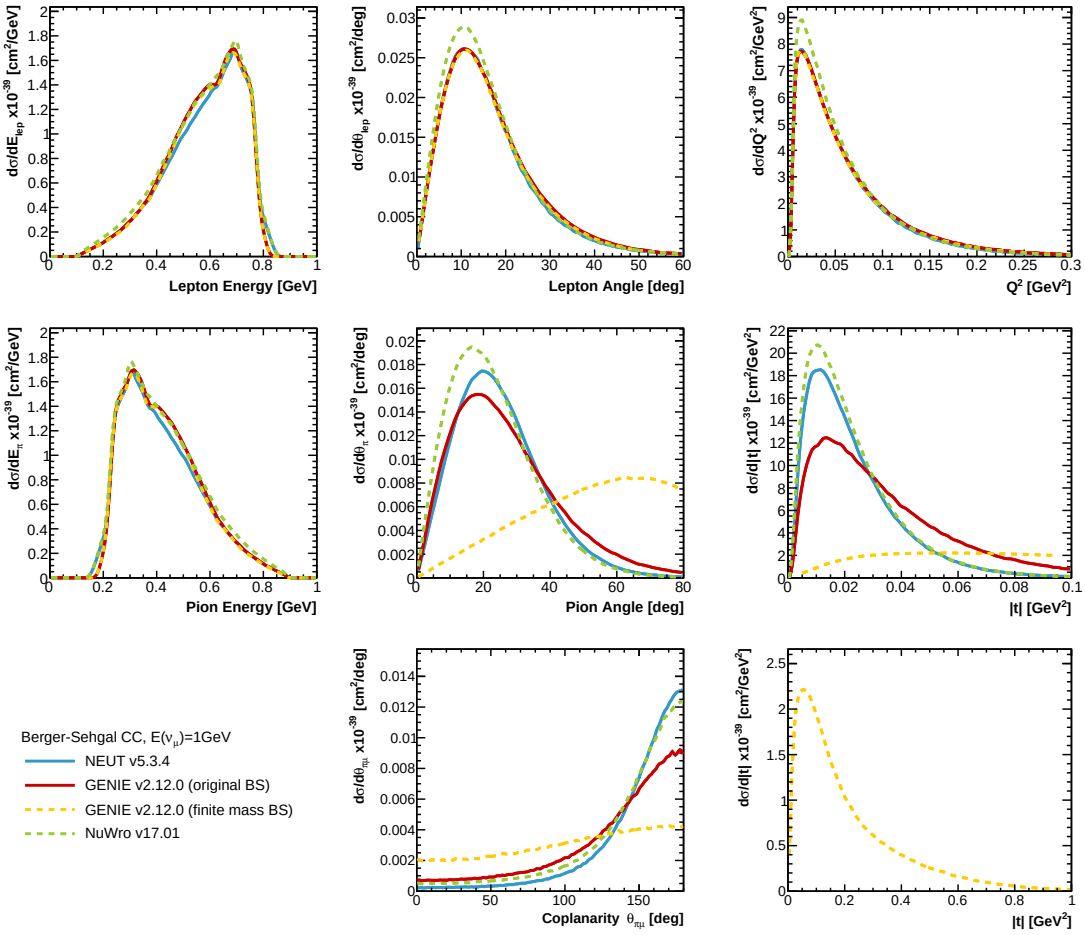

Figure 7.10: Comparison of lepton energy (top left), angle (top center), Q^2 (top right) and pion energy (middle left), angle (middle center), t (middle and bottom right) distributions for **charged current** interaction with E_ν=1 GeV. The coplanarity angle between the muon and the pion $\theta_{\pi\mu}$ is also given. The results are given for different implementations of the Berger-Sehgal model: NEUT (plain blue), NuWro (dashed green), GENIE (plain red), and GENIE where the nucleus has a finite mass (dashed yellow).

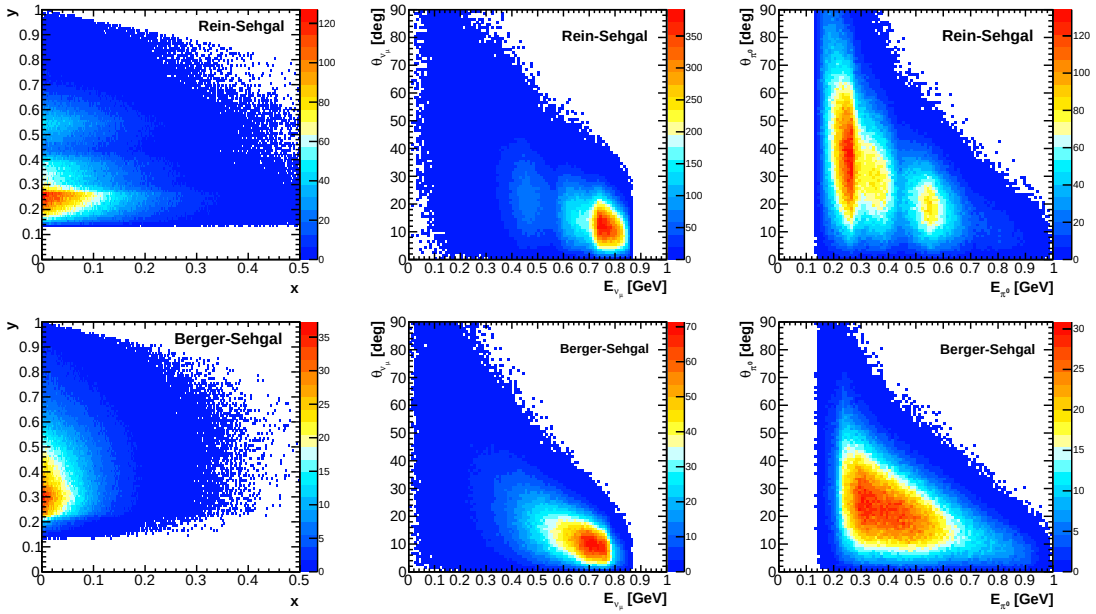

Figure 7.11: Phase space comparison for Rein-Sehgal (top row) and Berger-Sehgal (bottom row) NEUT predictions given in terms of (x_B, y_B) (left column), (E_μ, θ_μ) (middle column) and (E_π, θ_π) (right column) . These are for a ν_μ **neutral current** interaction where the neutrino energy is **1 GeV**.

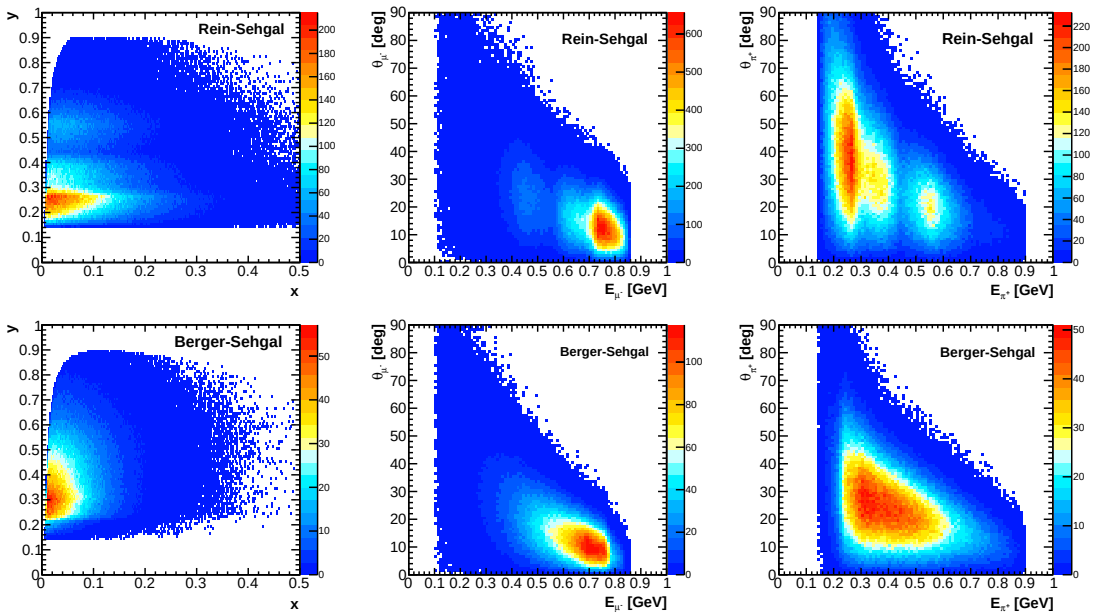

Figure 7.12: Phase space comparison for Rein-Sehgal (top row) and Berger-Sehgal (bottom row) NEUT predictions given in terms of (x_B, y_B) (left column), (E_μ, θ_μ) (middle column) and (E_π, θ_π) (right column). These are for a ν_μ **charged current** interaction where the neutrino energy is **1 GeV**.

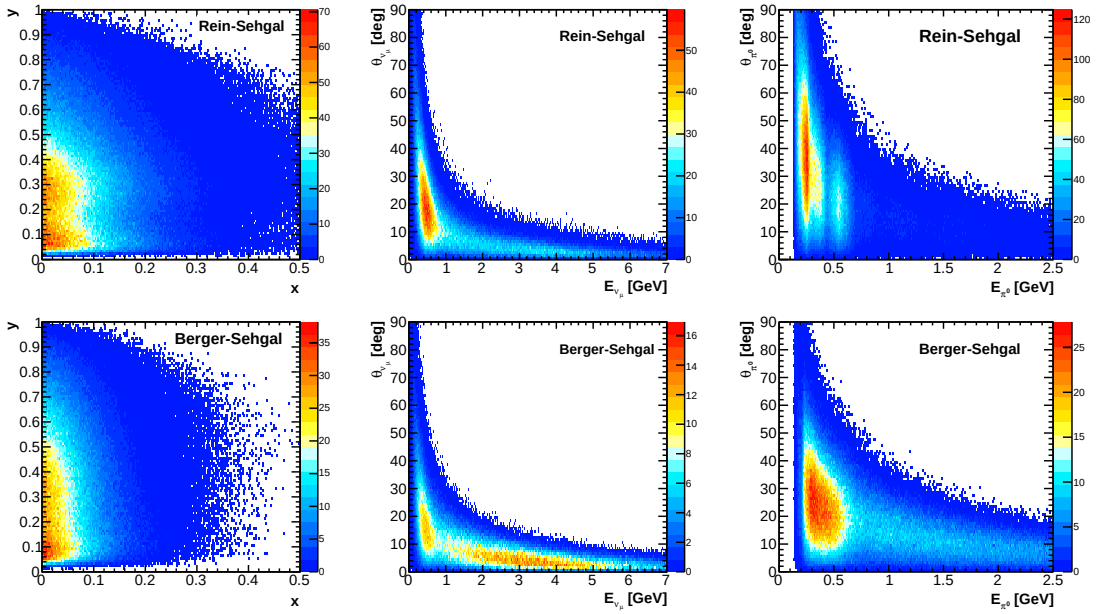

Figure 7.13: Phase space comparison for Rein-Sehgal (top row) and Berger-Sehgal (bottom row) predictions given in terms of (x_B, y_B) (left column), (E_μ, θ_μ) (middle column) and (E_π, θ_π) (right column). These are for a ν_μ **neutral current** interaction where the neutrino energy follows the **ND280 flux** prediction

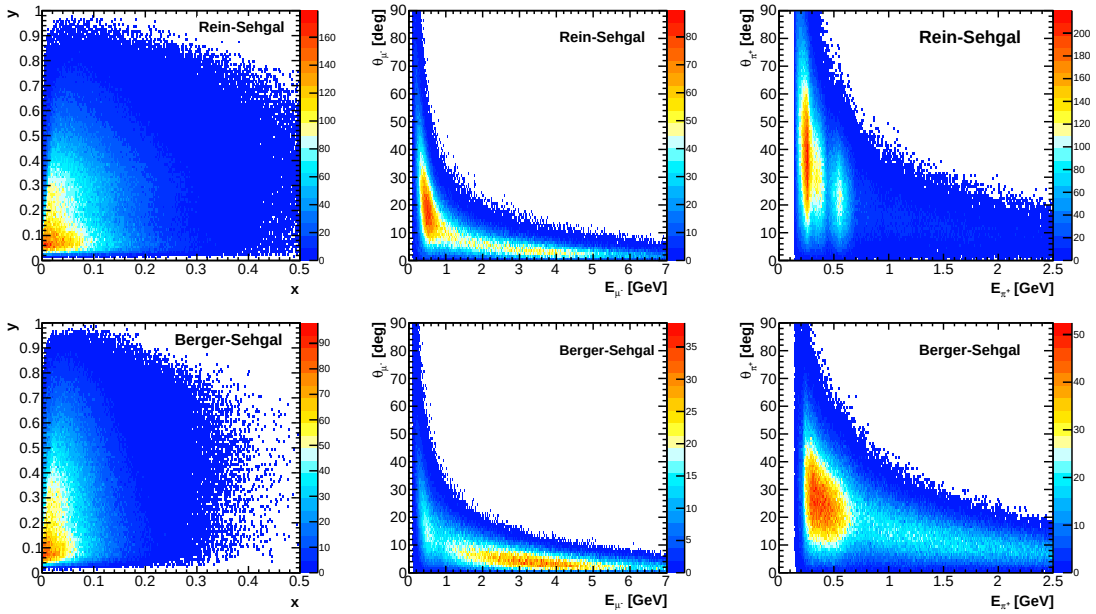

Figure 7.14: Phase space comparison for Rein-Sehgal (top row) and Berger-Sehgal (bottom row) predictions given in terms of (x_B, y_B) (left column), (E_μ, θ_μ) (middle column) and (E_π, θ_π) (right column). These are for a ν_μ **charged current** interaction where the neutrino energy follows the **ND280 flux** prediction.

7.3 Reweighting

A reweight from RS to BS was performed using an internal T2K software called T2KReWeight[iii]. It is built as an interface between the neutrino events generators and the analysis files so that we can see directly the effects of changing the values of various model parameters into the analysis. Tuning these model parameters, (also called dials), is very useful as it avoid having to deal with different MC productions. In this specific case, a new parameter is introduced into the interface to be able to switch between both coherent models. Others parameters are also available to change the values of the parameters of the BS model f_{A_1}, f_{b_1} and m_A^{COH}, which is the axial mass related to coherent intereactions.

7.3.1 From Rein-Sehgal to Berger-Sehgal

The weights for going from RS to BS are calculated for each coherent event by doing the ratio between the BS and RS total cross sections at the given neutrino energy. To check if this reweight introduces a bias in the shape or in the normalisation of the reweighted RS with respect to the true BS, a comparison is done where we use the MINERvA flux as input. It was found that the reweighted RS agreed with the true BS within 5 % as we see in Figures 7.15, 7.16 and 7.17.

7.3.2 Berger-Sehgal Parameters

The Berger-Sehgal model has 3 parameters that one can tweak with T2KReWeight. To check that the reweight is working properly, four values of f_{A_1}, f_{b_1} and m_A^{COH} are tested for a fixed neutrino energy of $E_{\nu_\mu} = 1\,\text{GeV}$. A NEUT monte-carlo file is generated with the default values (f_{A_1}, f_{b_1}, m_A^{COH}) = (0, 0, 1) and then each parameter is reweighted independently.

7.3.2.1 Shape Comparisons

The shape comparison is given in Figures 7.18, 7.19 and 7.20. It is clear from these plots that the reweight is working as expected since similar results have been found in Section 7.1.1, which means no change in the shape for f_{A_1} and large variations for f_{b_1}. A

[iii] Available on request

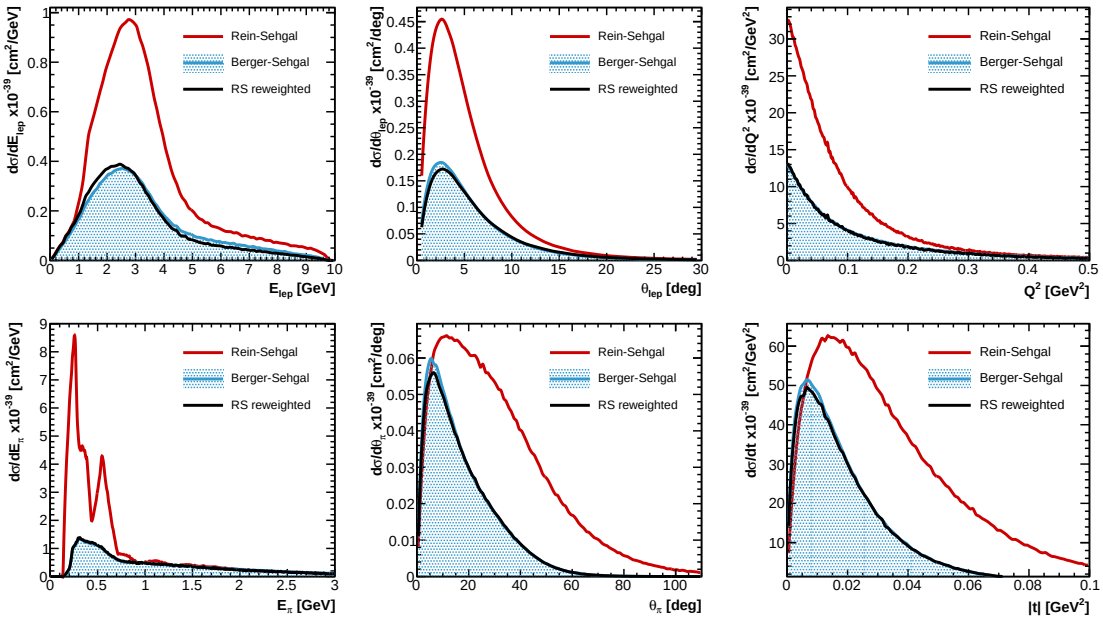

Figure 7.15: Comparison of RS (red), BS (blue) and RS reweighted to BS (black) differential cross sections for ν_μ **neutral current** interaction.

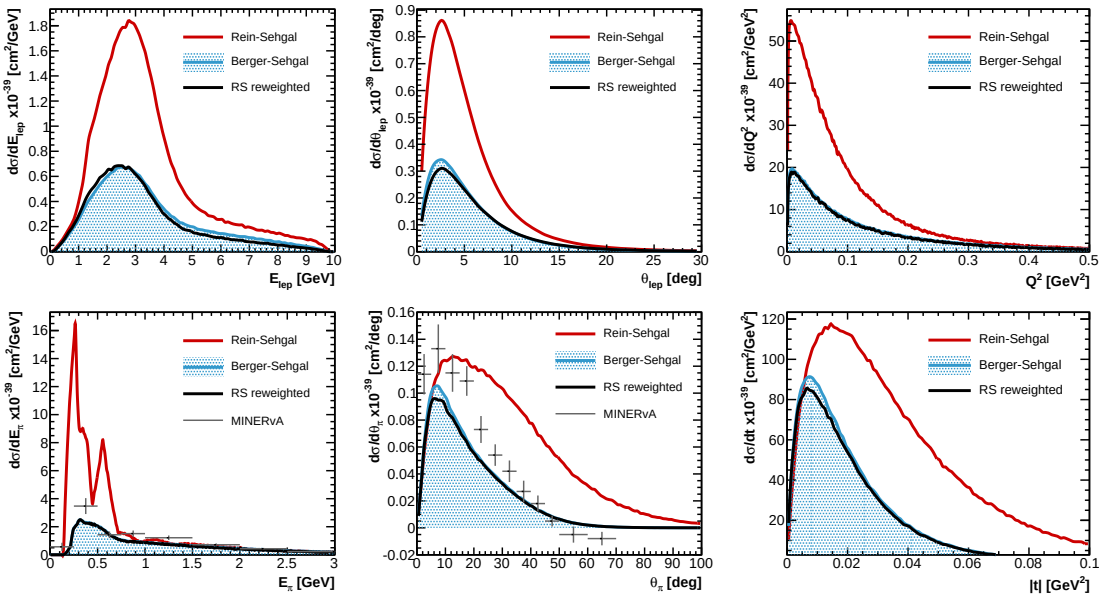

Figure 7.16: Comparison of RS (red), BS (blue) and RS reweighted to BS (black) differential cross sections for ν_μ **charged current** interaction. The MINERvA data points are also given when available (grey).

similar comparison for m_A^{COH} is available in Appendix 3 where we see that only a decrease of m_A^{COH} by 50 % slightly affect the shapes of the differential cross sections, except for the

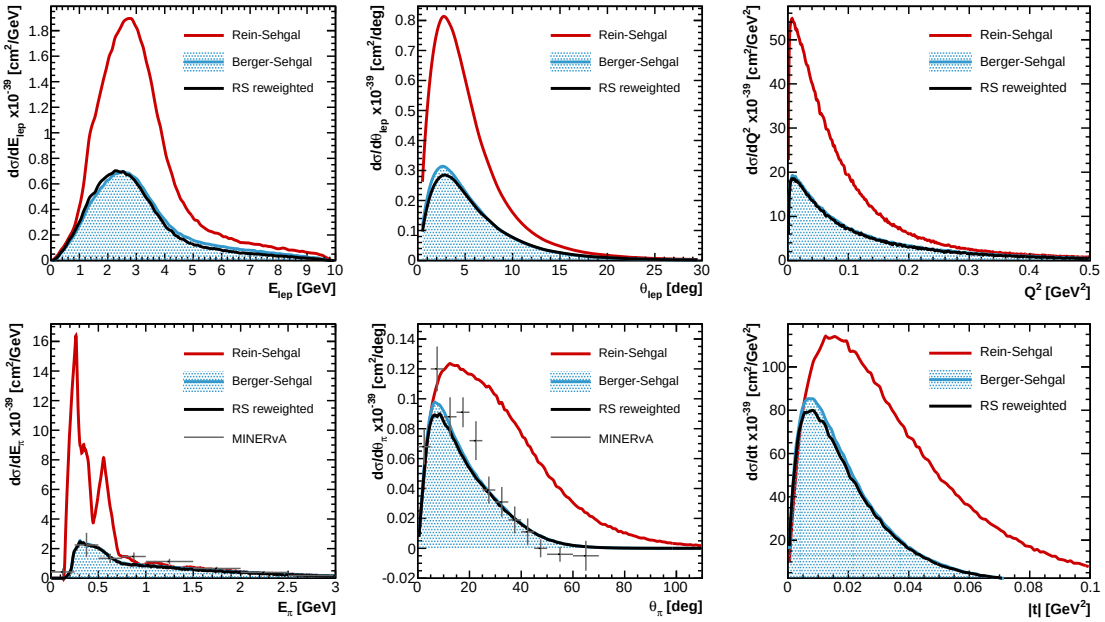

Figure 7.17: Comparison of RS (red), BS (blue) and RS reweighted to BS (black) differential cross sections for $\bar{\nu}_\mu$ **charged current** interaction. The MINERvA data points are also given when available (gray).

pion angle.

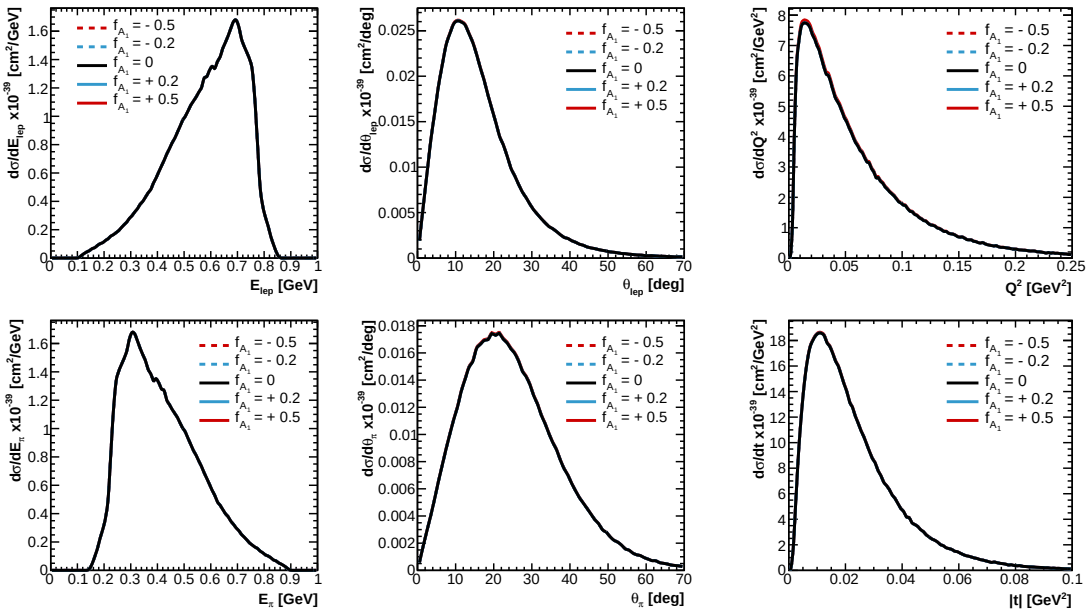

Figure 7.18: Shape comparison of the differential cross section for different reweight of f_{A_1} as a function of kinematic variables for $E_\nu = 1\,\text{GeV}$. From top left to bottom right: muon energy, muon angle w.r.t. neutrino direction, Q^2, pion energy, pion angle w.r.t. neutrino direction and transferred energy t. All the graphs are normalised using the area of the nominal distribution.

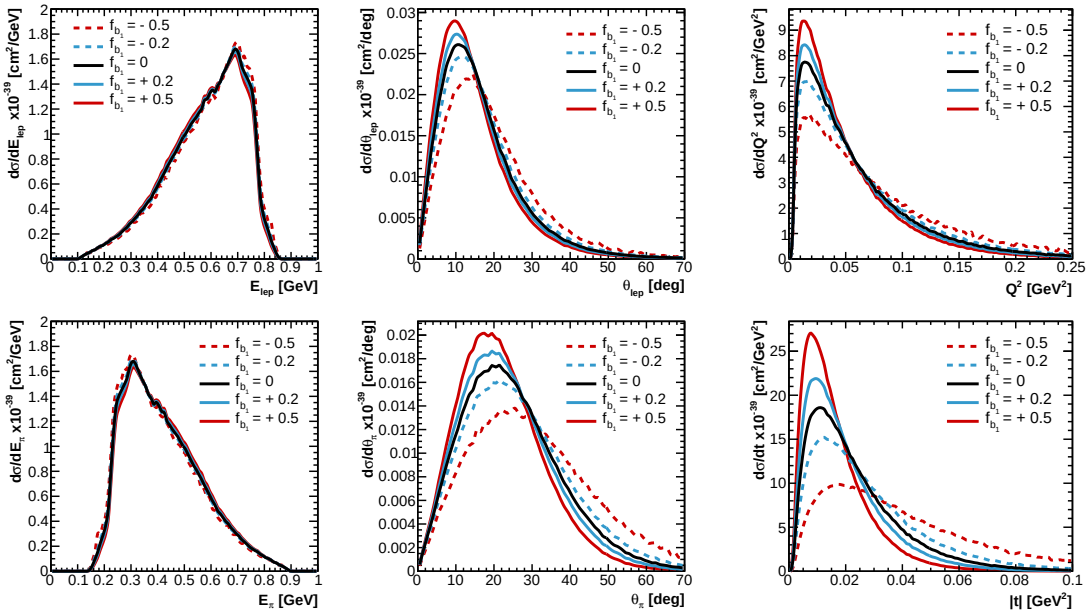

Figure 7.19: Shape comparison of the differential cross section for different reweight of f_{b_1} as a function of kinematic variables for $E_\nu = 1\,\text{GeV}$. From top left to bottom right: muon energy, muon angle w.r.t. neutrino direction, Q^2, pion energy, pion angle w.r.t. neutrino direction and transferred energy t. All the graphs are normalised using the area of the nominal distribution

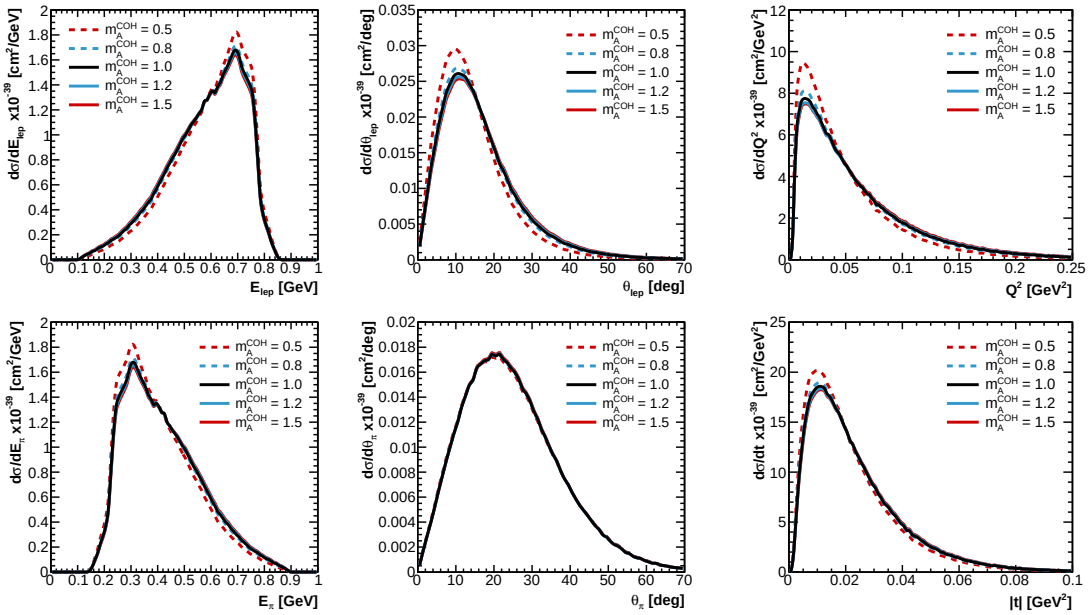

Figure 7.20: Shape comparison of the differential cross section for different reweight of m_A^{COH} as a function of kinematic variables for $E_\nu = 1\,\text{GeV}$. From top left to bottom right: muon energy, muon angle w.r.t. neutrino direction, Q^2, pion energy, pion angle w.r.t. neutrino direction and transferred energy t. All the graphs are normalised using the area of the nominal distribution

7.3.2.2 Normalisation Comparisons

We also check the variations in the normalisation for different values of the parameters. The normalisation is done by weighting each event with the total nominal cross section (from the cross section tables) times the weight calculated for this event. Note that the weight corresponds to the cross section with the new parameter value divided by the cross section with the nominal parameter value. Results are shown in Figures 7.21, 7.22 and 7.23.

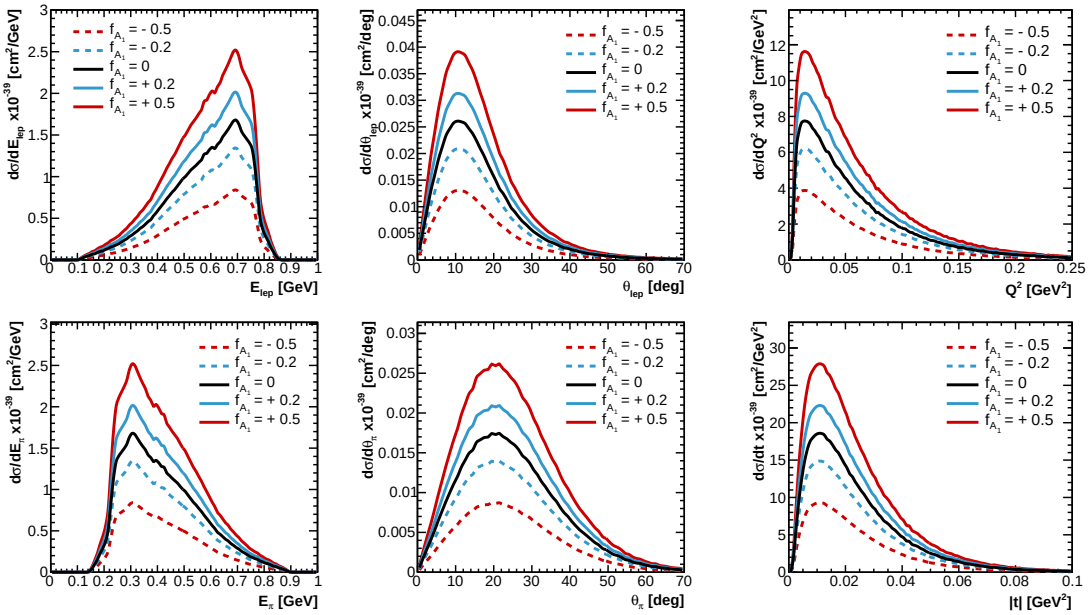

Figure 7.21: Normalisation comparison of the differential cross section for different reweight of f_{A_1} as a function of kinematic variables for $E_\nu = 1\,\text{GeV}$. From top left to bottom right: muon energy, muon angle w.r.t. neutrino direction, Q^2, pion energy, pion angle w.r.t. neutrino direction and transferred energy t.

We observe that f_{A_1} acts like an overall normalisation parameters as varying its value from $\pm 50\,\%$ scales all the distributions by the same amount. We also note that increasing f_{b_1} scales down the distributions while decreasing this parameter scales up the differential cross sections more drastically. Finally, we see that increasing m_A^{COH} by $50\,\%$ has a very small effect whereas decreasing it by $50\,\%$ scales down the differential cross sections by $20\,\%$ at most (the pion angle distribution being the most sensitive).

To summarise, we presented in this Chapter the addition of a new coherent model to the NEUT events generator. We compare the predictions of the old and new models to the

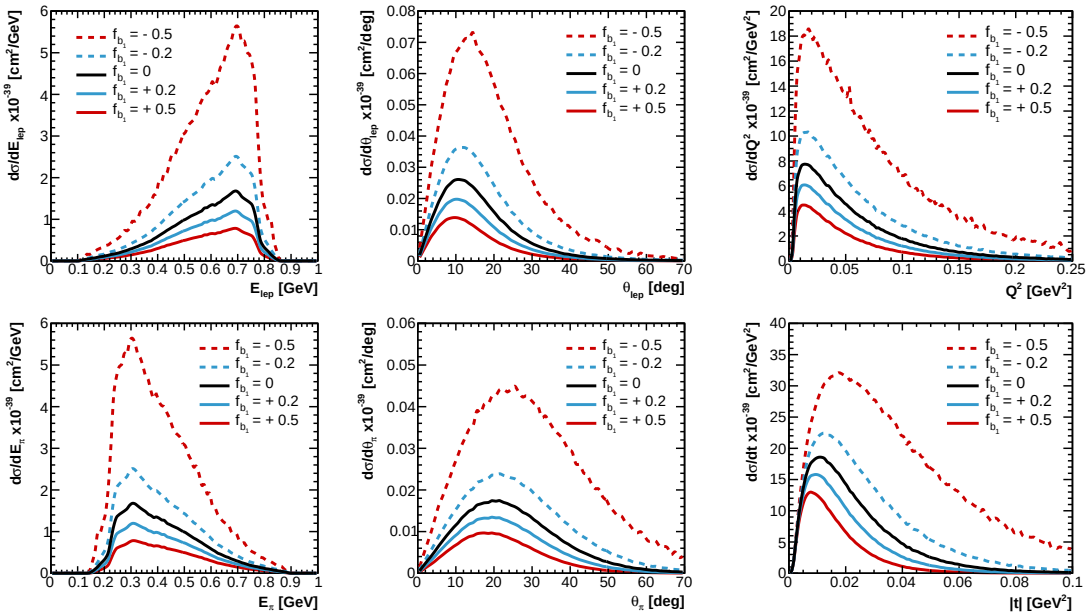

Figure 7.22: Normalisation comparison of the differential cross section for different reweight of f_{b_1} as a function of kinematic variables for $E_\nu = 1\,\text{GeV}$. From top left to bottom right: muon energy, muon angle w.r.t. neutrino direction, Q^2, pion energy, pion angle w.r.t. neutrino direction and transferred energy t.

available experimental data to make sure the linear scaling with the atomic number gives a acceptable results. We also checked the effects of varying 3 parameters on the differential cross section. This model will be used as a MC sample in the following cross section analysis. This will also reduce the error on the normalisation of coherent interactions prior to the oscillation parameter fits, contributing to reduce the overall systematic error on the oscillation parameters.

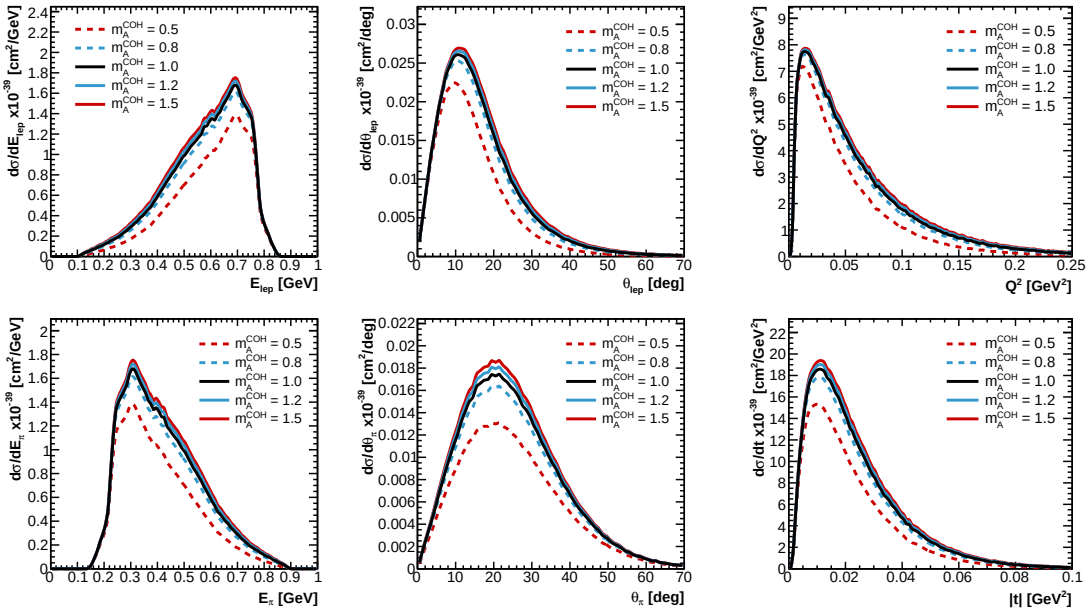

Figure 7.23: Normalisation comparison of the differential cross section for different reweight of m_A^{COH} as a function of kinematic variables for $E_\nu = 1\,\text{GeV}$. From top left to bottom right: muon energy, muon angle w.r.t. neutrino direction, Q^2, pion energy, pion angle w.r.t. neutrino direction and transferred energy t.

8

Samples Definition

We describe here the data set and MC samples that are used for the measurement of the neutrino-induced coherent pion production cross section on carbon and oxygen nuclei. After a brief explanation of the analysis strategy, we review different corrections applied to the samples before the start of the selection. The selection of coherent events is then detailed. Finally Section 8.3 gives the phase space reduction and the cross section binning chosen for the differential cross section.

8.1 Introduction

Measuring a neutrino cross section on oxygen is challenging as the oxygen nucleus is a passive target material. However the specific geometry of the T2K near detector with its alternate layers of scintillator and water allows to extract such a parameter. The signal we aim to select is charged-current coherent pion production induced by muon neutrino scattering off both carbon and oxygen nuclei.

8.1.1 General Strategy

The signal is split into two sub-samples according to the FGD which is used as a target. The FGD1 selection is a carbon-enhanced coherent sample while the FGD2 selection contains coherent scattering off both carbon and oxygen nuclei as illustrated in Figure 8.1. In these two samples, the non-coherent backgrounds are constrained and removed from their respective FGD selections using control samples. Different approaches of background removal are investigated in Chapter 9. Finally, for the oxygen measurement, the coherent carbon background is removed from the FGD2 sample by using the FGD1 sample as discussed in Chapter 9.

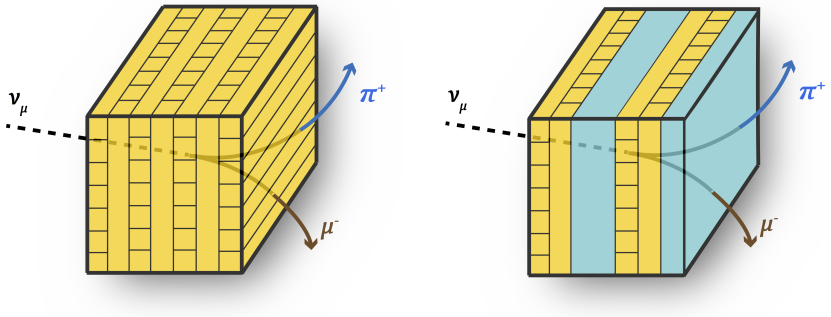

Figure 8.1: Sketch of charged current coherent pion production in FGD1 (left) and FGD2 (right). Note that the water layers of FGD2 are not scaled.

8.1.2 Analysis Samples

This analysis uses the ND280 data accumulated from November 2010 to April 2013. They correspond to three data taking periods:

- T2K run 2: November 2010 - March 2011
- T2K runs 3b and 3c: March 2012 - June 2012
- T2K run 4: October 2012 - April 2013

T2K run 1 is not used because the barrel ECal modules were not installed yet. As the focusing horns were turned off during the run 3a, these data are not used either.

8.1.2.1 Monte Carlo Data Set

The MC simulations are produced with the NEUT event generator [117] version 5.3.2. In order to better model the energy, position, direction and flavours of the interacting neutrinos, the beam group provides flux files used as an input in the generator. The interactions are then simulated according to the models that are implemented in NEUT (see Chapter 5). Note that the default coherent pion production model is the one by Rein-Sehgal. It is the model included in what we will mention thereafter as NEUT nominal. It is also worth recalling that the NEUT nominal predictions do not include diffractive scattering off nucleons. All the figures in this chapter use this MC production.

As shown in Chapter 7, it is possible to weight each coherent event to obtain the Berger-Sehgal predictions.

8.1.2.2 Processing Details

The detector geometry is simulated with GEANT. Note that the runs 2 and 4 are split into two according to the presence of water in the P0D. The different horn currents in run 3b and run 3c are reproduced by applying adequate flux re-weighting for 200 kA and 250 kA respectively. Interactions occurring in the materials around the detector are simulated with the so-called MC "sand muon" production although their contribution is negligible in this analysis as none of these events remain after the event selection. The raw data and MC files are then processed through the usual chain briefly described in Chapter 5.

Finally, the MC is normalised to the number of protons on target (POT) accumulated in the previously defined T2K runs. These POT must come from good spills as defined by the beam group and should contain good quality events as defined by the data quality group. The number of good POT and the total number of MC processed are given in Table 8.1. For all the figures in this chapter, the MC have been scaled to the data POT.

Table 8.1: Numbers of good POT and MC files processed for each T2K run.

T2K run	ND280 runs	good POT ($\times 10^{19}$)	MC files	MC POT ($\times 10^{20}$)
2 water in	6462-7663	4.2858	2401	12.004
2 water out	7664-7754	3.5445	1824	9.119
3b	8309-8453	2.146	800	3.999
3c	8550-8753	13.4779	5061	25.307
4 water in	8995-9422	16.2699	6845	34.201
4 water out	9423-9798	17.6246	6982	34.911
Total	-	57.349	-	119.541

8.1.3 Corrections to the Data Sets

Data and MC can exhibit discrepancies that have been understood (hardware failures or specific studies using control samples). In order to improve the agreement between them, a set of corrections is applied to the data and MC samples. These corrections are listed below:

- **Data quality correction**: an FGD Front End Board (FEB) was not working during three periods [i] while the data quality was set as good. This correction changes the data quality to bad for these periods.

- **Pile up correction**: a weight is applied to all the events in the MC production to take into account the possible coincidence of sand muon events with beam data.

- **Ignore right ECal**: During the March 2011 earthquake, two electronics boards in the right-side of the barrel ECal broke. As it affected the reconstruction, PID and energy estimation of the tracks entering this area, it was decided to not consider any track passing through the right ECal segment in both data and MC samples.

- **TPC Energy loss** dE/dx: Several corrections are applied to the energy loss for both data and MC samples. They involve re-evaluating the energy loss with updated values of the parameters entering in the dE/dx formula as well as normalising the data and MC dE/dx values. These corrections are important as they allow a better estimation of the TPC pulls that are used for PID.

- **TPC PID pulls**: This is an extra correction to the TPC dE/dx that allows the pulls to be centred around 0.

- **Momentum resolution**: A smearing factor up to almost 40% and depending of the drift distance x_{drift} is applied to the inverse transverse momentum of all TPC and global tracks, to account for the difference in momentum resolution between data and MC. These factors are computed by comparing the momentum in two consecutive TPCs, using control samples of tracks that cross multiple TPCs.

8.2 Event Selection

The goal of this section is to describe all the cuts necessary to obtain a sample with as many coherent pion production events as possible (purity optimisation). The first cuts are inherited from the ν_μ CC inclusive selections, in both FGDs. Cuts dedicated to select

[i] 22/03/2010 20:52 to 23/10/2010 13:53, 16/04/2010 15:13 to 16/04/2010 17:16, 26/05/2010 15:41 to 01/07/2010 00:00

coherent interaction are then described. Finally the purity and efficiency of the final samples are given.

8.2.1 Selection Cuts

All the cuts are applied to each bunch, where a bunch is a group of tracks that are close in time. The bunch width was 7 ns in Monte Carlo and 15 ns in data. The bunching criteria associates tracks to a bunch that deviate from the mean bunch position by less than 60 ns (i.e. 4 times the bunch width in data). This method reduces the number of accidental pile-up events. Selection cut numbers from 1 to 7 consist of usual one pion selection cuts while the cuts from 8 to 10 are specific to coherent pion production interactions and have been optimised based on the signal/background ratio (purity driven). However, as the backgrounds will be constrained by control samples, it is necessary to keep some resonant and DIS interactions in the selected samples (too low background events would lead to inaccurate constraints as we will see in Chapter 9).

1 **Data Quality Flag**. The full spill must have a good global ND280 data quality flag.

2 **Total Multiplicity**: All the events without any TPC track are rejected. For the FGD2 selection, events with tracks in FGD1 are also rejected.

3 **Quality and fiducial cut**. The event is selected when there is at least one reconstructed track inside FGD1 (or FGD2) fiducial volume. It is also required that there must be at least one track with segments in the FGD1 (FGD2) and any TPC. Such a track must have its starting point (vertex) inside the FGD1 (FGD2) fiducial volume. The fiducial volumes (FV) had to be changed since the vertex activity variables will be used. The vertex activity, also named vertex energy, corresponds to the energy deposit in the FGD scintillator bars around the vertex. The new fiducial volumes for FGD1 and FGD2 are defined in Table 8.2.

Table 8.2: Definition of the fiducial volumes for FGD1 and FGD2.

	x_{min}	x_{max}	y_{min}	y_{max}	z_{min}	z_{max}
FGD1	-874.51	874.51	-819.51	929.51	136.25	426.125
FGD2	-860.00	860.00	-805.00	915.00	1483.74	1797.26

This excludes five FGD1 bars in the x and y directions and two FGD1 bars in the z direction. For FGD2, seven bars are excluded in the x and y directions and one bar in the z direction. This FV assures that the bars considered in the vertex activity do not correspond to any bar located near the edges of the detector. Moreover, in order to reject short tracks where reconstruction in the TPCs is less reliable, only tracks with more than 18 TPC clusters, vertical or horizontal, are selected.

The highest momentum negatively charged particle that originates in the FGD1 FV and enters TPC2 (or originates in FGD2 FV and enters TPC3) is identified as the μ^- candidate.

4 **External veto**. Some reconstruction failures can lead to a muon track starting in the FGD FV even if the real muon started far upstream. For example a muon originating from the P0D and undergoing a large scattering in FGD1 may be reconstructed as two tracks instead of one (one P0D-TPC1-FGD1, and the other FGD1-TPC2-...). In order to exclude such events, this cut vetoes events in which the second highest momentum track starts 150 mm upstream of the muon candidate. Additionally, for FGD2 selection, the event is vetoed if a secondary track starts in FGD1 FV.

5 **Broken track veto**. This cut was applied to reject events with mis-reconstructed tracks, where instead of one muon candidate track originating in FGD FV our reconstruction procedure breaks this track into two components: one FGD-only track (fully contained in FGD) followed by second track which starts in last layers of FGD and passes through a TPC module. Therefore the second track is considered as the muon candidate. To reject such events, it is required that the start position of the muon candidate track is less than 425 mm away from the FGD upstream edge if the same event has at least one reconstructed FGD-only track.

6 **Muon PID**. The TPC PID relies on the energy loss dE/dx measurement. The measured energy loss is compared to the expected energy loss for the particle α, where α can be electron, muon, proton or pion. For each particle hypothesis, one can build the Pulls

$$Pull_\alpha = \frac{dE/dx^{meas} - dE/dx_\alpha^{exp}}{\sigma_{(dE/dx^{meas} - dE/dx_\alpha^{exp})}} \tag{8.1}$$

and the discrimination functions L_α and L_{MIP}:

$$L_\alpha = \frac{e^{-Pull_\alpha^2}}{\sum_{i=e,\mu,p,\pi} e^{-Pull_i^2}}, \tag{8.2}$$

$$L_{MIP} = \frac{L_\mu + L_\pi}{1 - L_p} \tag{8.3}$$

A cut on the muon candidate $L_\mu > 0.05$ removes all the electrons. Another cut on $L_{MIP} > 0.8$ is applied in case $p_{\mu \text{ candidate}} < 500\,\text{MeV}$ which removes electrons, pions and protons. These two cuts are given in Figure 8.2

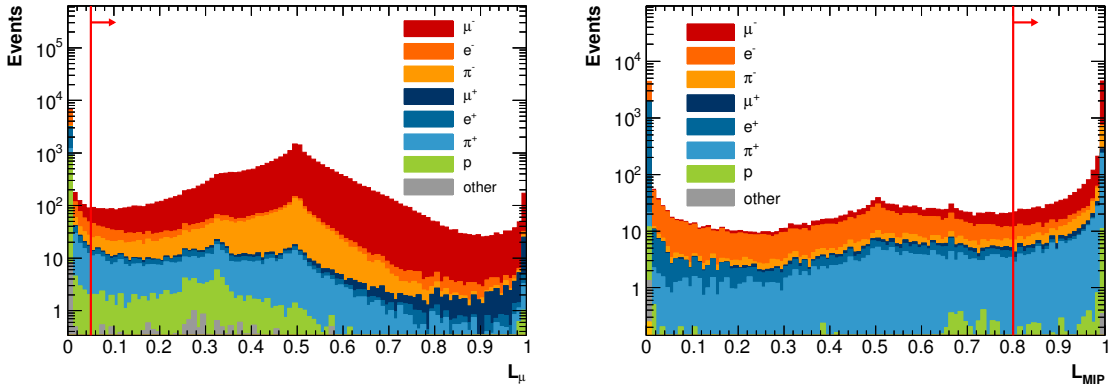

Figure 8.2: Left: L_μ distribution of the muon candidate. Events with $L_\mu > 0.05$ are kept. Right: L_{MIP} distribution of the muon candidate with $p < 500\,\text{MeV}$. Events with $L_{MIP} > 0.8$ are kept. These plots are for neutrino vertex in FGD1 and POT normalised.

7 **Single pion**. The search for charged pions can be split into three approaches, detailed here in order of importance:

– **TPC pions**. We need to select event with secondary tracks different from the muon candidate but in the same bunch. Then they must start in the same FGD fiducial volume used for the muon candidate and enter TPC2 or TPC3, for FGD1 or FGD2 selection, respectively. Similarly to the muon candidate, they are also required to satisfy the TPC quality cut by having more than 18 clusters in the TPC. For tracks which pass those criteria the particle identification in TPC is performed. In case of positive tracks, three pulls are considered by the particle identification procedure: pion, positron and proton. The PID is then based on the most probable particle method, ie the probability P_α defined in equation (8.4) is calculated for $\alpha = e^+$, π^+, p and the particle is tagged

with the type that has the highest probability, unless P_e is the highest and the momentum is larger than 900 MeV. In that specific case, the particle is most probably a proton.

$$P_\alpha = \frac{L_\alpha}{\sum\limits_{i=e^+,\pi^+,p} L_i} \tag{8.4}$$

When a particle's momentum is too low or its angle is too high to enter a TPC, the FGD information can be used to identify whether it is a charged pion or not. Here two methods of pion identification are considered depending on the length, and therefore momentum of the pion track.

– **Michel electrons**. For pion tracks too short to leave enough hits in the FGD to be reconstructed as independent tracks, the Michel electron tagging is used. Michel electrons are found by searching for delayed signals in FGD due to the 2.19 μs decay time of the muon. The Michel electron delayed signal associated with a hit cluster is required to be outside of the beam bunch window. The hit cluster is now required to have at least 7 hits in the case of FGD1 selection and 6 hits for FGD2 selection.

– **Isolated FGD pions**. For higher momentum pions, the FGD particle identification is performed. When a pion produces a reconstructed secondary track in a FGD, this track is required to be in the same time bunch as the muon candidate. It is also required to start in the same FGD fiducial volume and be fully contained in the FGD (FGD-only track). A pion pull is defined in order to identify charged pions based on the information of energy deposited by the particle as a function of track length. This method provides a discrimination between protons and muons/pions for tracks which start and stop inside an FGD detector.

The single pion cut requires that the sum of the number of TPC pions and Michel electron equals to 1. If there is no Michel electron, then the sum of TPC pions and isolated FGD pion must be 1.

8 **FGD multiplicity**. Coherent events consist of only one muon and one pion in the final state. Therefore, any events with more than two reconstructed tracks in an

FGD are rejected, as illustrated in Figure 8.3.

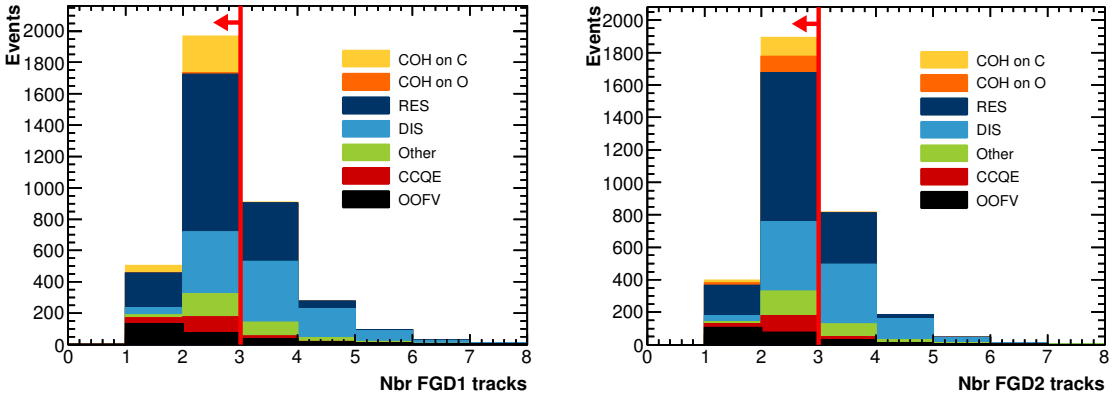

Figure 8.3: Cut on the total number of reconstructed FGD tracks for FGD1 (left) and FGD2 (right) selections.

9 **Vertex Energy**. As the nucleus should stay in its ground state during a coherent interaction along with a minimum recoil, the energy deposit around the vertex must remain small. Here, we sum the energy in a cubic volume of $5 \times 5 \times 5$ bars in FGD1 and $7 \times 7 \times 2$ bars in FGD2 around the reconstructed vertex. The reason for the different volumes is due to the water layers in FGD2 that constrain the number of bars in the z direction. The events with a vertex energy larger than 14 MeV in FGD1 and 7 MeV in FGD2 are rejected, as shown in Figure 8.4.

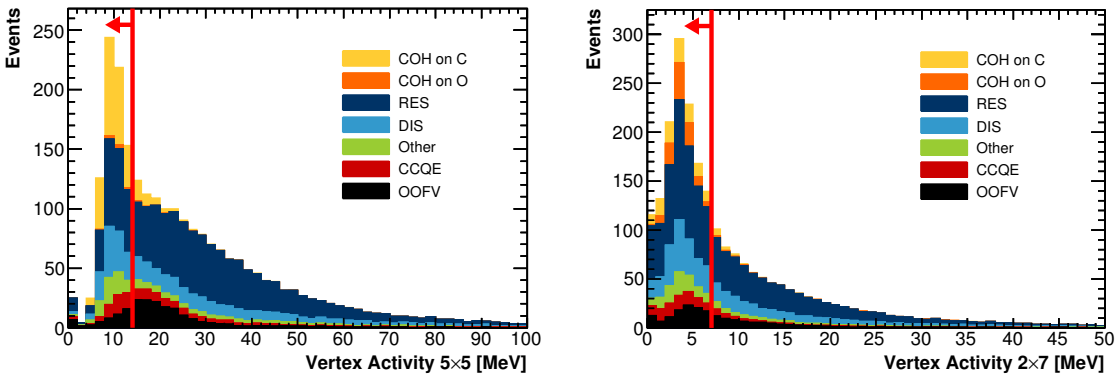

Figure 8.4: Cut on the vertex energy for FGD1 (left) and FGD2 (right) selections.

10 **Energy transferred**. The energy transferred to the nucleus corresponds to the $|t|$ variable defined in equation (3.14). Unfortunately, the energy and momentum of the initial neutrino is not known and must be inferred. Assuming that the recoiling nucleus takes only momentum and no energy from the interaction and the neutrino

is propagating along the beam direction, one can reconstruct $|t|$ as a function of the kinematics of the outgoing particles as expressed in (8.5), where $p^L = pcos\theta_\pi$ is the longitudinal momentum, $p^T = psin\theta_\pi$ the transverse momentum and θ_π is the pion angle with respect to the neutrino beam direction.

$$|t| = \left(\sum_{i=\mu,\pi} (E_i - p_i^L) \right)^2 + \left(\sum_{i=\mu,\pi} p_i^T \right)^2 \tag{8.5}$$

The cut on $|t| > 0.4\,\text{GeV}^2$ in FGD1 and $|t| > 0.3\,\text{GeV}^2$ in FGD2 are rejected as

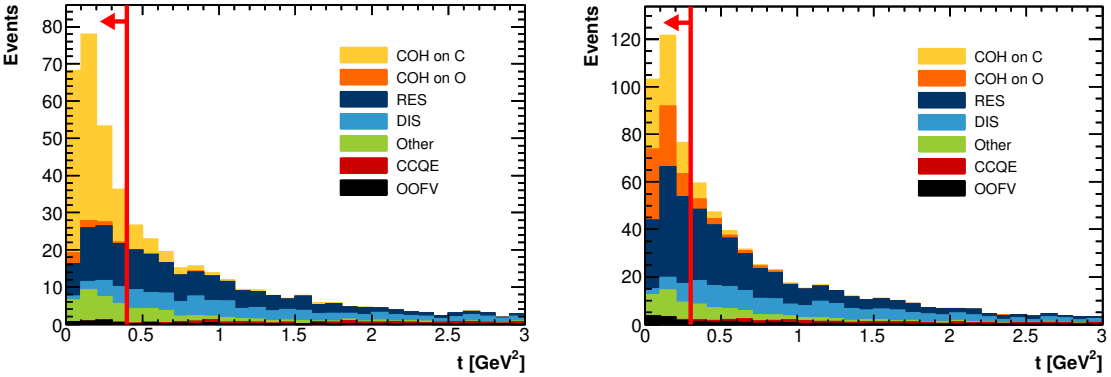

Figure 8.5: Cut on the energy transfer $|t|$ for FGD1 (left) and FGD2 (right) selections.

Before studying performances of the cuts (i.e. the variation of purity and efficiency after each step), all the selection cuts are summarised in Table 8.3.

Table 8.3: Summary of the selection cuts.

Order	Name	FGD1	FGD2
1	Data quality	good quality	good quality
2	Total multiplicity	# TPC track > 0	# TPC track > 0 and no FGD1 track
3	Quality and fiducial volume	# FGD1 track in FV > 0	# FGD2 track in FV > 0
4	External veto	2^{nd} highest momentum track is vetoed if it starts near the muon candidate	
5	Broken track veto	muon candidate doesn't start in the last bars of the FGD	
6	Muon PID	$L_\mu > 0.05$ and $L_{MIP} > 0.8$ is $p_{\mu\ \text{candidate}} < 0.5\,\text{GeV}$	
7	Single pion	# TPC pion + # Michel elec. or FGD pion $= 1$	
8	FGD multiplicity	# FGD1 tracks < 3	# FGD2 tracks < 3
9	Vertex energy	VE $5\times5 \leq 14\,\text{MeV}$	VE $2\times7 \leq 7\,\text{MeV}$
10	Energy transferred	$\lvert t\rvert \leq 0.4\,\text{GeV}^2$	$\lvert t\rvert \leq 0.3\,\text{GeV}^2$

8.2.2 Efficiency and Purity

The composition of the FGD1 and FGD2 selected MC samples in terms of true reactions is summarised in Table 8.4. The purity defined in equation (8.6) can be read in bold in the coherent row. The purity in coherent events is 62.8±3.1 % for FGD1 and 46.0±2.8 % for FGD2. The reason for such a big difference in purity between FGD1 and FGD2 is that the vertex energy cuts are different. As illustrated by Figure 8.4 and Figure 8.6, this cut is more efficient in FGD1 than in FGD2 due to the different volumes considered.

$$\text{Purity} = \frac{N^{selected,trueCOH}}{N^{selected,tot}} \tag{8.6}$$

The efficiencies defined by (8.7) are also given at the bottom of the table. They are 22.3±1.6 % for FGD1 and 22.5±1.6 % for FGD2, which means that about 80 % of the true MC coherent events are lost by performing the selection cuts. The total number of POT-weighted MC events that have passed the last cut is also given for each selection.

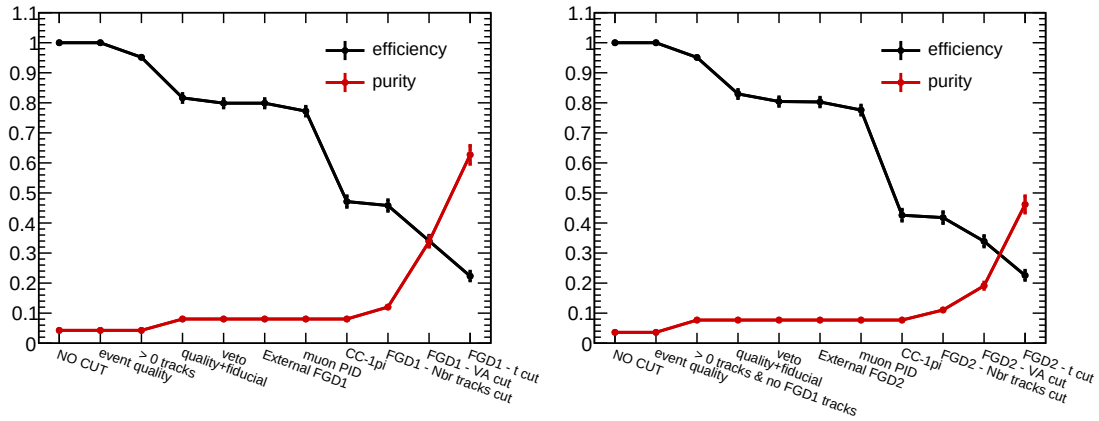

Figure 8.6: Efficiency and Purity at different cut levels. The left plot is for FGD1 selection and the right plot for FGD2.

$$\text{Efficiency} = \varepsilon = \frac{N^{selected,trueCOH}}{N^{tot,trueCOH}} \tag{8.7}$$

From Table 8.4, we observe that the main background is the resonant channel, followed by DIS and $\overline{\nu}_\mu$ interactions and neutral current (NC).

Table 8.4: Composition of the selected samples for FGD1 and FGD2 in terms of interaction. The coherent purity is in bold. At the bottom of the table, the total number of MC events are given along with the efficiency. The number of events corresponds to the number of POT-weighted MC events that passed the last cut

	FGD1		FGD2	
	Purities	# Events	Purities	# Events
COH	**62.82 %**	148.0	**46.00 %**	138.6
RES	20.98 %	49.4	37.18 %	112.0
DIS	5.21 %	5.20	5.17 %	15.5
$\bar{\nu}_\mu$	5.58 %	5.58	4.18 %	12.60
NC	3.86 %	3.85	3.97 %	11.95
CCQE	0.04 %	0.10	0.27 %	0.82
2p-2h	0.13 %	0.30	0.25 %	0.75
$\nu_e, \bar{\nu}_e$	0.24 %	0.56	0.29 %	0.88
out of FV	1.14 %	2.68	2.69 %	8.11
Total	100 %	235.65	100 %	301.3
Efficiency	22.32 %	-	22.55 %	-

8.2.3 Kinematic Distributions

We present here the distributions of the reconstructed momentum and cosine of the angle for the muon and the pion for both FGD1 and FGD2 selections in Figure 8.9 and Figure 8.10 respectively. We also give the distribution of the sum of the pion and muon energies along with the coplanarity angle $\theta_{\pi^+\mu^-}$ between the muon and the pion tracks, as defined in Figure 8.7. These distributions are all normalised with respect to the number of data POT. The categories are defined by the true interaction channels and for coherent pion production, we distinguish also between the two main target nuclei: carbon and water. The small amount of coherent interaction on oxygen in FGD1 may be due to neutrinos interacting in the glue between FGD bars. As expected there are much more coherent interactions on oxygen in FGD2, where the proportion of oxygen to carbon is 43% / 57%. The category "Other" contains neutral current, 2p-2h, $\overline{\nu}_\mu$ and $\nu_e, \overline{\nu}_e$ interactions. The label "OOFV" in the legend stands for the "out of fiducial volume" interactions.

We observe in both FGD selections a very forward going muon and a relatively forward going pion. Both particles' momenta peak in the region between 200 MeV and 800 MeV.

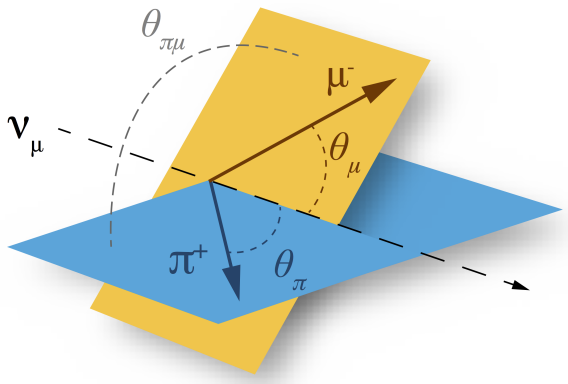

Figure 8.7: Definition of the angles θ_μ, θ_π and $\theta_{\pi\mu}$.

The sum of their reconstructed energy is given as in the case of a coherent interaction, it should be very close to the incoming neutrino energy. This is highlighted in Figure 8.8, where only the coherent contribution has been plotted against the true value of the neutrino energy. Thus we define

$$E_\nu^{\text{reco}} = E_{\mu^-} + E_{\pi^+} \tag{8.8}$$

Finally, the coplanarity angle peaks at 180 degrees, which means that most of the time, the muon and the pion are emitted in opposite directions.

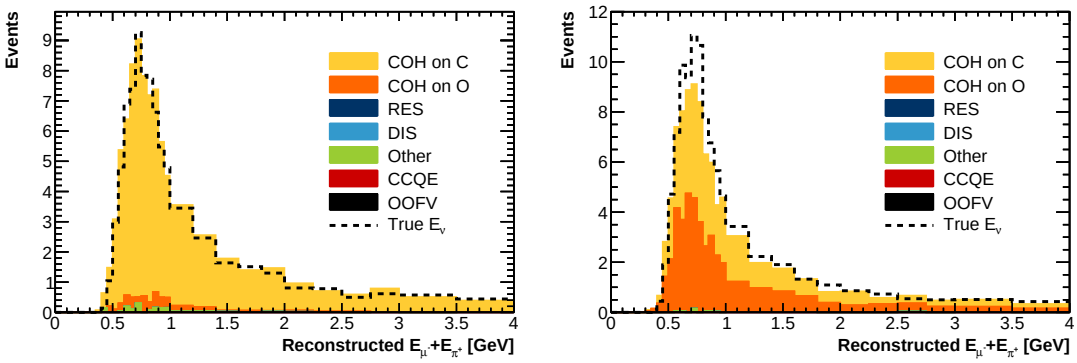

Figure 8.8: Comparison between the sum of the muon and pion reconstructed energies (stacked) with the true neutrino energy (dash line) for coherent interaction only. The left (right) plot is for FGD1 (FGD2).

The implementation of the Berger-Sehgal coherent model together with the reweighted method detailed in Chapter 7 gives us access to the same distributions presented in

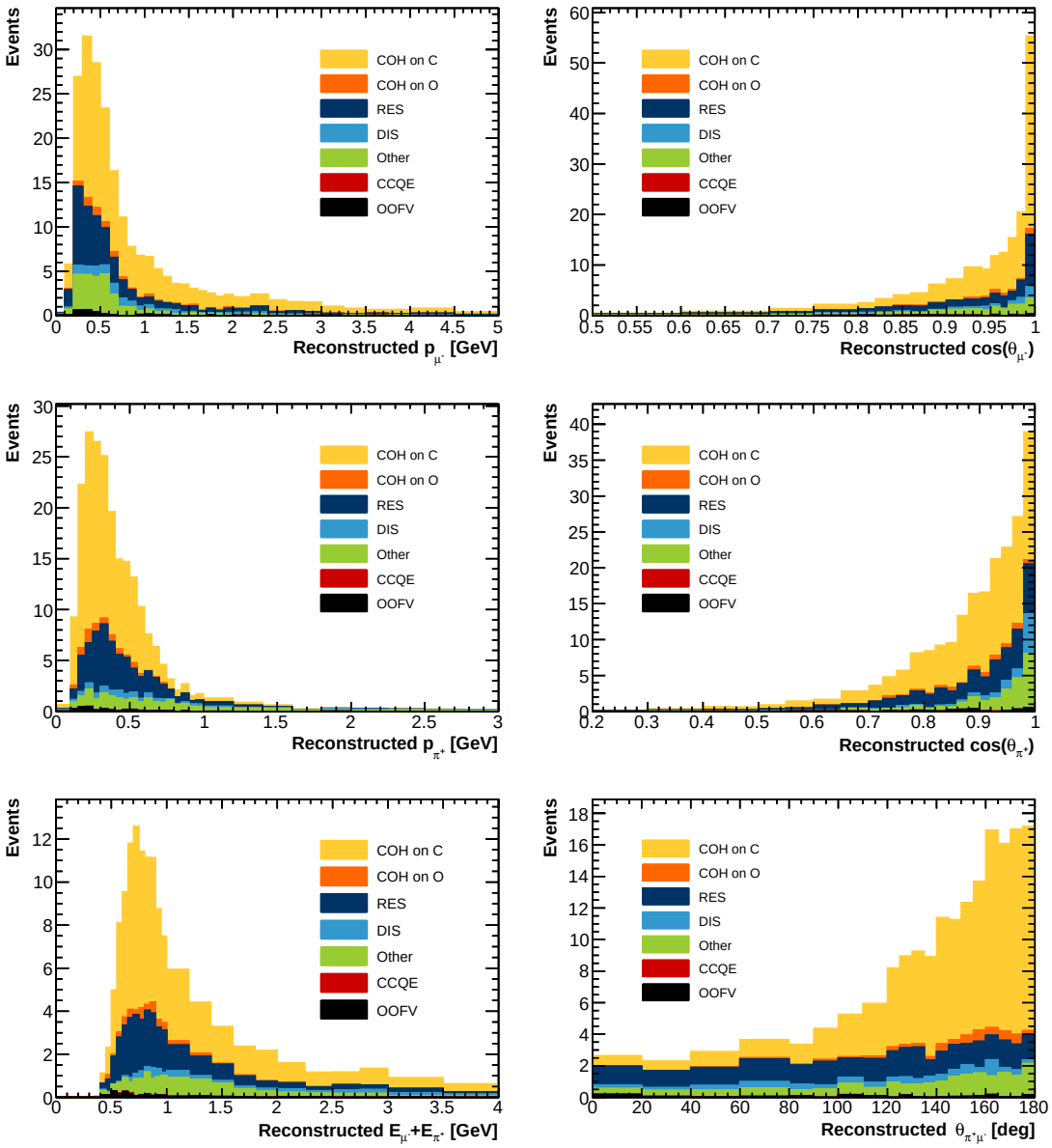

Figure 8.9: Reconstructed kinematic distributions of the **NEUT nominal** MC at the end of the FGD1 selection. From top left to bottom right: p_μ, $\cos(\theta_\mu)$, p_π, $\cos(\theta_\pi)$, $E_\mu + E_\pi$, $\theta_{\pi\mu}$.

Figures 8.9 and 8.10, but for the Berger-Sehgal (BS) model. As we already discussed, this model predicts a cross section about 50 % smaller than the nominal Rein-Sehgal and this difference is clearly seen in Figures 8.11 and 8.12. However, one must keep in mind that the selection has been optimised with the NEUT nominal sample.

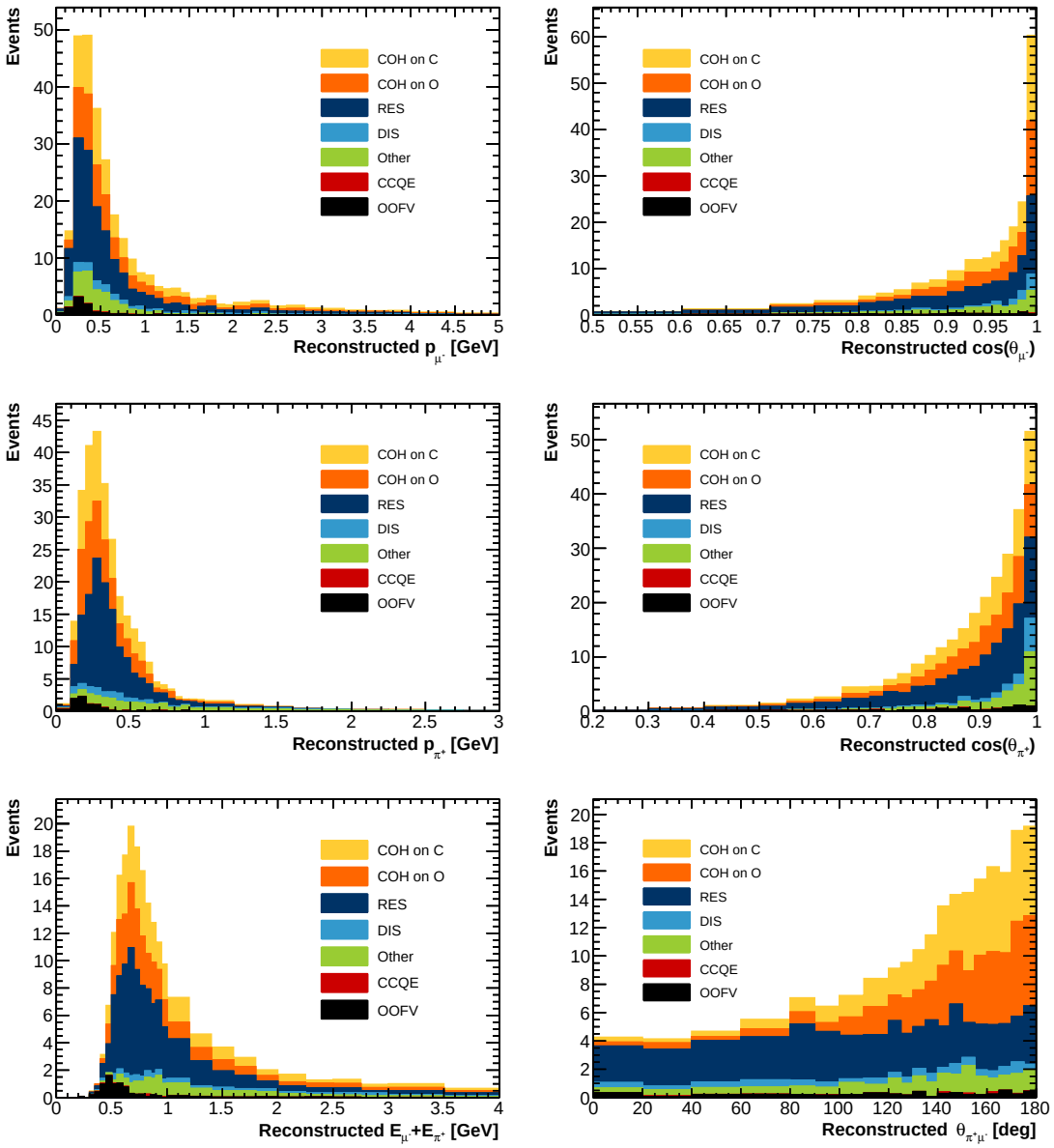

Figure 8.10: Reconstructed kinematic distributions of the **NEUT nominal** MC at the end of the FGD2 selection. From top left to bottom right: p_μ, $\cos(\theta_\mu)$, p_π, $\cos(\theta_\pi)$, $E_\mu + E_\pi$, $\theta_{\pi\mu}$.

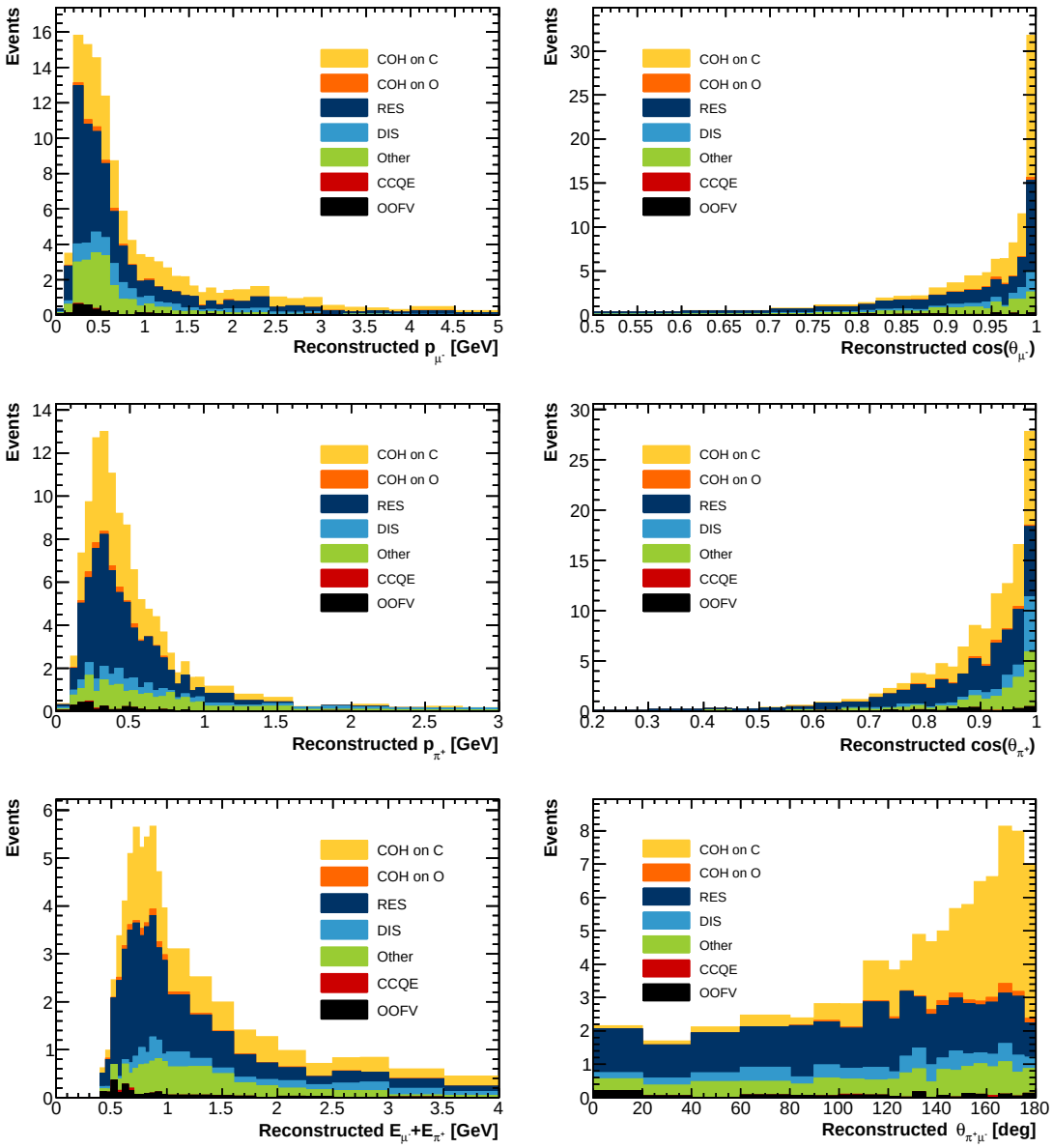

Figure 8.11: Reconstructed kinematic distributions at the end of the FGD1 selection for the **NEUT Berger-Sehgal reweighted** MC. From top left to bottom right: p_μ, $\cos(\theta_\mu)$, p_π, $\cos(\theta_\pi)$, $E_\mu + E_\pi$, $\theta_{\pi\mu}$.

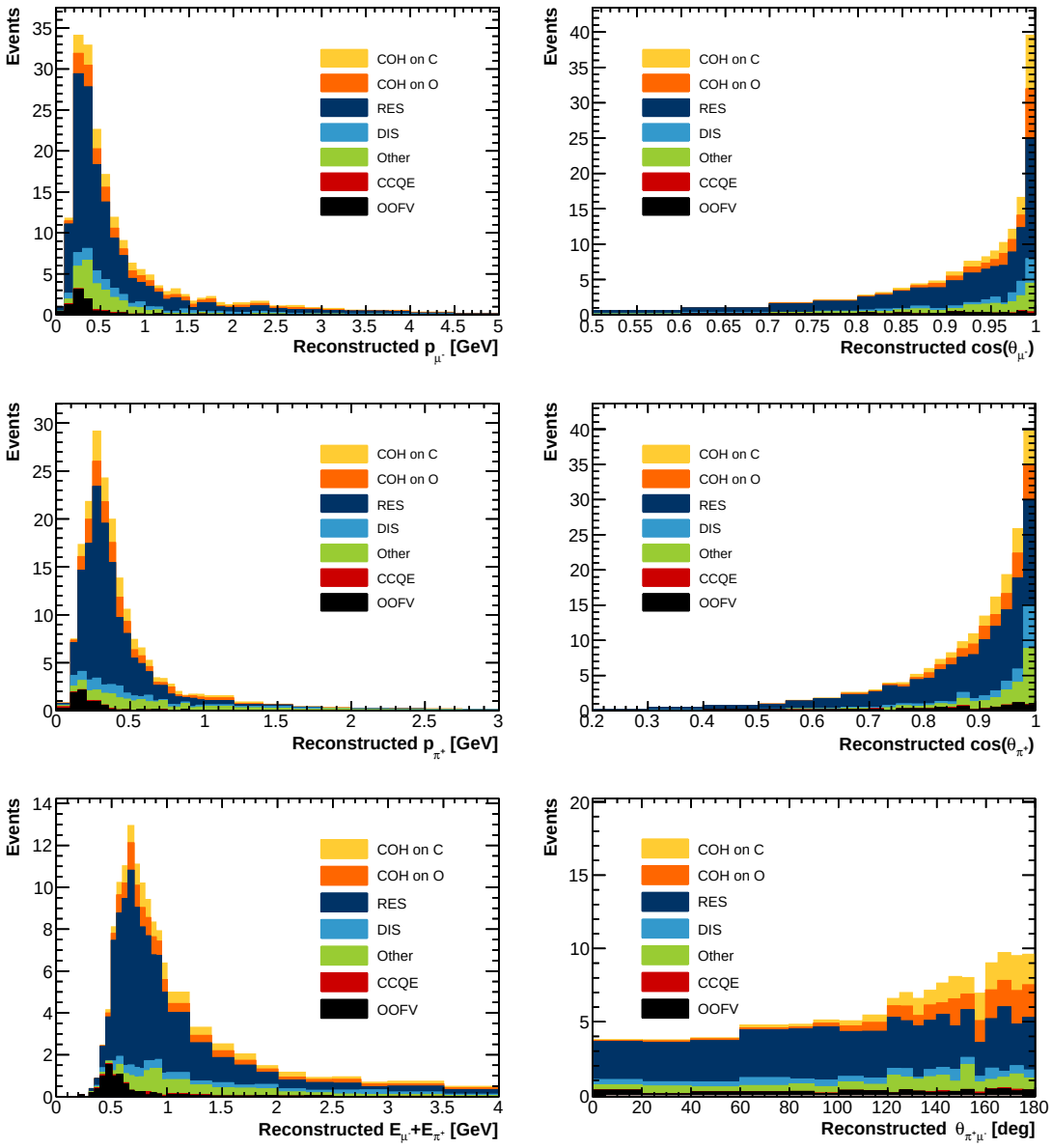

Figure 8.12: Reconstructed kinematic distributions at the end of the FGD2 selection for the **NEUT Berger-Sehgal reweighted** MC. From top left to bottom right: p_μ, $\cos(\theta_\mu)$, p_π, $\cos(\theta_\pi)$, $E_\mu + E_\pi$, $\theta_{\pi\mu}$.

8.3 Phase Space and Binning

In general, it is good to measure cross section with the finest possible binning and with the largest momentum and angular coverage. However, the statistics and the detector smearing are often the limiting factors in the number of bins to choose. Moreover, as we saw that coherent events are low energy and very forward, it might not be worth including large angle and momentum bins as the efficiency in these will be poor.

8.3.1 Efficiency Studies

We present in Figures 8.13 and 8.14 the efficiencies as a function of different kinematic variables, for FGD1 and FGD2 selections. As we can see from equation (8.7), they are calculated based on the true information of the NEUT nominal MC. Applying cuts on these variables allows to remove the low efficiency phase space regions and therefore increases the overall efficiency. However, these cuts inevitably add model dependance to the analysis (as they purely rely on MC predictions) and reduce the number of selected events. Ideally one would look at these efficiencies in a multidimensional space in order to better select the high efficiency regions but here the statistics are limited so the cuts are tuned one after the other for each of the variables. The phase space cuts are given in Table 8.5 where E_ν is calculated with equation (8.8) where we use the true pion and muon momentum. The efficiencies after the phase space cuts are given by the red triangles in Figures 8.13 and 8.14, where we observe a few percents increase.

Table 8.5: Restricted phase space definition. Note that E_ν is calculated using equation (8.8) where the true muon and pion momentum have been used.

True variable	Lower limit	Upper limit
Muon momentum	$p_{\mu^-} > 0.2\,\text{GeV}$	$p_{\mu^-} < 5.0\,\text{GeV}$
Muon angle	$\cos(\theta_{\mu^-}) > 0.75$	
Pion momentum	$p_{\pi^+} > 0.15\,\text{GeV}$	$p_{\pi^+} < 1.5\,\text{GeV}$
Pion angle	$\cos(\theta_{\pi^+}) > 0.45$	
Neutrino energy	$E_\nu > 0.50\,\text{GeV}$	$E_\nu < 6.5\,\text{GeV}$
Coplanar angle	$\theta_{\pi^+\mu^-} > 90\,\text{deg}$	

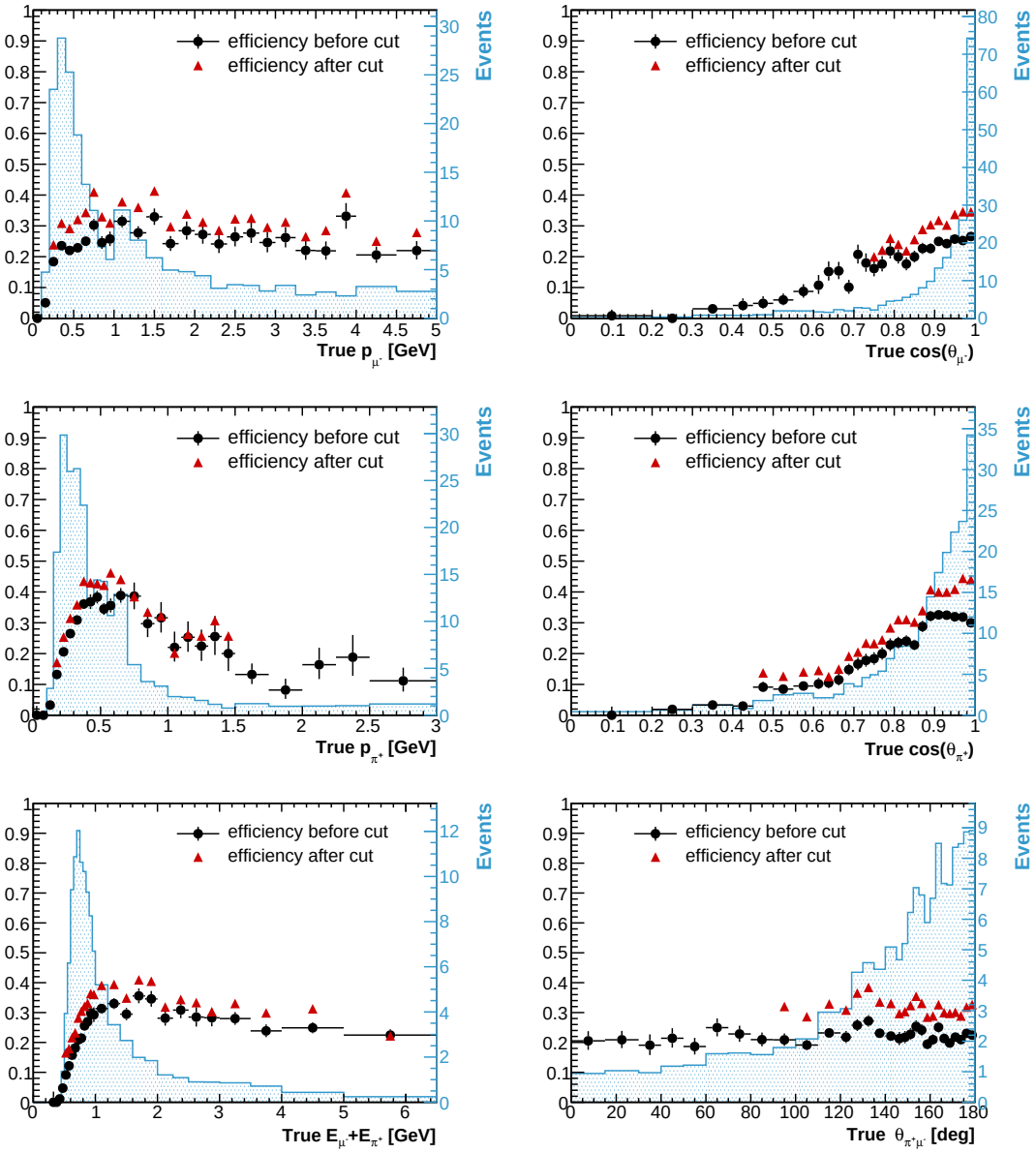

Figure 8.13: Efficiency as a function of different true kinematic variables in the FGD1 selection. From top left to bottom right: p_μ, $\cos(\theta_\mu)$, p_π, $\cos(\theta_\pi)$, $E_\mu + E_\pi$, $\theta_{\pi\mu}$. The black points represent the efficiency before the phase space cuts. The red triangles show the efficiencies once all the kinematic cuts have been applied. Note that the number of true events in each bin is also given in blue for indication.

8.3.2 Binning

The poor statistics is a limiting factor in the choice of binning. Therefore it was decided to have only two bins for each of the variables presented so far. The bins are given in Table 8.6 and the number of total events, coherent and coherent on oxygen events in each bin is given in Figure 8.15. A similar plot for the reweighted MC is shown in Figure 8.16.

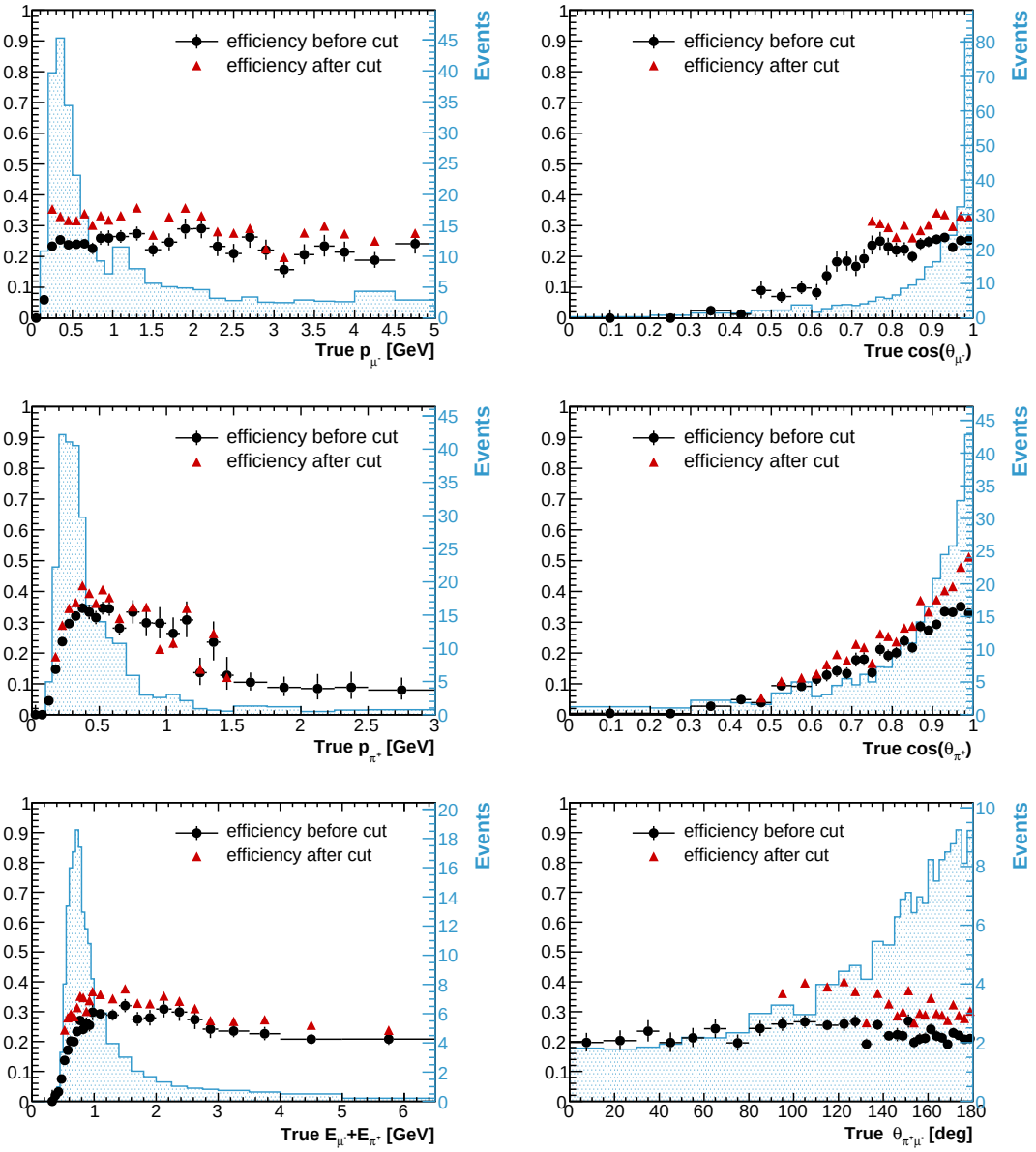

Figure 8.14: Efficiency as a function of different true kinematic variables in the FGD2 selection. From top left to bottom right: p_μ, $\cos(\theta_\mu)$, p_π, $\cos(\theta_\pi)$, $E_\mu + E_\pi$, $\theta_{\pi\mu}$. The black points represent the efficiency before the phase space cuts. The red triangles show the efficiencies once all the kinematic cuts have been applied. Note that the number of true events in each bin is also given in blue for indication.

We can tell from these figures that we have about 70 events in each bin, of which 50 events are coherent interactions.

We have in total four MC samples to study and optimise the extraction of the cross section: NEUT nominal and NEUT reweighted in both FGD1 and FGD2. These samples are the results of a set of selection cuts chosen to optimise the coherent signal/background

Table 8.6: Binning definition.

Variables	Binning
p_{μ^-}	[0.2 - 0.7 - 5] GeV
$\cos(\theta_{\mu^-})$	[0.7 - 0.95 - 1]
p_{π^+}	[0.15 - 0.40 - 1.5] GeV
$\cos(\theta_{\pi^+})$	[0.45 - 0.9 - 1]
E_ν^{reco}	[0.5 - 1.25 - 6.5] GeV
$\theta_{\pi\mu}$	[90 - 155 - 180] deg

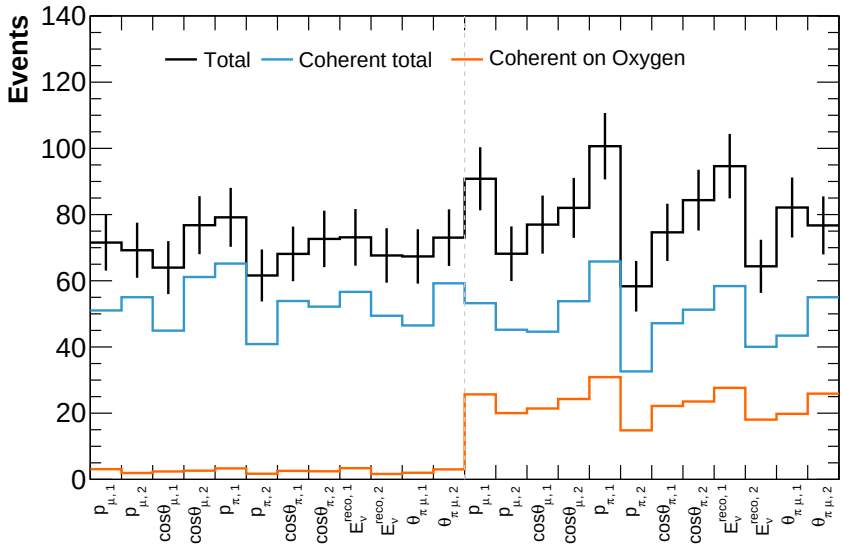

Figure 8.15: Total number of reconstructed events in each bin once the restricted phase space cuts have been applied to the reconstructed variables. The total number of coherent events along with the number of coherent events on oxygen are given, based on the true **NEUT nominal** MC information. The error on the total distribution is statistical only. The 12 leftmost bins represents the FGD1 selection while the 12 rightmost bins are for the FGD2 selection, where the oxygen contribution is more important.

ratio. The NEUT nominal samples contain more events than the NEUT reweighted as Rein-Sehgal overestimates the rate of coherent pion production by a factor 2. Moreover, the FGD1 samples correspond to interaction on carbon only while the FGD2 samples also have interaction on oxygen.

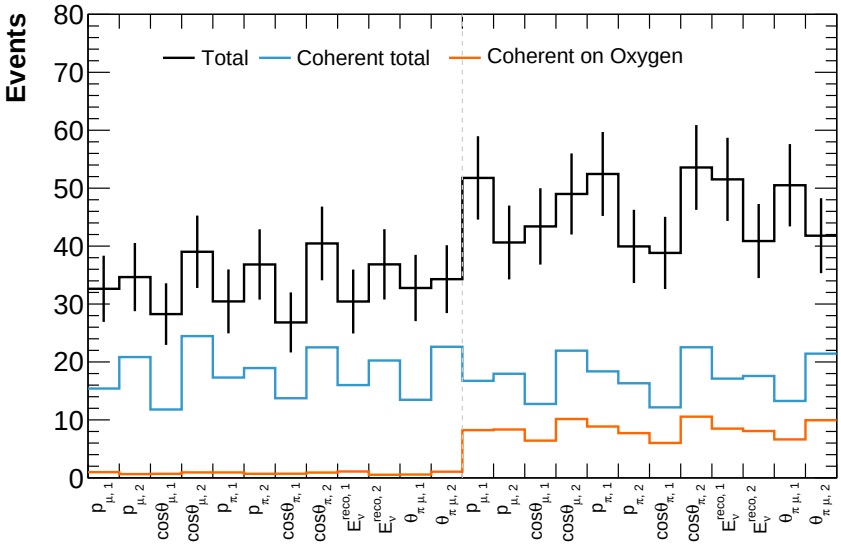

Figure 8.16: Total number of reconstructed events in each bin once the restricted phase space cuts have been applied to the reconstructed variables. The total number of coherent events along with the number of coherent events on oxygen are given, based on the true **NEUT reweighted** MC information (BS model). The error on the total distribution is statistical only. The 12 leftmost bins represents the FGD1 selection while the 12 rightmost bins are for the FGD2 selection, where the oxygen contribution is more important.

9

Cross Section Calculation

This chapter reports the different steps performed to extract the flux-integrated cross section and differential cross sections on carbon and oxygen. We start by describing the general procedure before discussing in-depth studies about the non-coherent backgrounds removal, the calculation of the number of oxygen target nuclei and the performance of the removal of the detector smearing effects (unsmearing).

9.1 Extraction Procedure

Given a variable $X \in \{p_\mu, \cos\theta_\mu, p_\pi, \cos\theta_\pi, E_\nu, \theta_{\pi\mu}\}$, the flux integrated differential cross section on oxygen in bin k reads

$$\left\langle \frac{d\sigma}{dX} \right\rangle_k = \frac{\tilde{N}_k^O}{T_O \, \phi \, \Delta X_k} \tag{9.1}$$

where $\tilde{N}_k^O$ is the efficiency-corrected number of true coherent interaction on oxygen, T_O is the number of oxygen nuclei in the FGD2 fiducial volume, ϕ is the integrated flux and ΔX_k is the width of the true bin k. In order to obtain $\tilde{N}_k^O$, the two FGD samples can be used as FGD2 is composed of pure water and FGD1-like scintillator modules.

$$\begin{aligned}
\tilde{N}_k^O &= \tilde{N}_k^{\text{FGD2}} - \tilde{N}_k^{\text{FGD1-like}} \\
\tilde{N}_k^O &= \tilde{N}_k^{\text{FGD2}} - \sigma_k^{\text{FGD1}} \cdot T^{\text{FGD1-like}} \cdot \phi^{\text{FGD2}} \\
\tilde{N}_k^O &= \tilde{N}_k^{\text{FGD2}} - \frac{\tilde{N}_k^{\text{FGD1}}}{T^{\text{FGD1}} \, \phi^{\text{FGD1}}} \cdot T^{\text{FGD1-like}} \cdot \phi^{\text{FGD2}}
\end{aligned} \tag{9.2}$$

where $\tilde{N}_k^{\text{FGD1(2)}}$ is the number of true events in FGD1 (FGD2), $T^{\text{FGD1(2)}}$ is the number of target nuclei in FGD1(2), while $\phi^{\text{FGD1(2)}}$ is the neutrino flux in FGD1(2). Neglecting the

flux variations between FGD1 and FGD2, $\phi^{\text{FGD1}} = \phi^{\text{FGD2}} = \phi$, we can write

$$\tilde{N}_k^O = \tilde{N}_k^{\text{FGD2}} - \frac{T^{\text{FGD1-like}}}{T^{\text{FGD1}}} . \tilde{N}_k^{\text{FGD1}} \tag{9.3}$$

The estimation of $T^{\text{FGD1-like}}$, T^{FGD1} and T_O is discussed in Section 9.3. In order to obtain the true event numbers $\tilde{N}$, the reconstructed signal distribution is unsmeared using the unsmearing (or unfolding) matrix U_{kl} built upon the MC predictions, where the indices k and l indicate the true and reconstructed bins respectively.

$$\tilde{N}_k = \frac{U_{kl} N_l^{\text{reco}}}{\varepsilon_k} \tag{9.4}$$

This step is detailed in Section 9.4. However, before unsmearing, the non-coherent backgrounds have to be removed from both FGD1 and FGD2 reconstructed distributions obtained at the end of the previous chapter.

9.2 Backgrounds

The backgrounds in both FGD selections are constrained by sidebands, which are control samples populated with background-like events which do not contain any events from the signal selection. The comparison of the data and MC in sidebands allows to extract normalisation factors α_i that are used to correct the different background rates in the MC selection, and therefore provides a data driven constraint on the background that reduces the model dependance.

We consider two ways of removing the background events from our signal selection: background subtraction (BG) and purity correction (PC). Using the same notation as in equation (9.4) where N_l^{reco} is the number of reconstructed signal events in bin l, the background subtraction method gives:

$$\begin{aligned} N_l^{\text{reco}} &= N_l^d - B_l \\ N_l^{\text{reco}} &= N_l^d - \left(\sum_i \alpha_i . B_l^i + \sum_j B_l^j \right) \end{aligned} \tag{9.5}$$

where N_l^d is the number of measured events in the data and B_l is the number of background events in the MC, which can be decomposed in number of constrained background B_l^i and un-constrained background B_l^j. The purity correction method gives a more complicated equation. Assuming p is to the signal purity, it corresponds to 1 minus the background purity. The latter is then expressed in terms of the number of background events and the total events in the MC $N_l^{\text{tot}} =$.

$$\begin{aligned} N_l^{\text{reco}} &= N_l^d \times p \\ N_l^{\text{reco}} &= N_l^d \times \left(1 - \frac{\sum\limits_i \alpha_i . B_l^i + \sum\limits_j B_l^j}{N_l^{\text{tot}} - \sum\limits_{k=i,j} B_l^k + \sum\limits_i \alpha_i . B_l^i + \sum\limits_j B_l^j} \right) \\ N_l^{\text{reco}} &= N_l^d \times \left(1 - \frac{\sum\limits_i \alpha_i . B_l^i + \sum\limits_j B_l^j}{N_l^{\text{tot}} + \sum\limits_i (\alpha_i - 1) . B_l^i} \right) \end{aligned} \tag{9.6}$$

The denominator in the right side of equation (9.6) is the total number of events (signal and background) renormalised in order to take into account the variations due to the scale factors.

We see from (9.5) that the background subtraction approach relies on the MC predictions to estimate the number of background events to remove B_l, which remains independent from N_l^d. B_l being constrained by the sidebands, the model dependence introduced is minimised. However, for low statistic samples, an over-estimation of B_l could lead to a negative number of reconstructed signal events N_l^{reco}, thus an unphysical negative cross section. This problem is avoided in the purity correction method as N_l^{reco} always remains positive: it corresponds to the number of events in the data scaled by the purity $p > 0$. Unlike background subtraction, the background estimate now depends on the measured data.

9.2.1 Sidebands Definition

Two sidebands are used in this analysis: one for each FGD. The two selections of the sidebands are similar to the signal selections up to the FGD multiplicity cuts. Indeed, to get better statistics in the sidebands, there is no requirement on the number of tracks in the FGDs. Then only events with high vertex energy are considered: more than 14 MeV

in FGD1 and more than 7 MeV in FGD2. These cuts ensure that there is no overlap with the signal selection samples (see Table 8.3). The events are also asked to have a $|t|$ value below 0.5 GeV^2. This cut is to ensure that the sidebands have the same phase space coverage than the signal samples. Indeed, high $|t|$ events are mostly DIS, where the muon and pion momentum and angles can be much larger than in the coherent case. The kinematic distributions of the two sidebands before any phase space reduction are available in appendix C. The composition of the two sidebands in terms of interaction types in the restricted phase space is given in Table 9.1. For comparison, the contribution of each background from the signal region is also given.

Table 9.1: Composition of the FGD1 and FGD2 sidebands after the restricted phase space cuts for reconstructed variables only. The backgrounds in the signal selection broken down by true reactions in the reduced reconstructed phase space is also given

	FGD1		FGD2	
	Sideband	Background	Sideband	Background
N_{evts}	212.7	34.0	166.9	58.9
COH	2.07 %	-	3.85 %	-
RES	55.0 %	56.0 %	51.4 %	69.3 %
DIS	30.3 %	10.1 %	30.9 %	7.75 %
CCQE	0.29 %	0.00 %	0.33 %	0.17 %
out of FV	2.13 %	2.78 %	3.13 %	2.21 %
Other (total)	10.1 %	31.1 %	10.3 %	20.6 %
Other ($\bar{\nu}_\mu$)	1.95 %	20.6 %	2.05 %	11.7 %
Other (NC)	7.17 %	9.65 %	7.32 %	7.93 %
Other (2p-2h)	0.30 %	0.32 %	0.21 %	0.54 %
Other ($\nu_e, \bar{\nu}_e$)	0.68 %	0.46 %	0.67 %	0.37 %

We observe that the composition in terms of contributing processes are rather different: the sidebands contain in general more DIS interactions and less $\bar{\nu}_\mu$ interactions than the actual in-signal background. For FGD2, we also notice a lower percentage of resonant interaction in the sideband. These differences are worth mentioning but they should not affect the estimation of the background as each interaction modes can be fitted independently. Finally, the signal contamination in the sidebands is below 4 %.

9.2.2 Reliability Checks

In order to make sure that the sidebands correspond to background-like events, a comparison between the sidebands and the in-signal backgrounds is performed. The goal is to check that the shapes of the distributions are similar and that the sidebands have a similar phase space coverage that the background. Both sideband and background distributions have been area normalised and plotted against each other for the resonance channel in Figure 9.1 and 9.2. Because of the poor statistics in the other channels, it is hard to do such a comparison as the binning needs to be rather fine to distinguish the shape. The shapes of the two distributions look indeed similar. The relative difference per bin is always smaller than 50 %, except for the high pion momentum bins where the sideband statistics are too small.

It is also relevant to compare the MC with the data in the sidebands as the scale factors to constrain the in-signal background will be given based on that comparison. Figure 9.3 shows the NEUT nominal and the data with statistical error only for each of the bin described by Table 8.6. The few discrepancies we observe can be attributed to the mis-modelling of the resonance or DIS interactions as these two channels contribute to more that 80 % of the sideband samples. By fitting these two channels, we expect to reduce these discrepancies and to constrain the resonance and DIS backgrounds in the signal regions.

9.2.3 Fit Performances

Given the statistics and the composition of the sidebands, it seems relevant to only fit the resonance and DIS channels and let the other reactions unconstrained. The purpose of such a fit is to extract a scale factors α_k for each background $k \in \{\mathrm{RES}, \mathrm{DIS}\}$ by minimising the likelihood function $L(\alpha_k)$ given in (9.7).

$$\sum_k L(\alpha_k) = N^{\mathrm{sb}}_{\mathrm{MC}} - N^{\mathrm{sb}}_{\mathrm{data}} \times \ln(N^{\mathrm{sb}}_{\mathrm{MC}}) \tag{9.7}$$

where $N^{\mathrm{sb}}_{\mathrm{MC}}$ and $N^{\mathrm{sb}}_{\mathrm{data}}$ are the total number of events in the MC and data sideband respectively. $N^{\mathrm{sb}}_{\mathrm{MC}}$ can further be decomposed as the sum of its fitted categories so that

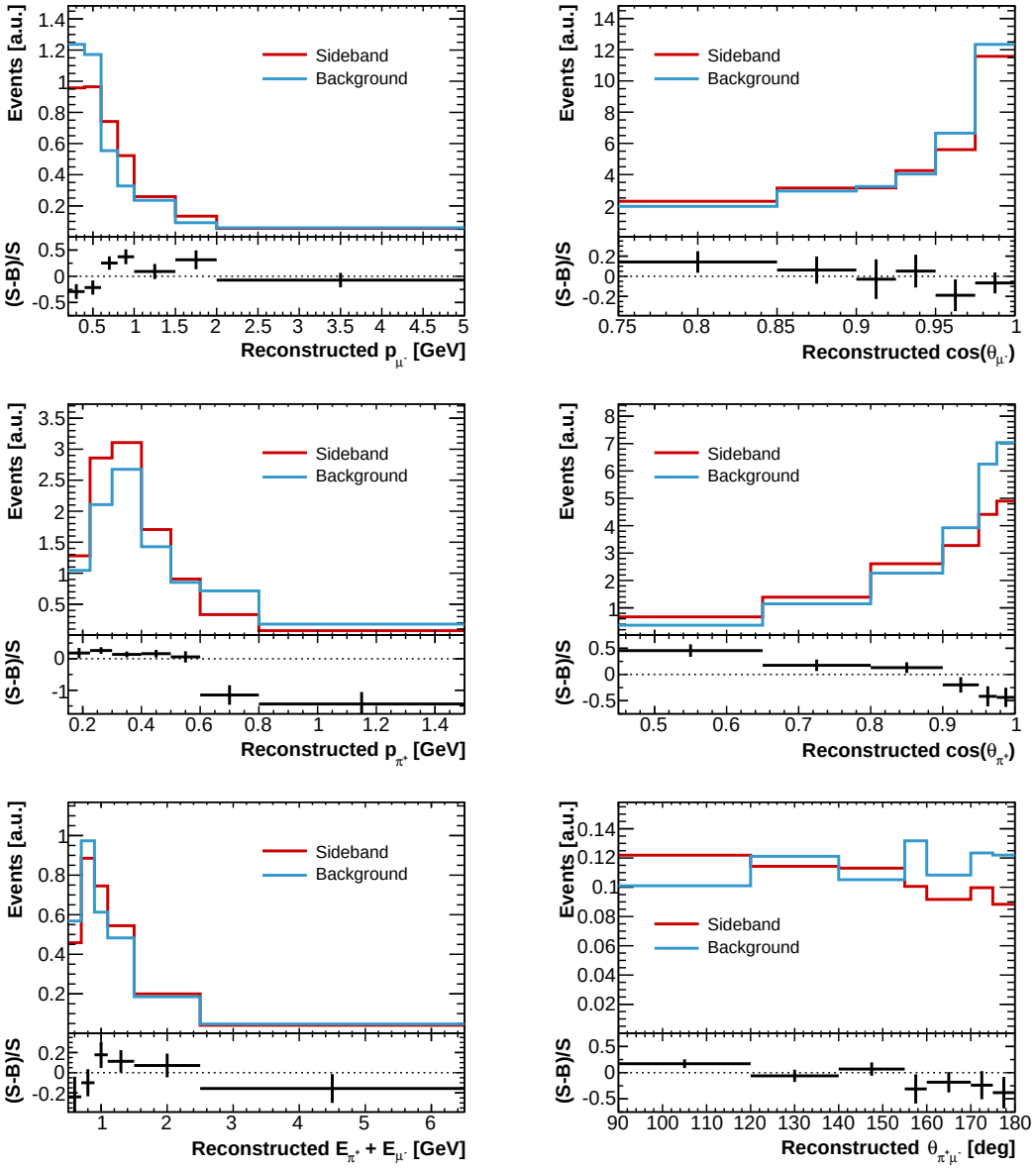

Figure 9.1: Shape comparison between the FGD1 sideband (S) and background (B) for the resonant contributions in the reduced phase space. The two distribution are area normalised, hence the arbitrary unit (a.u.). The relative difference is also given in the bottom pad.

the scaling factors appears explicitly:

$$N_{\mathrm{MC}}^{\mathrm{sb}} = \frac{\mathrm{POT}_{\mathrm{data}}}{\mathrm{POT}_{\mathrm{MC}}} \times \sum_{i \in \mathrm{RES,DIS}} \alpha_i . N_i^{\mathrm{sb}} \tag{9.8}$$

where N_i^{sb} is the number of resonant or DIS events in the sideband sample. A perfect data/MC agreement in the sideband would therefore gives $\alpha_i = 1$. Negative values of α_i

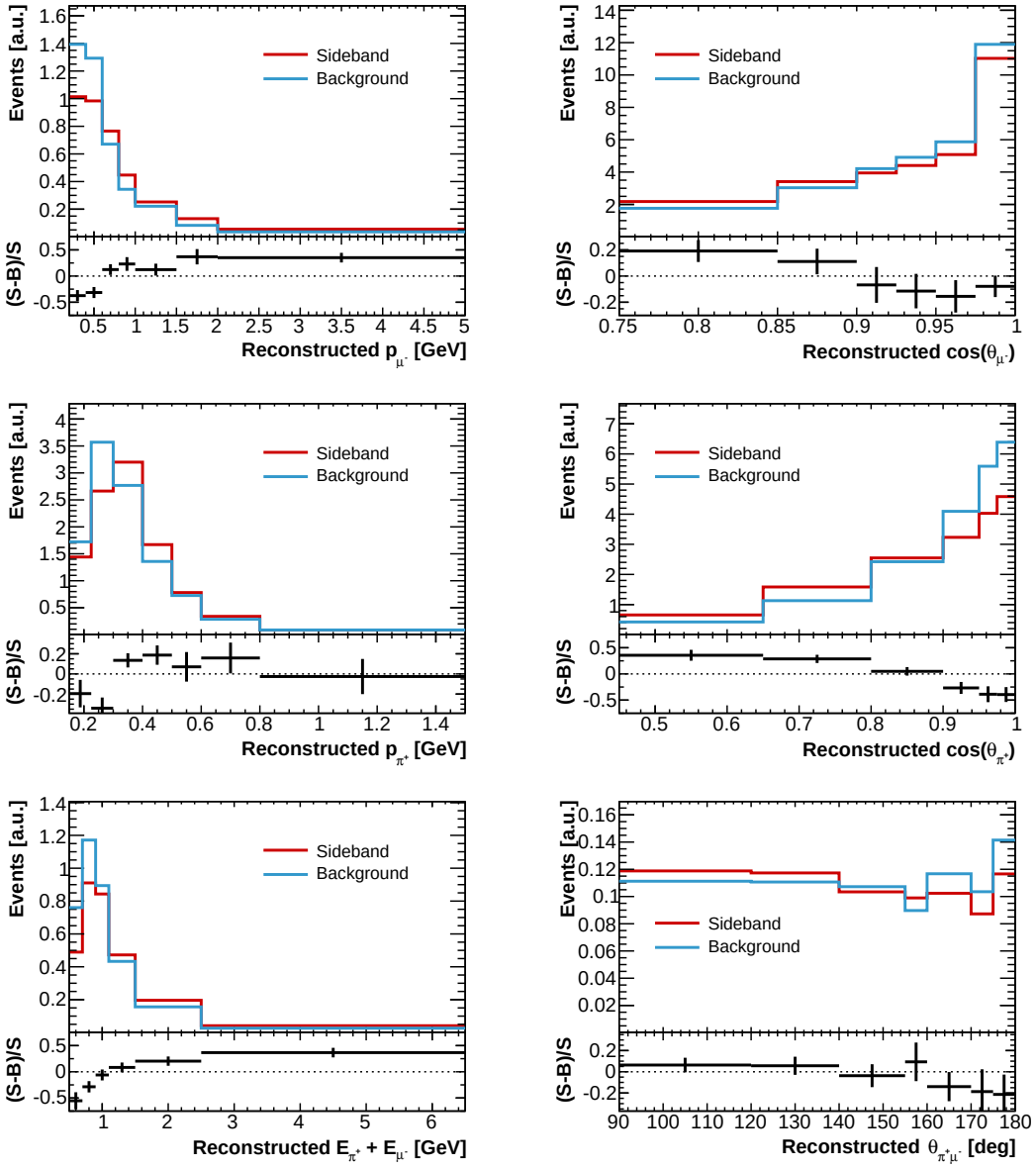

Figure 9.2: Shape comparison between the FGD2 sideband (S) and background (B) for the resonant contributions in the reduced phase space. The two distribution are area normalised, hence the arbitrary unit (a.u.). The relative difference is also given in the bottom pad.

would introduce a strong bias in the number of reconstructed signal events. Therefore the condition $\alpha_i > 0$ is required.

9.2.3.1 Convergence Studies

We test here the convergence performance of the fit. Because the analysis has very limited statistic, only the RES and DIS backgrounds are fitted for 2000 toy experiments where we

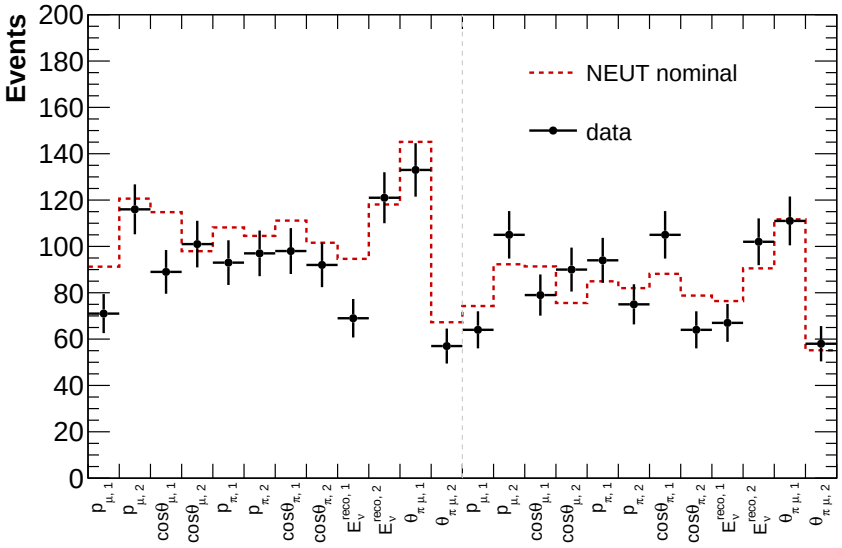

Figure 9.3: Comparison between data and MC NEUT nominal event numbers in each bin of the sidebands after phase space cuts. Leftmost bins are for FGD1 while rightmost bins are for FGD2. The error on the data is statistical only.

vary the number of fake data events in each bin l according to a Poisson distribution:

$$P(N_l^{\text{throw}}) = e^{-N_l^{\text{nom.}}} \times \frac{(N_l^{\text{nom.}})^{N_l^{\text{throw}}}}{N_l^{\text{throw}}!} \tag{9.9}$$

Each variable is investigated independently. Several fake data (FD) tests are performed in order to simulate the potential variations in number of events between the MC and the real data. These fake data samples correspond to different reweights of the NEUT nominal predictions (see Section 7.3). The resonant parameters C_A^5 and M_A^π and the parameter that control the normalisation and shape rate of DIS δ_{DIS} are modified as described by Table 9.2.

While the factors C_A^5 and M_A^π are directly related to the resonant cross section model briefly described in Section 3.1.2, the parameter δ_{DIS} is used to change the shape and normalisation of the DIS predictions as a function of neutrino energy: $\sigma_{\text{DIS}} \rightarrow (1 + \frac{\delta_{\text{DIS}}}{E_\nu})\, \sigma_{\text{DIS}}$. A comparison between these fake data and the NEUT nominal predictions in the sidebands is given in Figure 9.4.

We give the scale factor distributions and their correlation obtained while fitting FD2 with NEUT nominal in Figure 9.5 These scale factors are extracted with the pion momentum in

Table 9.2: Variations of the C_A^5 and M_A^π parameters (dials) with respect to the nominal and value of δ_{DIS} for the different fake data. The σ represents the 1σ error of the parameter. It corresponds to 0.24 for C_A^5 and 0.15 for M_A^π.

Parameters	C_A^5	M_A^π	δ_{DIS}
NEUT nominal	1.0	1.0	0.4
NEUT fake data 1 (FD1)	+ 0.3 σ	+ 0.2 σ	+ 0.3
NEUT fake data 2 (FD2)	- 0.5 σ	- 0.2 σ	- 0.3
NEUT fake data 3 (FD3)	- 0.5 σ	- 0.5 σ	+ 2.0
NEUT fake data 4 (FD4)	- 4 σ	+ 2 σ	+ 3.0

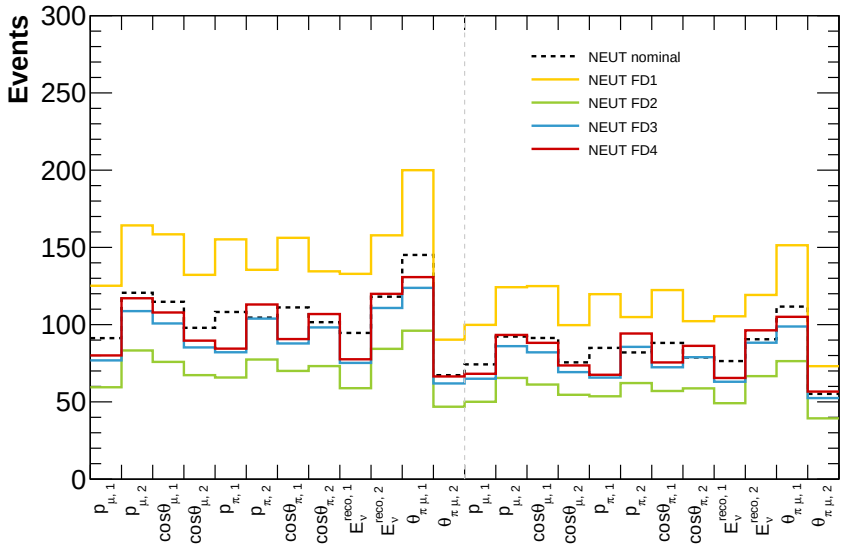

Figure 9.4: Comparison of the number of total events in each bin for different fake data and MC NEUT nominal predictions, in the sidebands after phase space cuts. Leftmost bins are for FGD1 while rightmost bins are for FGD2. The fake data are numbered according to Table 9.2.

FGD1. We observe that, as the fake data 2 and the NEUT nominal have different resonant and DIS predictions, the scale factors are not centred around 1. Moreover, we see on the right plot that they are anti-correlated.

We observe that for less than 2.0 % of the throws, the fit does not converge and sets the RES or DIS scale factor at the lower limit 0. This is one drawback of using a multi-category sideband fit with relatively low statistics when the backgrounds are not well understood. One needs to make sure that the percentage of fit failure remains low. For this purpose, all the variables have been tested for the 4 fake data samples and the percentage of fit

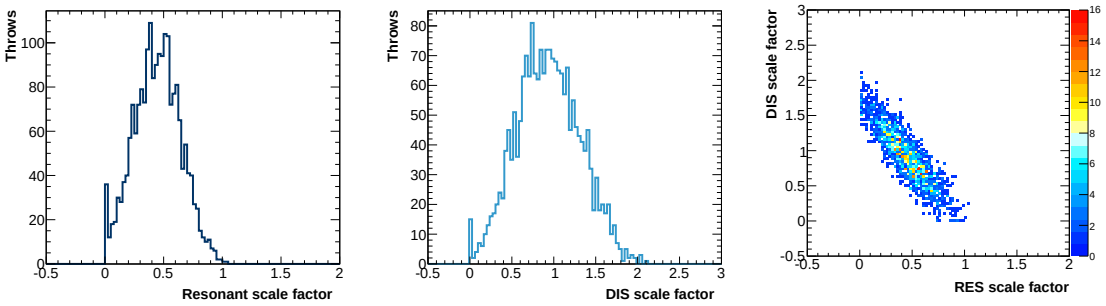

Figure 9.5: Resonant and DIS scale factors distributions for 2000 statistical toy experiments (throws) and their correlations. These scale factors are calculated by a sideband fit to fake data 2 with the pion momentum distribution in FGD1.

failure is reported in Figure 9.6. In the fake data studies, there is a clear trend in favour of the pion variables and the sum of pion and muon energy (here labelled as E_ν^{reco}). It comes from the fact that the pion momentum and the energy sum are more powerful to discriminate between resonant and DIS interactions. Indeed a low neutrino energy and/or low pion momentum would be more likely to characterise a baryonic resonant while high E_ν and/or p_π correspond to DIS interaction. The more extreme is the parameters variation, the less the fit converges for the pion momentum. However, E_ν^{reco} keeps showing good convergence rate. Therefore the scale factor of this variable will be use to constrain the resonant and DIS backgrounds for any other variable as well. In other words, the RES and DIS background constraints will come from the E_ν^{reco} fit only. Finally, the same trends are observed in the real data, where we see that the best fitting performances are achieved with E_ν^{reco} too.

9.2.3.2 Scale Factor Values

To ensure that the scale factors extracted by this fit are relevant, a fake data test is performed where the NEUT nominal is used as MC. The fake data was tuned such that it contains twice as much resonant and three times more DIS interactions than in the MC. This study is performed with both FGD1 and FGD2 selections and the scale factors are extracted by fitting the backgrounds in the $E_\nu^{\text{reco}} = E_{\pi^+\mu^-}$ distribution. The results are presented in Figure 9.7. As expected, the resonant and DIS scale factors follow a gaussian distribution centred around 2 and 3 respectively[i]. We also present the background

[i]Because the scale factors central value is larger than 1, there is no convergence problem here.

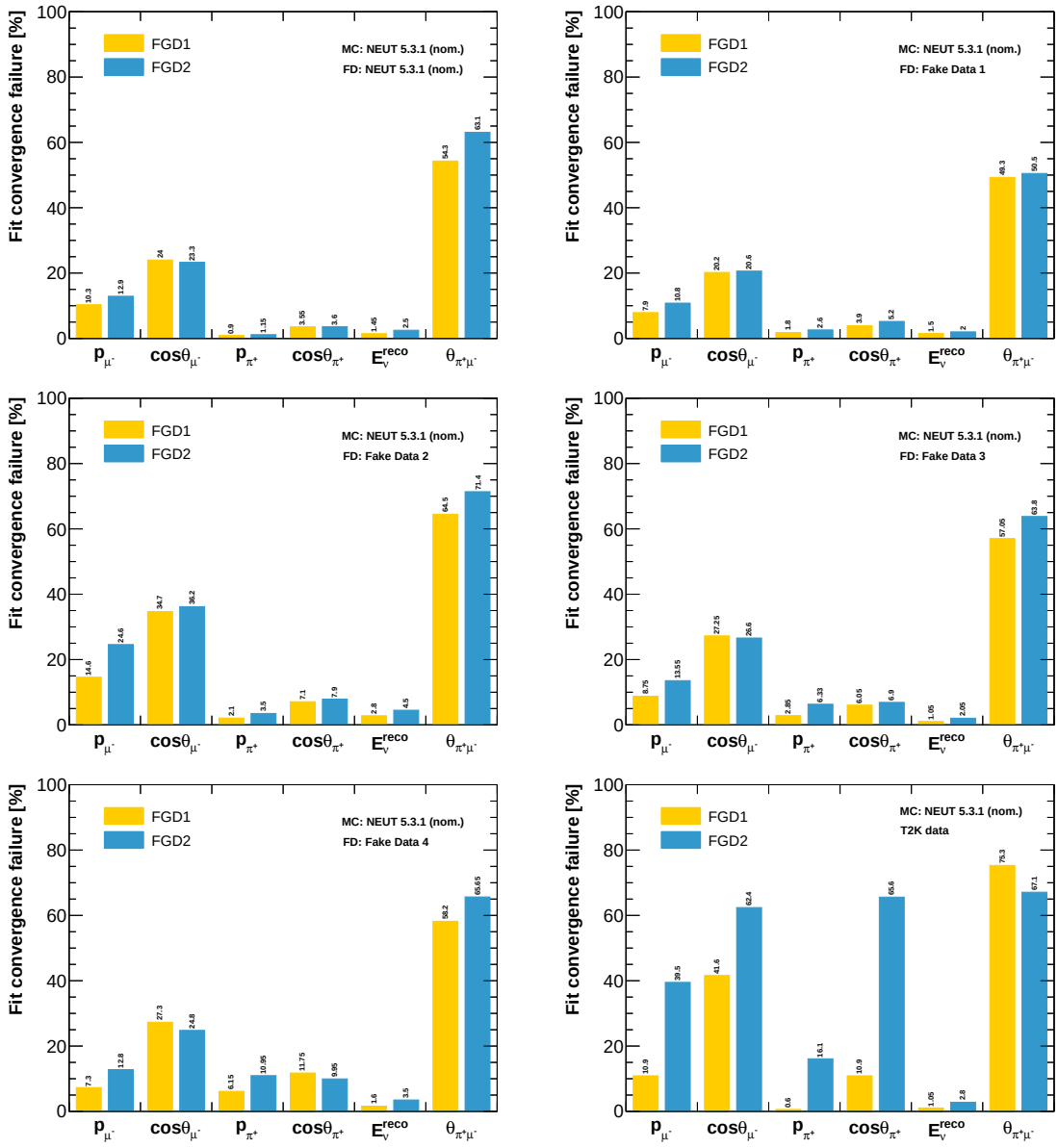

Figure 9.6: Percentage of fit convergence failure calculated for 2000 statistical throws given for each variable, each FGD and each Fake data. The bottom right plot is for real data.

distribution before and after the constraint in top right of Figure 9.7 : the backgrounds seem to be scaled properly.

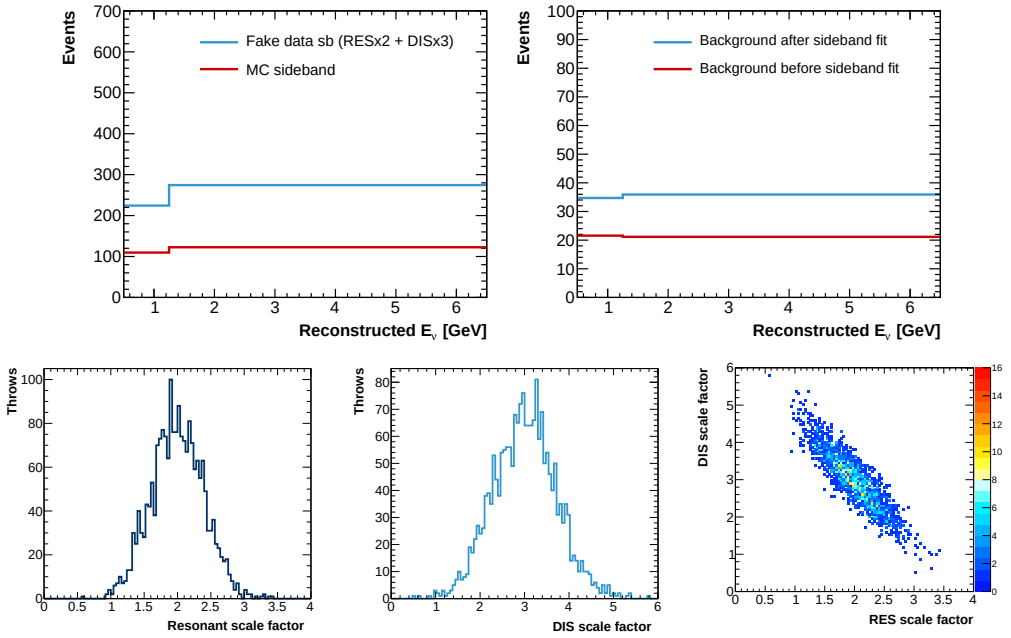

Figure 9.7: Top: results of the background constraint imposed by the sideband fit. Bottom: Scale factor distributions and correlation.

9.3 Number of Targets

The calculation of the exact number of targets in both FGDs results from an accurate consideration of the geometry and the material densities used in the building of the detector. This is detailed in several T2K internal notes[ii] and we summarised their contents here.

9.3.1 FGD1 Composition

The FGD1 is composed of alternate xy scintillator modules. An x layers consists of 192 scintillator bars glued to a thin sheet of G10 fibreglass (the bars are not glued to each other). A y layer is then glued to this x layer with Plexus MA590 adhesive. A typical xy module therefore contains:

- Scintillator bars made of 99 % polystyrene (CH) doped with PPO ($C_{15}H_{11}NO$) weighted by 1 %. The composition of the TiO_2 coating and the hole for the wavelength shifting fibre ere account for as well.

[ii] T2K Technical notes 091, 122 and 198

- G10 sheets on the front and back of the module. The composition of these sheets can vary according to the manufacturer. Different combinations of SiO_2 and epoxy have been considered.

- Wavelength-shifting fibres, made of 100 % polystyrene

- The Plexus MA590 adhesive composed of 27.8 % C, 62.5 % O, 8.4 % H and 1.2 % N.

The composition of one *xy* module is given in Table 9.3 in terms of areal density ρ_a of each nucleus.

9.3.2 FGD2 Composition

The FGD2 composition is trickier to evaluate due to the water layers. There are six water panels in FGD2, each glued to a *xy* module similar to the FGD1 ones. The water panels are made of hollow sheets of polycarbonate sealed together with HE 1908 polyurethane adhesive. A skin of polypropylene was glued to each side of the panel with CLR 1390/CLH 6025 epoxy resins to improve the balance of each vessel. Acrylic bars were then glued to the corners and side of the vessels such that the width of the water module match with the one of the *xy* module. Additional structures were added for integrating the water panels to the *xy* modules. The FGD2 empty panel (without water) is then broken down into three categories: FGD2 *xy* module-like, water-like and remnant. All the carbon content of the empty panel was used in the FGD2 *xy* module-like and the other element were scaled by 0.228 (= 422/1848). Note that the numbers in Table 9.3 are for the most upstream water panel. Other panels can have a slightly different structure but the same method is applied.

9.3.3 Fiducial Volume Cuts

The number of target nuclei required in the cross section calculation, as defined in Section 9.1, are derived from the areal densities and fiducial volume:

$$T = \mathcal{N}_A \times V_{FV} \times \frac{\rho_a}{\Delta z} \tag{9.10}$$

Table 9.3: Elemental composition of FGD modules in terms of areal densities ρ_a [mg.cm^{-2}] for each element

	FGD1	FGD2 empty panel			FGD2 water
Element	xy module	xy module-like	water-like	remnant	
C	1848 ± 9.2	422 ± 7	0	0	0
O	79.4 ± 4.8	18.1 ± 2	74.8 ± 2.7	0	1967.4 ± 3.3
H	157.9 ± 2.1	36.1 ± 1	8.9 ±1	-1.0 ±1.1	248.0 ± 0.4
Ti	35.5 ± 2.1	8.1 ± 1.3	0	-8.1 ± 1.3	0
Si	21.8 ± 4.3	4.9 ± 1	0	6.3 ± 1.7	0
N	3.1 ± 1.2	0	0	0	0
Mg	neg.	neg.	0	6.8 ± 0.9	0
Total	2147 ± 14.4	490 ± 8	84 ± 7	4.0 ± 13.9	2215.4 ± 3.7

where $\mathcal{N}_A = 6.022 \times 10^{23}$ mol^{-1} is the Avogadro number, V_{FV} is the fiducial volume given by Table 8.2 and Δz is the width of one xy module for FGD1 or one xy module + water panel for FGD2. We obtain the following numbers:

- $T^{\text{FGD1}} = 3.567{\times}10^{28}$ nuclei targets of which 86 % are Carbon nuclei.
- $T^{\text{FGD1-like}} = T^{\text{FGD1}xy} + T^{\text{FGD2 }xy\text{-like}} = 2.079{\times}10^{28}$ target nuclei.
- $T_O = T^{\text{FGD2 water}} + T^{\text{FGD2 water-like}} = 1.864{\times}10^{28}$ target nuclei of which 88 % are Oxygen nuclei.

The number of targets coming from the remnant category of the FGD2 water panel is three order of magnitude smaller than T_O. It was decided that the contribution from these target can be neglected. From the previous calculation, we observe that both carbon and oxygen cross section measurements are actually performed on a composite target material made of 86 and 88 % of carbon and oxygen, respectively.

9.4 Unsmearing Tests

As described by equation (9.4), unfolding is the process that allows to recover the true number of events in bin k, $\tilde{N}_k$, from the reconstructed number of event in bin l, N_l. In this step we also include the efficiency correction, dividing by ε_k. The values of these

efficiencies are given in Table 9.4 in case the true MC is the nominal NEUT and in table 9.5 if the true is the NEUT reweighted to BS model. The errors on those efficiencies are at the percent level.

Table 9.4: Efficiencies ε_k in each true bin for each variables in FGD1 and FGD2 given the MC is the nominal NEUT.

Sample	Bin	p_μ	$\cos\theta_\mu$	p_π	$\cos\theta_\pi$	$E_\mu + E_\pi$	$\theta_{\pi\mu}$
FGD1	1	0.30	0.29	0.28	0.25	0.30	0.33
	2	0.34	0.34	0.41	0.42	0.34	0.31
FGD2	1	0.33	0.31	0.30	0.24	0.32	0.34
	2	0.30	0.32	0.35	0.44	0.31	0.29

Table 9.5: Efficiencies ε_k in each true bin for each variables in FGD1 and FGD2 given the MC is NEUT reweighted to BS model.

Sample	Bin	p_μ	$\cos\theta_\mu$	p_π	$\cos\theta_\pi$	$E_\mu + E_\pi$	$\theta_{\pi\mu}$
FGD1	1	0.39	0.36	0.36	0.32	0.38	0.42
	2	0.40	0.41	0.43	0.44	0.40	0.37
FGD2	1	0.41	0.38	0.38	0.28	0.40	0.43
	2	0.35	0.37	0.37	0.44	0.35	0.34

The unfolding matrix is built using the D'Agostini method, also known as bayesian unfolding [148, 149], where in our case the so-called "causes" correspond to the true variables and the "effects" are the reconstructed variables. The detector mis-reconstruction and inefficiencies will smear the correspondence between true and reconstruction variables. Using the MC predictions, one can calculate the smearing matrix $S_{lk} = P(N_l|\tilde{N}_k)$, which represents the probability of having $\tilde{N}$ events in the true bin k being reconstructed as N events in bin l, therefore this accounts for bin migration. Bayes' theorem then gives the expression of the posterior probability, or unfolding matrix:

$$U_{kl} = P(\tilde{N}_k|N_l) = P(N_l|\tilde{N}_k)\frac{P(\tilde{N}_k)}{P(N_l)} \tag{9.11}$$

where $P(\tilde{N}_k)$ is the probability of having $\tilde{N}$ events in the true bin k

$$P(\tilde{N}_k) = \frac{\tilde{N}_k}{\sum_k \tilde{N}_k} \tag{9.12}$$

and $P(N_l)$ is a prior estimate of the probability of finding N events in the reconstructed bin l

$$P(N_l) = \sum_k S_{lk} P(\tilde{N}_k) \tag{9.13}$$

In the case of this analysis, we only have two bins, therefore, multiplying U_{kl} to the two dimensional vector containing the number of reconstructed events would give us a first estimate of the number of true events per bin. This estimate could then be inserted in (9.13) to start an iterative process. The unfolding matrices for the FGD1 selection are given in Figure 9.8 and for FGD2 in Figure 9.9. They are calculated based on the NEUT nominal predictions. All of the six matrices are mostly diagonal, which is good as we expect a small amount of bin migration. Moreover the amount of event migration in bins that are outside of the phase space remains very low ($< 1\,\%$). We also normalise the matrices column by column, so that for a given reconstructed value we are sure to get its corresponding true value. Additionally, we give the same matrices calculated with the Berger-Sehgal predictions in Figures 9.10 and 9.11. Several iterations were tested for both background treatments with different fake data. In the case of background subtraction, the NEUT nominal is chosen to be the MC simulation and both NEUT nominal and NEUT reweighted to Berger-Sehgal predictions are used as fake data. Because the purity correction relies more on MC predictions, the MC was chosen to be the NEUT reweighted, and both NEUT nominal and NEUT reweighted were tested as fake data. Ideally, one would select different MC subsamples in the efficiencies calculation and in the unfolding, however splitting the samples here would increase the errors on the efficiencies and increase the MC statistical error on the cross section results. However this will be considered in the upgrade of the analysis using the recently acquired ND280 data.

The results are presented in Figure 9.12 where the error bars are statistical only and the subtraction between FGD1 and FGD2 selection is performed. In order to interpret these plots, we assume that the effect of the sideband constraint does not have any influence on the results as both MC and fake data have the same background predictions and the

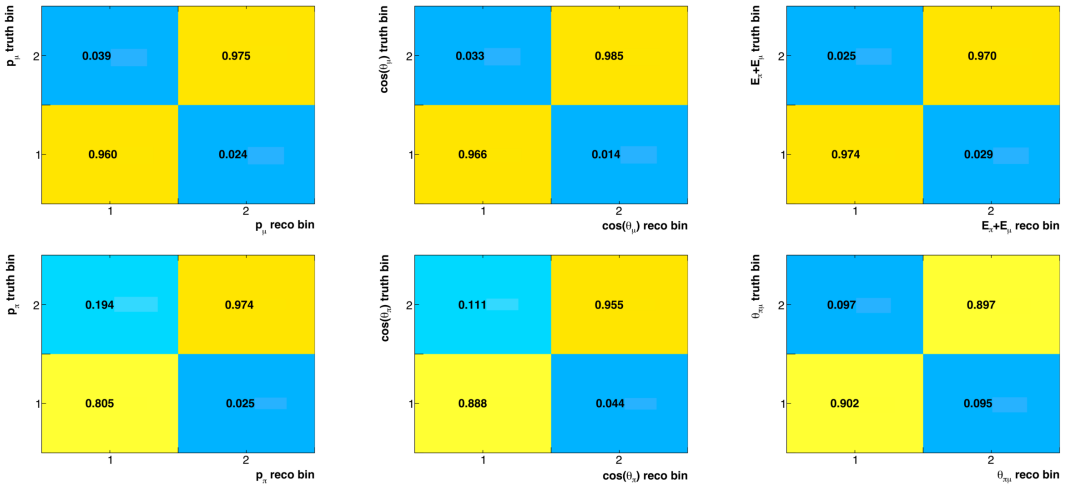

Figure 9.8: Unfolding matrices for the FGD1 selection for each of the kinematic variables calculated with NEUT nominal.

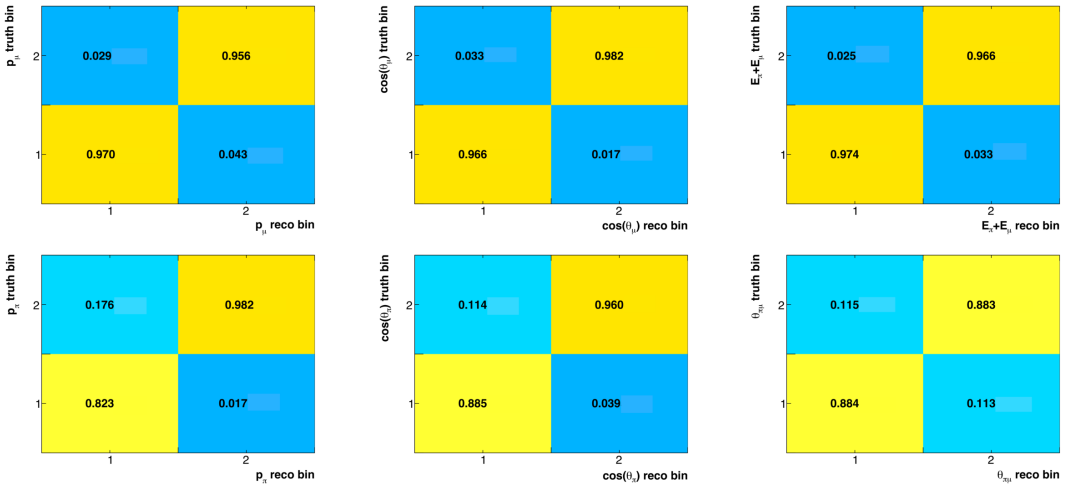

Figure 9.9: Unfolding matrices for the FGD2 selection for each of the kinematic variables calculated with NEUT nominal.

sideband fit performances have already been discussed.

- When the MC and fake data correspond to the same sample, the truth information is well recovered by both background subtraction and purity correction methods, as shown by the two leftmost plots on Figure 9.12. It is expected since the signal definition is unchanged and the unfolding matrix is built on the MC, and therefore fake data.

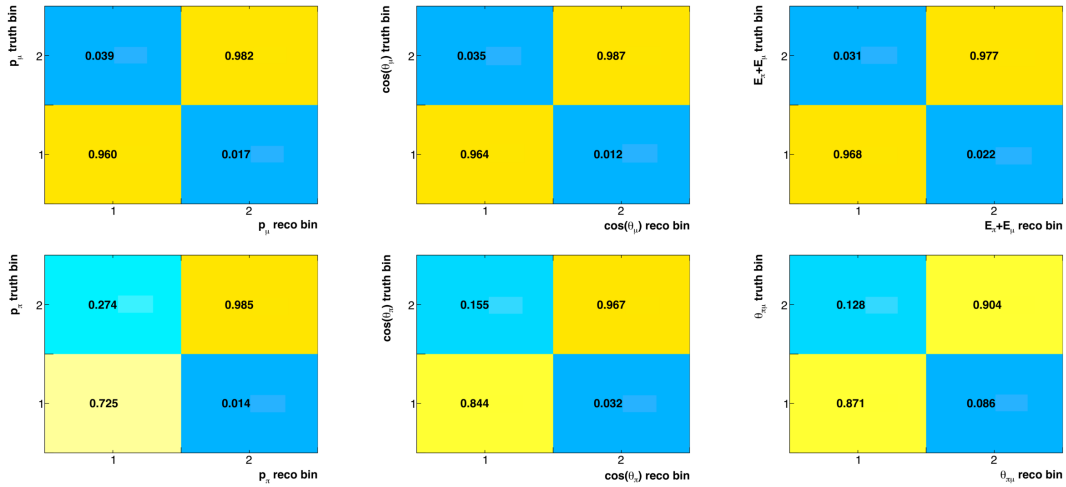

Figure 9.10: Unfolding matrices for the FGD1 selection for each of the kinematic variables when the MC predictions follow the Berger-Sehgal model.

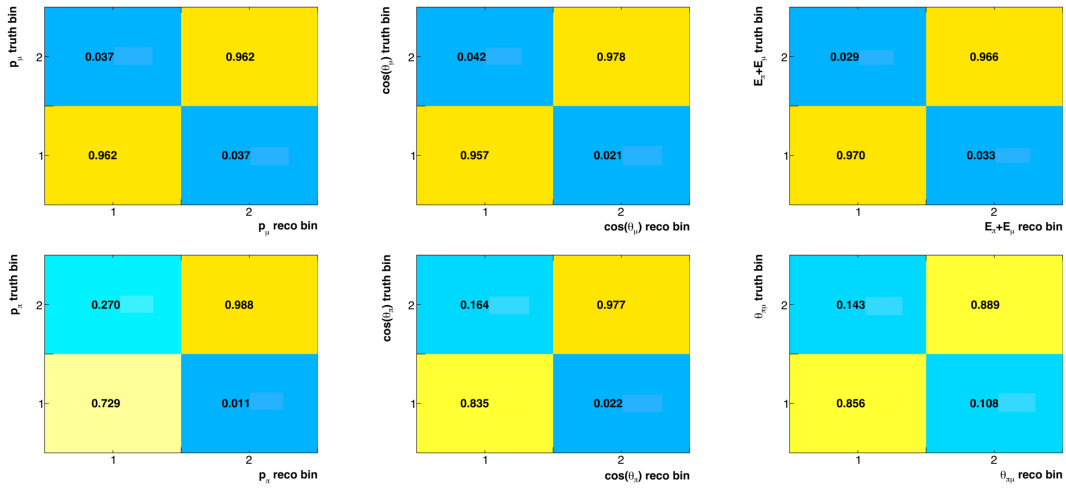

Figure 9.11: Unfolding matrices for the FGD2 selection for each of the kinematic variables when the MC predictions follow the Berger-Sehgal model.

- In the case where the fake data differs from the MC, we observe better results by the background subtraction. As we already discussed, the number of signal in the (fake) data is independent from the background estimate in the background subtraction, which gives a less model dependent result.

$$N^{\text{reco}} = N^{FD} - Bg^{MC} = Sig^{FD} + Bg^{FD} - Bg^{MC} = Sig^{FD} \tag{9.14}$$

However, the unfolding matrix requires the truth MC information which is using a

different signal model than the FD, which is why a small bias is introduced during the unfolding process.

For purity correction, there is a strong correlation between the background estimate and the number of reconstructed fake data events. The purity p is evaluated based on the MC, which predictions follow Berger-Sehgal in our example. Then this purity is multiplied by the number of fake data, which is largely overestimated as it corresponds to the Rein-Sehgal model.

$$N^{\text{reco}} = N^{FD} \times p = (Sig^{FD} + Bg^{FD}) \times \frac{Sig^{MC}}{Sig^{MC} + Bg^{MC}} \neq Sig^{FD} \tag{9.15}$$

Therefore, if the model used for the signal is not describing the data very well, the background should rather be subtracted instead of correcting the signal with purity factor. One should keep in mind that the two signal models we use are drastically different. According to MINERvA result, the data should agree better with the Berger-Sehgal predictions, therefore the disagreement observed in the bottom right plot between the "true" and unfolded data might be reduced.

- For the purity correction, we notice smaller statistical errors than in the background subtraction case. This can be explained with the naive approach: purity correction just scales the errors while background subtraction adds them. The propagation of statistical error will be discussed in more detail in Chapter 10.

However, we can see on Figure 7.16 that in the case of MINERvA, the Berger-Sehgal model under-estimates the data in most of the bins of the pion. Hence an additional fake data test was performed where the background subtraction was used and the fake data corresponds to the Berger-Sehgal prediction with an increase of the overall normalisation by 50 %. This test was inconclusive and the unfolded results still show a too big statistical error.

Given the size of the statistical error bars and the performance of the unfolding, different approaches are considered:

1 Set an upper limit on the oxygen cross section using a background subtraction treatment and the NEUT reweighted to the Berger-Sehgal model predictions.

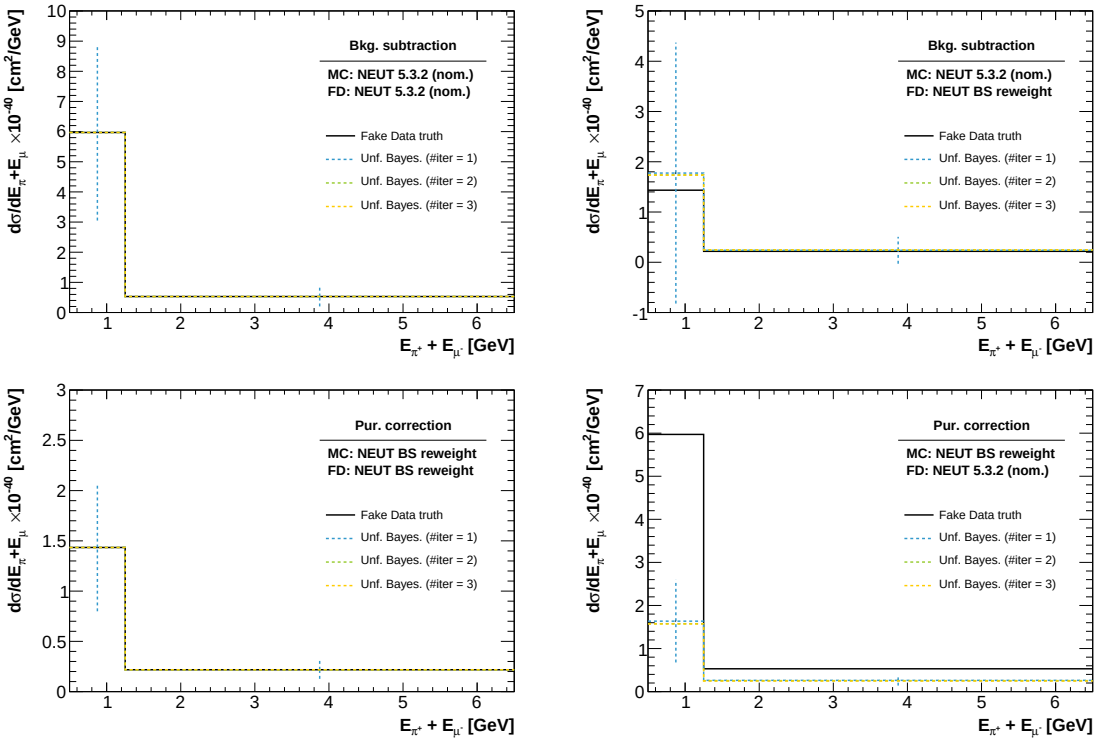

Figure 9.12: Results of the Bayesian unfolding for several iterations and different background treatments. The top plots are considering a background subtraction while the bottom plots use a purity correction method. The differential cross section are given per oxygen nucleus.

2 Measure the cross section and differential cross section on carbon (FGD1-only) using background subtraction treatment and a Bayesian unfolding with a single iteration.

3 In the spirit of moving towards a new way of presenting cross section results and to avoid adding bias via the unfolding process, an update of this analysis would be to use a "forward folding" approach, which enables to compare theory with experimental data at the reconstruction level.

This thesis will focus on the upper limit on oxygen and the cross section measurement on carbon.

9.4.1 Bayesian Upper Limit on Oxygen

The calculation of the upper limit on oxygen can be done with either a pure Bayesian method or by integrating the cross section probability density function. Both methods are relevant but they lead to a different interpretation of the results. We start by describing

the Bayesian method while the integration approach is discussed later. The probability of observing n events when we expect a total of $\lambda = s + b$ events is given by the Poisson distribution

$$\mathcal{L}(n, \lambda) = e^{-\lambda} \frac{\lambda^n}{n!} \tag{9.16}$$

Calling Bayes' theorem, one can derive the posterior probability assuming a prior probability ("knowledge") on the number of expected events $\pi(\lambda)$

$$\mathcal{P}(\lambda|n) = \frac{\mathcal{L}(n, \lambda)\pi(\lambda)}{\int_0^\infty \mathcal{L}(n, \lambda')\pi(\lambda')d\lambda'} \tag{9.17}$$

The upper limit on the total number of events λ^{95} at 95 % confidence level (C.L.) is then calculated according to

$$\int_0^{\lambda^{95}} \mathcal{P}(\lambda|n)d\lambda = 0.95 \tag{9.18}$$

Choosing a given distribution for the prior π based on the MC would introduce an important model dependence on the upper limit. Therefore a flat prior was chosen ($\pi(\lambda)$=1 if $\lambda > 0$ and 0 otherwise). We now want to find the upper limit on the number of signal events s given an expected number of background b and a confidence level δ. This is derived in [150] and the formula is recalled here:

$$\frac{\sum_{i=0}^{n} \mathcal{L}(i, s + b)}{\sum_{i=0}^{n} \mathcal{L}(i, b)} = 1 - \delta \tag{9.19}$$

For this analysis, we subtract the coherent interaction on carbon in FGD2 with the FGD1 sample. Therefore, the upper limit must account for the uncertainty on the number of events in FGD1. To that extend, the FGD1 sample is regarded as a sideband with a constant scale factor α which has a value of $\frac{T^{\text{FGD1-like}}}{T^{\text{FGD1}}} = 0.582$. This modifies equation (9.19) and the new expression taken from [151] is found to be

$$\frac{\sum_{i=0}^{n} \sum_{k=0}^{i} \mathcal{L}(i - k, s) \frac{\alpha^k (b' + k)!}{(1 + \alpha)^k k!}}{\sum_{k=0}^{n} \frac{\alpha^k (b' + k)!}{(1 + \alpha)^k k!}} = 1 - \delta \tag{9.20}$$

where b' is the number of events in the FGD1 sample. We give few examples of upper limits calculated with (9.20) in Table 9.6 and a graph of the 95% C.L. upper limit given n and b' is given in Figure 9.13. The unfilled area in the latter figure corresponds to an unphysical region where the expected number of signal events is negative: $n - \alpha b' < 0$.

Table 9.6: Example of upper limit calculated with (9.20). We assume that n is the total number of events observed in FGD2, b' is the number of events observed in FGD1 and s is the upper limit at a confidence level of δ. The number of expected signal events is also given and corresponds to $n - \alpha b'$.

n	b'	signal expected	δ	limit s
40	47	12.6	0.68	16.7
40	47	12.6	0.95	26.0
22	19	10.9	0.68	13.8
22	19	10.9	0.95	20.8

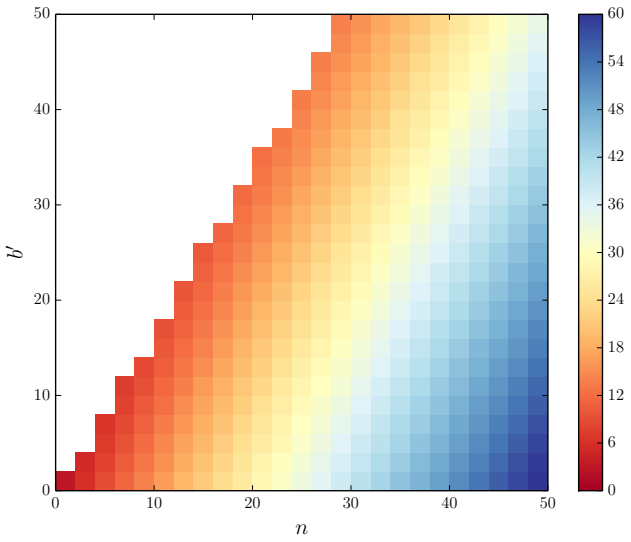

Figure 9.13: Values of the 95% C.L. upper limit for a given number of observed event in FGD2 n and background events in FGD1 b'.

The upper limits on the differential cross sections are derived from the upper limit on the number of coherent events given in Table 9.7 based on equation (9.1). The flux integral is calculated with the ν_μ contribution from Figure 4.9, multiplied by the corresponding POT

of the data sample from Table 8.1:

$$\int_0^{30\,GeV} \phi(E_{\nu_\mu}) dE_{\nu_\mu} \times \mathrm{POT}_{\mathrm{data}} = 1.106 \times 10^{13}\,\mathrm{cm}^{-2} \tag{9.21}$$

Table 9.7: Number of events in each unfolded bin after efficiency correction and upper limit calculated with (9.20). We assume that n is the total number of events observed in FGD2, b' is the number of events observed in FGD1 and s is the upper limit at a confidence level of δ=0.95. The number of expected signal events is also given and corresponds to $n - \alpha b'$. The last column correspond to the upper limit on the differential cross section calculated with equation (9.1) where $\tilde{N}_k^O = s$.

Variable X [unit]	Bin	# FGD1 b'	# FGD2 n	signal expected $n - {}^{T^{FGD1}}/_{T^{FGD2}} b'$	limit s	$\left\langle \frac{d\sigma}{dX} \right\rangle$ [10^{-40}cm^2/unit/^{16}O]
p_{μ^-} [GeV]	1	42.7	43.6	18.7	32.7	3.47
	2	56.3	53.9	21.1	36.5	0.45
$\cos(\theta_{\mu^-})$	1	34.5	36.0	15.9	29.1	6.18
	2	64.4	61.5	23.9	40.2	42.7
p_{π^+} [GeV]	1	41.9	40.8	16.4	30.0	6.37
	2	57.0	56.7	23.4	39.4	1.90
$\cos(\theta_{\pi^+})$	1	41.3	40.9	16.8	30.4	3.59
	2	57.7	56.6	22.9	39.0	20.7
$E_{\pi^+} + E_{\mu^-}$ [GeV]	1	44.7	45.6	19.5	34.0	2.41
	2	54.2	51.9	20.3	35.4	0.36
$\theta_{\pi^+\mu^-}$ [deg]	1	40.4	39.7	16.1	29.8	0.024
	2	58.2	57.6	23.7	39.8	0.084

The upper limit on the total number of signal events is 69.4 $\pm$0.2, which leads to an upper limit on the total flux-integrated cross section of 3.68$\times 10^{-40}$cm^{-2}/^{16}O.

9.4.2 Cross Section on Carbon

The coherent pion production on carbon has already been measured for a neutrino energy below 2 GeV using the T2K near detector [142], however the MC adopted was GENIE with the predictions from the Alvarez-Ruso [80] and Rein-Sehgal [77] models. Therefore, using the NEUT generator reweighted to the Berger-Sehgal predictions [79] would allow an interesting comparison between the different results. Figure 9.14 illustrates different fake data studies to test the single-iteration Bayesian unfolding. As expected, when the same model is used in MC and fake data, the unfolded does not show any bias. In the case where the signal models differ, the bias remains small, contained with the statistical errors.

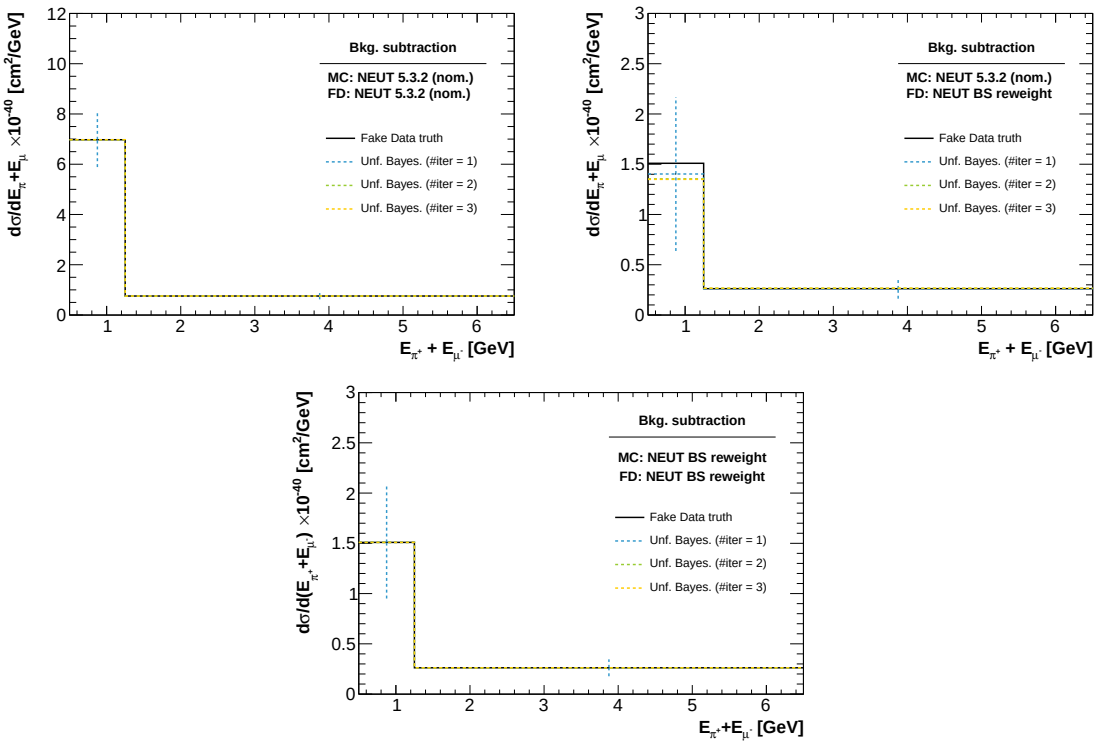

Figure 9.14: Results of the Bayesian unfolding for FGD1 selection only. Several iterations are considered and background subtraction treatment is used. The differential cross section are given per carbon nucleus.

10

Uncertainties

We present in this chapter how the statistical errors and systematic uncertainties are taken into account in the carbon measurement and how they are used to build a cross section probability density function for the upper limit on the oxygen cross section. All the plots shown in this chapter are obtained by subtracting the non-coherent background, unfolding both FGD1 and FGD2 distributions with a single iteration Bayesian method and finally subtracting the coherent interaction on carbon as described in the previous chapter. The MC and fake data both correspond to NEUT reweighted to Berger-Sehgal, unless mentioned otherwise.

10.1 Calculation and Propagation

To calculate the uncertainties we use pseudo experiments in which we vary a parameter relevant to a given error. The selection, unfolding and efficiencies are therefore computed for each toy experiment which gives a different cross section and differential cross section values. In order to treat correlations between the bins, we built covariance matrices C_{ij}. Assuming two random variables X_i and X_j that correspond to the unfolded results in bins i and j respectively, the covariance is calculated according to

$$C_{ij} = \mathrm{cov}(X_i, X_j) = \frac{1}{T-1}\sum_{t=1}^{T}(X_{ti} - \mu_i)(X_{tj} - \mu_j) \tag{10.1}$$

where T is the total number of throws, X_{ti} the value of the cross section for the toy t in bin i and μ_i is the mean of the cross section value across all toy experiments. There is one covariance matrix for each type of error sources:

- **Statistical** uncertainties, they are calculated by varying the number of events in each bin according to the poisson distribution in equation (9.16).
- **Detector systematics** are assessed with the `HighLAND` framework mentioned at the end of Chapter 5.
- **Flux, cross section models** and **FSI parameters systematics** are calculated by altering parameters values via the `T2KReWeight` software.

To get the overall uncertainty on the cross section for each bin, the covariance matrices for different sources of error are added.

10.2 Statistical Errors

The statistical errors have already been discussed in the previous chapter. To get the statistical data error, each bin of the data reconstructed distribution and data $E_\pi + E_\mu$ sideband is thrown 2000 times according to Poisson distribution. That explains the variations of the scale factors for each toy. For the MC statistics, the reconstructed and true distributions are thrown. The unfolding matrix, which is based on both true and reconstructed MC, is therefore re-calculated for each toy experiment. The statistical errors on the total cross section correspond to 25.8 % and 6.23 % for the variation of the number of data and MC events, respectively. The fractional covariance matrices for data and MC statistical errors are given for $E_\pi + E_\mu$ in Figure 10.1. The differential cross section for that same variable is also shown in Figure 10.1. Similar plots for the other variables are given in Appendix D, where the non-coherent background is constrained by a fit to the $E_\pi + E_\mu$ sideband.

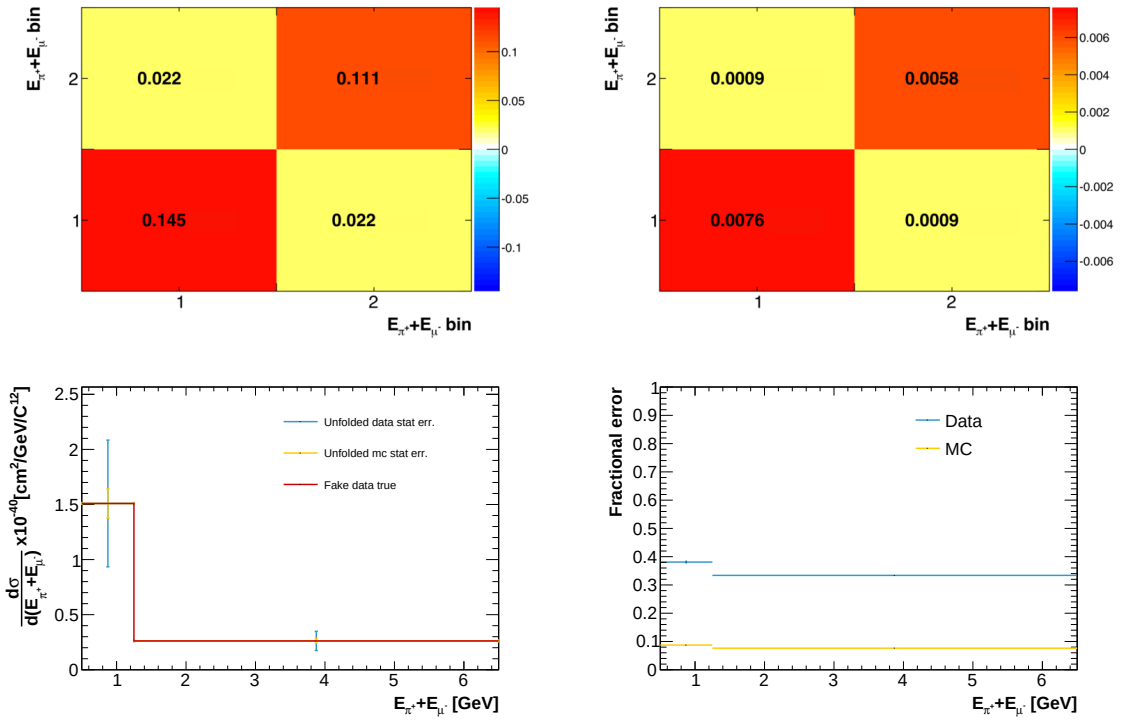

Figure 10.1: Fractional covariance matrices for data (top left) and MC (top right) statistical errors for the $E_\pi + E_\mu$ variable. Differential cross section results as a function of $E_\pi + E_\mu$ (bottom left) and fractional statistical errors for the same variable (bottom right). MC and FD are NEUT BS reweighted.

10.3 Systematic Errors

Systematics errors encompass the effects related to detector reconstruction efficiencies, uncertainties on the neutrino flux and on the cross section and nucleus models.

10.3.1 Detector Systematics

This analysis shares systematics with the ν_μ CC inclusive analysis that is described in detailed in [152]. Specific systematics such as the vertex activity reconstruction needed to be evaluated for this analysis. All these errors can be split into three categories:

- **Variation-like** systematics applies to variables which can have different mean value or resolution in data and MC. Propagating this kind of error consists in running the selection with altered values of the variable to see the effect they have on the total

number of selected events. An example of alteration would be

$$x'_{rec} = x_{rec} + \delta_{var}(x_{rec}^{alter} - x_{rec}) \tag{10.2}$$

where δ_{var} represents a random variable following a given distribution that varies according to the error (it is often normally distributed).

- **Efficiency-like** systematics are caused by reconstruction and detection probabilities. A weight w_e is computed based on a data/MC efficiency comparison in a control sample and applied to each event. The efficiency ε_{MC} in the MC analysis sample can be computed using the truth information. The predicted efficiency ε_{data} in the analysis data sample can be computed using MC and data efficiencies in the control sample ε_{data}^{CS} and ε_{MC}^{CS}:

$$\varepsilon_{data} = \frac{\varepsilon_{data}^{CS}}{\varepsilon_{MC}^{CS}} \cdot \varepsilon_{MC} \tag{10.3}$$

However, the statistical errors on the control sample efficiencies $\sigma_{\varepsilon_{data}^{CS}}$ and $\sigma_{\varepsilon_{MC}^{CS}}$ must be taken into account. Therefore we define the variation of the predicted efficiency in the analysis data sample ε'_{data}:

$$\varepsilon'_{data} = \frac{\varepsilon_{data}^{CS} + \delta_{data} \cdot \sigma_{\varepsilon_{data}^{CS}}}{\varepsilon_{MC}^{CS} + \delta_{MC} \cdot \sigma_{\varepsilon_{MC}^{CS}}} \tag{10.4}$$

where δ_{data} and δ_{MC} are random variables representing the variations in number of standard deviations of the data and MC control samples efficiencies, respectively. The weight applied to each event is then defined as

$$w_e = \frac{\varepsilon'_{data}}{\varepsilon_{MC}} \tag{10.5}$$

The variation on the total number of events N_{tot} is obtained by summing the weights over the events e which required the systematic error to be applied (for example,

there is no need to apply the TPC reconstruction systematic to events that are fully contained in FGD1):

$$N_{tot} = \sum_{e} \delta w_e + \sum_{\text{remaining events}} 1 \tag{10.6}$$

- **Normalisation-like** systematics are associated to the total event normalisation. It scales up or down the total number of event in a sub-sample given their rate uncertainties. The weight w_{norm} is found to be

$$w_{norm} = 1 + \delta_{norm}\sigma_{err} \tag{10.7}$$

where σ_{norm} is the error on the normalisation caused by the given systematic and δ_{norm} is a random variable corresponding to the variation in number of standard deviations. The variation of the total number of events in that case becomes:

$$N'_{tot} = w_{norm} \cdot N_{tot} \tag{10.8}$$

where N'_{tot} is the number of events after considering the systematic and N_{tot} is the number of events before considering the systematic error.

10.3.1.1 Inherited from ν_μ CC Analysis

Most of the systematic errors were calculated by the ν_μ analysis group as they are shared by several analysis. They are listed in Table 10.1 where they are grouped according to their propagation type. A brief description of each error follows, however they are all described in more details in [152].

- **TPC fields distortion**

  A small variation of the magnetic field leads to a bias in the estimation of the TPC momentum. To estimate the effect of such variations, a laser system which illuminates dots on the cathode is used. The resulting photo-electrons drift and are recorded by the TPC readout plates. The expected and measured positions of each dot are

Table 10.1: List of the detector systematics sort by type of propagation.

Variation-like	Efficiency-like	Normalisation-like
B field distortion	TPC charge ID	Out Of Fiducial Volume
TPC momentum scale	TPC tracking	Pile-Up
TPC momentum resolution	FGD hybrid tracking	FGD mass
TPC PID	TPC-FGD matching	Pion secondary interactions
FGD PID	Michel electron	Proton secondary interactions
	TPC cluster	

compared with B field turned on and off in order to remove the effect of centroid location and keep only the effect of the field distortion. The systematic due to electric field distortion is not use here but its effects are encompassed in the TPC momentum resolution.

- **TPC momentum scale**

  The TPC momentum scale systematic is cross-checked by comparing the TPC momentum with the momentum by range of stopping cosmic muons in the FGD.

- **TPC momentum resolution**

  This systematics uses a control sample of tracks crossing multiple TPC. The difference of the inverse transverse momentum between the two TPC segments $\Delta 1/p_t$, corrected by the energy loss in the intermediate FGD, can be fitted by a Gaussian centred in 0. From the standard deviation $\sigma_{\Delta 1/p_t}$, the momentum resolution of the TPC can be extracted, for different momentum, transverse momentum and angle.

- **TPC particle identification (PID)**

  The TPC PID relies on the measurement of the energy loss of the charged particles described in Section 5.2.2. It is very important to know the PID efficiency since the muon candidate could be a pion. Similarly, our pion candidate can be mis-identified as a proton, leading to the selection of an event with the wrong topology. This systematics is calculated by comparing and fitting the data and MC pulls distributions for different particle hypotheses. The data/MC difference between the pull mean

values gives an estimate of the systematic bias while the ratio between the pull sigma values gives an estimate of the smearing to apply when running the toy experiment.

- **FGD PID**

  The FGD PID systematic is similar to the TPC one. The energy loss is obtained from the ionisation of particles in the FGD scintillator bars. Then the standard deviation of the gaussian fit to the pull distribution allows to estimate the particle identification uncertainties. Note that the FGD PID is only applied to fully contained track, and so is this systematic.

- **TPC charge ID**

  This systematics parametrises the charge misidentification as a function of observables and estimates the effect of the global reconstruction on the final particle charge sign determination. The charge misidentification probability depends on the length, momentum, curvature and number of hits of a given local track (TPC segment). The charge misidentification of a global track is therefore correlated with the number of TPC segments the global track contains and on the fact that the segments predict the same charge or not. A data/MC comparison is done for the probability of conserving the charge in the global tracking, where the charge sign of one of the TPC segments is swap, for various number of TPC segments in the global track. This procedure allows us to determine the weights to apply in the error propagation (efficiency-like).

- **TPC tracking**

  This systematics accounts for the reconstruction efficiency with which the TPC successfully reconstructs the tracks of particles crossing it. Using control samples of through-going muons from beam and cosmic triggers, the reconstruction algorithm and pattern recognition performances (in the case of two nearby tracks) are investigated. The conclusion was that, for the three TPCs, the reconstruction efficiency is excellent and does not depend on the momentum, angle and length of the track, or the presence of another track in the same TPC.

- **FGD hybrid tracking**

  The FGD tracking efficiency corresponds to the probability of reconstructing a given track in the FGD. It is called hybrid as it uses vertices from real data and MC events and adds to them tracks generated via particle guns. The positions of vertices without fully contained FGD track are extracted. Protons and positive pions tracks are then added as separate samples and the files are processed through the FGD reconstruction. It is then possible to extract the efficiency of reconstructing a pion and a proton in both FGDs.

- **TPC-FGD matching**

  Using muons that cross at least two TPC, the rate of events that also have a track in the intermediate FGD can be computed. The FGD-TPC matching systematics error corresponds to the rate difference between data and MC.

- **Michel electron**

  An event is considered to have a Michel electron if it has at least one delayed (out-of-bunch) FGD time bin with six hits (five for FGD2), in the same FGD as the event occurred in. However, particles that enter the FGD from outside can leave energy deposition that pass the Michel electron cuts, resulting in the identification of a CC0π event to be identify as CC1π. The detection efficiency of Michel electrons is calculated using external background from in-magnet interaction and material surrounding the detector. This way the rate of Michel electron mis-identification can be computed.

- **TPC cluster**

  A TPC cluster is a group of adjacent TPC pad hits corresponding to one point in the ionised gas when a charged particle crosses the TPC. If the local angle of the track with the z axis is larger than 55°, the pad hits are clustered horizontally. They are clustered vertically otherwise. This systematic calculates the efficiency (and inefficiency) of the clustering algorithm via a data/MC comparison of the number of clusters per track in vertical and horizontal track control samples. This will affect

the number of events passing the quality cut where it is required that the event must contain at least one track with more than 18 TPC clusters.

- **Out of fiducial volume (OOFV)**

  Out of fiducial volume interactions correspond to events where the reconstructed vertex is inside the FGD FV but the true vertex is outside. In order to determine the rate uncertainty of these events, we use the data/MC difference of interaction rate where the vertex is in the SMRD, POD or ECal. Rate uncertainties for interactions occurring in the magnet or electronics are calculated based on a GENIE-NEUT comparison.

- **Pile-up**

  It can happen that neutrinos interact in the material surrounding the detector and produce a track which is recorded (called sand muon events). The simulation of such event is not taken into account by NEUT and therefore a correction (or weight) is applied to all MC events (Section 8.1.2). The pile-up systematic takes into account the uncertainties on the weight applied via a data/MC comparison of the number of TPC events per bunch, where the MC has the correction applied.

- **FGD mass**

  The number of target calculation done in Section 9.3 uses the areal densities of each FGD modules. The FGD mass systematics is determined from the uncertainties on these areal densities ($<0.7\,\%$).

- **Pion secondary interactions (Pion SI)**

  Pions can re-interact inside the detector once they escape the nucleus (absorption, decay, ...), which can cause them not to be detected. The GEANT4 model used to simulate these interactions differs significantly from the available external data, therefore a correction weight is applied to the NEUT nominal events to account for this discrepancy. A systematic weight is also applied to allow variation based on the uncertainties in the external data sets.

- **Proton secondary interactions (Proton SI)**

  Similarly to pion, protons can re-interact within the FGD. Even if we do not select protons, the FGD multiplicity cut is affected by the presence of short track protons. Moreover, the products of the proton re-scattering can be identify as our pion candidate. An approach similar to pion SI was taken to propagate this systematic error.

10.3.1.2 Vertex Activity Systematics

The bias induced by the detector on the vertex activity variable is calculated by doing a data/MC comparison in four control samples (CS):

- CS 1: protons stopping in FGD1 FV
- CS 2: protons stopping in FGD2 FV
- CS 3: muons stopping in FGD1 FV
- CS 4: muons stopping in FGD2 FV

Because these samples are stopping particles in the FGDs, the relevant variable we need to look at is the end activity (the neutrino vertex is most of the time outside of the FGD fiducial volume). End activities are the equivalent of the vertex activity from the detector point of view. It is the energy deposition in a given FGD volume centred on the end of a particle's track. The muon samples will scan relatively low energy deposit whereas the proton samples will be used for higher energy deposit. All available data and MC statistics are used, ie. runs 2, 3 and 4. The selection cuts are described below.

Protons in FGD1 (FGD2)	Muons in FGD1 (FGD2)
0 - Event quality	0 - Event quality
1 - Positive track	1 - Negative track
2 - End in FGD1 FV (FGD2 FV)	2 - End in FGD1 FV (FGD2 FV)
3 - Proton PID	3 - Muon PID
4 - No FGD2 track (No TPC3 track)	4 - No FGD2 track (No TPC3 track)
5 - No TPC2 track (No cut)	5 - No TPC2 track (No cut)

Note that the cut number 5 is only applied to FGD1 samples. In order to maximise the statistics in the FGD2 samples, there is no requirement on the number of FGD1 track. The fiducial volume and muon PID cuts are the same as the one detailed in Section 8.2. The proton PID is similar to the one used in the ν_μ CC0π analysis: the cut on $L_p > 0.9$ is performed, where L_p is defined as:

$$L_p = \frac{e^{-Pull_p^2}}{\sum_\alpha e^{-Pull_\alpha^2}}, \text{ with } \alpha = e, p, \mu, \pi \tag{10.9}$$

Figure 10.2 illustrates that cut for FGD1 (left) and FGD2 (right) samples.

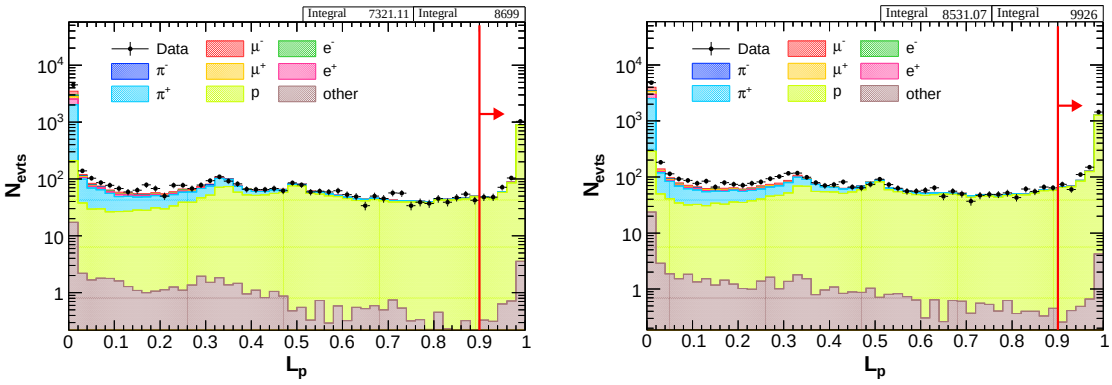

Figure 10.2: Proton PID cut for FGD1 (left) and FGD2 (right) samples. The variable L_p is defined by equation (10.9).

The particles composition of the 4 control samples (after the last cut) is given in Table 10.2. There is more than 91 % of true muon in the muon sample and more than 99 % of true proton in the proton sample.

Table 10.2: Particle composition (in %) of the 4 control samples according to the NEUT nominal true predictions.

CS	μ^-	e^-	π^-	μ^+	e^+	π^+	p	other
1	0.02	0.01	0.03	0.02	0.04	0.14	**99.4**	0.32
2	0.15	0.01	0.03	0.01	0.05	0.23	**99.2**	0.24
3	**91.5**	0.27	7.36	0.09	0.02	0.57	0.14	0.01
4	**93.0**	0.22	6.18	0.06	0.02	0.34	0.14	0.01

The end activity distributions are given in Figure 10.3 for FGD1 and Figure 10.4 for FGD2. Note that these plots are area normalised to enhance the data/MC shape comparison. We observe that for the FGD2 end activities, the three different volumes (2×3, 2×5 and 2×7) give identical distributions. Therefore, the addition of FGD bars in the x and y directions has less effect than including more bars in the z direction. Indeed, for the FGD1 plots, the energy is increasing with the number of bars taken into account in the z direction. The overall data/MC agreement looks quite good.

The end activity distributions are fitted using a simple gaussian function. The results of the fits for data and MC are given in Table 10.3.

Table 10.3: Gaussian mean μ and width σ extracted from the fit of the FGD1 and FGD2 end activities. Top (bottom) table shows the results for the stopping proton (muon) sample.

Stopping proton	3×3	5×5	7×7	2×3	2×5	2×7
$\mu_{MC} \pm \delta\mu_{MC}$ (MeV)	24.8±0.11	35.3±0.11	43.8±0.12	4.24±0.004	4.25±0.004	4.26±0.004
$\mu_{data} \pm \delta\mu_{data}$ (MeV)	25.8±0.41	36.4±0.41	44.3±0.44	4.16±0.019	4.18±0.020	4.18±0.029
$\sigma_{MC} \pm \delta\sigma_{MC}$ (MeV)	8.78±0.11	8.57±0.12	9.16±0.13	1.27±0.004	1.28±0.004	1.29±0.004
$\sigma_{data} \pm \delta\sigma_{data}$ (MeV)	7.05±0.35	7.02±0.38	7.43±0.35	1.22±0.017	1.24±0.018	1.25±0.023

Stopping muon	3×3	5×5	7×7	2×3	2×5	2×7
$\mu_{MC} \pm \delta\mu_{MC}$ (MeV)	12.07±0.04	16.69±0.04	20.53±0.04	2.17±0.003	2.17±0.003	2.18±0.003
$\mu_{data} \pm \delta\mu_{data}$ (MeV)	12.11±0.11	16.53±0.11	20.46±0.12	2.19±0.012	2.19±0.012	2.19±0.012
$\sigma_{MC} \pm \delta\sigma_{MC}$ (MeV)	3.90±0.04	4.00±0.04	4.25±0.05	0.66±0.002	0.65±0.002	0.66±0.002
$\sigma_{data} \pm \delta\sigma_{data}$ (MeV)	3.51±0.11	3.80±0.12	4.10±0.13	0.64±0.010	0.64±0.010	0.64±0.010

The vertex activity scale error is propagated as a variation-like systematics and is using the mean results μ of the fit with its associated error $\delta\mu$. A small correction C is also applied to take into account any potential shift between the data and MC. For each throw, the

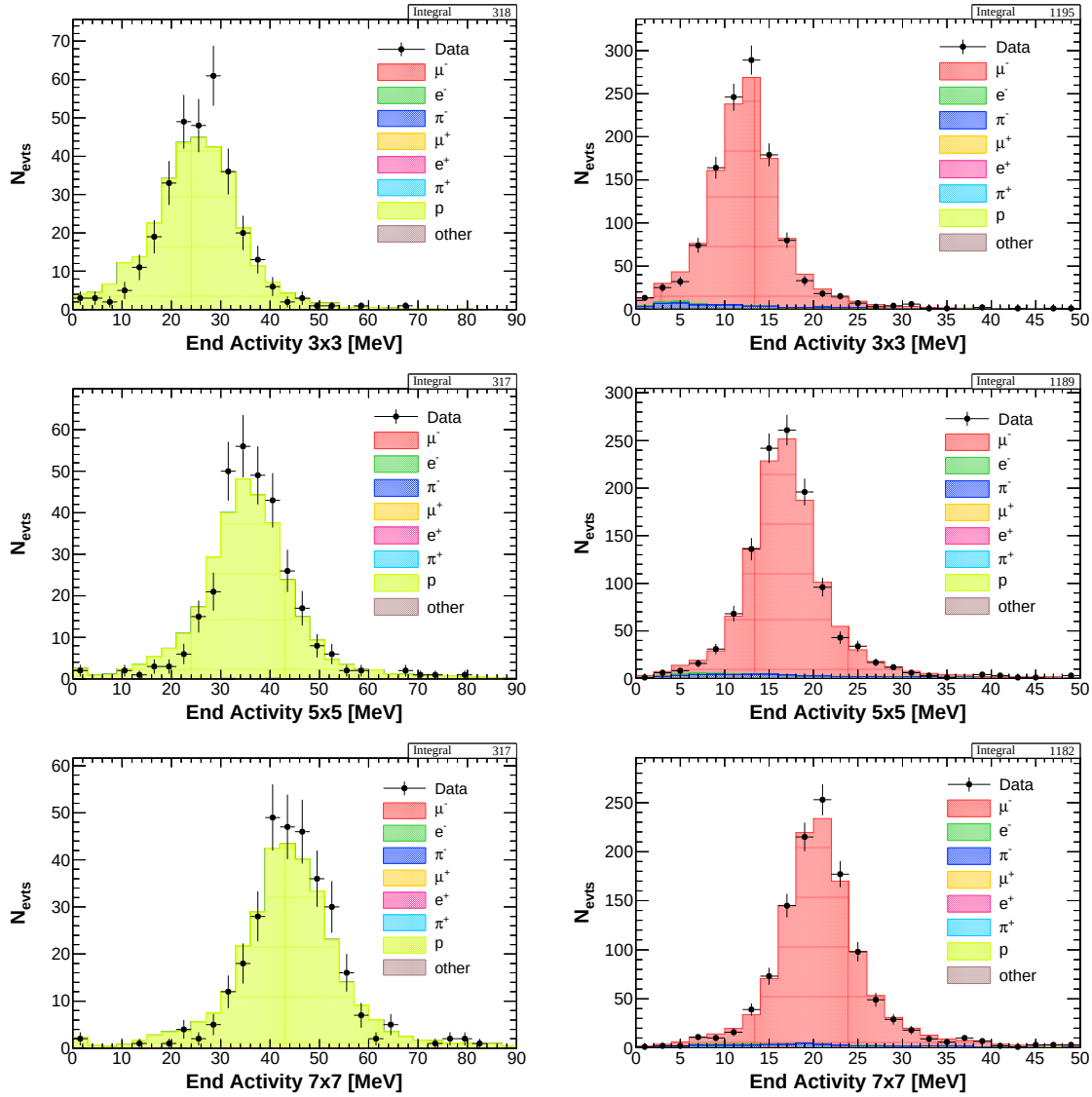

Figure 10.3: End Activity distributions for stopping protons (left) and muons (right) in the FGD1. The three volumes 3×3, 5×5 and 7×7 are represented in each row.

value of the vertex activity is replaced according to equation (10.10).

$$VA_{new} = VA_{old} + C + \delta_{var} \cdot \sqrt{|C|^2 + \delta\mu^2_{MC} + \delta\mu^2_{data}} \tag{10.10}$$

where $C = \mu_{data} - \mu_{MC}$ and δ_{var} a gaussian distributed random variable.

The vertex activity resolution error is propagated as a variation-like systematics and is using the width σ results of the fit with its associated error $\delta\sigma$. For each throw, the value

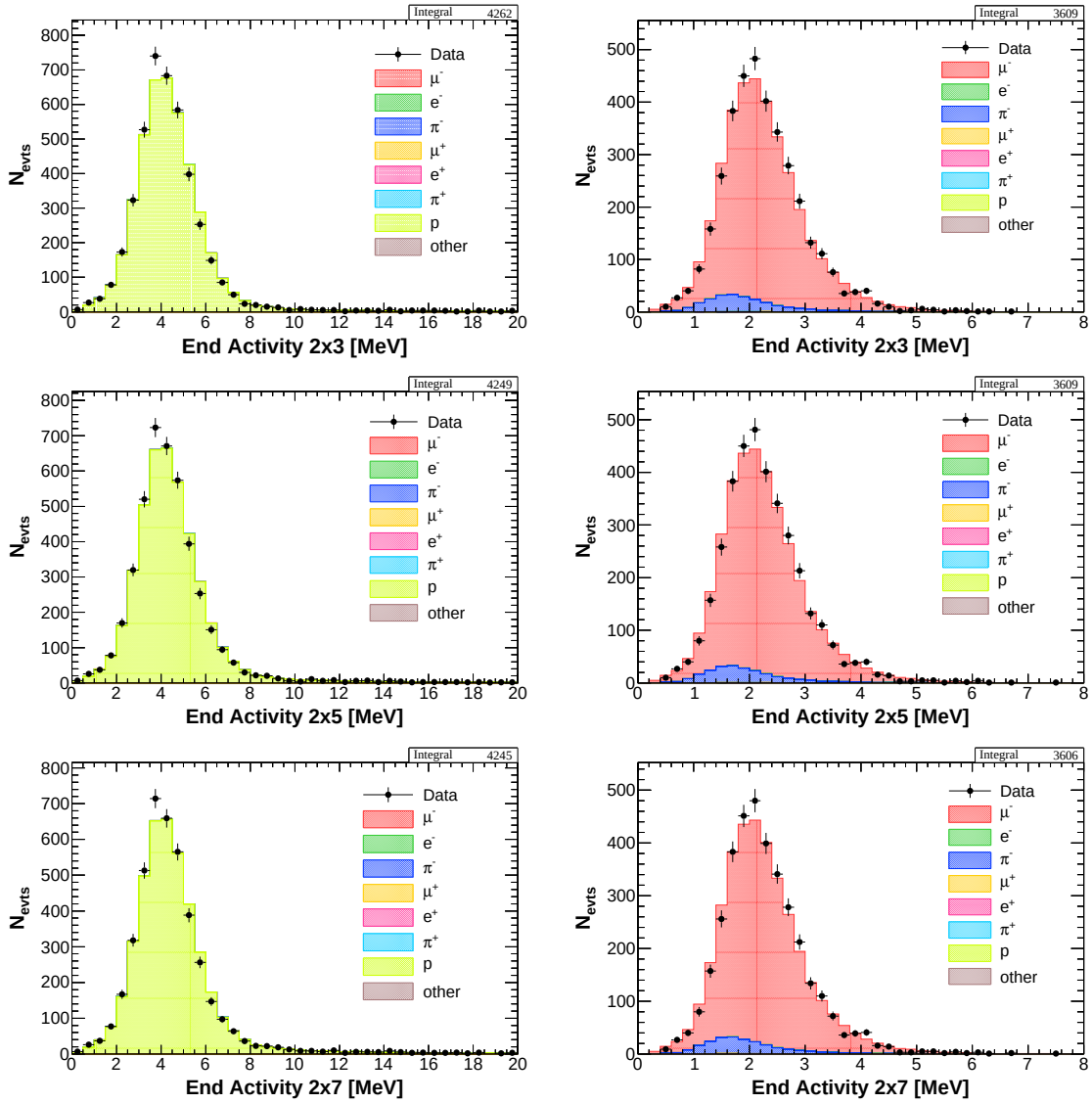

Figure 10.4: End Activity distributions for stopping protons (left) and muons (right) in the FGD2. The three volumes 2×3, 2×5 and 2×7 are represented in each row

of the vertex activity is replaced according to equation (10.11)

$$VA_{new} = VA_{old} \cdot (s + \delta_{var} \cdot \delta s) \tag{10.11}$$

where $s = \frac{\sigma_{data}}{\sigma_{MC}}$ and $\delta s = s \cdot |\frac{\delta\sigma_{data}}{\sigma_{data}} - \frac{\delta\sigma_{MC}}{\sigma_{MC}}|$.

10.3.1.3 Neutrino Parent Decay Position

In order to have a better reconstruction of the muon and pion directions, the neutrino

direction was extrapolated from the neutrino parent decay point (PDP) and the vertex positions (instead of just taking the z axis). This requires to assess the systematic error on the position of the neutrino parent decay point. This systematics was investigated in the ν_μ CC0π (or CCQE-like) analysis. It is a variation systematic, therefore, for each throw, the parent decay position (PDP) was randomly sampled from a 3 dimensions density distribution shown in Figure 10.5 and the neutrino direction extrapolated. The selection cuts are finally applied with this modified neutrino direction.

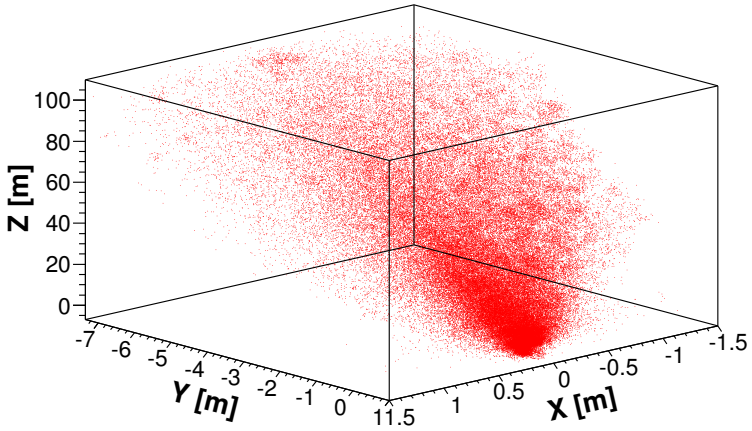

Figure 10.5: Probability density distribution of the neutrino parent decay point shown in the ND280 coordinates.

10.3.1.4 Covariances and Fractional Errors

The covariance matrix of the overall detector error along with the fractional error is given in Figure 10.6 for the $E_\pi + E_\mu$ variable. Other variables are available in Appendix D. The fractional error for each of the variation, efficiency and normalisation systematics is shown in Figure 10.7 (again, see Appendix D for other variables). Note that the latter figure corresponds to the relative error on the number of selected FGD1 events at the end of the selection in the reduced phase space **before** the coherent model reweight was performed (and not the fractional error on the final BS cross section). We notice that the FGD PID and the TPC cluster systematics are negligible as their contributions to the relative error on the number of selected events is less than 10^{-7}. On the other hand, the dominant error corresponds to the pion secondary interactions. Its contribution leads to about 5% error on the number of selected events. After constraining and subtracting the non-coherent

background, unfolding and efficiency correct, the total detector fractional systematic error on the differential cross-section becomes 24.3 %. It is much larger than the previously mentioned 5 % of the pion SI, but this increase is expected since we remove background events and scale the relative error to the Berger-Sehgal predictions.

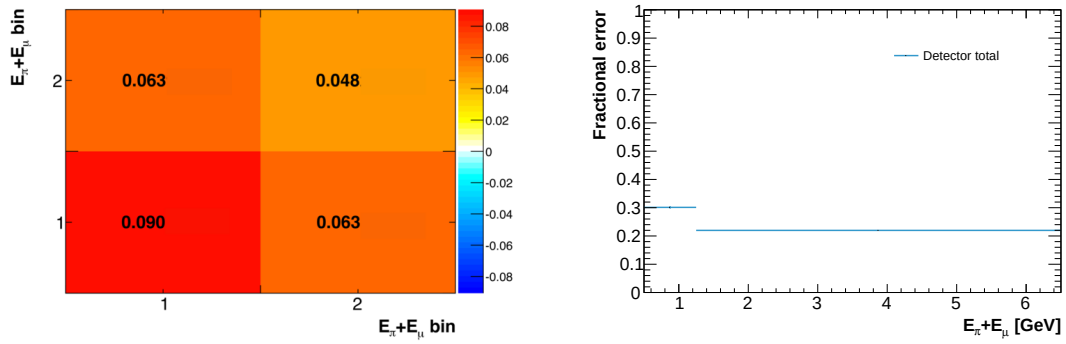

Figure 10.6: Fractional covariance matrix for all detector systematics (left) and relative error (right) for the $E_\pi + E_\mu$ variable (MC: NEUT reweighted, FD: NEUT reweighted).

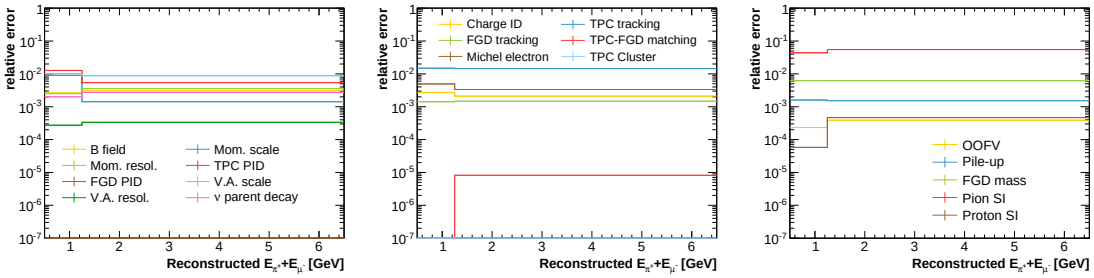

Figure 10.7: Contributions of each of the variation (left), efficiency (middle) and normalisation (right) detector systematics for the $E_\pi + E_\mu$ variable. They correspond to the relative errors on the total number of reconstructed events in the reduced phase space of the FGD1 selection, where the MC corresponds to the **NEUT nominal** predictions.

10.3.2 Flux Systematics

The flux uncertainty is assessed via a reweighting procedure. The near detector ν_μ, $\overline{\nu}_\mu$, ν_e and $\overline{\nu}_e$ fluxes for the forward horn current shown in Figure 4.9 are binned into different energy ranges according to Table 10.4. For each bin, the relative uncertainty is known and the correlations between different bins are also taken into account as illustrated by the "pre-fit" covariance matrix in Figure 10.8. This corresponds to our prior estimation of the flux uncertainty. The values of the flux in all the bins are then varied within their errors and the effect of such variations on the cross section gives an estimate of the flux

systematic error. The total systematic error on the integrated cross section due to flux uncertainties is found to be 8.43 %.

Table 10.4: Energy bins of each of the ND280 flux components as shown in the covariance matrix

Flux	Energy bins (in GeV)	Bin range in matrix
ν_μ	[0.0; 0.4; 0.5; 0.6; 0.7; 1.0; 1.5; 2.5; 3.5; 5.0; 7.0; 30]	0-11
$\overline{\nu}_\mu$	[0.0; 0.7; 1.0; 1.5; 2.5; 30]	11-16
ν_e	[0.0; 0.5; 0.7; 0.8; 1.5; 2.5; 4.0; 30]	16 - 23
$\overline{\nu}_e$	[0.0; 2.5; 30]	23-25

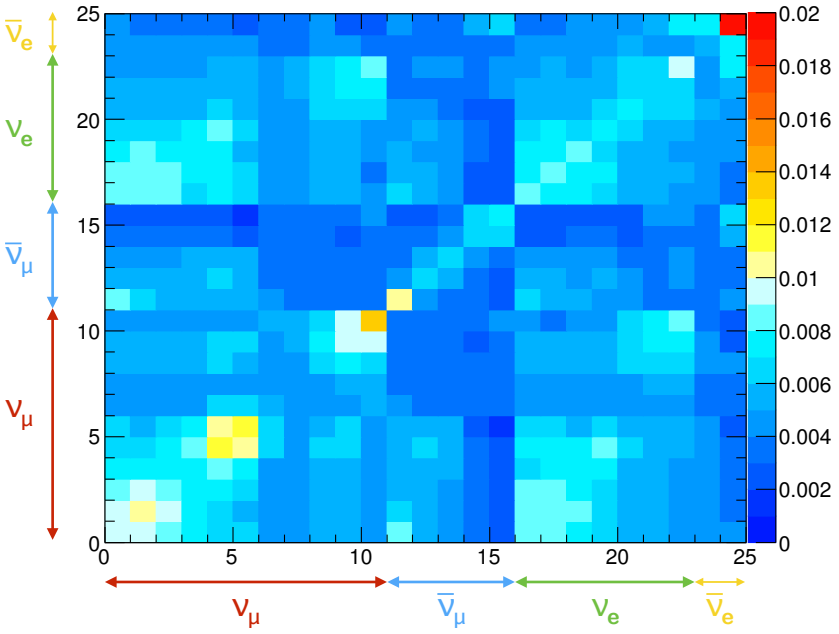

Figure 10.8: Flux input covariance matrix. The diagonal elements show the prior errors for each energy bin and the off-diagonal elements show the correlation between energy bins described in Table 10.4.

10.3.3 Theory and FSI Systematics

The errors due to the uncertainties on the cross section models and FSI parameters are calculated in a similar way. We vary different parameters within their given error range and we see how it affects the final cross section. The list of parameters with their definition are given below. More detailed information about the parameter variations and input priors is available in [153].

10.3.3.1 Cross Section Model Parameters

There are a total of nine cross section parameters (also called dials) that are listed in Table 10.5 along with their uncertainties used in the near detector fit to constrain the oscillation analysis parameters. The uncertainty ranges in which the parameters are allowed to vary are thoroughly determined by the Neutrino Interaction Working Group (NIWG) based on fits to external data sets. When a fit cannot be performed, a conservative approach is taken where the error ranges are based on the current reliability of the MC model. For example, the Berger-Sehgal coherent model, according to latest MINERvA result, agrees with data within 30 % uncertainty at low pion energies. Therefore a 30 % prior was set on the coherent normalisation parameter. Considering all these parameters as uncorrelated, the relative error of each of them on the total flux-integrated cross section is reported in the last column of Table 10.5.

Table 10.5: Cross section model parameters with their prior uncertainties and their variation effects on the differential cross section. The total row is calculated by throwing all the parameter together, therefore it includes correlations.

Name	prior	definition	effects	rel. error on σ
CA5	11.8 %	Value of the resonant axial form factor at Q^2=0 ($C_A^5(0)$)	Norm.	0.64 %
MANFFRES	15.8 %	Axial mass $M_A^{1\pi}$ for resonant pion production	Norm. + shape	0.46 %
BgRES	15.4 %	Fraction of non-resonant bkg. of isospin I=½	Norm.	6.94 %
CCNUE	2.0 %	Second-class current F_{3V} form factor	Norm.	0.03 %
DISMPISHP	40 %	CC-DIS and multi-pi cross section scaling δ_{DIS}	Norm. + shape	1.40 %
CCCOH	30 %	Normalisation factor of coherent pion production	Norm.	18.0 %
ANTINU	30 %	$\nu/\overline{\nu}$ cross section differences	Norm.	2.99 %
NCINCL	30 %	Normalisation factor for NC inclusive mode	Norm.	0.01 %
CCQENorm	30 %	Normalisation factor of CCQE	Norm.	0.08 %
Total				19.8 %

10.3.3.2 FSI Model Parameters

Similarly to the cross section model parameters, six pion final state interaction parameters that contribute to the cascade model are varied. They are listed in Table 10.6 where the given prior uncertainties originate from fits to pion scattering data. The relative error on the total cross section due to each parameter is also given in the table.

We summarise in Table 10.7 the uncertainties we obtained from the various sources described previously. Note that while the data and MC statistic errors are added in quadrature, the flux, FSI and cross section model systematic errors are thrown all together in order to

Table 10.6: Final state interaction parameters with their prior uncertainties. The low (high) energy parameters are for pion whose momentum is $< 500\,\text{MeV}$ ($>400\,\text{MeV}$). The total row is calculated by varied all the parameter together, therefore it includes correlations.

Name	uncertainty	definition	rel. error on σ
FrAbsPi	41.1 %	FSI absorption	0.37 %
FrCExLowPi	56.6 %	Single charge exchange, low energy	0.38 %
FrInelLowPi	41.2 %	Quasi-elastic scattering, low energy	2.50 %
FrPiProdPi	50.0 %	Inelastic scattering (hadron production)	1.14 %
FrCExHighPi	27.8 %	Single charge exchange , high energy	0.06 %
FrInelHighPi	33.8 %	Quasi-elastic scattering, high energy	0.54 %
Total			2.68 %

include the full correlations between all the reweighted parameters for the flux-integrated cross section on carbon, obtained by integrating over the $E_{\pi^+} + E_{\mu^-}$ variable. The cross section error is dominated by the statistical error that reaches 26.5 %, followed by the detector uncertainties of 25.2 %. Finally the cross section flux, FSI and model parameters and their correlations give an error 21.8 % on the total flux-integrated cross section.

Table 10.7: Summary of the uncertainties calculated with the $E_{\pi^+} + E_{\mu^-}$ variable for various error sources. The correlations between the flux, FSI and model parameters are taken into account while the statistical errors are added in quadrature.

σ [10^{-40} cm^2/C^{12}]	stat data	stat MC	Detector	Flux	FSI	Model
2.505	25.8 %	6.23 %	25.2 %	8.43 %	2.68 %	19.8 %
Total errors	26.5 %		25.2 %		21.8 %	

The throw distribution for all the error sources are given in Figure 10.9. We notice that apart from the detector error, the mean of the throw distribution is very close to the unfolded value (which is also the fake data truth result since there is no bias in the unfolding in this case). The reason for such a shift in the detector error is that the error is calculated with respect to the NEUT nominal (Rein-Sehgal model). It is however reasonable to assume that both models have the same detector fractional error, therefore the ratio width/mean is kept constant when the error is propagated to the Berger-Sehgal model.

Moreover, the distributions are fitted by two half-gaussian sharing the same mean in order to check for their symmetries. All the errors are rather symmetric (flux and FSI are slightly skewed to the right) apart from the model throws, for which the fit is skewed by several

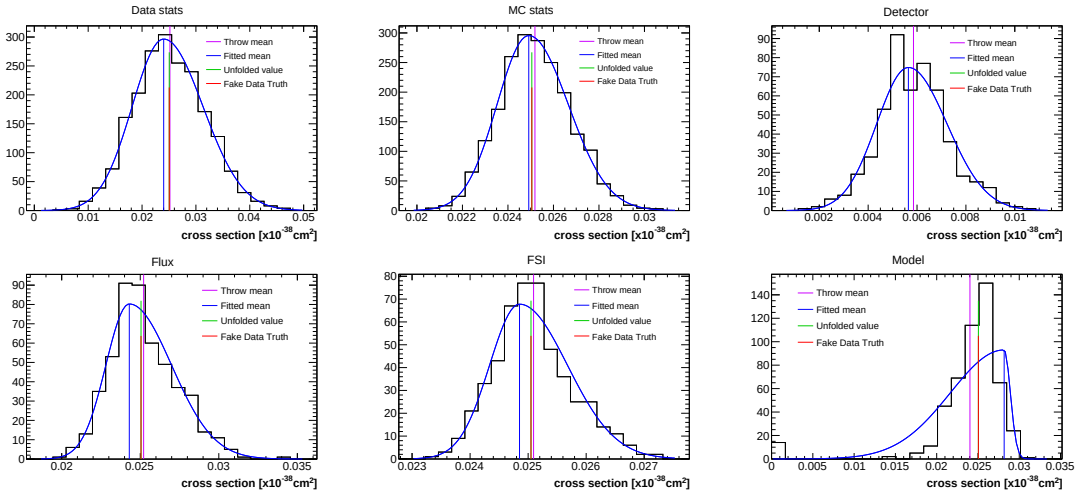

Figure 10.9: Throw distributions for the total flux-integrated cross section, extracted with the $E_{\pi^+} + E_{\mu^-}$ variable. There are 2000 throws for the statistical error and 500 throws for the systematics.

throw results giving a null cross section. A deeper investigation showed that such throws correspond to an extreme variation of the CC coherent normalisation parameter. Indeed for this parameter only, the truth information change as the true number of coherent events is scaled. The effect of such variation on the truth total cross section is represented in Figure 10.10 where we notice that the cross section reaches 0 for 17 throws. This means that for these throws, the unfolding fails as there is no valid truth information.

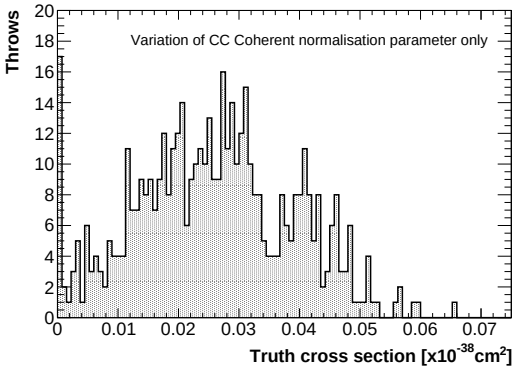

Figure 10.10: Effect of the variation of the coherent normalisation parameter on the truth cross section.

In order to compare the throw distribution with each other, we scale the detector, flux, FSI and model errors by 4 so that it is similar to the 2000 statistical throws. We can tell from Figure 10.11 that the broader gaussian the larger is the error on the cross section.

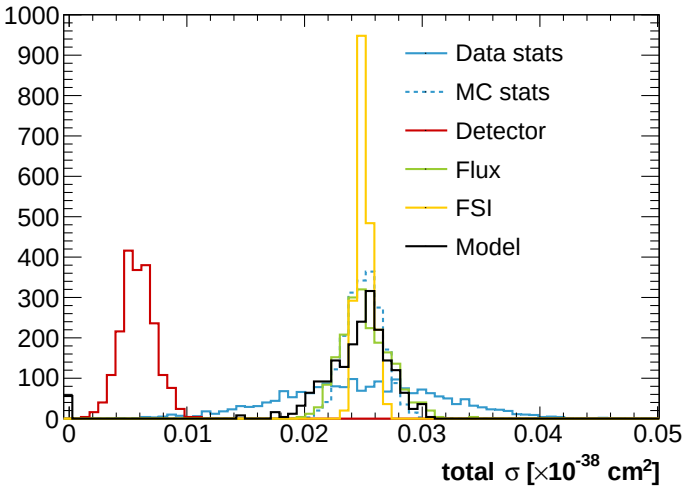

Figure 10.11: Throw distributions for the total flux-integrated cross section, extracted with the $E_{\pi^+} + E_{\mu^-}$ variable. There are 2000 throws for the statistical error and the systematics, which are initially calculated with 500 toys, have been rescaled to 2000 throws.

10.4 Probability Density Approach to the Upper Limit

Fake data toy experiments are also performed for the oxygen nucleus measurement. In this situation, both FGD1 and FGD2 unfolding matrices are recalculated for each error source. The cross section on oxygen is then extracted by integration over the $E_{\mu^-} + E_{\pi^+}$ bins. Note that for the data statistical error, the width of the throw distribution is too large and the cross section can get an unphysical negative value in a given bin. Even if the integration over the 2 bins can still give a positive flux-integrated total cross section[i], any throw giving a negative cross section in any bin is rejected. This corresponds to 33 % of the 2000 statistical toy experiments. This process induces a small bias of the throw results towards the higher cross section values. The final throw distributions for each error source for $E_{\pi^+} + E_{\mu^-}$ are shown in Figure 10.12. All the histograms are renormalised to 2000 throws and fitted with a skewed gaussian defined as:

$$f(x) = \begin{cases} N.\exp\left(-\dfrac{(x-\mu)^2}{2\sigma_1^2}\right) & \text{if } x < \mu \\ N.\exp\left(-\dfrac{(x-\mu)^2}{2\sigma_2^2}\right) & \text{if } x \geq \mu \end{cases} \tag{10.12}$$

[i] in the case where the second bin value compensate the negative value in the first bin

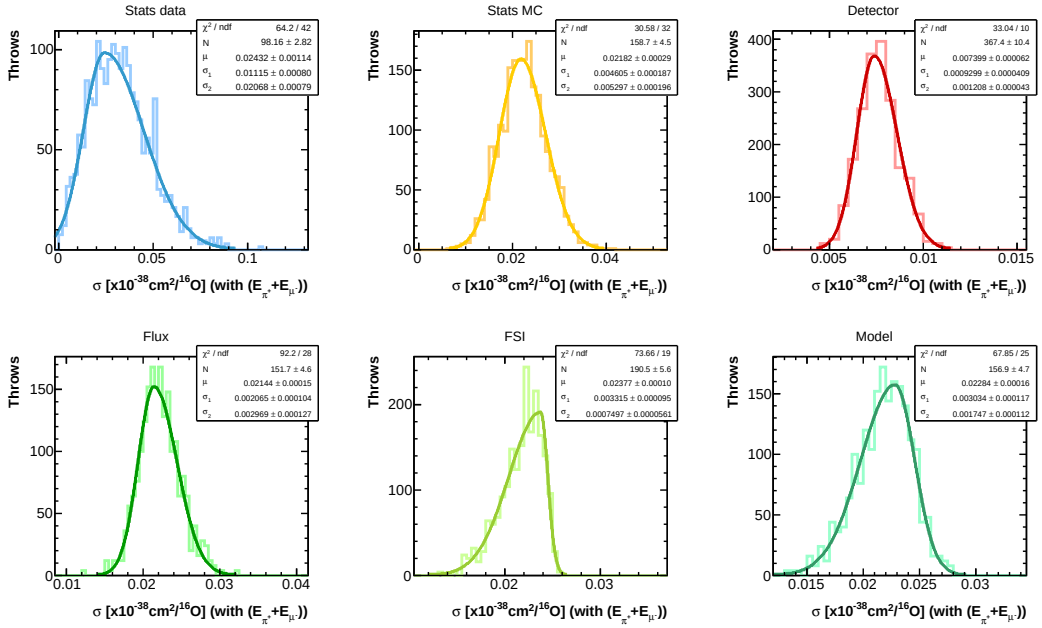

Figure 10.12: Throw distribution for each error source of the $E_{\pi^+} + E_{\mu^-}$ variable. The throws are fitted with skewed gaussian and the fit results are given in the top right pad.

We observe that, while the statistical MC and detector throw give a rather symmetric distribution where $\sigma_1 \sim \sigma_2$, the statistical data and flux toy experiments are skewed toward the right ($\sigma_1 < \sigma_2$) and the FSI and Model parameters variation give a gaussian skewed to the left ($\sigma_1 > \sigma_2$). To correctly propagate the detector systematic, its gaussian fit is translated such that its mean μ (i.e. the throw average) matches with the nominal unfolded result. The ratio width/mean is kept constant while doing this translation to keep the fractional error constant. The correlation between the flux, FSI and model parameters are taken into account as all of their parameters are varied together. Hence the statistical data, statistical MC, detector and flux+FSI+model formed four independent groups of error for which we extract the fit parameters. In order to obtain the final throw distribution, we average the result of the means μ and we add in quadrature the widths σ from the independent error sources.

$$\mu_{\text{tot}} = \frac{1}{4}\left(\mu_{\text{data stat}} + \mu_{\text{MC stat}} + \mu_{\text{det}} + \mu_{\text{flux+fsi+model}}\right) \tag{10.13}$$

$$\sigma_{i,\text{tot}} = \left(\sigma^2_{i,\text{data stat}} + \sigma^2_{i,\text{MC stat}} + \sigma^2_{i,\text{det}} + \sigma^2_{i,\text{flux+fsi+model}}\right)^{1/2} \tag{10.14}$$

Adjusting the normalisation parameter N such that the integral is 1, the total probability density distribution of the cross section and differential cross section are given in Figure 10.13.

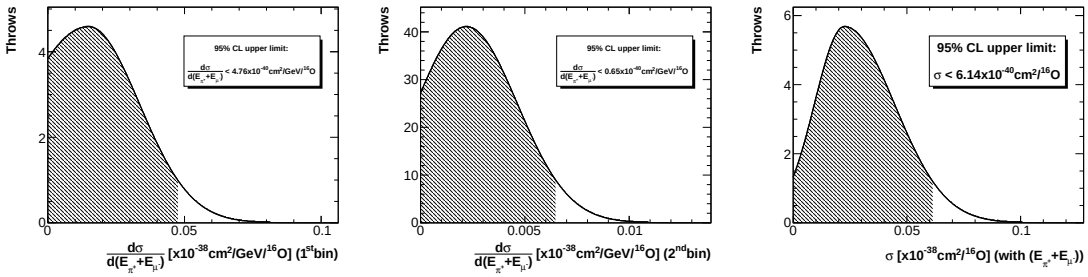

Figure 10.13: Integration of the probability density function for the first (left) and second (centre) bins and for the total cross section (right). The 95 % CL upper limit is given in each case.

Table 10.8 summarises the upper limits obtained with different variables where the NEUT reweighted to the BS predictions are taken as MC and fake data. For comparison, the number obtained in the previous chapter with Bayes theorem are given in grey parenthesis. It is found that the upper limit calculated by the integration over the toy experiment always lies above the limits calculated with Bayes theorem, which do not account for any systematic errors.

Table 10.8: Summary of the 95 % upper limit calculated with different variables using the integration over the throw distributions. See appendix D for detailed plots. In the grey parenthesis, the numbers obtained in the previous chapter using a Bayesian approach are recalled.

	Bin 1	Bin 2	Integrated	
Variable [unit]	[$\times10^{-40}$cm^2/unit/^{16}O]	[$\times10^{-40}$cm^2/unit/^{16}O]	[$\times10^{-40}$cm^2/^{16}O]	
p_{μ^-} [GeV]	6.74 (3.47)	0.83 (0.45)	6.19	(3.68)
$\cos\theta_{\mu^-}$	13.9 (6.18)	74.1 (42.7)	6.43	
p_{π^+} [GeV]	16.1 (6.37)	3.14 (1.90)	6.42	
$\cos\theta_{\pi^+}$	8.20 (3.59)	35.5 (20.7)	6.57	
$E_{\pi^+}+E_{\mu^-}$ [GeV]	4.76 (2.41)	0.65 (0.36)	6.14	
$\theta_{\pi^+\mu^-}$ [deg]	0.051 (0.024)	0.15 (0.084)	6.24	

11

Results

This chapter reports the final cross section results obtained with the T2K data samples. The differential results are presented for all the variables p_{μ^-}, $\cos\theta_{\mu^-}$, p_{π^+}, $\cos\theta_{\pi^+}$, $E_{\pi^+} + E_{\mu^-}$ and $\theta_{\pi^+\mu^-}$ in the reduced phase space defined in Table 8.5. Like in the previous chapter, the MC considered in all the plots is the NEUT reweighted to Berger-Sehgal model. First the cross section measurement on carbon is described before discussing the upper limit on oxygen.

11.1 Measurement on Carbon

The results for the cross section measurement using the FGD1 detector as target are detailed below. The non-coherent backgrounds (resonant and DIS) have been constrained by a control sample and subtracted. The remaining signal only contains coherent interaction on carbon nucleus as well as a small fraction of diffractive interaction on nucleon. The latter being missing in the MC simulation, it is hard to estimate the amount of diffractive events selected, especially at low neutrino energy. It is therefore included in the measurement.

11.1.1 Muon Kinematics

The muon kinematic variables have never been investigated in the case of charged-current coherent pion production. The following results are therefore the first data available for the muon momentum and angle for this specific interaction. The data for the muon momentum differential cross section showed in Figure 11.1 are in good agreement with the Berger-Sehgal model. This is also indicated in Table 11.1 where the numerical values are given. Regarding the cosine of the muon angle, an excess is found in the small angle bin

($\cos\theta_{\mu^-} > 0.95$) as shown in Figure 11.2. The Berger-Sehgal prediction in this bin overlaps with the lower bound of the error bar at 32.6 $\times 10^{-40}\mathrm{cm}^2/^{12}\mathrm{C}$, for a central value of 47.1 $\times 10^{-40}\mathrm{cm}^2$ per carbon nucleus. A good agreement is observed in the higher angle bin. This indicates that the muon produced by a CC coherent interaction tends to be more forward going that Berger-Sehgal predicted.

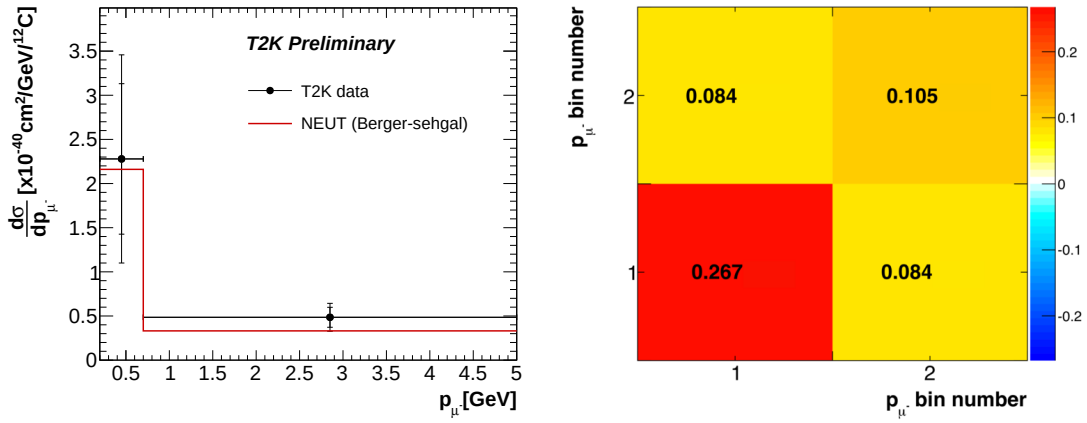

Figure 11.1: Left: Differential cross section on carbon as a function of the muon momentum. The inner error bars correspond to statistical errors only. The outer represent the quadrature sum of statistical and systematics error. Right: Fractional covariance matrix for the total error.

Table 11.1: Muon momentum differential and integrated cross section results with the absolute and relative errors detailed.

Measured quantity	$d\sigma/dp_{\mu^-}$				σ	
Unit	$\times 10^{-40}\mathrm{cm}^2/\mathrm{GeV}/^{12}\mathrm{C}$				$\times 10^{-40}\mathrm{cm}^2/^{12}\mathrm{C}$	
Range (GeV)	[0.20-0.70]		[0.70-5.0]		[0.20-5.0]	
Value	2.27		0.48		3.23	
NEUT (BS model)	2.16		0.33		2.50	
Statistical errors	0.85	(37.4 %)	0.11	(23.3 %)	0.68	(21.3 %)
MC					0.18	(5.50 %)
Data					0.66	(20.5 %)
Systematic errors	0.81	(35.7 %)	0.11	(22.7 %)	0.82	(25.3 %)
Detector					0.49	(15.2 %)
Flux					0.28	(8.65 %)
FSI					0.059	(1.83 %)
Model					0.59	(20.5 %)
Total	1.18	(51.7 %)	0.16	(32.5 %)	1.06	(32.9 %)

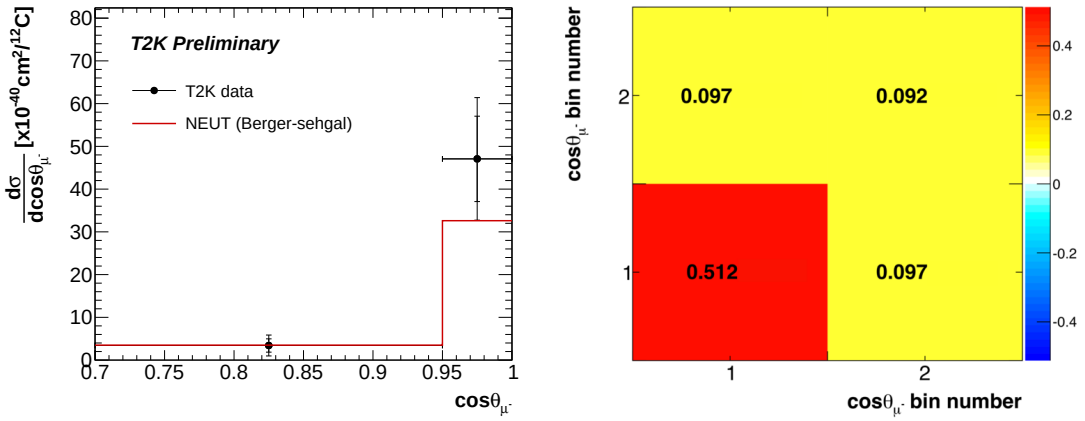

Figure 11.2: Left: Differential cross section on carbon as a function of the muon angle cosine. The inner error bars correspond to statistical errors only. The outer represent the quadrature sum of statistical and systematics error. Right: Fractional covariance matrix for the total error.

Table 11.2: Muon angle differential and integrated cross section results with the absolute and relative errors detailed.

Measured quantity	$d\sigma/dcos\theta_{\mu^-}$				σ	
Unit	$\times 10^{-40}$cm^2/^{12}C				$\times 10^{-40}$cm^2/^{12}C	
Range	[0.70-0.95]		[0.95-1.0]		[0.70-1.0]	
Value	3.41		47.1		3.20	
NEUT (BS model)	3.50		32.6		2.50	
Statistical errors	1.55	(45.5 %)	9.98	(21.2 %)	0.66	(20.7 %)
MC					0.19	(5.83 %)
Data					0.64	(19.8 %)
Systematic errors	1.88	(55.2 %)	10.3	(21.8 %)	0.78	(24.4 %)
Detector					0.43	(13.5 %)
Flux					0.28	(8.69 %)
FSI					0.059	(1.85 %)
Model					0.59	(18.2 %)
Total	2.44	(71.5 %)	14.3	(30.4 %)	1.02	(31.9 %)

11.1.2 Pion Kinematics

The differential cross section as a function of the pion momentum in the restricted phase space is given in Figure 11.3. A significant excess with respect to the Berger-Sehgal model is observed in the first bin (0.15 GeV $< p_{\pi^+} <$ 0.35 GeV), while in the second bin a good

agreement is found. This observation is consistent with the MINERvA measurement [135].

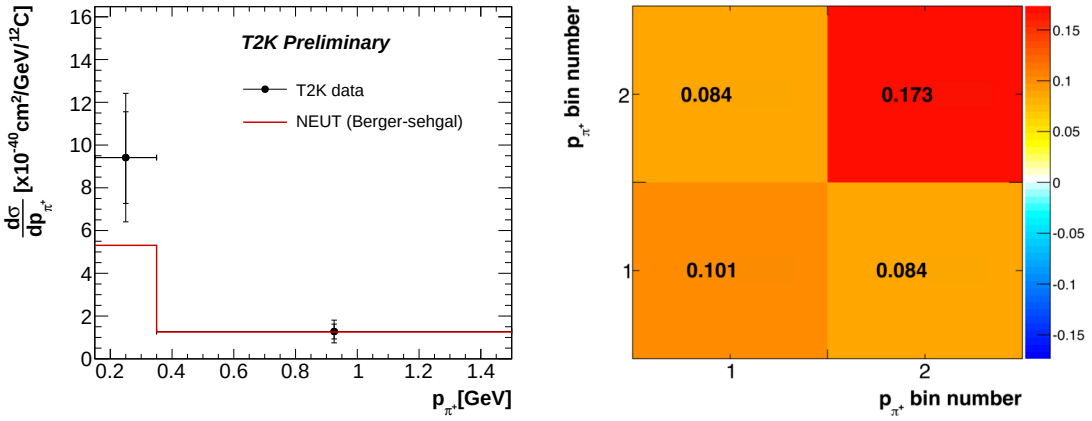

Figure 11.3: Left: Differential cross section on carbon as a function of the pion momentum. The inner error bars correspond to statistical errors only. The outer represent the quadrature sum of statistical and systematics error. Right: Fractional covariance matrix for the total error.

Table 11.3: Pion momentum differential and integrated cross section results with the absolute and relative errors detail.

Measured quantity	$d\sigma/dp_{\pi+}$				σ	
Unit	$\times 10^{-40}$cm^2/GeV/^{12}C				$\times 10^{-40}$cm^2/^{12}C	
Range (GeV)	[0.15-0.35]		[0.35-1.50]		[0.15-1.50]	
Value	9.41		1.27		3.35	
NEUT (BS model)	5.31		1.25		2.50	
Statistical errors	2.14	(22.8 %)	0.35	(27.2 %)	0.67	(20.2 %)
MC					0.19	(5.74 %)
Data					0.65	(19.3 %)
Systematic errors	2.10	(22.4 %)	0.40	(31.5 %)	0.87	(26.1 %)
Detector					0.56	(16.8 %)
Flux					0.29	(8.65 %)
FSI					0.056	(1.68 %)
Model					0.60	(18.0 %)
Total	3.00	(31.9 %)	0.53	(41.6 %)	1.09	(32.7 %)

Despite having a different neutrino energy and phase space, MINERvA also observed an excess compared to the Berger-Sehgal model at low pion energy, as indicated by Figure 7.16. This discrepancy probably comes from the elastic pion-nucleon cross section used

in the model, which is slightly overestimated (see Figure 7.3). Integrating over these two momentum bins give a value of the total flux-integrated cross section of 3.35 ± 0.67 (stat) ± 0.87 (syst.) $\times 10^{-40}$cm^2 per carbon nucleus. Integrating over other parameter often gives lower cross section around 3.20 $\times 10^{-40}$cm$^2/^{12}$C.

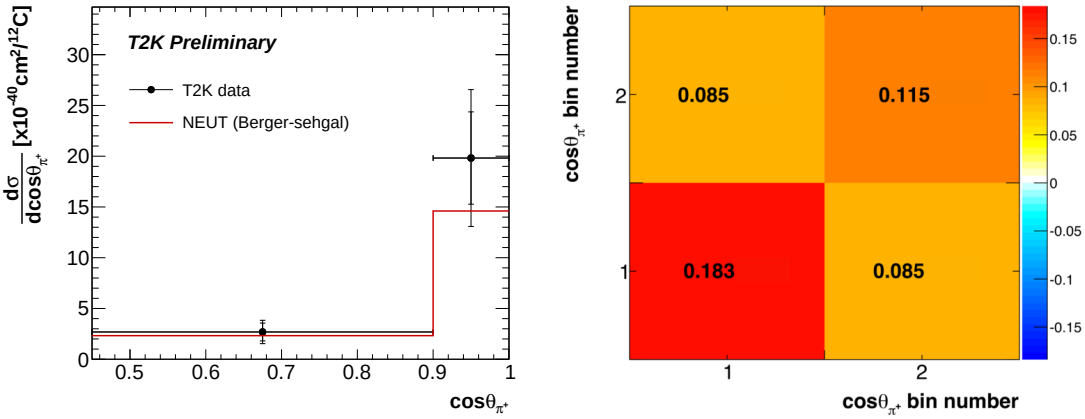

Figure 11.4: Left: Differential cross section on carbon as a function of the pion angle cosine. The inner error bars correspond to statistical errors only. The outer represent the quadrature sum of statistical and systematics error. Right: Fractional covariance matrix for the total error.

Table 11.4: Pion angle differential and integrated cross section results with the absolute and relative errors detail.

Measured quantity	$d\sigma/dcos\theta_{\pi+}$				σ	
Unit	$\times 10^{-40}$cm$^2/^{12}$C				$\times 10^{-40}$cm$^2/^{12}$C	
Range	[0.45-0.90]		[0.90-1.0]		[0.45-1.0]	
Value	2.68		19.8		3.19	
NEUT (BS model)	2.32		14.6		2.50	
Statistical errors	0.88	(32.7 %)	4.54	(22.9 %)	0.67	(21.1 %)
MC					0.19	(5.91 %)
Data					0.64	(20.2 %)
Systematic errors	0.74	(27.7 %)	4.97	(25.1 %)	0.81	(25.6 %)
Detector					0.50	(15.6 %)
Flux					0.28	(8.64 %)
FSI					0.058	(1.82 %)
Model					0.58	(18.2 %)
Total	1.15	(42.8 %)	6.74	(34.0 %)	1.05	(32.9 %)

A more detailed decomposition of the errors are given in Table 11.3. Similarly to the

muon angle, a small excess at 19.8 $\times 10^{-40}$cm^2/^{12}C is found in the small pion angle bin ($\cos\theta_{\pi^+} > 0.9$), even if the Berger-Sehgal, predicted at 14.6 $\times 10^{-40}$cm^2/^{12}C, still lies within the total error bands as displayed in Figure 11.4. Once more, this result summarised in Table 11.4 indicates that the pion is emitted in a more forward direction compared to what the Berger-Sehgal suggests.

11.1.3 Pion and Muon Energy Sum

The sum of the pion and muon energy can be regarded as the neutrino energy, and therefore is an important quantity to study. A 20 % excess is observed in the data lowest energy bin (0.5 GeV $< E_{\pi^+} + E_{\mu^-} <$ 1.25 GeV) where the neutrino energy peak is located (Figure 11.5). Indeed the data value is 1.87 $\pm$ 0.76 $\times 10^{-40}$cm^2/GeV/^{12}C, to be compared with the 1.51 $\times 10^{-40}$cm^2/GeV/^{12}C value from the BS model. A similar excess is found in the higher energy bin (1.25 GeV $< E_{\pi^+} + E_{\mu^-} <$ 6.5 GeV) where the data is 0.35 $\times 10^{-40}$cm^2/GeV/^{12}C. However one should note that there is a 41 % and 35.7 % total relative error in the first and second bin respectively as written in Table 11.5, which makes the BS prediction contained within the error bars.

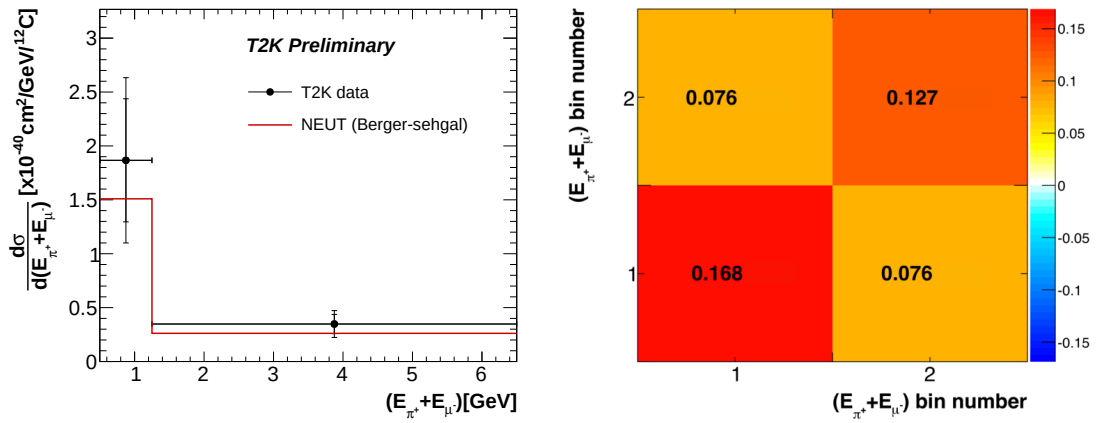

Figure 11.5: Left: Differential cross section on carbon as a function of the sum of the pion and muon energies. The inner error bars correspond to statistical errors only. The outer represent the quadrature sum of statistical and systematics error. Right: Fractional covariance matrix for the total error.

11.1.4 Coplanarity Angle

The coplanarity angle is more often used as a cutting parameter in the selection, however in

Table 11.5: Pion and muon summed energies differential and integrated cross section results with the absolute and relative errors detail.

Measured quantity	$d\sigma/d(E_{\pi^+}+E_{\mu^-})$				σ	
Unit	$\times 10^{-40}\mathrm{cm}^2/\mathrm{GeV}/^{12}\mathrm{C}$				$\times 10^{-40}\mathrm{cm}^2/^{12}\mathrm{C}$	
Range (GeV)	[0.50-1.25]		[1.25-6.5]		[0.50-6.5]	
Value	1.87		0.35		3.23	
NEUT (BS model)	1.51		0.26		2.50	
Statistical errors	0.57	(30.6 %)	0.09	(25.6 %)	0.67	(20.9 %)
MC					0.18	(5.55 %)
Data					0.65	(20.1 %)
Systematic errors	0.51	(27.4 %)	0.087	(24.9 %)	0.82	(25.6 %)
Detector					0.50	(15.6 %)
Flux					0.28	(8.65 %)
FSI					0.059	(1.83 %)
Model					0.59	(18.2 %)
Total	0.76	(41.0 %)	0.12	(35.7 %)	1.06	(32.8 %)

the case of coherent interaction it can be interesting to express the differential cross section as a function of this angle. If the neutrino interacts with the global nucleus wave function transferring a small amount of its energy to it, like in the PCAC-based models, the muon and pion are expected to be emitted in opposite directions, i.e. $\theta_{\pi^+\mu^-} = 180°$. However if the interaction occurs at the nucleon level as described by Alvarez-Ruso [80], the pion can rescatter within the nuclear medium and one would assume the coplanarity angle distribution to be a bit flattened. Figure 11.6 actually suggests that the data is less peaked at 180° than the Berger-Sehgal model (which is PCAC-based). A significant excess is found in the first bin ($90° < \theta_{\pi^+\mu^-} < 155°$) where $d\sigma/d\theta_{\pi^+\mu^-} = 3.03 \pm 1.04 \times 10^{-42}\mathrm{cm}^2/\mathrm{deg}/^{12}\mathrm{C}$ while BS predicts only 1.57 $\times 10^{-42}\mathrm{cm}^2/\mathrm{deg}/^{12}\mathrm{C}$. On the other hand, the second bin shows the BS value higher than the data point but still contained within the statistical error.

Table 11.7 summarises all the results obtained for the cross section measurements on carbon. The value of the flux-integrated cross section, integrated over the two bins, varies according to which variable is being integrated. It goes from 3.16 $\times 10^{-40}\mathrm{cm}^2/^{12}\mathrm{C}$ when using the coplanarity angle to 3.35 $\times 10^{-40}\mathrm{cm}^2/^{12}\mathrm{C}$ for the pion momentum. These differences are expected since the efficiencies differ from one bin to another and it directly affects the

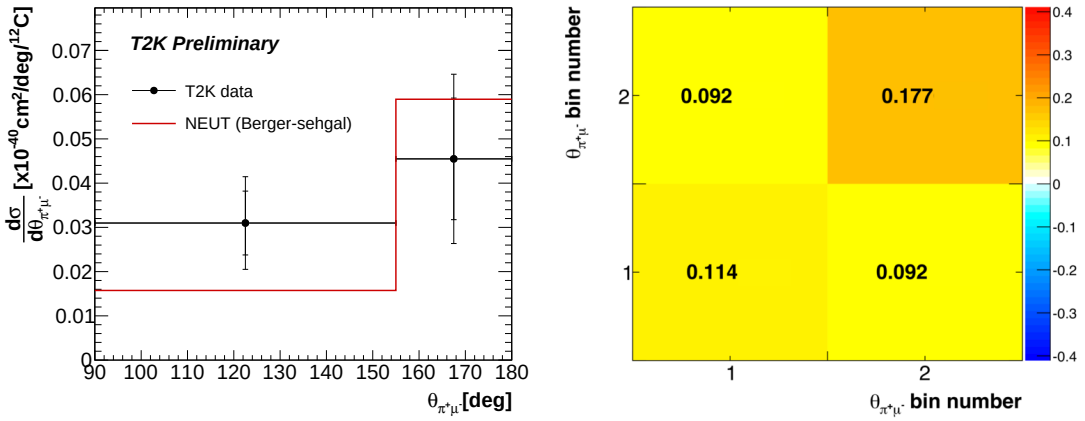

Figure 11.6: Left: Differential cross section on carbon as a function of the coplanarity angle. The inner error bars correspond to statistical errors only. The outer represent the quadrature sum of statistical and systematics error. Right: Fractional covariance matrix for the total error.

Table 11.6: Coplanarity angle differential and integrated cross section results with the absolute and relative errors detail.

Measured quantity	$d\sigma/d\theta_{\pi^+\mu^-}$				σ	
Unit	$\times 10^{-42}$cm^2/deg/^{12}C				$\times 10^{-40}$cm^2/^{12}C	
Range (deg)	[90-155]		[155-180]		[90-180]	
Value	3.09		4.54		3.16	
NEUT (BS model)	1.57		5.89		2.50	
Statistical errors	0.72	(23.3 %)	1.37	(30.2 %)	0.67	(21.2 %)
MC					0.19	(6.01 %)
Data					0.64	(20.3 %)
Systematic errors	0.76	(24.5 %)	1.33	(29.3 %)	0.82	(26.0 %)
Detector					0.51	(16.3 %)
Flux					0.27	(8.62 %)
FSI					0.058	(1.84 %)
Model					0.57	(18.2 %)
Total	1.04	(33.8 %)	1.91	(42.1 %)	1.06	(33.5 %)

differential cross section results.

Table 11.7: Results of the differential cross section measurement on carbon target for each bin, and for the integrated cross section.

	Bin 1	Bin 2	Integrated
Variable [unit]	$\times 10^{-40}$cm^2/unit/^{12}C	$\times 10^{-40}$cm^2/unit/^{12}C	$\times 10^{-40}$cm^2/^{12}C
p_{μ^-} [GeV]	2.27 ± 0.85 (stat.) ± 0.81 (syst.)	0.48 ± 0.11 (stat.) ± 0.11 (syst.)	3.23 ± 0.68 (stat.) ± 0.82 (syst.)
$\cos\theta_{\mu^-}$	3.41 ± 1.55 (stat.) ± 1.88 (syst.)	47.1 ± 9.98 (stat.) ± 10.3 (syst.)	3.20 ± 0.66 (stat.) ± 0.78 (syst.)
p_{π^+} [GeV]	9.41 ± 2.14 (stat.) ± 2.11 (syst.)	1.27 ± 0.34 (stat.) ± 0.40 (syst.)	3.35 ± 0.67 (stat.) ± 0.87 (syst.)
$\cos\theta_{\pi^+}$	2.68 ± 0.88 (stat.) ± 0.74 (syst.)	19.8 ± 4.54 (stat.) ± 4.97 (syst.)	3.19 ± 0.67 (stat.) ± 0.81 (syst.)
$E_{\pi^+} + E_{\mu^-}$ [GeV]	1.87 ± 0.57 (stat.) ± 0.51 (syst.)	0.35 ± 0.09 (stat.) ± 0.087 (syst.)	3.23 ± 0.67 (stat.) ± 0.82 (syst.)
Variable [unit]	$\times 10^{-42}$cm^2/unit/^{12}C	$\times 10^{-42}$cm^2/unit/^{12}C	$\times 10^{-40}$cm^2/^{12}C
$\theta_{\pi^+\mu^-}$ [deg]	3.09 ± 0.72 (stat.) ± 0.76 (syst.)	4.54 ± 1.37 (stat.) ± 1.91 (syst.)	3.16 ± 0.67 (stat.) ± 0.82 (syst.)

11.2 Upper Limit on Oxygen

In order to obtain the 95% C.L. upper limit on the coherent pion production on oxygen target, we use two methods already described. The first one which relies on Bayes' theorem uses the number of true signal events $\tilde{N}_k^{\mathrm{FGD1}}$ and $\tilde{N}_k^{\mathrm{FGD2}}$ for each bin k to obtain the upper limit on the number of coherent events on oxygen target. Table 11.8 shows these results for each bin and each variable. Given that the limit on the total number of signal events is

Table 11.8: Number of events in each unfolded bin after efficiency correction and subtraction of the non coherent background. In the last column, the 95 % upper limit is calculated with (9.20) and (9.1) where $\tilde{N}_k^O = s$. n is the total number of true events observed in FGD2, b' is the number of true events observed in FGD1 and s is the upper limit on the number of events. The number of expected signal events is also given and corresponds to $n - \alpha b'$.

Variable X	Bin	$\tilde{N}_k^{\mathrm{FGD1}}$	$\tilde{N}_k^{\mathrm{FGD2}}$	signal expected	limit	limit on $\left\langle \frac{d\sigma}{dX} \right\rangle$
[unit]		b'	n	$n - \alpha b'$	s	[10^{-40}cm^2/unit/^{16}O]
p_{μ^-} [GeV]	1	45.0	89.0	62.7	80.8	8.58
	2	82.4	89.5	41.4	60.5	0.75
$\cos(\theta_{\mu^-})$	1	33.7	88.4	68.7	86.6	18.4
	2	92.9	90.9	36.7	56.2	59.7
p_{π^+} [GeV]	1	74.4	89.5	46.1	65.5	13.9
	2	58.0	91.7	57.9	76.8	3.71
$\cos(\theta_{\pi^+})$	1	47.7	79.5	51.7	66.9	7.89
	2	78.3	102.2	56.2	76.8	40.8
$E_{\pi^+} + E_{\mu^-}$ [GeV]	1	55.3	97.1	64.9	84.3	5.97
	2	72.2	80.7	38.7	57.0	0.57
$\theta_{\pi^+\mu^-}$ [deg]	1	79.6	91.6	45.2	64.8	0.053
	2	44.9	84.4	58.2	76.0	0.16

142, after applying the flux and bin width normalisation, we obtain the upper limit on the

total flux-integrated cross section $\sigma_O^{95\,\%} = 7.54 \times 10^{-40}\,\mathrm{cm}^2/^{16}O$.

The second method to find the upper limit is to repeat multiple times the extraction of the cross section using toy experiments where different parameters vary as described in Section 10.4. Figure 11.7 shows the integration over the throw results for all the bins of the differential cross sections and the total flux-integrated cross section. The 95 % upper limits are indicated in the top right pads of each plots and are also reported in Table 11.9. Similar to what was observed in the fake data studies, the integration over the throws gives higher limits that the Bayes theorem approach. Similarly to the results on carbon, the total flux-integrated cross section differs according to which variable is used in the integration.

Rein-Sehgal and Berger-Sehgal coherent events scattering off an oxygen nucleus have been generated with NEUT where the input neutrino energy corresponds to the ND280 flux. The distributions of these events in the reduced phase space are shown in Figure 11.8 where both calculations of the upper limits are plotted. It is clear that the Rein-Sehgal predictions are overestimated however, regardless of how the limit is calculated, the Berger-Sehgal model seems to always be compatible with the upper limit.

To summarise, the upper limit of coherent pion production on oxygen nucleus has been assessed with two different methods. The first method relies on Bayes theorem to find the upper limit on the number of events, which can then be normalised in order to obtain a cross section value. The second method studies the effect of parameters variations on the cross section value. This allows to build a probability distribution function for the cross section which is then integrated to extract the cross section limit. While the first approach only accounts for statistical variation, the integration method contains statistical and systematic effects. Table 11.9 summarises the values obtained from both approaches.

Table 11.9: Summary of the 95 % upper limit calculated with different variables using the integration over the throw distributions. In the green parenthesis, the numbers obtained in the previous chapter using a Bayesian approach are recalled.

Variable [unit]	Bin 1 [$\times 10^{-40}$cm^2/unit/^{16}O]	Bin 2 [$\times 10^{-40}$cm^2/unit/^{16}O]	Integrated [$\times 10^{-40}$cm^2/^{16}O]
p_{μ^-} [GeV]	11.3 (8.58)	1.07 (0.75)	9.47
$\cos\theta_{\mu^-}$	23.9 (18.4)	88.8 (59.7)	9.68
p_{π^+} [GeV]	23.6 (13.9)	4.77 (3.71)	9.97
$\cos\theta_{\pi^+}$	11.6 (7.89)	52.8 (40.8)	10.0
$E_{\pi^+} + E_{\mu^-}$ [GeV]	8.01 (5.97)	0.82 (0.57)	9.57
$\theta_{\pi^+\mu^-}$ [deg]	0.077 (0.053)	0.20 (0.16)	9.58

(7.54)

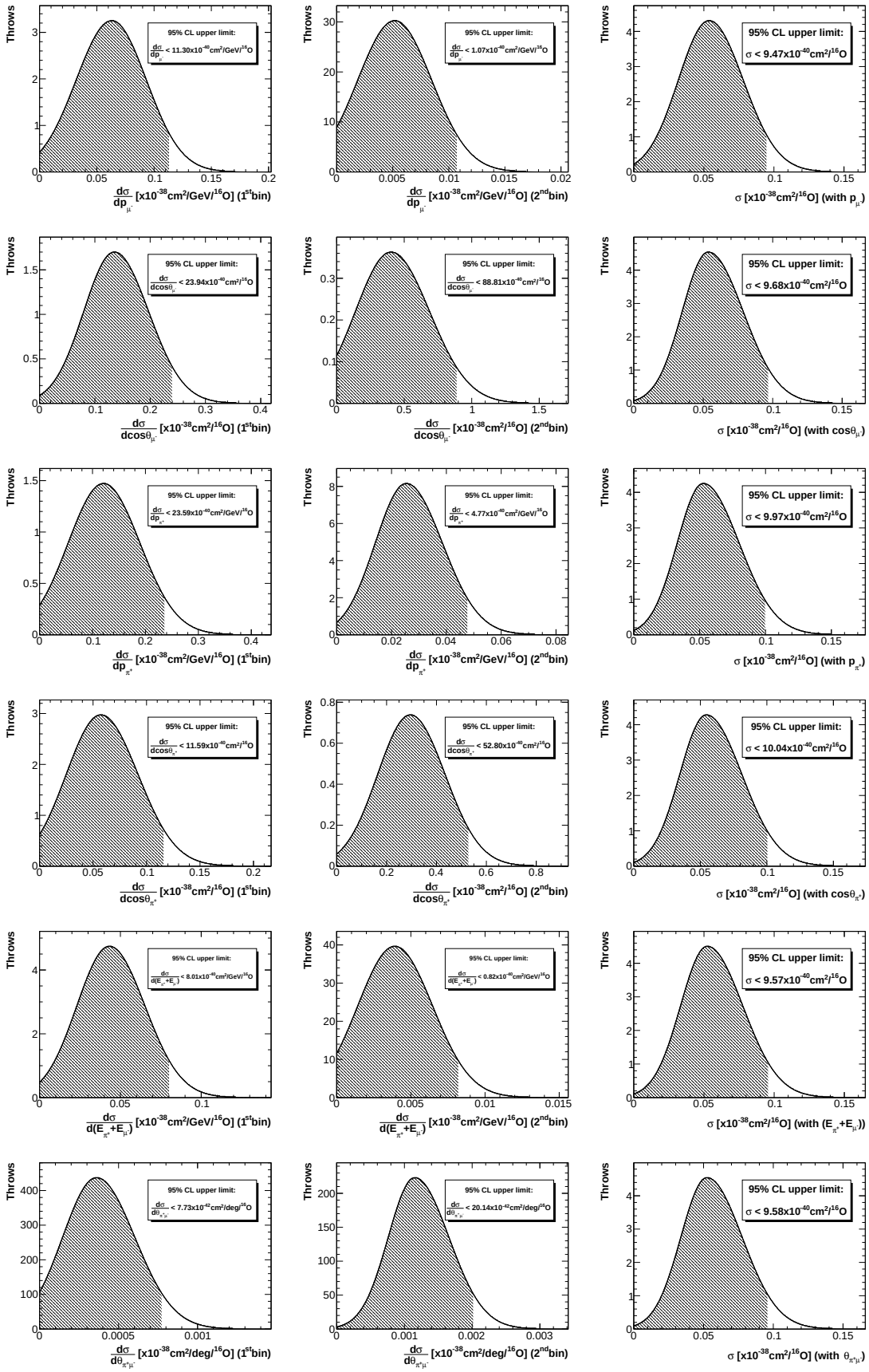

Figure 11.7: Integration of the probability density function for the first (left) and second (centre) bins and for the total cross section (right). The 95 % CL upper limit is given in each case.

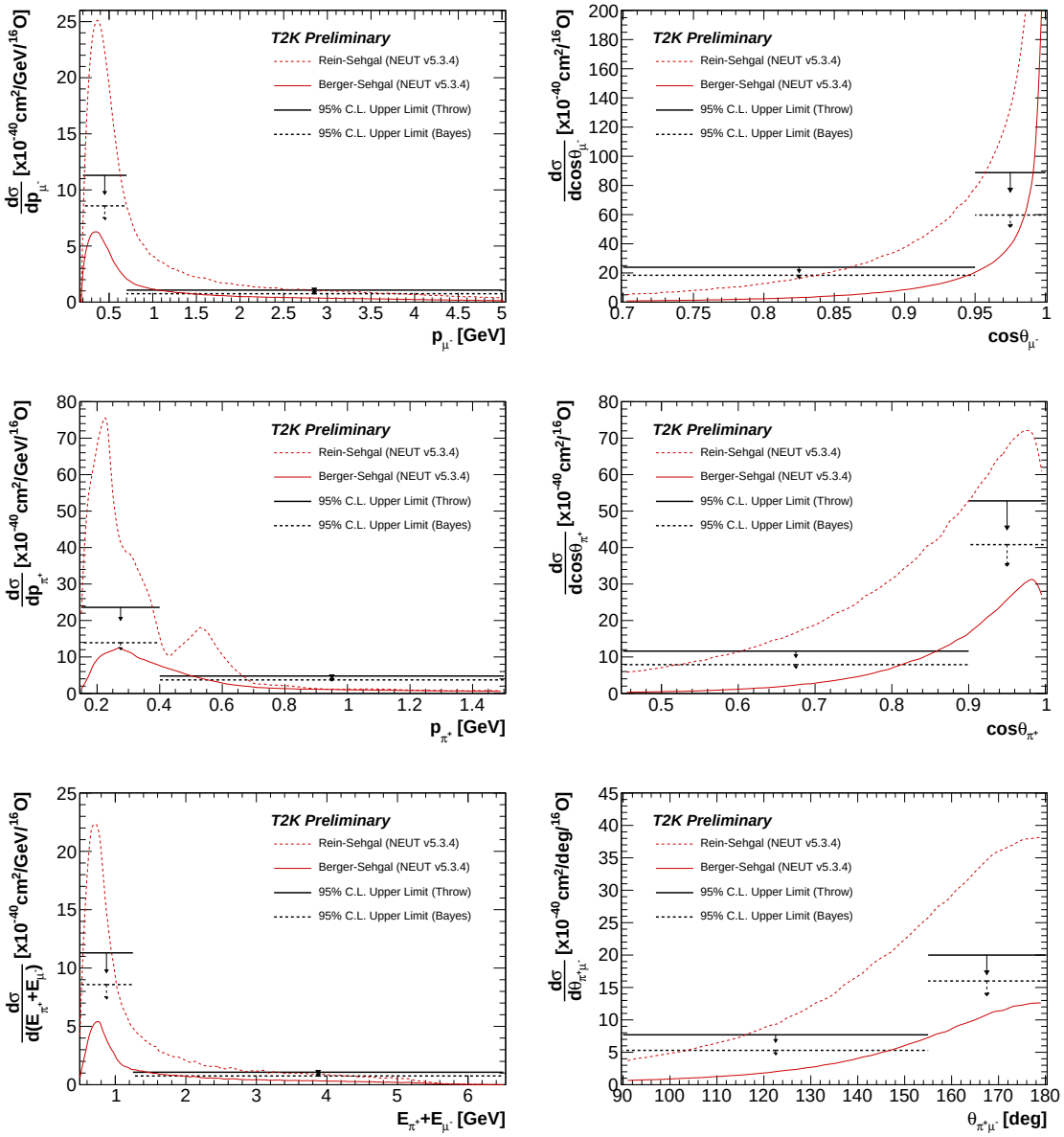

Figure 11.8: Comparison of the 95 % upper limits obtained with the bayesian method (dashed black line) and throw integration method (plain black line) with the NEUT predictions. The dashed red line correspond to the Rein-Sehgal model while the solid red line shows the Berger-Sehgal prediction, both from NEUT v5.3.4.

12

Conclusion

The Rein-Sehgal model used by the NEUT neutrino events generator disagreed with the low energy MINERvA results. In order to improve the quality of the ND280 Monte-Carlo simulations, the new Berger-Sehgal model was implemented. Because the latter model is based on the pion-carbon scattering cross section, a linear ad-hoc scaling with the target atomic number was added.

Following this upgrade, coherent pion production events interacting in the T2K near detector ND280 are selected in an attempt to measure the flux-integrated cross section on both carbon and oxygen targets. The main selection steps consist of a low vertex energy and energy transfer $|t|$ cuts. Differential cross sections are also investigated as a function of muon and pion momentum and angles, sum of muon and pion energies and coplanarity angle between the two tracks. Thanks to the geometry of ND280, it is possible to select events interacting on both carbon only in FGD1 and carbon plus water in FGD2. Oxygen events are then extracted via the FGD subtraction method. Even though the selection cuts and binning are optimised with the Rein-Sehgal model, a reweight of these events allows to extract the efficiency corrections and event numbers in each bin for the Berger-Sehgal model. The resonant and DIS backgrounds are constrained with control samples selected by reversing the vertex activity cut. The other backgrounds such as NC and $\overline{\nu}_\mu$ events are subtracted based on the MC predictions. The results are presented in a reduced phase space where ND280 has a good sensitivity. The true cross section values were extracted with a single iteration bayesian unfolding algorithm. Statistical and systematic errors (detector, model and flux) are accounted for. The flux-integrated cross section on carbon is equal to

$$< \sigma_C >= 3.23 \pm 0.67(\text{stat.}) \pm 0.82(\text{syst.}) \times 10^{-40}\text{cm}^2 \text{ per carbon nucleus} \qquad (12.1)$$

There is not enough events to measure the value of the cross section on oxygen with the same procedure than for the carbon one. Therefore a 95 % confidence level upper limit is set. Two methods are studied to calculate the upper limit. The first exclusively uses the Bayes theorem, including a poissonian variation of the number of events in FGD1 and FGD2. The upper limit on the number of events is found and normalised with flux integral, efficiency and number of targets to obtain the upper limit on the cross section. The second method is based on the concept of toy experiment. The cross sections are extracted several thousands of time where for every toy, a different parameter is varied. Hence the probability density function of the cross section and differential cross sections are build and one can integrate this function to find the 95 % confidence level limit. This second method has the advantage of taking both statistical and systematic errors into account. The limits obtained with the bayesian method are always lower than the ones obtained with the probability density function (PDF) integration:

$$\sigma_O^{\mathrm{PDF}} \leq 9.57 \times 10^{-40}\mathrm{cm}^2 \text{ per oxygen nucleus, with } 95\,\% \text{ probability} \tag{12.2}$$

$$\sigma_O^{\mathrm{Bayes}} \leq 7.54 \times 10^{-40}\mathrm{cm}^2 \text{ per oxygen nucleus, with } 95\,\% \text{ probability} \tag{12.3}$$

Because it includes systematic error and to adopt a conservative approach, the upper limit calculated with the throw integration is considered to be more relevant. Note that the upper limits are also given for the differential cross section. Finally, note that the lack of diffractive scattering model in the simulation prevent us from estimating the amount of diffractive backgrounds on hydrogen in the selected sample. So far, MINERvA is the only experiment which observed an excess consistent with diffractive scattering [127]. With the accumulation of more statistics and development of new detectors such as liquid argon chambers, future neutrino cross section experiments should be able to better characterise this diffractive scattering.

A

Standard Model Lagrangian

The standard model lagrangian for the weak interaction is written:

$$\mathcal{L}_{GWS} = \mathcal{L}_{\text{fermion}} + \mathcal{L}_{\text{boson}} + \mathcal{L}_H + \mathcal{L}_Y \tag{A.1}$$

This decomposition separates different interaction terms. First is the interactions between fermions and bosons.

$$\begin{aligned}
\mathcal{L}_{\text{fermion}} &= i\bar{\psi}\gamma_\mu D^\mu\psi \\
\mathcal{L}_{\text{fermion}} &= i\bar{\psi}\gamma_\mu\partial^\mu\psi \\
&\quad + \frac{g}{\sqrt{2}}\bar{\psi}\gamma_\mu(W_+^\mu T_+ + W_-^\mu T_-)\psi \\
&\quad + \frac{g}{\cos\theta_w}\bar{\psi}\gamma_\mu Z^\mu(T_3 - \sin^2\theta_w Q)\psi + e\bar{\psi}\gamma_\mu A^\mu\psi
\end{aligned} \tag{A.2}$$

The boson self couplings reads:

$$\begin{aligned}
\mathcal{L}_{\text{boson}} &= -\frac{1}{4}W_a^{\mu\nu}W_{a,\mu\nu} - \frac{1}{4}B^{\mu\nu}B_{\mu\nu} \\
&= \mathcal{L}_{\text{cubic}} + \mathcal{L}_{\text{quartic}}
\end{aligned} \tag{A.3}$$

where we have:

$$\begin{aligned}
\mathcal{L}_{\text{cubic}} = &-i\frac{g^2}{\sqrt{g^2+g'^2}} \quad \Big[(\partial^\mu W_+^\nu - \partial^\nu W_+^\mu)W_{-\mu}Z_\nu - (\partial^\mu W_-^\nu - \partial^\nu W_-^\mu)W_{+\mu}Z_\nu \\
&\qquad\qquad + W_{+\mu}W_{-\nu}(\partial^\mu Z^\nu - \partial^\nu Z^\mu)\Big] \\
&-i\frac{gg'}{\sqrt{g^2+g'^2}} \quad \Big[(\partial^\mu W_+^\nu - \partial^\nu W_+^\mu)W_{-\mu}A_\nu - (\partial^\mu W_-^\nu - \partial^\nu W_-^\mu)W_{+\mu}A_\nu \\
&\qquad\qquad + W_{+\mu}W_{-\nu}(\partial^\mu A^\nu - \partial^\nu A^\mu)\Big]
\end{aligned} \tag{A.4}$$

$$\begin{aligned}\mathcal{L}_{\text{quartic}} = &-\frac{1}{2}g^2 \qquad \left[(W_{-\mu}W_{+}^{\mu})^2 - W_{-\mu}W_{-}^{\mu}W_{+\nu}W_{+}^{\nu}\right] \\ &-\frac{g^4}{g^2+g'^2} \quad \Big[W_{-\mu}W_{+}^{\mu}Z_{\nu}Z^{\nu} - W_{-\mu}Z^{\mu}W_{+\nu}Z^{\nu} + 2W_{-\mu}W_{+}^{\mu}Z_{\nu}A^{\nu} \\ &\qquad\qquad -W_{-\mu}Z^{\mu}W_{+\nu}A^{\nu} - W_{-\mu}A^{\mu}W_{+\nu}Z^{\nu}\Big] \\ &-\frac{(gg')^2}{g^2+g'^2} \quad \left[W_{-\mu}W_{+}^{\mu}A_{\nu}A^{\nu} - W_{-\mu}A^{\mu}W_{+\nu}A^{\nu}\right]\end{aligned} \tag{A.5}$$

We note that in $\mathcal{L}_{\text{cubic}}$ and $\mathcal{L}_{\text{quartic}}$, all the coupling terms contain at least one W_- and one W_+ operator. Indeed, the electro-weak interaction doesn't allow coupling between Z and A only. Next comes the Higgs coupling to bosons (boson mass terms) and self-coupling (Higgs mass term).

$$\begin{aligned}\mathcal{L}_H = &\frac{1}{2}(\partial_\mu h)^2 - \frac{1}{2}\left[\sqrt{2\lambda}v\right]^2 h^2 - \lambda v h^3 - \frac{\lambda}{4}h^4 \\ &+\frac{1}{2}\left[\frac{gv}{2}\right]^2 (W_{+\mu}W_{+}^{\mu} + W_{-\mu}W_{-}^{\mu}) + \frac{1}{2}\left[\frac{gv}{2\cos\theta_w}\right]^2 Z_\mu Z^\mu \\ &+\frac{g^2 v}{4}(W_{+\mu}W_{+}^{\mu} + W_{-\mu}W_{-}^{\mu})h + \frac{g^2}{8}(W_{+\mu}W_{+}^{\mu} + W_{-\mu}W_{-}^{\mu})h^2 \\ &+\frac{g^2 v}{4\cos^2\theta_w}Z_\mu Z^\mu h + \frac{g^2}{8\cos^2\theta_w}Z_\mu Z^\mu h^2\end{aligned} \tag{A.6}$$

Finally, the Higgs couples to the fermion fields giving fermion masses that correspond to Yukawa couplings:

$$\begin{aligned}\mathcal{L}_Y = &-\sum_{\alpha=e,\mu,\tau}\left(\left[\frac{vM^{\ell}_{\alpha\alpha}}{\sqrt{2}}\right]\overline{\ell}_{\alpha L}.\ell_{\alpha R} + \frac{M_{\alpha\alpha}}{\sqrt{2}}\overline{\ell}_{\alpha L}.\ell_{\alpha R}.h\right) \\ &-\sum_{\alpha=1,2,3}\left(\left[\frac{vM^{u}_{\alpha\alpha}}{\sqrt{2}}\right]\overline{q_u}_{\alpha L}.q_{u\alpha R} + \frac{M_{\alpha\alpha}}{\sqrt{2}}\overline{q_u}_{\alpha L}.q_{u\alpha R}.h\right) \\ &-\sum_{\alpha=1,2,3}\left(\left[\frac{vM^{d}_{\alpha\alpha}}{\sqrt{2}}\right]\overline{q_d}_{\alpha L}.q_{d\alpha R} + \frac{M_{\alpha\alpha}}{\sqrt{2}}\overline{q_d}_{\alpha L}.q_{d\alpha R}.h\right) + \text{h.c.}\end{aligned} \tag{A.7}$$

B

Another Approach to the A-scaling in the Berger-Sehgal Model

Another approach tested in NEUT is to go back to equation (3.21) and assume that the inelastic cross section (which is hidden in the F_{abs} factor) does not contribute to the scaling. Hence the A dependance becomes

$$f(A,|t|) = A^2 exp\left(-\frac{r_0^2 A^{2/3}}{3}|t|\right) \tag{B.1}$$

which once plugged in the BS model, transforms the pion-nucleus cross section defined in equation (7.4) as follow:

$$\frac{d\sigma_{el}}{dt} = A_1 \left(\frac{A}{12}\right)^2 exp\left(-b_1 \left(\frac{A}{12}\right)^{2/3} t\right) \tag{B.2}$$

This scaling is tested for several nuclei and compared against the results obtained from experiments with targets other than carbon. The results of this comparison are shown in Table B.1. Moreover, the ratios $\sigma(^{16}O)/\sigma(^{12}C)$, $\sigma(^{40}Ar)/\sigma(^{12}C)$ and $\sigma(^{56}Fe)/\sigma(^{12}C)$ are shown as a function of neutrino energy in Figure B.1 for neutral (left) and charged (right) current. The total ν_μ CC section is also given as a function of the atomic number A for 4 different energies in Figure B.2.

NEUT uses cross-section lookup tables to access the total cross-section and, for example, to normalise differential distributions. In order to avoid having one table for each target, a

Table B.1: Total coherent cross sections measured by several experiments compared against Rein-Sehgal predictions (using the $A^{1/3}$ scaling rule) and the scaling according to eq. (B.2) for Berger-Sehgal predictions. The unit of the given cross sections is 10^{-40} cm^2.

Experiments	Mode	A	$< E_\nu >$ (GeV)	σ_{exp} (10^{-40} cm^2)	RS ($A^{1/3}$ rule)	BS (as eq. (B.2))
Aachen-Padova [136]	NC	27	2	29 ± 10	32.6	17.7
Gargamelle [137]	NC	30	2	31 ± 20	33.8	19.5
CHARM [138]	NC	20	30	96 ± 42	74.5	106
SKAT [139]	NC	30	7	79 ± 28	59.5	60.8
NOMAD [140]	NC	12.8	24.8	72.6 ± 10.6	61.9	58.2
ArgoNeuT [141]	ν_μ CC	40	9.6	260 ± 150	139.5	190
MINERvA [135]	ν_μ CC	12	4.11	34.9 ± 6.8	65.4	27.7

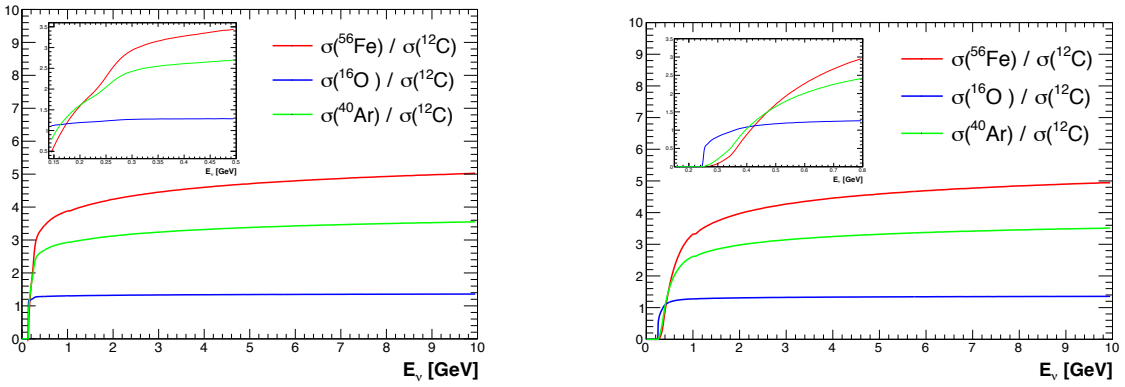

Figure B.1: Cross section ratio as a function of neutrino energy for different nuclei where the A scaling is described by eq. (B.2). Left: neutral current interaction. Right: charged current interaction. The snippets correspond to a zoom in the low energy regions.

general scaling is applied in these tables. The behaviour of the cross section while varying the atomic number A is studied for different neutrino energies. Figure B.3 represents the evolution of $\sigma^{BS}_{\nu_\mu CC}$ for a wide range of neutrino energies. It is a shape comparison, therefore all the predictions are area normalised, which explains the arbitrary unit on the Y axis. We can see that this scaling is not valid in the case where a neutrino with an **energy below 0.5 GeV** scatters off a nucleus with $A > 50$, as the cross section started to decrease. For the other cases, it seems that the power of A increases with the neutrino energy. This is also highlighted by the Figure B.4, where a direct comparison between the cross sections and 3 example of power law is performed. The bias, defined below as the

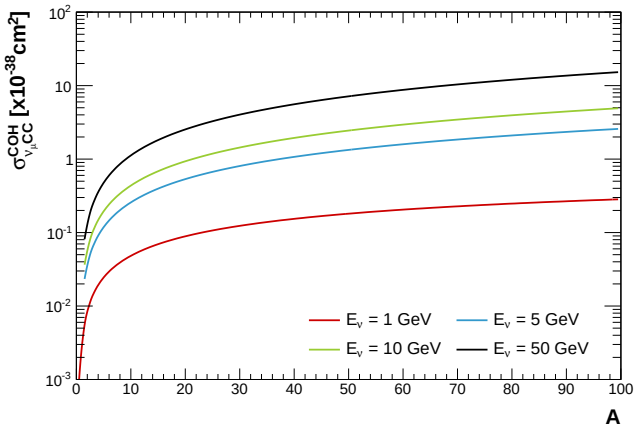

Figure B.2: Berger-Sehgal charged current coherent cross section as a function of atomic number A using the scaling described above for 4 neutrino energies: 1 GeV (red), 5 GeV (blue), 10 GeV (green) and 50 GeV (black).

deviation from a given power law, is also given for different power α.

$$\textbf{Bias} = \frac{\sigma(E_\nu, A) - (A/12)^\alpha}{\sigma(E_\nu, A)} \tag{B.3}$$

We see that it is difficult to extract a global scaling regardless of the neutrino energy, as the power laws seem to be different for each energy range investigated. This behaviour is enhanced in the low energy region, below 1 GeV where the cross section even tends to decrease as A increases. For these two reasons, a linear scaling in A was preferred.

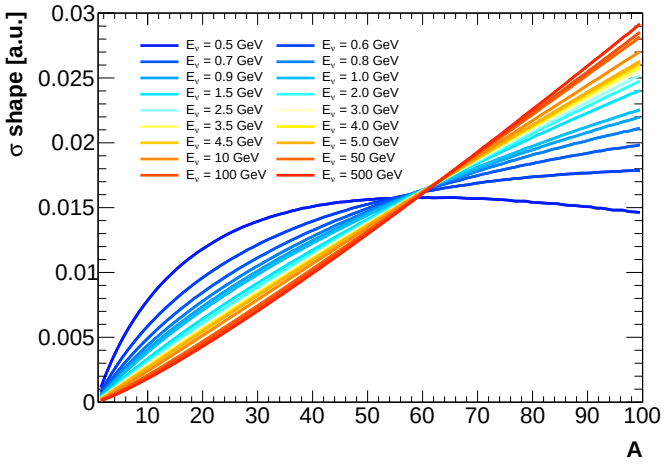

Figure B.3: Berger-Sehgal charged current coherent cross section as a function of atomic number A for a wide range of neutrino energies. All the curves are area normalised to facilitate the shape comparison.

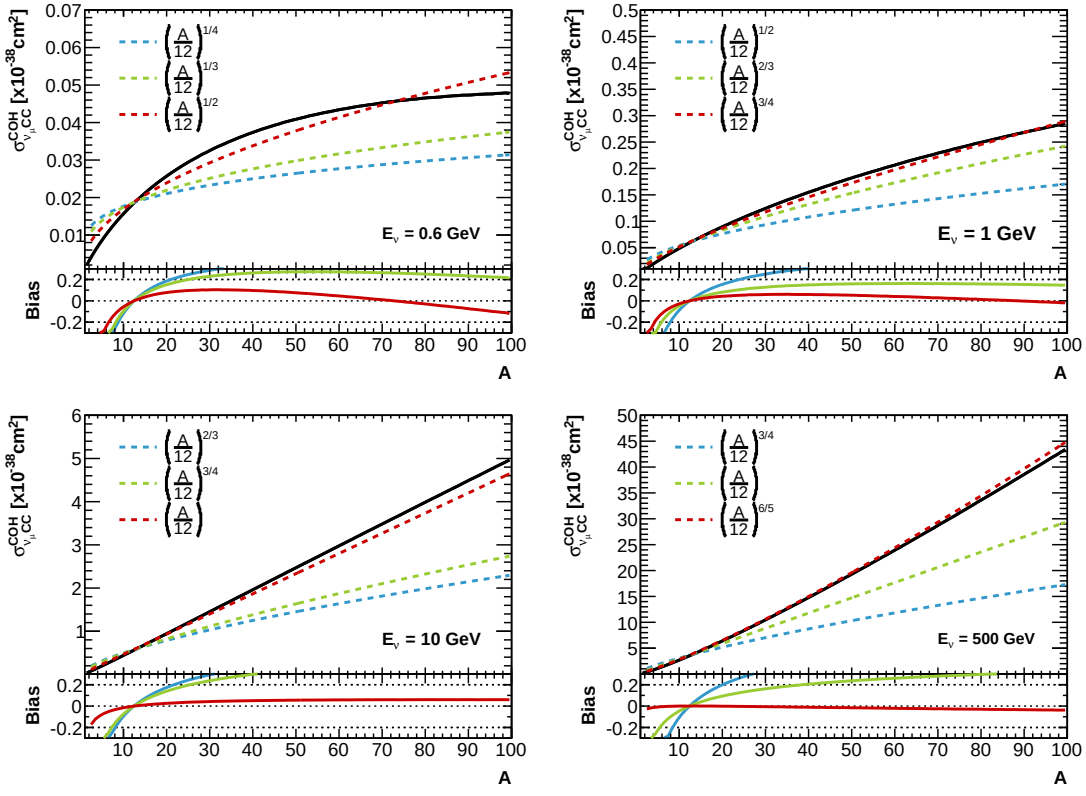

Figure B.4: Berger-Sehgal charged current coherent cross section as a function of atomic number A using the scaling described above for 4 neutrino energies: 1 GeV (red), 5 GeV (blue), 10 GeV (green) and 50 GeV (black).

C

Background control samples

Figures C.1 and C.2 illustrate the kinematic variables in each sideband before any phase space cuts are applied. Except for the coplanarity angle $\theta_{\pi\mu}$, the shapes look similar to the signal distributions.

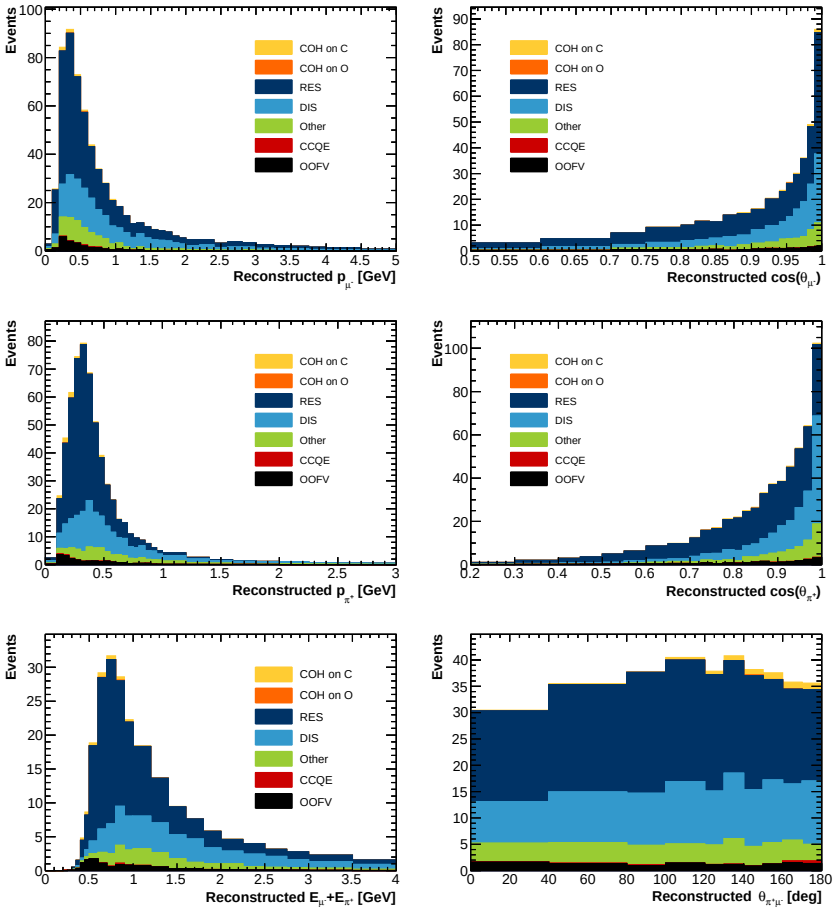

Figure C.1: Reconstructed kinematic distributions of the NEUT nominal MC in the FGD1 sideband. From top left to bottom right: p_μ, $\cos(\theta_\mu)$, p_π, $\cos(\theta_\pi)$, $E_\mu + E_\pi$, $\theta_{\pi\mu}$.

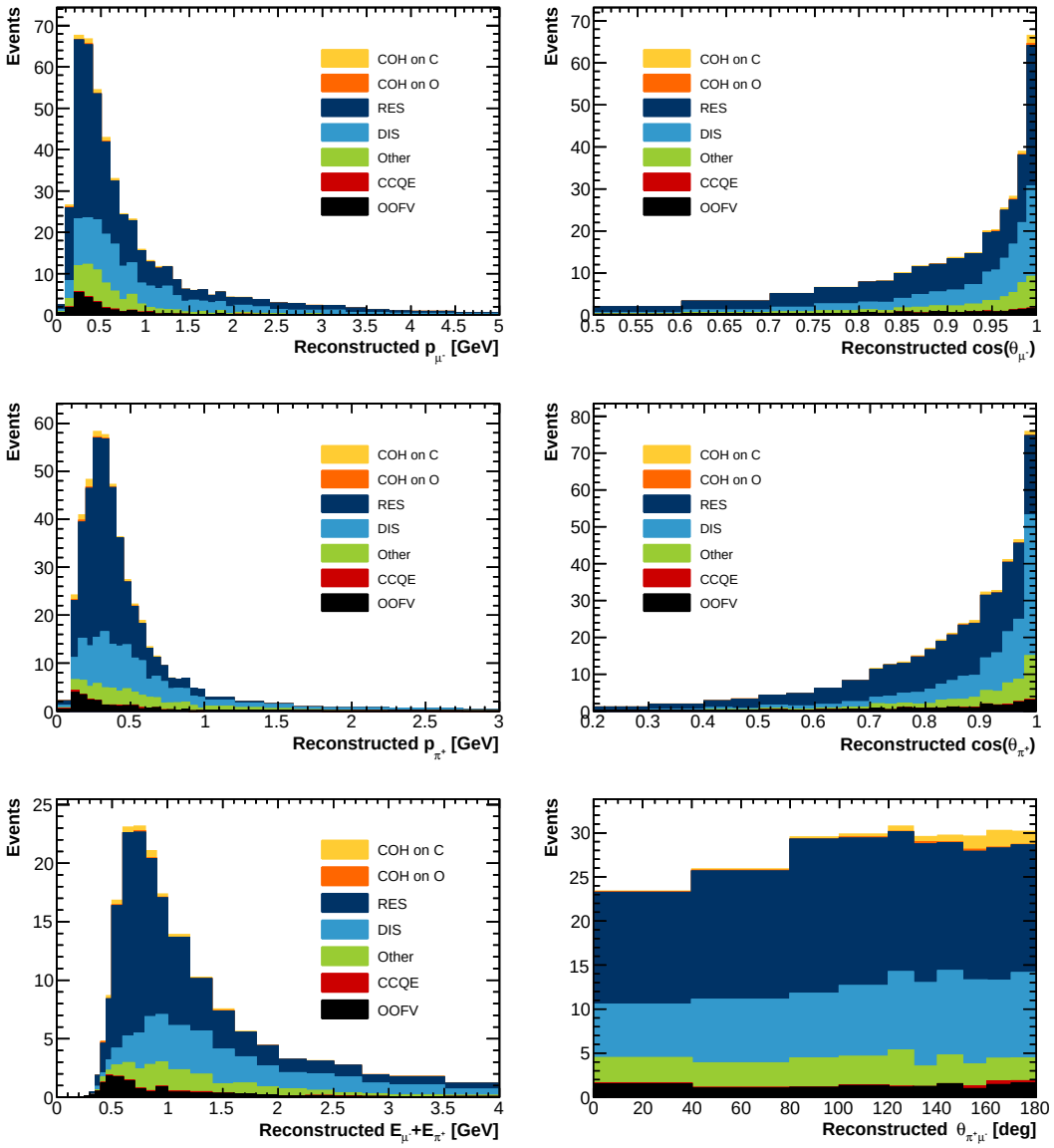

Figure C.2: Reconstructed kinematic distributions of the NEUT nominal MC in the FGD2 sideband. From top left to bottom right: p_μ, $\cos(\theta_\mu)$, p_π, $\cos(\theta_\pi)$, $E_\mu + E_\pi$, $\theta_{\pi\mu}$.

D

Additional Uncertainties plots

This appendix contains additional plots of the differential cross section measurement on carbon using the FGD1 selection and the upper limit measurement on oxygen using the FGD2-FGD1 subtraction. In all the the plots, the MC and the Fake Data correspond to the predictions of the NEUT events generator to match the **Berger-Sehgal** model. We give the covariance matrices for p_{μ^-}, $\cos(\theta_{\mu^-})$, p_{π^+}, $\cos(\theta_{\pi^+})$ and $\theta_{\pi^+\mu^-}$ along with the differential cross section result obtain via single iteration Bayesian unfolding. The non-coherent background is constrained by the $E_{\pi^+} + E_{\mu^-}$ sideband and then subtracted. Firstly, all the statistical errors are detailed for every variable investigated, then the detector fractional errors are presented with their covariance matrices. Finally the distributions of the toy experiments for the oxygen measurement are given.

D.1 Statistical errors

This section shows the differential cross section, covariance matrices and fractional errors of the 6 studied variables.

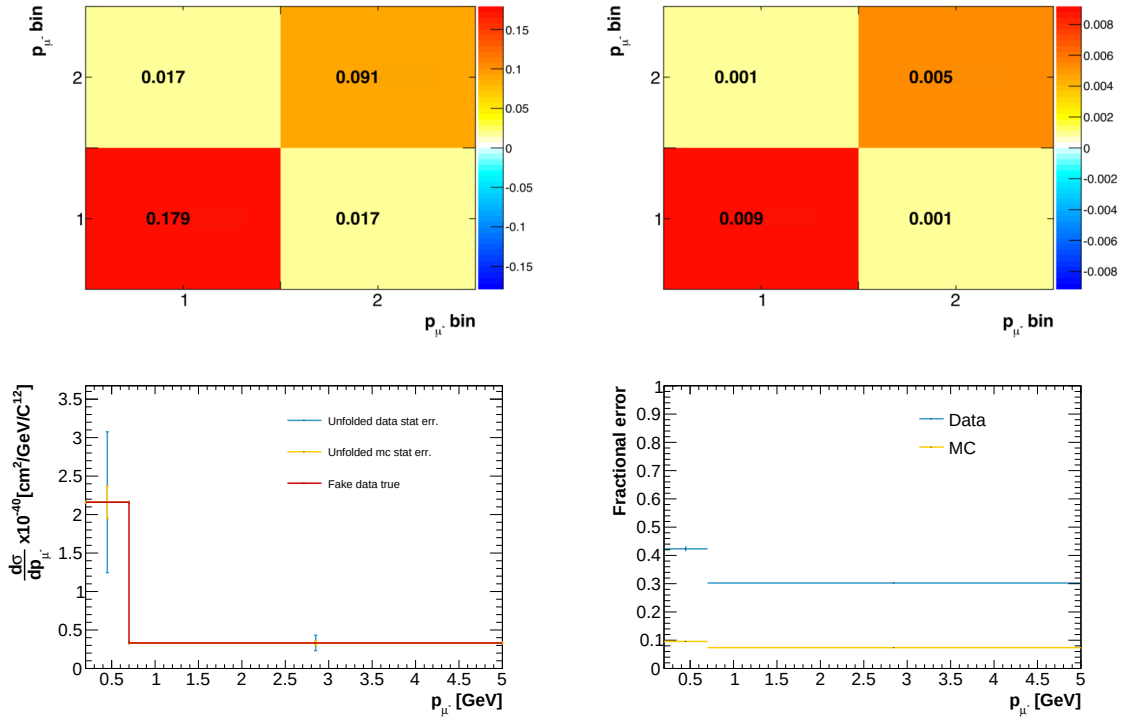

Figure D.1: Fractional covariance matrices for data (top left) and MC (top right) statistical errors for the p_{μ^-} variable. Differential cross section as a function of p_{μ^-} (bottom left) and statistical fractional error (bottom right)

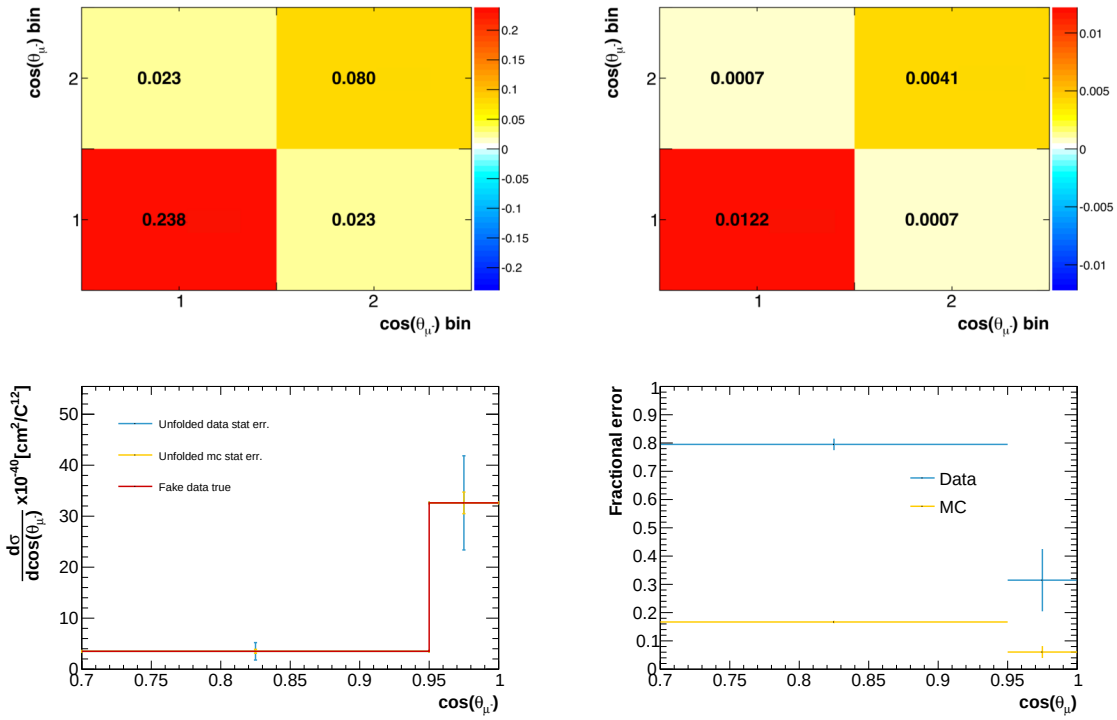

Figure D.2: Fractional covariance matrices for data (top left) and MC (top right) statistical errors for $\cos(\theta_{\mu^-})$ variable. Differential cross section as a function of $\cos(\theta_{\mu^-})$ (bottom left) and statistical fractional error (bottom right).

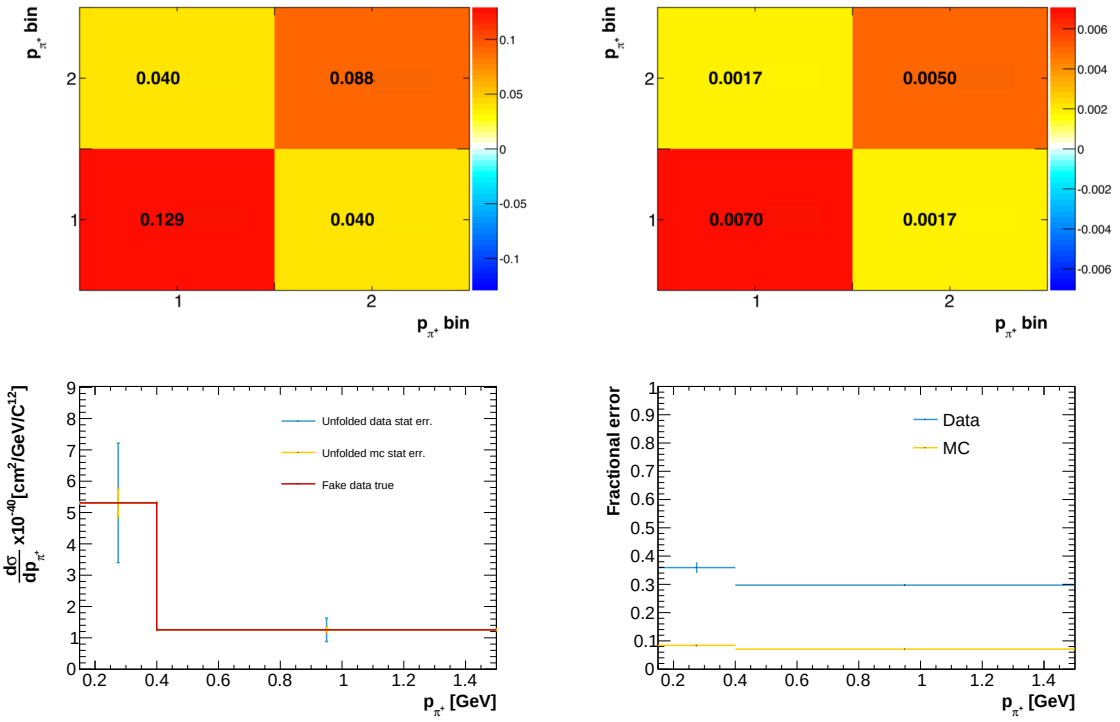

Figure D.3: Fractional covariance matrices for data (to left) and MC (to right) statistical errors for the $p_{\pi+}$ variable. Differential cross section as a function of $p_{\pi+}$ (bottom left) and statistical fractional error (bottom right)

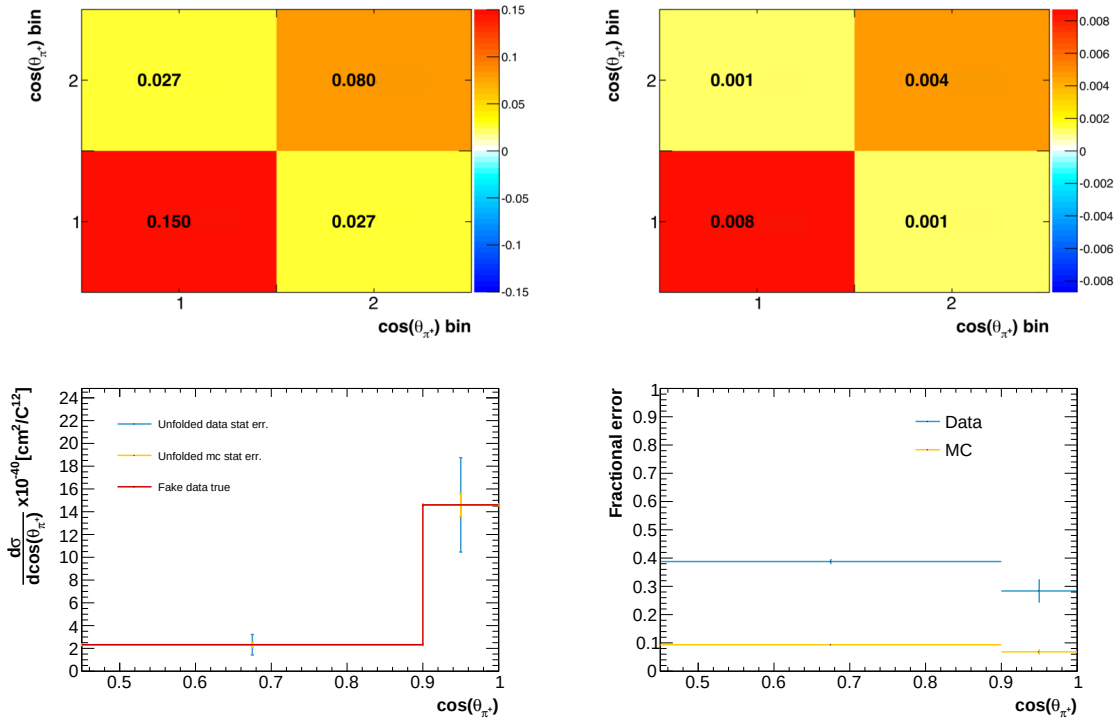

Figure D.4: Fractional covariance matrices for data (top left) and MC (top right) statistical errors for cos(θ_{π^+}) variable. Differential cross section as a function of cos(θ_{π^+}) (bottom left) and statistical fractional error (bottom right).

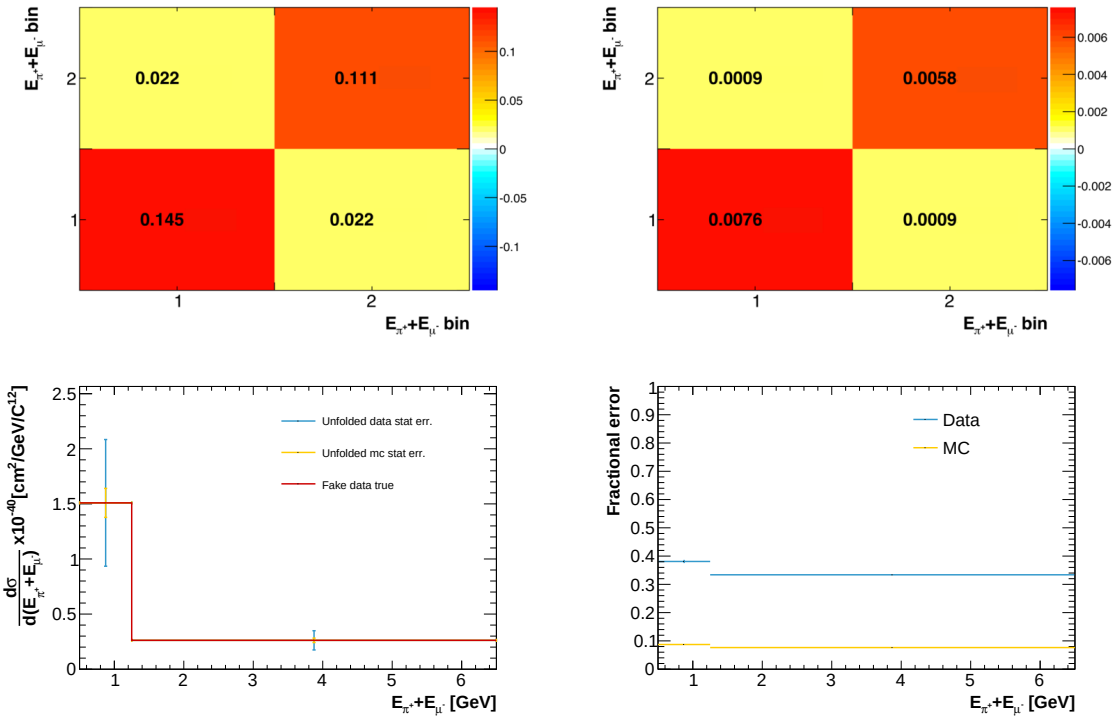

Figure D.5: Fractional covariance matrices for data (top left) and MC (top right) statistical errors for the $E_\pi + E_\mu$ variable. Differential cross section results as a function of $E_\pi + E_\mu$ (bottom left) and fractional statistical errors for the same variable (bottom right)

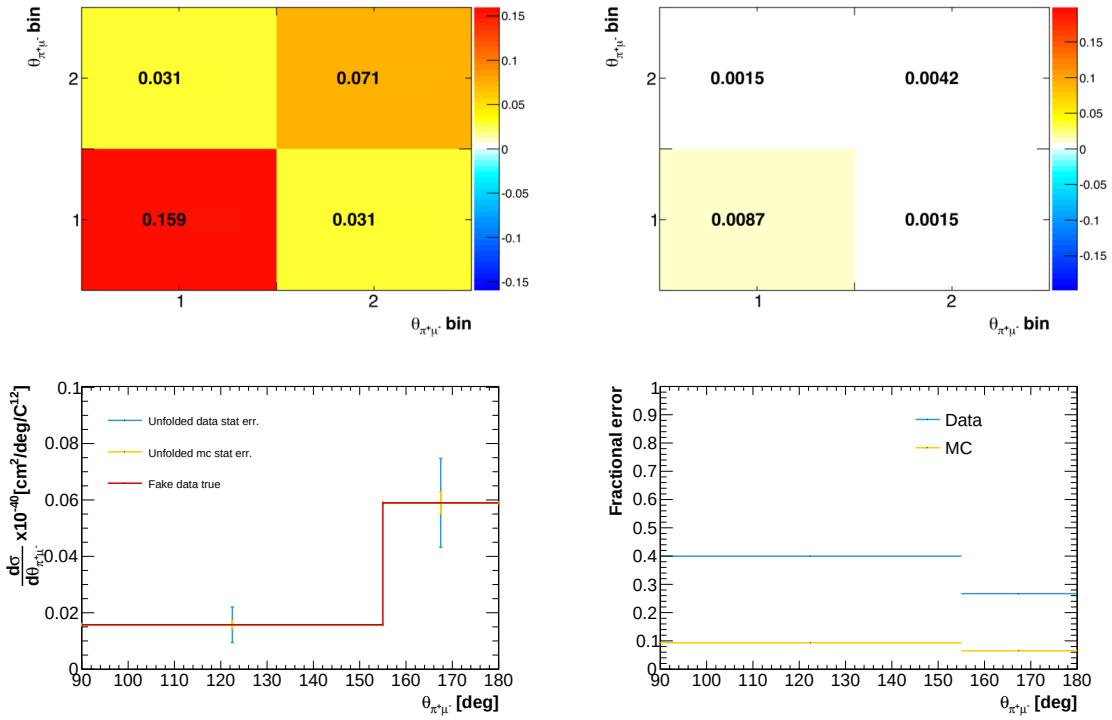

Figure D.6: Fractional covariance matrices for data (top left) and MC (top right) statistical errors for $\theta_{\pi^+\mu^-}$ variable. Differential cross section as a function of $\theta_{\pi^+\mu^-}$ (bottom left) and statistical fractional error (bottom right).

D.2 Detector systematics

This section displays the total detector systematic errors in the form of covariance matrices and fractional error for each variables. The relative contribution of each detector systematic is also given for the number of selected in in FGD1. We noticed that the TPC cluster and FGD PID systematics are negligible.

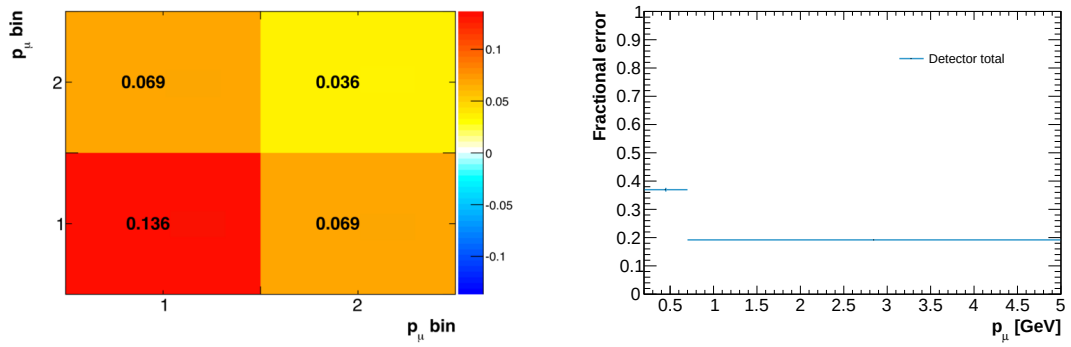

Figure D.7: Fractional covariance matrix for all detector systematics (left) and relative error (right) for the p_μ variable.

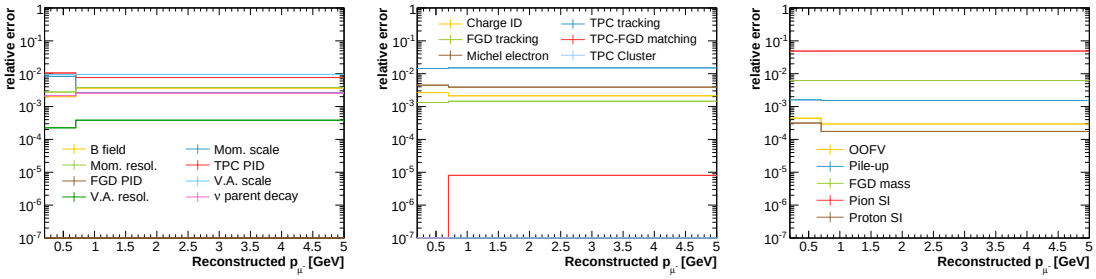

Figure D.8: Contributions of each of the variation (left), efficiency (middle) and normalisation (right) detector systematics for the p_μ variable. They correspond to the relative errors on the total number of events selected in FGD1 in the reduced phase space (NEUT nominal predictions).

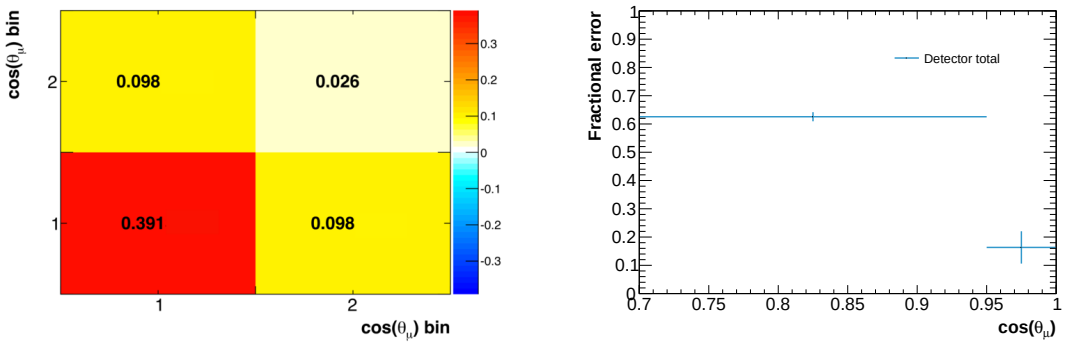

Figure D.9: Fractional covariance matrix for all detector systematics (left) and relative error (right) for the $\cos(\theta_\mu)$ variable.

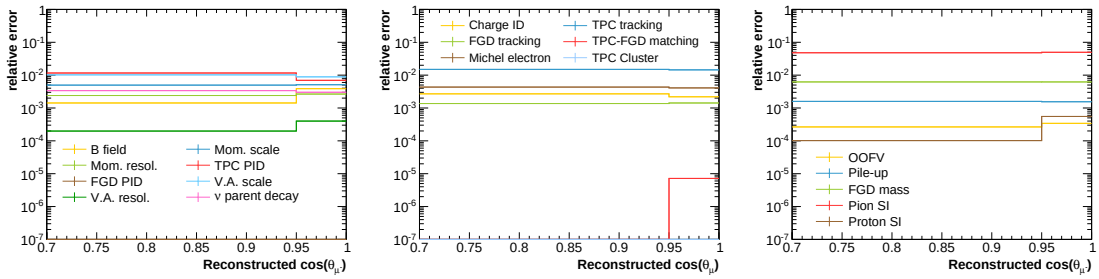

Figure D.10: Contributions of each of the variation (left), efficiency (middle) and normalisation (right) detector systematics for the $\cos(\theta_\mu)$ variable. They correspond to the relative errors on the total number of events selected in FGD1 in the reduced phase space (NEUT nominal predictions).

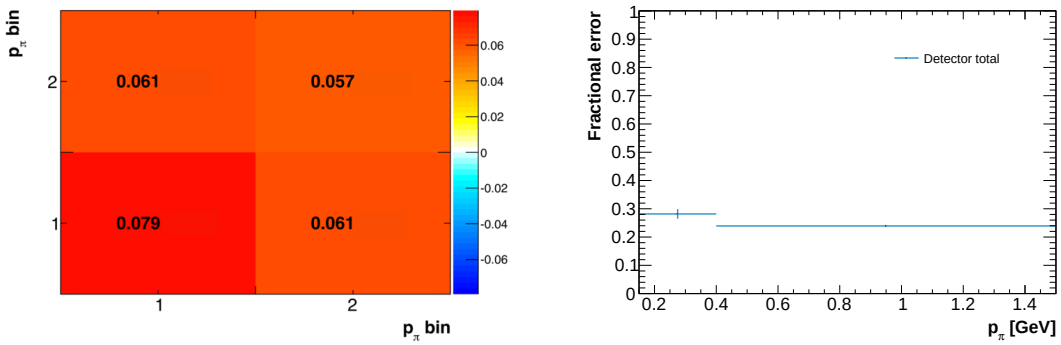

Figure D.11: Fractional covariance matrix for all detector systematics (left) and relative error (right) for the p_π variable.

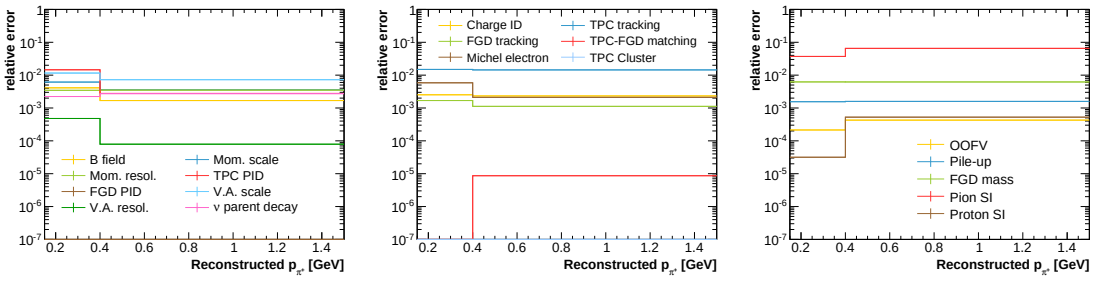

Figure D.12: Contributions of each of the variation (left), efficiency (middle) and normalisation (right) detector systematics for the p_π variable. They correspond to the relative errors on the total number of events selected in FGD1 in the reduced phase space (NEUT nominal predictions).

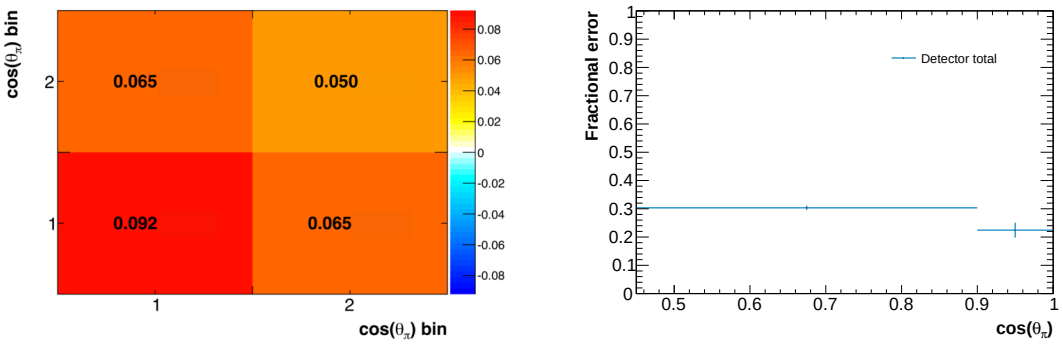

Figure D.13: Fractional covariance matrix for all detector systematics (left) and relative error (right) for the $\cos(\theta_\pi)$ variable.

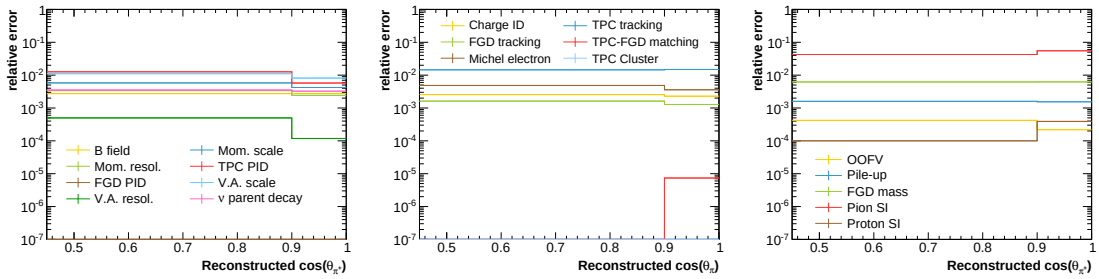

Figure D.14: Contributions of each of the variation (left), efficiency (middle) and normalisation (right) detector systematics for the $\cos(\theta_\pi)$ variable. They correspond to the relative errors on the total number of events selected in FGD1 in the reduced phase space (NEUT nominal predictions).

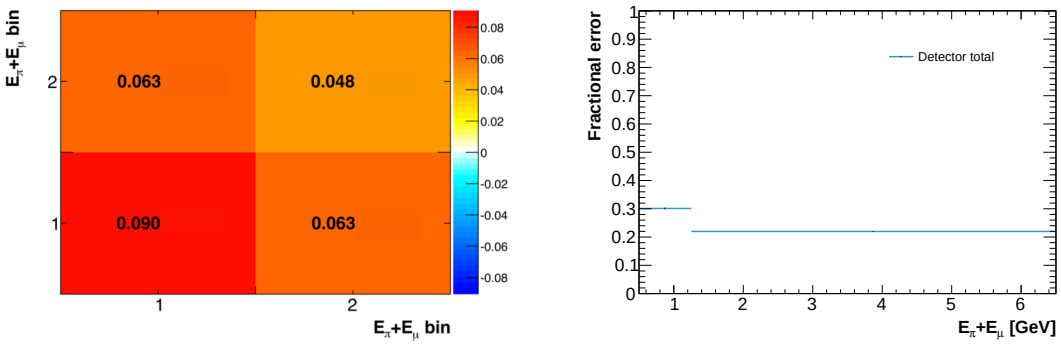

Figure D.15: Fractional covariance matrix for all detector systematics (left) and relative error (right) for the $E_\pi + E_\mu$ variable.

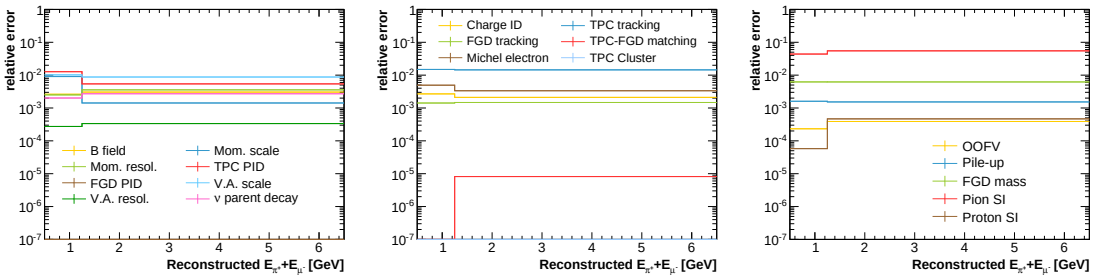

Figure D.16: Contributions of each of the variation (left), efficiency (middle) and normalisation (right) detector systematics for the $E_\pi + E_\mu$ variable. They correspond to the relative errors on the total number of events selected in FGD1 in the reduced phase space (NEUT nominal predictions).

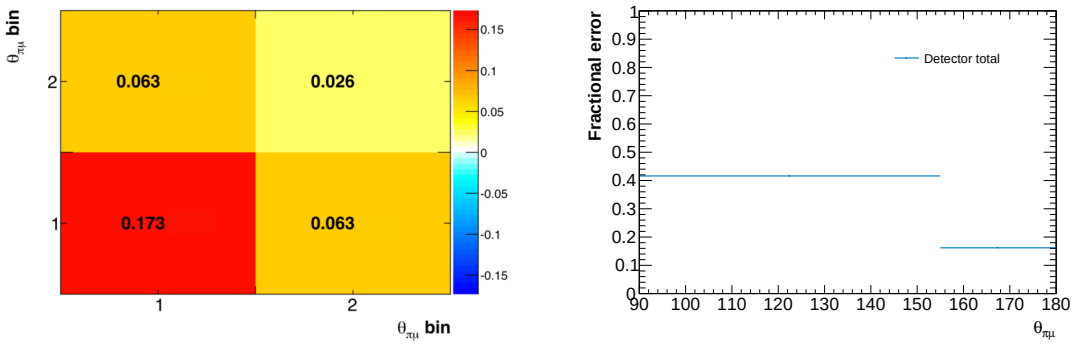

Figure D.17: Fractional covariance matrix for all detector systematics (left) and relative error (right) for the $\theta_{\pi\mu}$ variable.

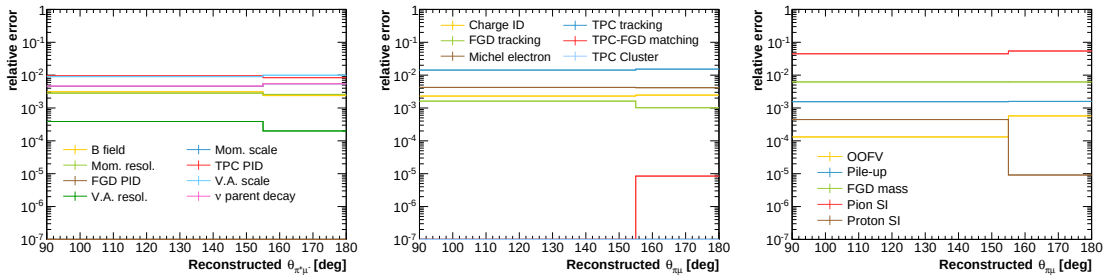

Figure D.18: Contributions of each of the variation (left), efficiency (middle) and normalisation (right) detector systematics for the $\theta_{\pi\mu}$ variable. They correspond to the relative errors on the total number of events selected in FGD1 in the reduced phase space (NEUT nominal predictions).

D.3 Probability density function integration

Below are the fit results of the throws used to set the upper limits on the differential cross section in each bins and on the integrated cross section.

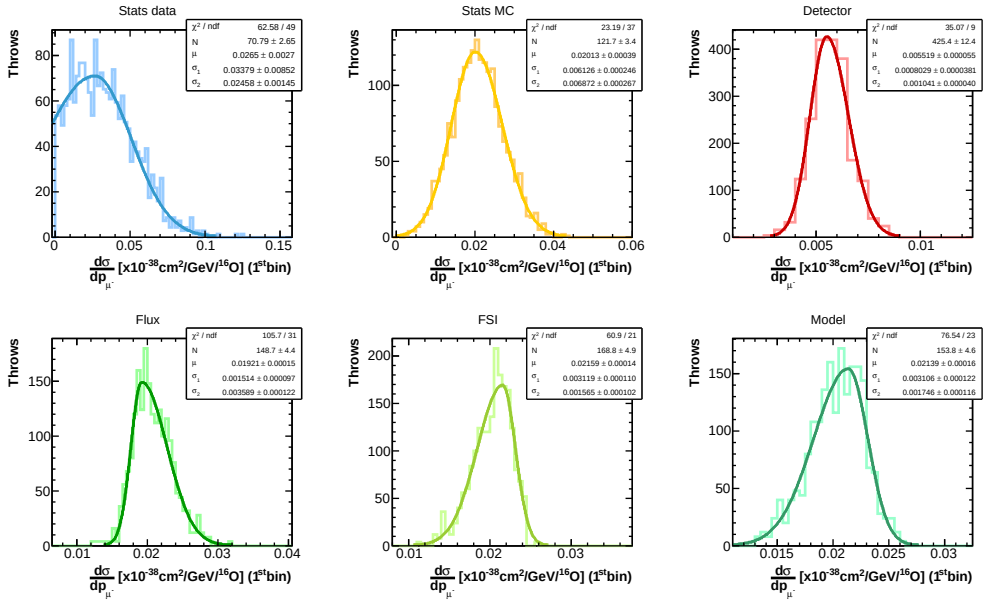

Figure D.19: Fits results for the different error sources for the first bin of p_{μ^-}.

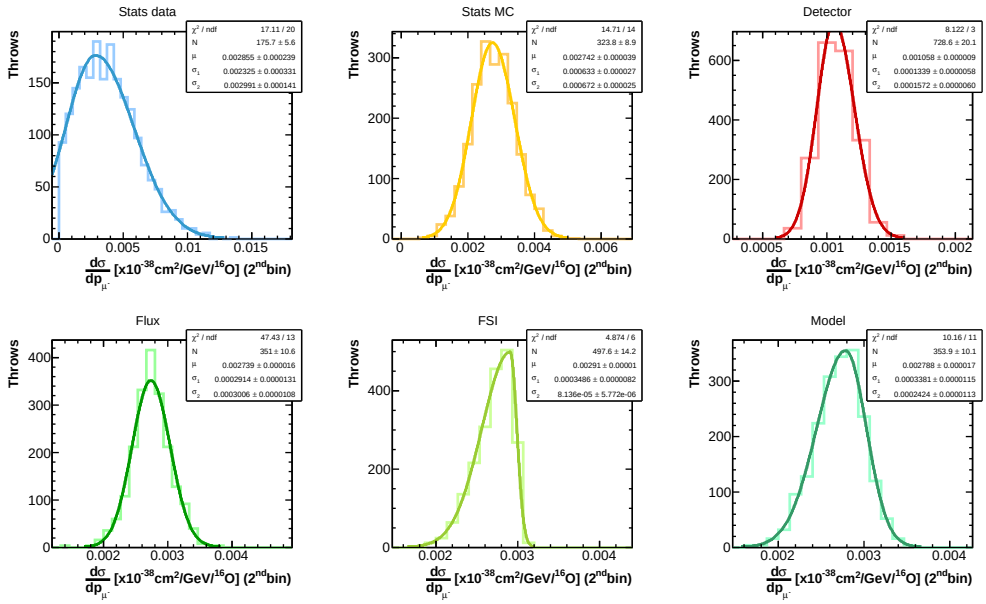

Figure D.20: Fits results for the different error sources for the second bin of p_{μ^-}.

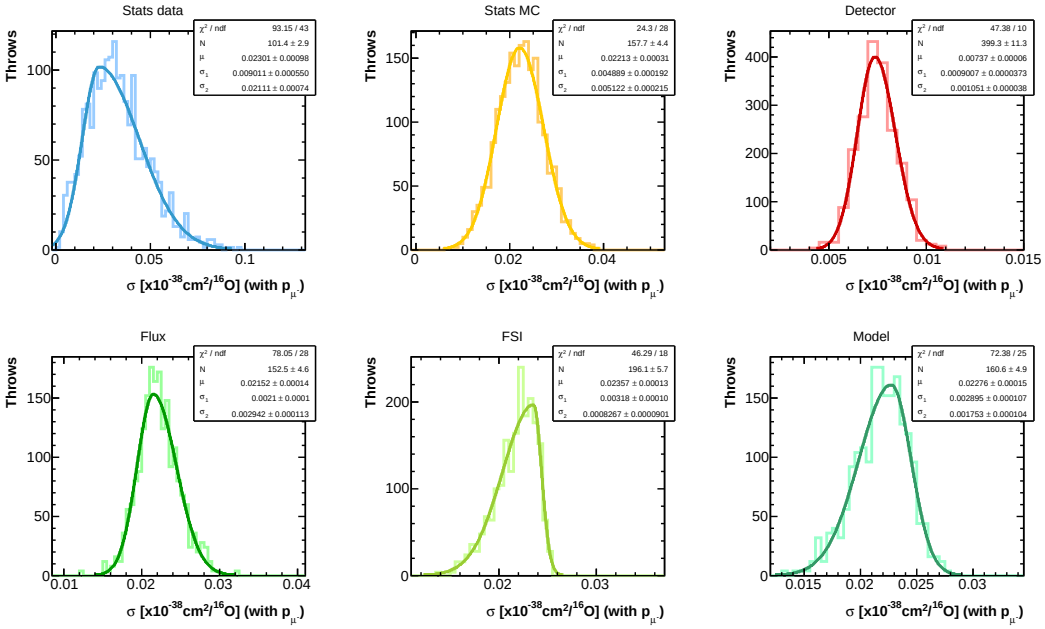

Figure D.21: Fits results for the different error sources for the cross section obtained by integrating over the p_{μ^-} bins.

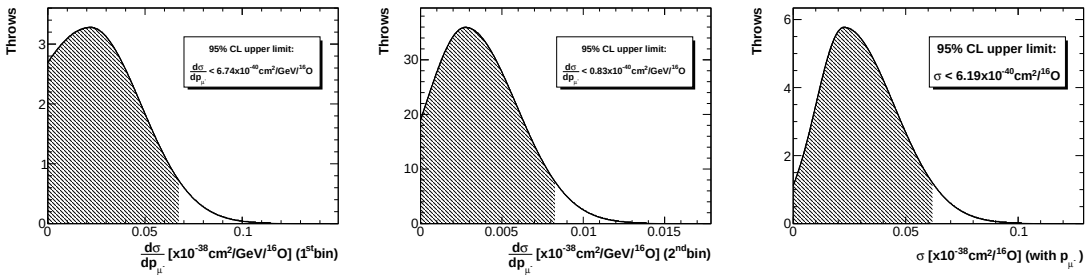

Figure D.22: Integration of the probability density function for the first (left) and second (centre) bins and for the total cross section (right). The 95 % CL upper limit is given in each case.

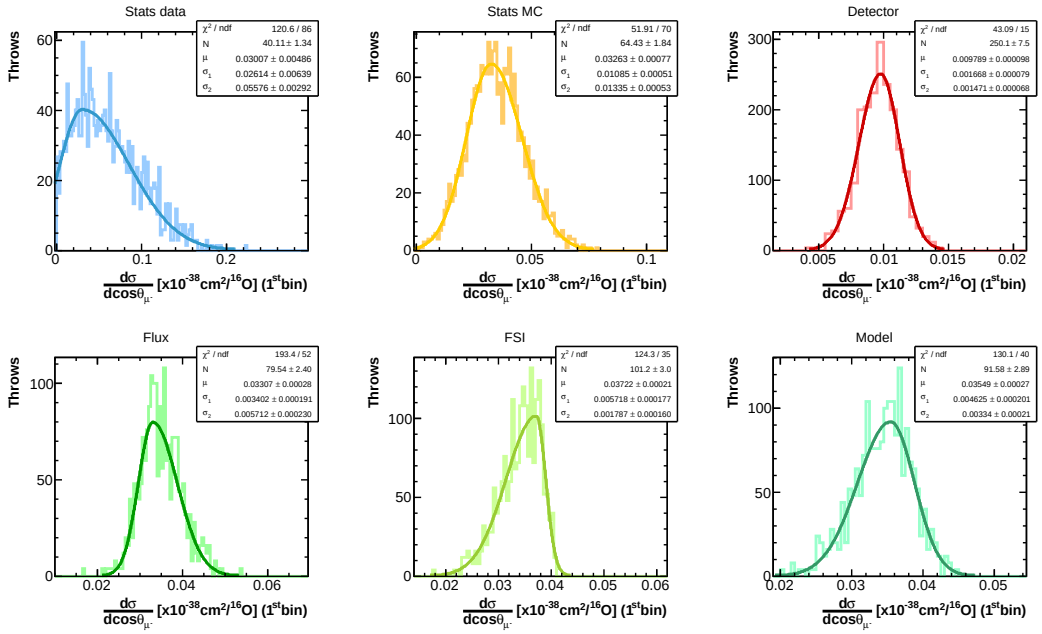

Figure D.23: Fits results for the different error sources for the first bin of $\cos\theta_{\mu^-}$.

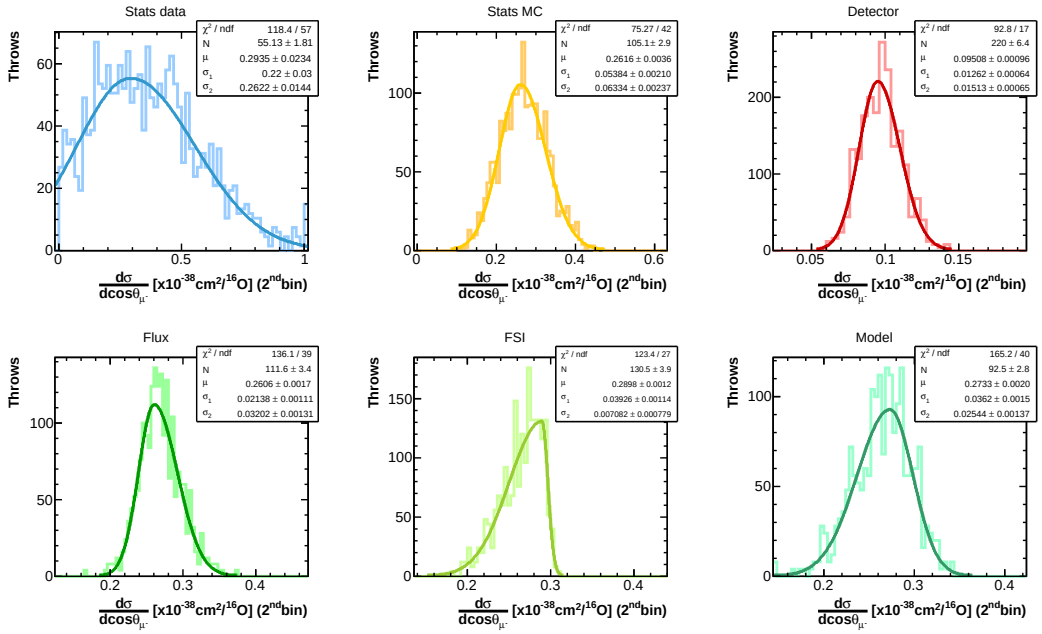

Figure D.24: Fits results for the different error sources for the second bin of $\cos\theta_{\mu^-}$.

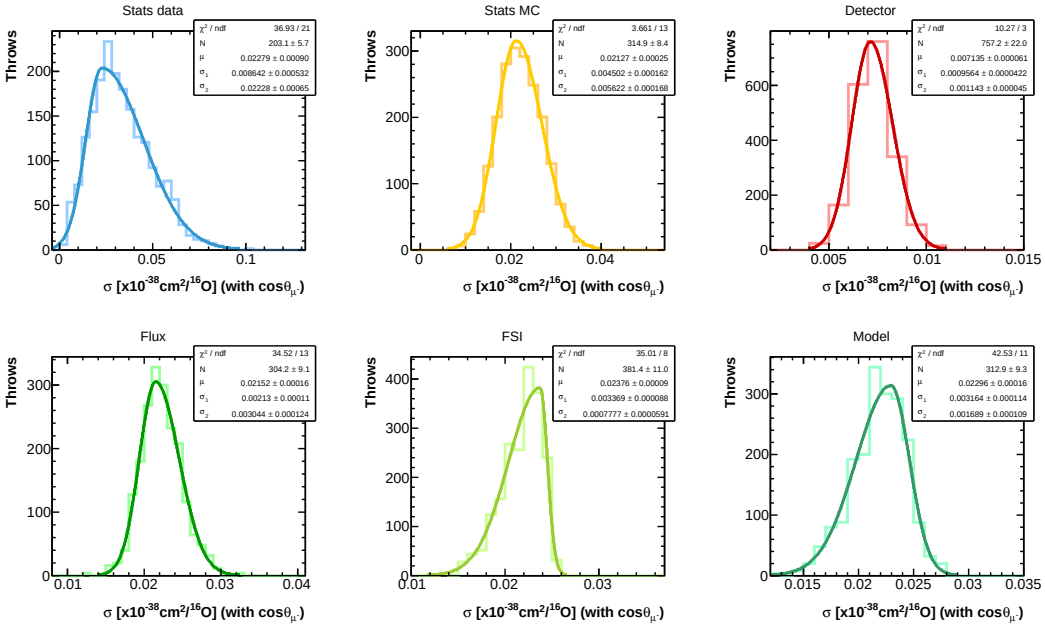

Figure D.25: Fits results for the different error sources for the cross section obtained by integrating over the $\cos\theta_{\mu^-}$ bins.

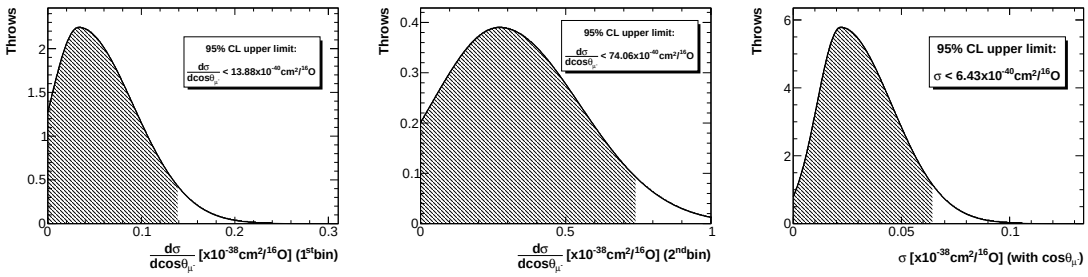

Figure D.26: Integration of the probability density function for the first (left) and second (centre) bins and for the total cross section (right). The 95 % CL upper limit is given in each case.

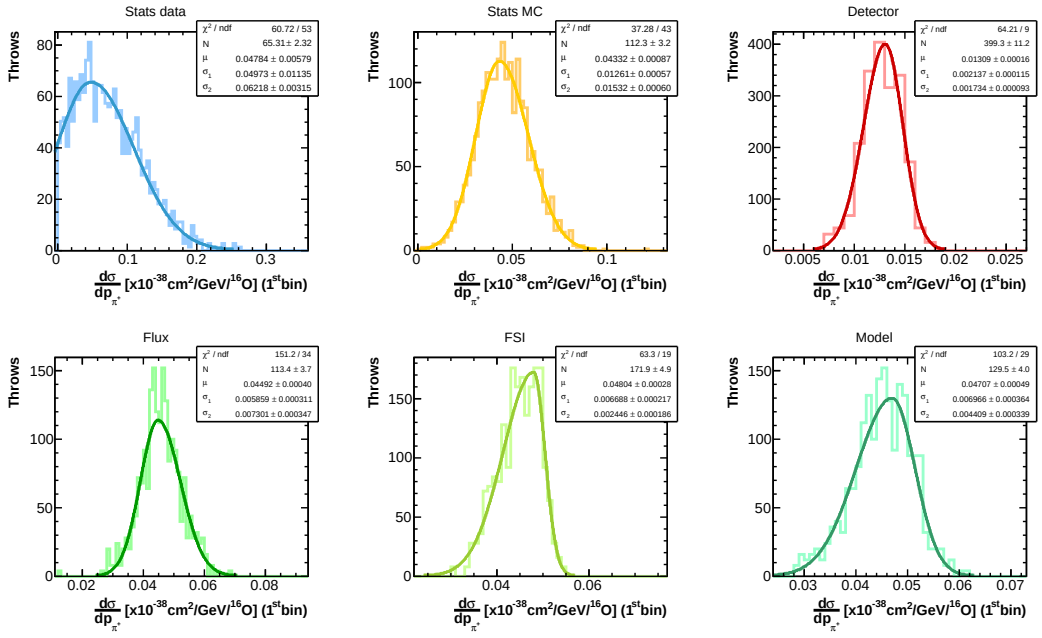

Figure D.27: Fits results for the different error sources for the first bin of p_{π^+}.

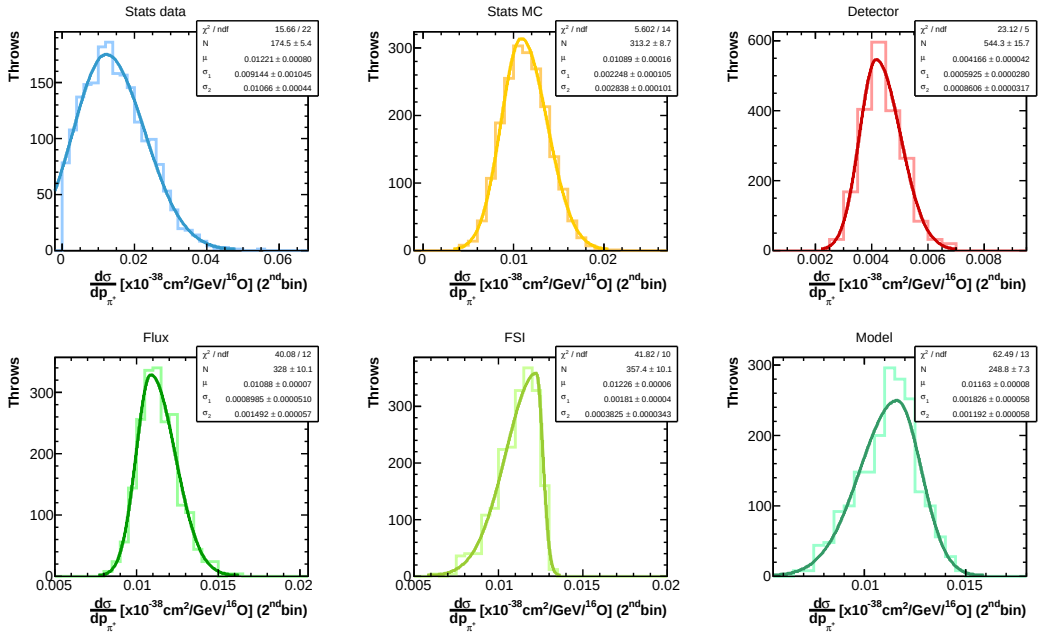

Figure D.28: Fits results for the different error sources for the second bin of p_{π^+}.

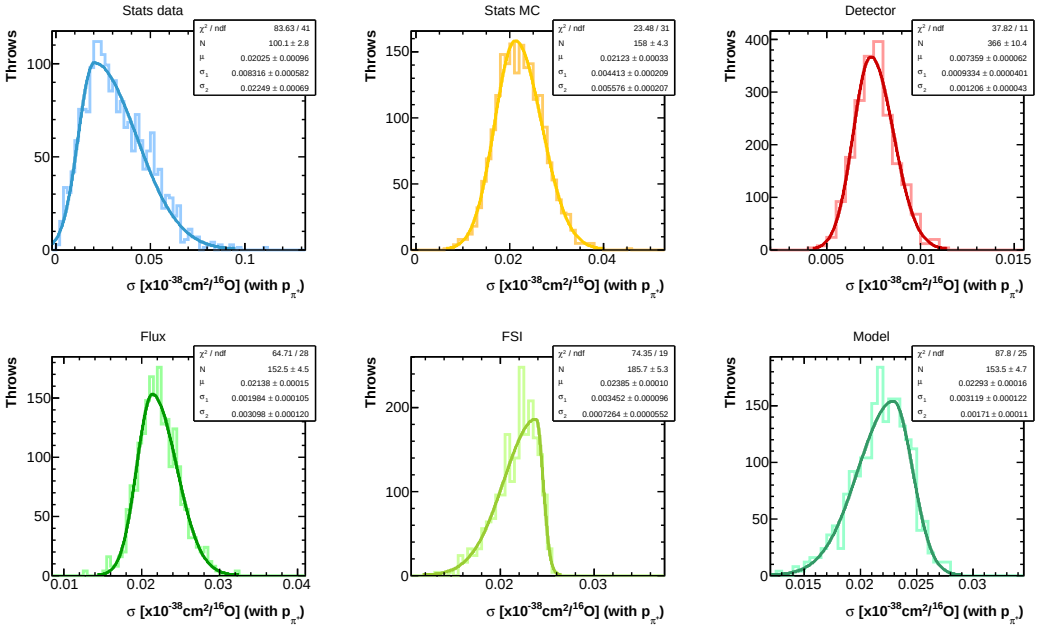

Figure D.29: Fits results for the different error sources for the cross section obtained by integrating over the $p_{\pi+}$ bins.

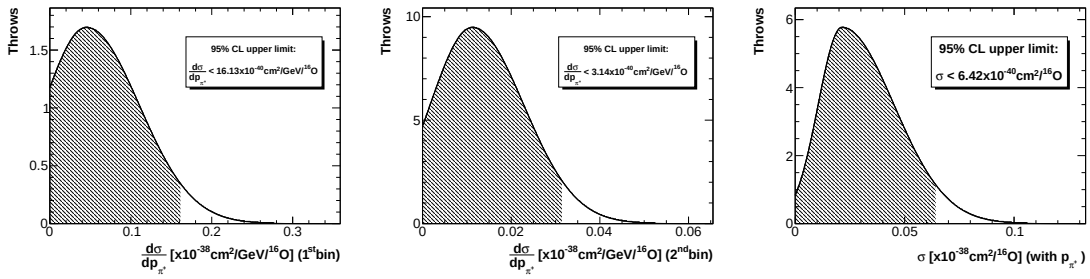

Figure D.30: Integration of the probability density function for the first (left) and second (centre) bins and for the total cross section (right). The 95 % CL upper limit is given in each case.

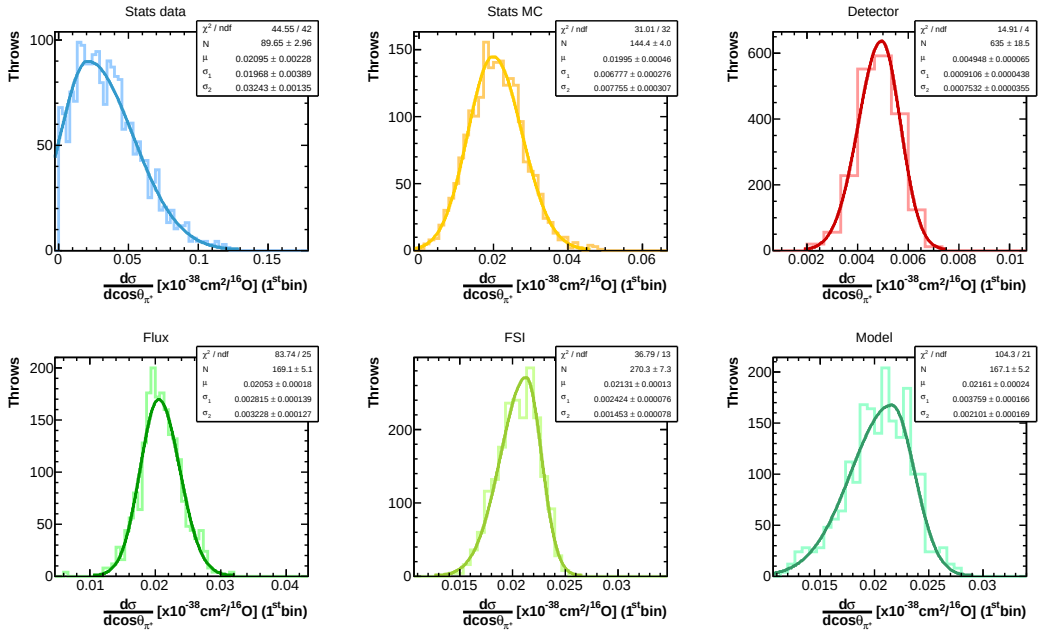

Figure D.31: Fits results for the different error sources for the first bin of $\cos\theta_{\pi^+}$.

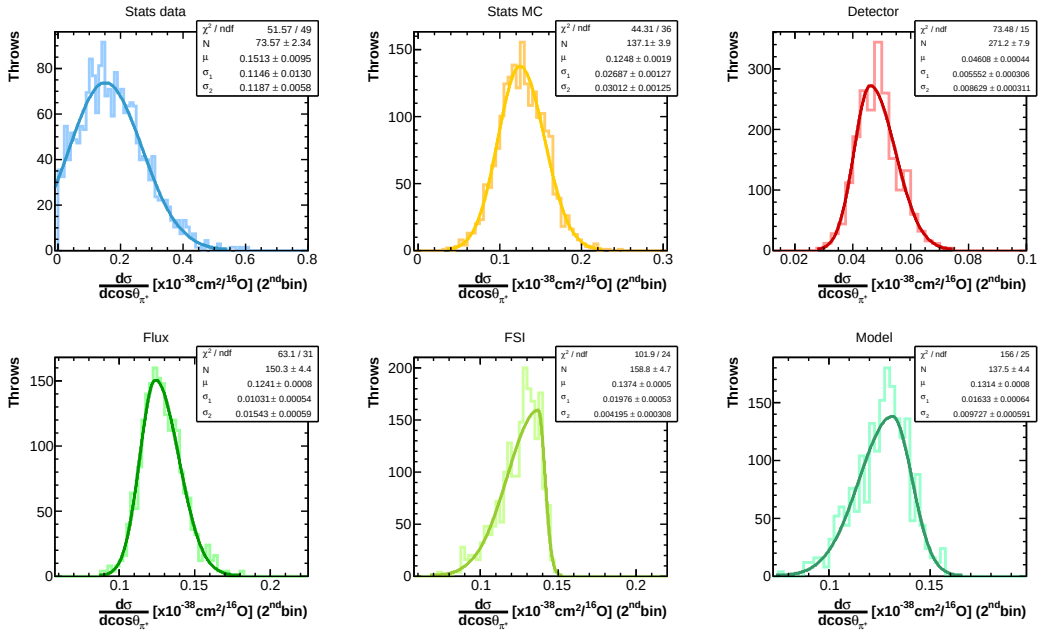

Figure D.32: Fits results for the different error sources for the second bin of $\cos\theta_{\pi^+}$.

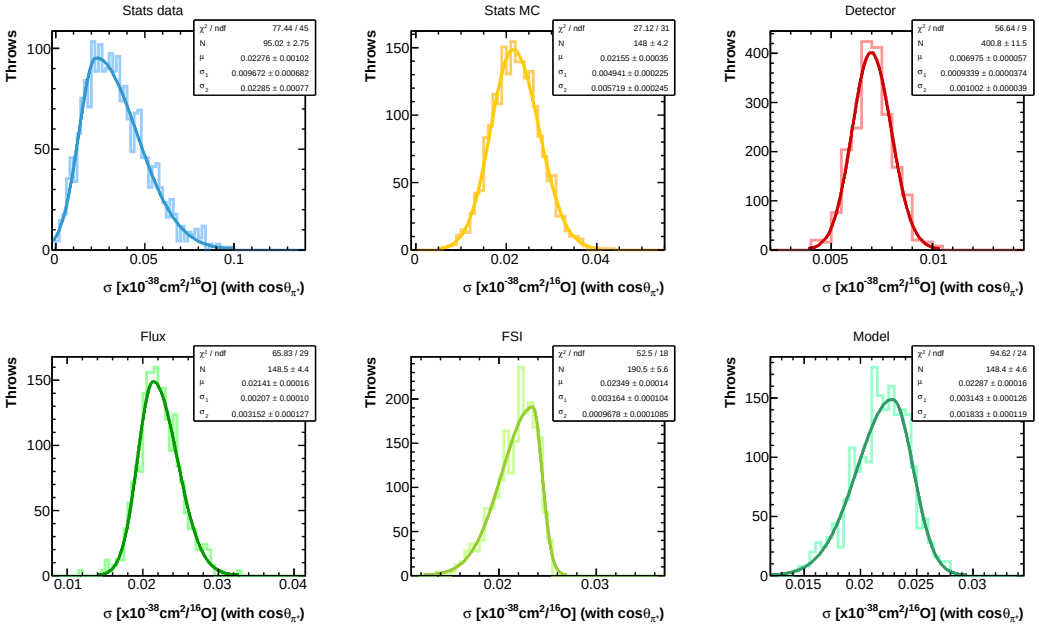

Figure D.33: Fits results for the different error sources for the cross section obtained by integrating over the $\cos\theta_{\pi^+}$ bins.

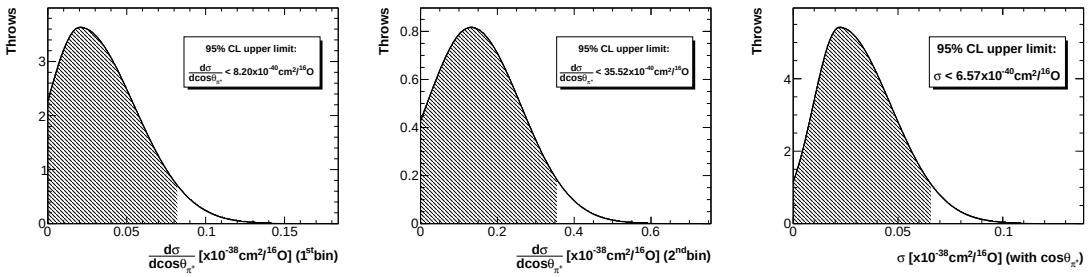

Figure D.34: Integration of the probability density function for the first (left) and second (centre) bins and for the total cross section (right). The 95 % CL upper limit is given in each case.

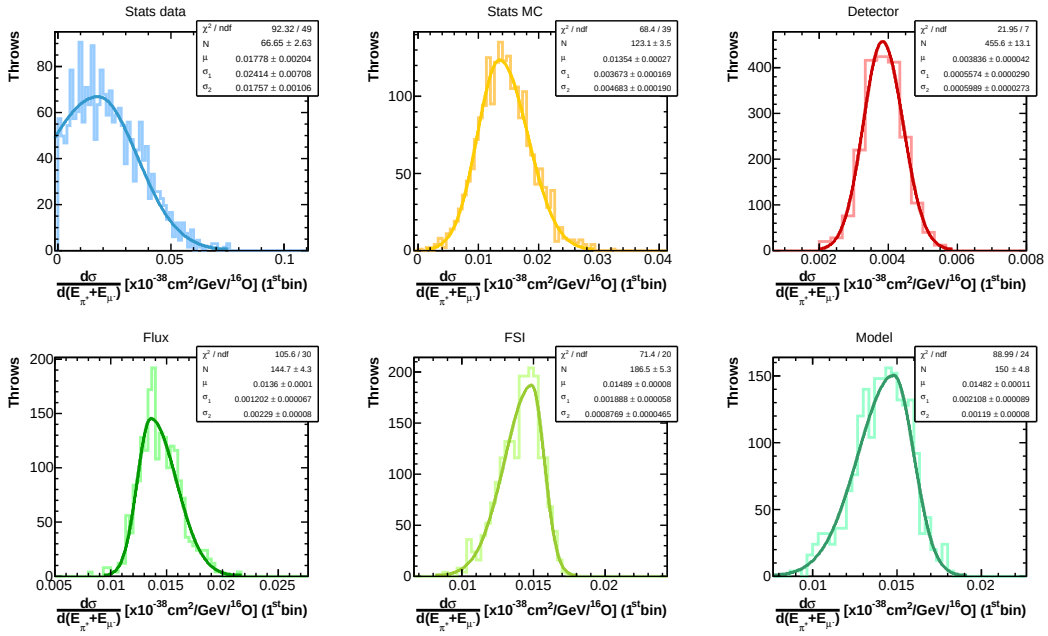

Figure D.35: Fits results for the different error sources for the first bin of $E_{\pi^+} + E_{\mu^-}$.

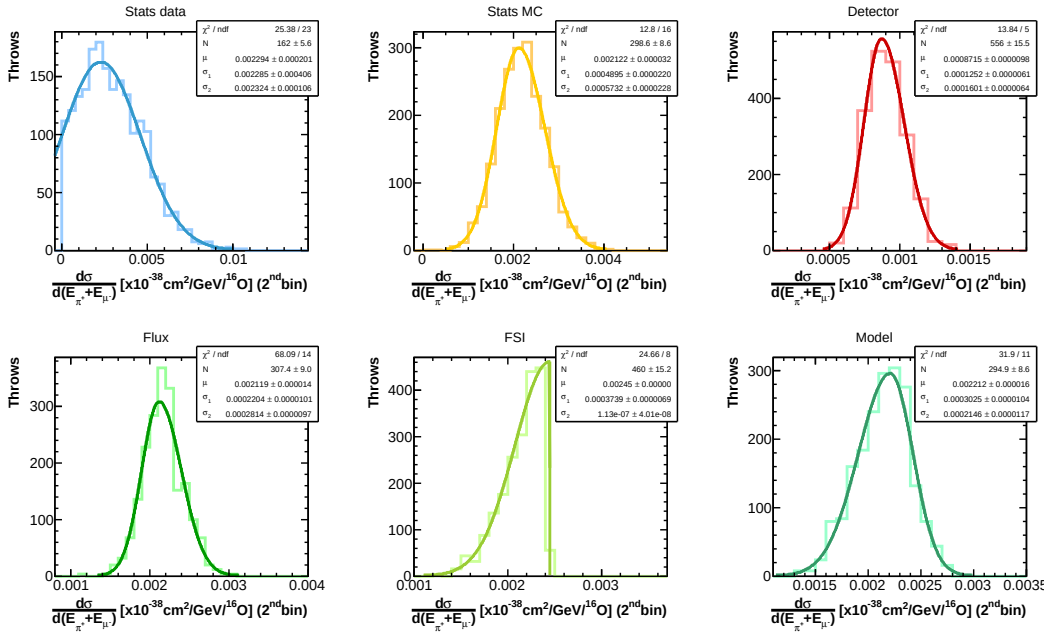

Figure D.36: Fits results for the different error sources for the second bin of $E_{\pi^+} + E_{\mu^-}$.

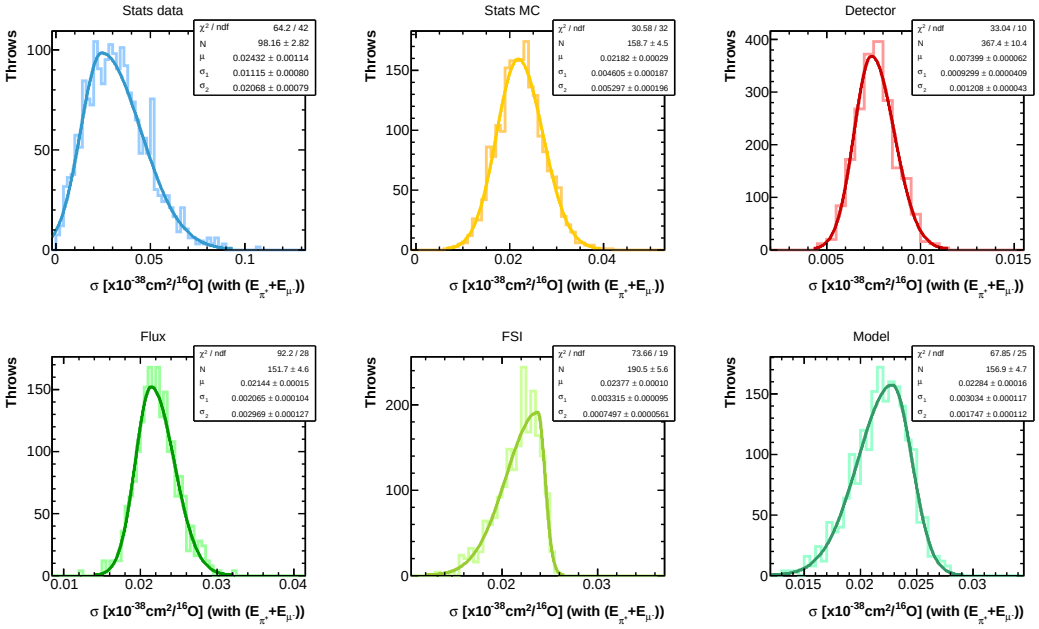

Figure D.37: Fits results for the different error sources for the cross section obtained by integrating over the $E_{\pi^+} + E_{\mu^-}$ bins.

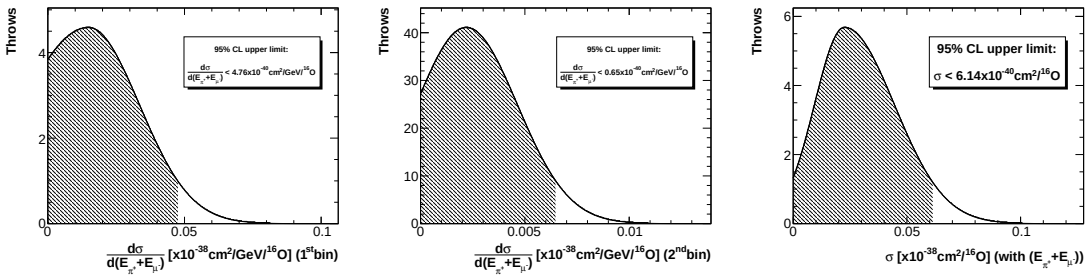

Figure D.38: Integration of the probability density function for the first (left) and second (centre) bins and for the total cross section (right). The 95 % CL upper limit is given in each case.

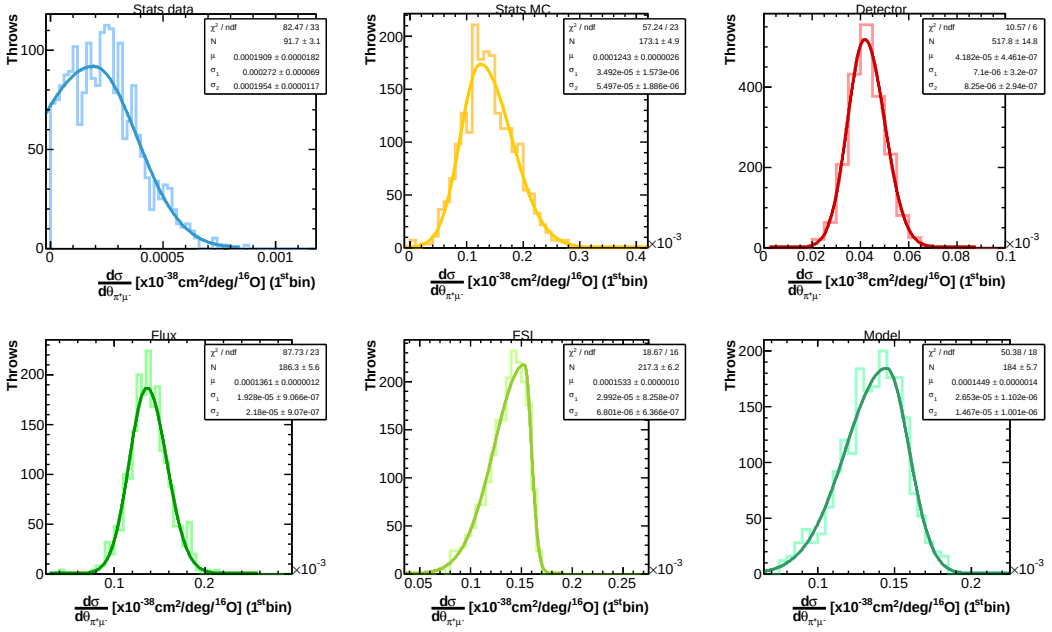

Figure D.39: Fits results for the different error sources for the first bin of $\theta_{\pi^+\mu^-}$.

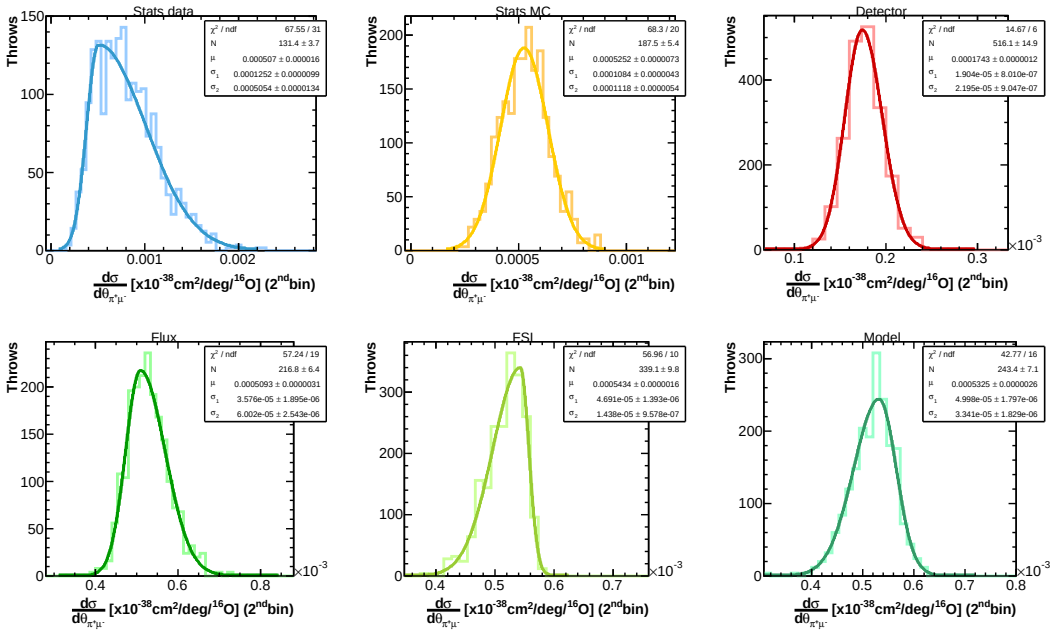

Figure D.40: Fits results for the different error sources for the second bin of $\theta_{\pi^+\mu^-}$.

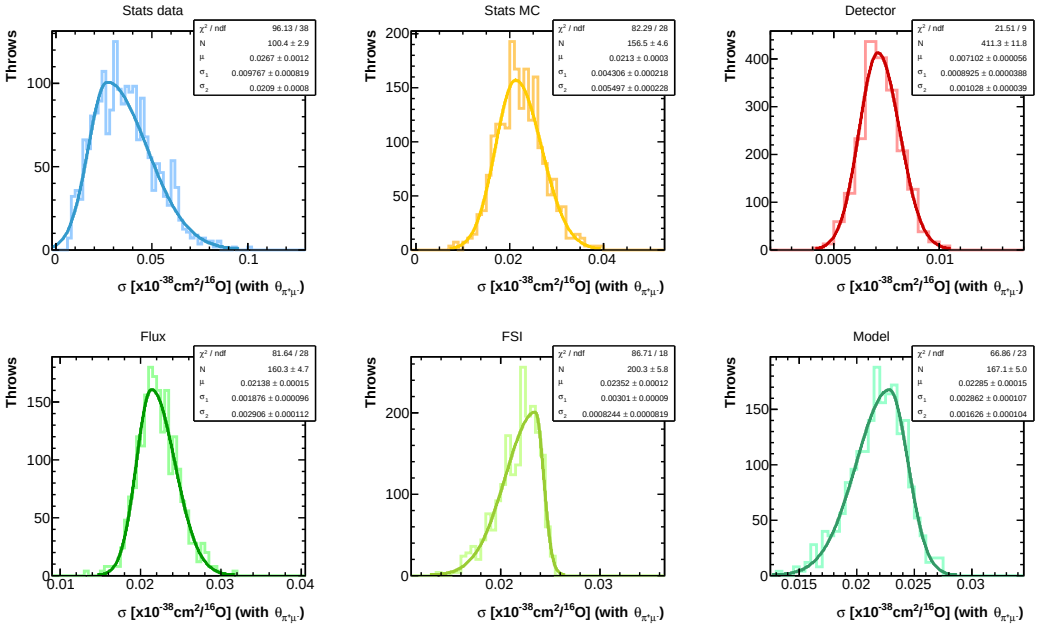

Figure D.41: Fits results for the different error sources for the cross section obtained by integrating over the $\theta_{\pi^+\mu^-}$ bins.

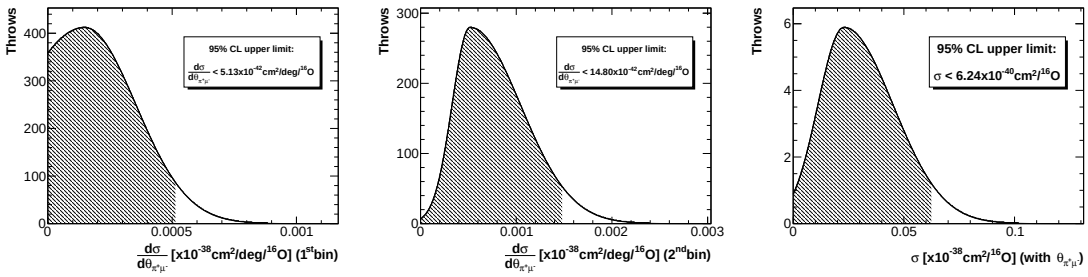

Figure D.42: Integration of the probability density function for the first (left) and second (centre) bins and for the total cross section (right). The 95 % CL upper limit is given in each case.

Bibliography

[1] Y. Fukuda et al. Evidence for oscillation of atmospheric neutrinos. *Phys. Rev. Lett.*, 81:1562–1567, 1998.

[2] Q. R. Ahmad et al. Measurement of the rate of $\nu_e + d \rightarrow p + p + e^-$ interactions produced by ^8b solar neutrinos at the sudbury neutrino observatory. *Phys. Rev. Lett.*, 87:071301, Jul 2001.

[3] K. Abe et al. Letter of Intent: The Hyper-Kamiokande Experiment — Detector Design and Physics Potential —. 2011.

[4] R. Acciarri et al. Long-Baseline Neutrino Facility (LBNF) and Deep Underground Neutrino Experiment (DUNE). 2016.

[5] Ellis, C. D. , Wooster, W. A. The Continuous Spectrum of β-Rays. *Nature*, 119:563–564, 1927.

[6] Bohr, Niels. Faraday lecture. chemistry and the quantum theory of atomic constitution. *J. Chem. Soc.*, pages 349–384, 1932.

[7] Wolfgang Pauli. Letter to Tübingen conference participants. Web document., December 1930.

[8] Chadwick, J. Possible Existence of a Neutron. *Nature*, 192:312, 1932.

[9] J. Chadwick. The existence of a neutron. *Proceedings of the Royal Society of London A: Mathematical, Physical and Engineering Sciences*, 136(830):692–708, 1932.

[10] E. Fermi. Trends to a Theory of beta Radiation. (In Italian). *Nuovo Cim.*, 11:1–19, 1934. [,535(1934)].

[11] E. Fermi. An attempt of a theory of beta radiation. *Z. Phys.*, 88:161–177, 1934.

[12] Sir A. Eddington. *The Philosophy of Physical Science*. Cambridge University Press, 1939.

[13] Carl D. Anderson. The positive electron. *Phys. Rev.*, 43:491–494, Mar 1933.

[14] Seth H. Neddermeyer and Carl D. Anderson. Note on the nature of cosmic-ray particles. *Phys. Rev.*, 51:884–886, May 1937.

[15] C. L. Cowan, F. Reines, F. B. Harrison, H. W. Kruse, and A. D. McGuire. Detection of the free neutrino: a confirmation. *Science*, 124(3212):103–104, 1956.

[16] C. S. Wu, E. Ambler, R. W. Hayward, D. D. Hoppes, and R. P. Hudson. Experimental test of parity conservation in beta decay. *Phys. Rev.*, 105:1413–1415, Feb 1957.

[17] M. Goldhaber, L. Grodzins, and A. W. Sunyar. Helicity of neutrinos. *Phys. Rev.*, 109:1015–1017, Feb 1958.

[18] T. D. Lee and C. N. Yang. Question of parity conservation in weak interactions. *Phys. Rev.*, 104:254–258, Oct 1956.

[19] T. D. Lee and C. N. Yang. Parity nonconservation and a two-component theory of the neutrino. *Phys. Rev.*, 105:1671–1675, Mar 1957.

[20] R. P. Feynman and M. Gell-Mann. Theory of the fermi interaction. *Phys. Rev.*, 109:193–198, Jan 1958.

[21] E. C. G. Sudarshan and R. E. Marshak. Chirality invariance and the universal fermi interaction. *Phys. Rev.*, 109:1860–1862, Mar 1958.

[22] G. Danby, J-M. Gaillard, K. Goulianos, L. M. Lederman, N. Mistry, M. Schwartz, and J. Steinberger. Observation of high-energy neutrino reactions and the existence of two kinds of neutrinos. *Phys. Rev. Lett.*, 9:36–44, Jul 1962.

[23] S. L. Glashow. Partial Symmetries of Weak Interactions. *Nucl. Phys.*, 22:579–588, 1961.

[24] Steven Weinberg. A model of leptons. *Phys. Rev. Lett.*, 19:1264–1266, Nov 1967.

[25] Abdus Salam and John Clive Ward. Electromagnetic and weak interactions. *Phys. Lett.*, 13:168–171, 1964.

[26] F. Englert and R. Brout. Broken symmetry and the mass of gauge vector mesons. *Phys. Rev. Lett.*, 13:321–323, Aug 1964.

[27] Peter W. Higgs. Broken symmetries and the masses of gauge bosons. *Phys. Rev. Lett.*, 13:508–509, Oct 1964.

[28] F. J. Hasert et al. Observation of Neutrino Like Interactions Without Muon Or Electron in the Gargamelle Neutrino Experiment. *Phys. Lett.*, B46:138–140, 1973.

[29] G. Arnison et al. Experimental Observation of Lepton Pairs of Invariant Mass Around 95-GeV/c**2 at the CERN SPS Collider. *Phys. Lett.*, B126:398–410, 1983.

[30] P. Bagnaia et al. Evidence for Z0 —> e+ e- at the CERN anti-p p Collider. *Phys. Lett.*, B129:130–140, 1983.

[31] Georges Aad et al. Observation of a new particle in the search for the Standard Model Higgs boson with the ATLAS detector at the LHC. *Phys. Lett.*, B716:1–29, 2012.

[32] Serguei Chatrchyan et al. Observation of a new boson at a mass of 125 GeV with the CMS experiment at the LHC. *Phys. Lett.*, B716:30–61, 2012.

[33] M. L. Perl et al. Evidence for anomalous lepton production in $e^+ - e^-$ annihilation. *Phys. Rev. Lett.*, 35:1489–1492, Dec 1975.

[34] K. Kodama et al. Observation of tau neutrino interactions. *Phys. Lett.*, B504:218–224, 2001.

[35] Michael Edward Peskin and Daniel V. Schroeder. *An introduction to quantum field theory*. Advanced book program. Westview Press Reading (Mass.), Boulder (Colo.), 1995. Autre tirage : 1997.

[36] K. A. Olive et al. Review of Particle Physics. *Chin. Phys.*, C38:090001, 2014.

[37] Ettore Majorana. Teoria simmetrica dell'elettrone e del positrone. *Il Nuovo Cimento (1924-1942)*, 14(4):171, 2008.

[38] S. Andringa et al. Current Status and Future Prospects of the SNO+ Experiment. *Adv. High Energy Phys.*, 2016:6194250, 2016.

[39] W Xu and Majorana Collaboration. The majorana demonstrator: A search for neutrinoless double-beta decay of 76 ge. *Journal of Physics: Conference Series*, 606(1):012004, 2015.

[40] M. Agostini et al. Background free search for neutrinoless double beta decay with GERDA Phase II. 2017. [Nature544,47(2017)].

[41] M. Auger et al. The EXO-200 detector, part I: Detector design and construction. *JINST*, 7:P05010, 2012.

[42] C. Alduino et al. Cuore Sensitivity to $0\nu\beta\beta$ Decay. 2017.

[43] Alberto Garfagnini. Neutrinoless Double Beta Decay Experiments. In *12th Conference on Flavor Physics and CP Violation (FPCP 2014) Marseille, France, May 26-30, 2014*, 2014.

[44] William D. Harkins. The abundance of the elements in relation to the hydrogen-helium structure of the atoms. *Proceedings of the National Academy of Sciences*, 2(4):216–224, 1916.

[45] H. A. Bethe. Energy production in stars. *Phys. Rev.*, 55:434–456, Mar 1939.

[46] John N. Bahcall, Aldo M. Serenelli, and Sarbani Basu. New solar opacities, abundances, helioseismology, and neutrino fluxes. *The Astrophysical Journal Letters*, 621(1):L85, 2005.

[47] John N. Bahcall. Solar neutrinos. i. theoretical. *Phys. Rev. Lett.*, 12:300–302, Mar 1964.

[48] Raymond Davis, Don S. Harmer, and Kenneth C. Hoffman. Search for neutrinos from the sun. *Phys. Rev. Lett.*, 20:1205–1209, May 1968.

[49] A. I. Abazov et al. First results from the Soviet-American gallium experiment. *Nucl. Phys. Proc. Suppl.*, 19:84–93, 1991. [,84(1991)].

[50] P. Anselmann et al. Solar neutrinos observed by gallex at gran sasso. *Physics Letters B*, 285(4):376 – 389, 1992.

[51] K. S. Hirata et al. Observation of b-8 solar neutrinos in the kamiokande-ii detector. *Phys. Rev. Lett.*, 63:16, 1989.

[52] John N. Bahcall. Solar models and solar neutrinos: Current status. *Phys. Scripta*, T121:46–50, 2005.

[53] B. Pontecorvo. Electron and Muon Neutrinos. *Sov. Phys. JETP*, 10:1236–1240, 1960. [Zh. Eksp. Teor. Fiz.37,1751(1959)].

[54] Ziro Maki, Masami Nakagawa, and Shoichi Sakata. Remarks on the unified model of elementary particles. *Prog. Theor. Phys.*, 28:870–880, 1962.

[55] L. Wolfenstein. Neutrino oscillations in matter. *Phys. Rev. D*, 17:2369–2374, May 1978.

[56] S. P. Mikheev and A. Yu. Smirnov. Neutrino Oscillations in an Inhomogeneous Medium: Adiabatic Regime. *Sov. Phys. JETP*, 65:230–236, 1987. [Zh. Eksp. Teor. Fiz.92,404(1987)].

[57] Stephen J. Parke. Nonadiabatic level crossing in resonant neutrino oscillations. *Phys. Rev. Lett.*, 57:1275–1278, Sep 1986.

[58] Q. R. Ahmad et al. Direct evidence for neutrino flavor transformation from neutral current interactions in the Sudbury Neutrino Observatory. *Phys. Rev. Lett.*, 89:011301, 2002.

[59] B. Aharmim et al. Electron energy spectra, fluxes, and day-night asymmetries of B-8 solar neutrinos from measurements with NaCl dissolved in the heavy-water detector at the Sudbury Neutrino Observatory. *Phys. Rev.*, C72:055502, 2005.

[60] K. Eguchi et al. First results from kamland: Evidence for reactor antineutrino disappearance. *Phys. Rev. Lett.*, 90:021802, Jan 2003.

[61] Hyper-Kamiokande Design Report. 2016.

[62] R. Acciarri et al. Long-Baseline Neutrino Facility (LBNF) and Deep Underground Neutrino Experiment (DUNE). 2015.

[63] J. A. Formaggio and G. P. Zeller. From eV to EeV: Neutrino Cross Sections Across Energy Scales. *Rev. Mod. Phys.*, 84:1307–1341, 2012.

[64] *Fundamental Physics at the Intensity Frontier*, 2012.

[65] C.H. Llewellyn Smith. Neutrino reactions at accelerator energies. *Physics Reports*, 3(5):261 – 379, 1972.

[66] Stephen L. Adler. Tests of the conserved vector current and partially conserved axial-vector current hypotheses in high-energy neutrino reactions. *Phys. Rev.*, 135:B963–B966, Aug 1964.

[67] Bastian Maerkisch and Hartmut Abele. Measurement of the Axial-Vector Coupling Constant g_A in Neutron Beta Decay. In *8th International Workshop on the CKM Unitarity Triangle (CKM 2014) Vienna, Austria, September 8-12, 2014*, 2014.

[68] Veronique Bernard, Latifa Elouadrhiri, and Ulf-G. Meissner. Axial structure of the nucleon: Topical Review. *J. Phys.*, G28:R1–R35, 2002.

[69] Carlo Giunti and Chung W. Kim. *Fundamentals of neutrino physics and astrophysics*. Oxford University Press, Oxford ;New York, 2007.

[70] H. Hassanabadi, A. Armat, and L. Naderi. Relativistic Fermi-Gas Model for Nucleus. *Found. Phys.*, 44(11):1188–1194, 2014.

[71] O. Benhar, A. Fabrocini, and S. Fantoni. The nucleon spectral function in nuclear matter. *Nuclear Physics A*, 505:267–299, December 1989.

[72] Dieter Rein and Lalit M. Sehgal. Neutrino Excitation of Baryon Resonances and Single Pion Production. *Annals Phys.*, 133:79–153, 1981.

[73] L. David Roper. Evidence for a P_{11} pion-nucleon resonance at 556 mev. *Phys. Rev. Lett.*, 12:340–342, Mar 1964.

[74] Richard P. Feynman. Very high-energy collisions of hadrons. *Phys. Rev. Lett.*, 23:1415–1417, Dec 1969.

[75] B. Z. Kopeliovich and P. Marage. Low Q**2, high neutrino nu physics (CVC, PCAC, hadron dominance). *Int. J. Mod. Phys.*, A8:1513–1602, 1993.

[76] D. Rein. Diffractive Pion Production in Neutrino Reactions. *Nucl. Phys.*, B278:61–77, 1986.

[77] Dieter Rein and Lalit M. Sehgal. Coherent pi0 Production in Neutrino Reactions. *Nucl. Phys.*, B223:29–44, 1983.

[78] D. Rein and L. M. Sehgal. PCAC and the Deficit of Forward Muons in pi+ Production by Neutrinos. *Phys. Lett.*, B657:207–209, 2007.

[79] Ch. Berger and L. M. Sehgal. PCAC and coherent pion production by low energy neutrinos. *Phys. Rev.*, D79:053003, 2009.

[80] L. Alvarez-Ruso, L. S. Geng, S. Hirenzaki, M. J. Vicente Vacas, T. Leitner, and U. Mosel. Neutrino-induced coherent pion production. *AIP Conf. Proc.*, 967:201–204, 2007.

[81] Stephen L. Adler. Photoproduction, electroproduction and weak single pion production in the (3,3) resonance region. *Annals Phys.*, 50:189–311, 1968.

[82] O. Dumbrajs, J. Fröhlich, U. Klein, and H. G. Schlaile. Analysis of $\pi^{\pm} -^{12}$ C elastic scattering. *Phys. Rev. C*, 29:581–591, Feb 1984.

[83] H. G. Schlaile. Amplitude analysis of $\pi^{\pm}-^{12}$C elastic scattering. *Phys. Rev. C*, 55:2584–2592, May 1997.

[84] Artur M. Ankowski and Omar Benhar. Electroweak nuclear response at moderate momentum transfer. *Phys. Rev. C*, 83:054616, May 2011.

[85] M. Martini, M. Ericson, G. Chanfray, and J. Marteau. Unified approach for nucleon knock-out and coherent and incoherent pion production in neutrino interactions with nuclei. *Phys. Rev. C*, 80:065501, Dec 2009.

[86] J. Nieves, J. E. Amaro, and M. Valverde. Inclusive quasielastic charged-current neutrino-nucleus reactions. *Phys. Rev. C*, 70:055503, Nov 2004.

[87] K. Arisaka et al. Search for nucleon decay into charged lepton + mesons. *J. Phys. Soc. Jap.*, 54:3213–3216, 1985.

[88] K. S. Hirata et al. Experimental study of the atmospheric neutrino flux. *Phys. Lett.*, B205:416, 1988.

[89] K. Hirata et al. Observation of a neutrino burst from the supernova sn1987a. *Phys. Rev. Lett.*, 58:1490–1493, 1987.

[90] Yuichi Oyama. K2K (KEK to Kamioka) neutrino - oscillation experiment at KEK PS. In *YITP Workshop on Flavor Physics Kyoto, Japan, January 28-30, 1998*, 1998.

[91] K. Abe et al. Measurements of neutrino oscillation in appearance and disappearance channels by the T2K experiment with 6.6×10^{20} protons on target. *Phys. Rev.*, D91(7):072010, 2015.

[92] K. Abe et al. The T2K Experiment. *Nucl. Instrum. Meth.*, A659:106–135, 2011.

[93] K. Abe et al. T2K neutrino flux prediction. *Phys. Rev.*, D87(1):012001, 2013. [Addendum: Phys. Rev.D87,no.1,019902(2013)].

[94] Y. Yamazaki, K. Hasegawa, M. Ikegami, Y. Irie, T. Kato, H. Kobayashi, S. Machida, Y. Mori, F. Noda, H. Suzuki, et al. Accelerator technical design report for J-PARC. 2003.

[95] T. Nakamoto et al. Design of superconducting combined function magnets for the 50 GeV proton beam line for the J-PARC neutrino experiment. *IEEE Trans. Appl. Supercond.*, 14(2):616–619, 2004.

[96] S. Bhadra, M. Cadabeschi, P. de Perio, V. Galymov, M. Hartz, B. Kirby, A. Konaka, A.D. Marino, J.F. Martin, D. Morris, and L. Stawnyczy. Optical transition radiation monitor for the T2K experiment. *Nuclear Instruments and Methods in Physics Research Section A, Accelerators, Spectrometers, Detectors and Associated Equipment*, 703:45 – 58, 2013.

[97] Densham, Baldwin, Fitton, Rooney, Woodward, Ichikawa, Koike, Nakadaira. Design Of The T2K Target For a 0.75-MW Proton Beam. In *46^{th} ICFA Advanced Beam Dynamics Workshop on High-Intensity and High-Brightness Hadron Beam, Morschach, Switzerland, October 2010*, 2010.

[98] Principle of focusing with a magnetic horn.

[99] K. Matsuoka et al. Design and performance of the muon monitor for the T2K neutrino oscillation experiment. *Nucl. Instrum. Meth.*, A624:591–600, 2010.

[100] G. De Lellis et al. Momentum measurement by the angular method in the Emulsion Cloud Chamber. *Nucl. Instrum. Meth.*, A512:539–545, 2003.

[101] Laura Zambelli. *Contraintes sur la prédiction des flux de neutrinos de T2K par les données de l'expérience de hadroproduction NA61/SHINE.* PhD thesis, Paris U., VI-VII, 2013.

[102] T. T. Böhlen, F. Cerutti, M. P. W. Chin, A. Fassò, A. Ferrari, P. G. Ortega, A. Mairani, P. R. Sala, G. Smirnov, and V. Vlachoudis. The FLUKA Code: Developments and Challenges for High Energy and Medical Applications. *Nuclear Data Sheets*, 120:211–214, June 2014.

[103] R. Brun, F. Bruyant, M. Maire, A. C. McPherson, and P. Zanarini. GEANT3. 1987.

[104] C. Zeitnitz and T. A. Gabriel. The GEANT - CALOR interface and benchmark calculations of ZEUS test calorimeters. *Nucl. Instrum. Meth.*, A349:106–111, 1994.

[105] N. Abgrall et al. Pion emission from the T2K replica target: method, results and application. *Nucl. Instrum. Meth.*, A701:99–114, 2013.

[106] Alexis Hasler. *T2K Replica Target Hadron Production Measurements in NA61/SHINE and T2K Neutrino Flux Predictions.* PhD thesis, Geneva U., 2015.

[107] A. Vacheret et al. Characterization and Simulation of the Response of Multi Pixel Photon Counters to Low Light Levels. *Nucl. Instrum. Meth.*, A656(1):69–83, 2011.

[108] G. Arnison et al. Experimental Observation of Events with Large Missing Transverse Energy Accompanied by a Jet Or a Photon(s) in p anti-p Collisions at s**(1/2)=540-GeV. *Phys. Lett.*, B139:115, 1984.

[109] J. Altegoer et al. The NOMAD experiment at the CERN SPS. *Nucl. Instrum. Meth.*, A404:96–128, 1998.

[110] CERN Courier Volume 48, Number 3, April 2008. 2008.

[111] S. Aoki et al. The T2K Side Muon Range Detector (SMRD). *Nucl. Instrum. Meth.*, A698:135–146, 2013.

[112] S. Assylbekov et al. The T2K ND280 Off-Axis Pi-Zero Detector. *Nucl. Instrum. Meth.*, A686:48–63, 2012.

[113] D. Allan et al. The Electromagnetic Calorimeter for the T2K Near Detector ND280. *JINST*, 8:P10019, 2013.

[114] P. A. Amaudruz et al. The T2K Fine-Grained Detectors. *Nucl. Instrum. Meth.*, A696:1–31, 2012.

[115] N. Abgrall et al. Time Projection Chambers for the T2K Near Detectors. *Nucl. Instrum. Meth.*, A637:25–46, 2011.

[116] K. Abe et al. Search for proton decay via $p \to \nu K^+$ using 260 kiloton $\cdot$ year data of super-kamiokande. *Phys. Rev. D*, 90:072005, Oct 2014.

[117] Yoshinari Hayato. A neutrino interaction simulation program library NEUT. *Acta Phys. Polon.*, B40:2477–2489, 2009.

[118] Rene Brun and Fons Rademakers. New computing techniques in physics research v root — an object oriented data analysis framework. *Nuclear Instruments and Methods in Physics Research Section A: Accelerators, Spectrometers, Detectors and Associated Equipment*, 389(1):81 – 86, 1997.

[119] S. Agostinelli et al. GEANT4: A Simulation toolkit. *Nucl. Instrum. Meth.*, A506:250–303, 2003.

[120] Omar Benhar and Adelchi Fabrocini. Two nucleon spectral function in infinite nuclear matter. *Phys. Rev.*, C62:034304, 2000.

[121] R. A. Smith and E. J. Moniz. NEUTRINO REACTIONS ON NUCLEAR TARGETS. *Nucl. Phys.*, B43:605, 1972. [Erratum: Nucl. Phys.B101,547(1975)].

[122] J. Nieves, I. Ruiz Simo, and M. J. Vicente Vacas. Inclusive charged-current neutrino-nucleus reactions. *Phys. Rev. C*, 83:045501, Apr 2011.

[123] Krzysztof M. Graczyk and Jan T. Sobczyk. Form factors in the quark resonance model. *Phys. Rev. D*, 77:053001, Mar 2008.

[124] A. Rodriguez et al. Measurement of single charged pion production in the charged-current interactions of neutrinos in a 1.3-GeV wide band beam. *Phys. Rev.*, D78:032003, 2008.

[125] M. Hasegawa et al. Search for coherent charged pion production in neutrino-carbon interactions. *Phys. Rev. Lett.*, 95:252301, 2005.

[126] K. Hiraide et al. Search for Charged Current Coherent Pion Production on Carbon in a Few-GeV Neutrino Beam. *Phys. Rev.*, D78:112004, 2008.

[127] J. Wolcott et al. Evidence for Neutral-Current Diffractive Neutral Pion Production from Hydrogen in Neutrino Interactions on Hydrocarbon. *Submitted to: Phys. Rev. Lett.*, 2016.

[128] M. Glück, E. Reya, and A. Vogt. Dynamical parton distributions revisited. *The European Physical Journal C - Particles and Fields*, 5(3):461–470, 1998.

[129] A. Bodek and U. K. Yang. Modeling neutrino and electron scattering inelastic cross- sections in the few GeV region with effective LO PDFs TV Leading Order. In *2nd International Workshop on Neutrino-Nucleus Interactions in the Few GeV Region (NuInt 02) Irvine, California, December 12-15, 2002*, 2003.

[130] Torbjorn Sjostrand. High-energy physics event generation with PYTHIA 5.7 and JETSET 7.4. *Comput. Phys. Commun.*, 82:74–90, 1994.

[131] A. Cervera-Villanueva, J. J. Gómez-Cadenas, and J. A. Hernando. RecPack, a reconstruction toolkit. *Nuclear Instruments and Methods in Physics Research A*, 534:180–183, November 2004.

[132] R. E. Kalman. A New Approach to Linear Filtering and Prediction Problems. *Transactions of the ASME – Journal of Basic Engineering*, (82 (Series D)):35–45, 1960.

[133] A Vacheret, S Greenwood, M Noy, M Raymond, and A Weber. The front end readout system for the t2k-nd280 detectors. pages 1984–1991. IEEE, 2007.

[134] T2K Collaboration. T2k internal note 209*: Data quality at the near detectors for run 5.

[135] A. Higuera et al. Measurement of Coherent Production of $\pi^{\pm}$ in Neutrino and Antineutrino Beams on Carbon from E_{ν} of 1.5 to 20 GeV. *Phys. Rev. Lett.*, 113(26):261802, 2014.

[136] H. Faissner et al. Observation of Neutrino and Anti-neutrino Induced Coherent Neutral Pion Production Off ^{27}Al. *Phys. Lett.*, B125:230, 1983.

[137] E. Isiksal, D. Rein, and J. G. Morfin. EVIDENCE FOR NEUTRINO AND ANTI-NEUTRINOS INDUCED COHERENT PI0 PRODUCTION. *Phys. Rev. Lett.*, 52:1096–1099, 1984.

[138] F. Bergsma et al. Measurement of the Cross-section of Coherent π^0 Production by Muon Neutrino and Anti-neutrino Neutral Current Interactions on Nuclei. *Phys. Lett.*, B157:469, 1985.

[139] H. J. Grabosch et al. COHERENT PION PRODUCTION IN NEUTRINO AND ANTI-NEUTRINO INTERACTIONS ON NUCLEI OF HEAVY FREON MOLECULES. *Z. Phys.*, C31:203, 1986.

[140] C. T. Kullenberg et al. A Measurement of Coherent Neutral Pion Production in Neutrino Neutral Current Interactions in NOMAD. *Phys. Lett.*, B682:177–184, 2009.

[141] R. Acciarri et al. First Measurement of Neutrino and Antineutrino Coherent Charged Pion Production on Argon. *Phys. Rev. Lett.*, 113(26):261801, 2014. [Erratum: Phys. Rev. Lett.114,no.3,039901(2015)].

[142] K. Abe et al. Measurement of coherent π^+ production in low energy neutrino-carbon scattering. *Phys. Rev. Lett.*, 117:192501, Nov 2016.

[143] C. Andreopoulos et al. The GENIE Neutrino Monte Carlo Generator. *Nucl. Instrum. Meth.*, A614:87–104, 2010.

[144] Costas Andreopoulos, Christopher Barry, Steve Dytman, Hugh Gallagher, Tomasz Golan, Robert Hatcher, Gabriel Perdue, and Julia Yarba. The GENIE Neutrino Monte Carlo Generator: Physics and User Manual. 2015.

[145] Cezary Juszczak, Jaroslaw A. Nowak, and Jan T. Sobczyk. Simulations from a new neutrino event generator. *Nucl. Phys. Proc. Suppl.*, 159:211–216, 2006. [,211(2005)].

[146] D. Ashery, I. Navon, G. Azuelos, H. K. Walter, H. J. Pfeiffer, and F. W. Schlepütz. True absorption and scattering of pions on nuclei. *Phys. Rev. C*, 23:2173–2185, May 1981.

[147] P. Adamson et al. Measurement of single π^0 production by coherent neutral-current ν Fe interactions in the MINOS Near Detector. *Phys. Rev.*, D94(7):072006, 2016.

[148] G. D'Agostini. A multidimensional unfolding method based on bayes' theorem. *Nuclear Instruments and Methods in Physics Research Section A: Accelerators, Spectrometers, Detectors and Associated Equipment*, 362(2):487 – 498, 1995.

[149] G. D'Agostini. Improved iterative Bayesian unfolding. *ArXiv e-prints*, October 2010.

[150] G Zech. Upper limits in experiments with background or measurement errors. *Nucl. Instrum. Methods Phys. Res., A*, 277(CERN-EP-88-164):608. 6 p, Nov 1988.

[151] K. K. Gan, J. Lee, and R. Kass. Incorporation of the statistical uncertainty in the background estimate into the upper limit on the signal. *Nucl. Instrum. Meth.*, A412:475–482, 1998.

[152] The T2K Collaboration. T2K internal note 212*: ν_μ CC event selections in the ND280 tracker using Run 2+3+4.

[153] The T2K Collaboration. T2K internal note 108*: Cross section parameters for the 2012a oscillation analysis.

*The T2K internal notes can be confidentially obtained if requested by the examiners for the purpose of assessing the thesis.